

Heat Transfer from Drops in Shearing Flows and Collective Motion in Micro-scale Swimmer Suspensions

A Thesis
Submitted for the Degree of
MASTER OF SCIENCE (ENGINEERING)

by
DEEPAK KRISHNAMURTHY



ENGINEERING MECHANICS UNIT
JAWAHARLAL NEHRU CENTRE FOR ADVANCED SCIENTIFIC RESEARCH
(A Deemed University)
Bangalore – 560 064

JULY 2014

My Parents

DECLARATION

I hereby declare that the matter embodied in the thesis entitled “**Heat Transfer from Drops in Shearing Flows and Collective Motion in Micro-scale Swimmer Suspensions**” is the result of investigations carried out by me at the Engineering Mechanics Unit, Jawaharlal Nehru Centre for Advanced Scientific Research, Bangalore, India under the supervision of **Prof. Ganesh Subramanian** and that it has not been submitted elsewhere for the award of any degree or diploma.

In keeping with the general practice in reporting scientific observations, due acknowledgment has been made whenever the work described is based on the findings of other investigators.

Deepak Krishnamurthy

CERTIFICATE

I hereby certify that the matter embodied in this thesis entitled “**Heat Transfer from Drops in Shearing Flows and Collective Motion in Micro-scale Swimmer Suspensions**” has been carried out by **Mr. Deepak Krishnamurthy** at the Engineering Mechanics Unit, Jawaharlal Nehru Centre for Advanced Scientific Research, Bangalore, India under my supervision and that it has not been submitted elsewhere for the award of any degree or diploma.

Prof. Ganesh Subramanian
(Research Supervisor)

Acknowledgements

It gives me immense pleasure to acknowledge the people who have made this thesis possible.

It has been a privilege to work with *Prof. Ganesh Subramanian* over the past three years. That he has fundamentally changed the way I think about fluid mechanics and heat transfer would be a massive understatement. His depth of understanding, clarity of thought and physical intuition have been a delight to observe and marvel at during each one of our interactions. It has been a rewarding experience intellectually to witness his physically motivated way of thinking about a problem, an approach which has an uncanny knack of laying bare mathematical errors. As an advisor, his ability to strike a balance between being fully aware of a student's research yet having the patience to give the student a free rein, is remarkable. At several points during the course of this thesis, his guidance has been like a light in the darkness. My (slightly) better understanding of this subject, I owe almost entirely to him.

Another person, without whose guidance this thesis would never have happened, is *Dr. Sai Jagan Mohan* from BITS-Pilani. It was upon his suggestion that I applied to JNCASR as a possible destination for my Masters. I thank him with all my heart, for providing me with the 'road less travelled', which indeed has made all the difference in the world. I also thank *Prof. Meheboob Alam* who graciously made it possible for me to attend the JNC interview without a GATE score. Without his help my stint at JNCASR may never have happened.

I wish to thank the faculty at the *Engineering Mechanics Unit (EMU), JNCASR* for their teaching and support. I had great fun doing my first (official) experiments as part of the *Heat Transfer* course offered by *Prof. K R Sreenivas*. I thank him also for his guidance and suggestions during my application for PhD positions; these were pivotal in making my priorities clearer. *Prof. Rama Govindarajan's* course on Math Methods gave me an opportunity to study the *Acoustics of the Mridangam*, something I had always wanted to do. For this and for creating a fun, informal learning atmosphere in the classroom, I give her my thanks. I also thank *Prof. Santosh Ansumali* for offering the course on Computational methods which was an extremely hectic yet rewarding experience. Though I have not known them personally, two other faculty at EMU have had an impact on me. Through anecdotes and legends which revolve around them *Prof. Roddam Narasimha* and *Prof. S. M. Deshpande* have been highly inspirational figures, and it has been an honour to work alongside them.

I believe no words are enough to describe the love and gratitude I feel for *My Parents*, who have made me what I am today. My mother, for being a friend and confidant and a constant source of inspiration. My father for his unflinching, unconditional support and enthusiasm for everything I do. *Thank you both!*

Preethi, for being by my side from the opposite end of the globe. For being an epitome of understanding and support, and an untiring listener to my many monologues. For making me feel younger at heart as a researcher and otherwise, and for countless other things, *Thank you!*

My friends at and outside EMU have made my stint here an enjoyable one. *Anubhab* who was here at JNC during my first year remains an immense source inspiration for his applied math skills. I also thank him, and *Senjuti* for their warm hospitality during my visit to Cornell. I also wish to thank *Vivek Prakash* for his advice, and for his hospitality at Stabford. I thank *Ponnu*, the god-mother of EMU and our one link to an era past, a great friend and source of useful advice on many matters. *Sumesh* (who made moustaches fashionable in JNC) was again a person to aspire to with his brilliant temperament and organized work ethic. My first semester at JNC was made memorable by my batch-mates: *Deepthi*, *Kanwar*, *Chakri* and *Rashmi*. I cherish the outings after each of our tests. In particular, *Rashmi* has been a source of inspiration to me for her skill in achieving the research/family balance. I thank my junior batch: *Vicky*, *Sankalp* and *Reddy* for being wonderful during the IFM course and for tolerating me as their TA!

My lab, *Students 105* and its inmates, have added colour to my life at JNC. Late night old-Hindi-film-music sessions with *Milind*, *PP*, *Rajesh* and *Vicky*; jamming sessions with *Milind*, *Nisha* and *Arpit* for Hostel-day; political discussions with *Rajesh*, *PP* and *Kanwar*; discussions on numerics with *Rajesh* and *PP*, have all meant that there was hardly a dull moment in the lab. Food has always been an important part of Student 105, EMU, and I thank *Swati Gardenia* (who ought to give us a life-time discount), *A2B* and my co-gluttons *PP*, *Vicky* and several others for helping me deflect at least some of the mess-food-induced trauma. Other memorable events during my stay included Enjoyable discussions on percussion, music and research philosophies with *Vybhav*; visits to the downstairs lab to observe experiments of *Shashank*, *Vybhav* and *Sachin*; *Siddharth* and *Chakri* my travel (and beer) buddies for the San Diego and San Francisco trip; politically (in)correct meal-time conversations with *Saikishan*.

A few people outside EMU have made for wonderful friends these past three years. I specially thank *Priyanka*, for her infectious enthusiasm and enjoyable companionship. Late night tea making sessions, innumerable delicious meals cooked in her room, and walks around JNC campus. I thank *Sarada* and *Sona* for being excellent company over countless coffee sessions in Chandriah and refreshing walks around Jakkur's plentiful lakes. I also thank my co-studreps: *Sarada*, *Vybhav*, *Nikhil* and *Anjali* for making my tenure a memorable one. Playing Table Tennis with *Abhilash*, *Dheeraj*, *Rajesh*, *Alok*, *Sanjeev*, *Bharath* and several others; and more recently Basket-ball with *Santosh*, *Devesh*, *Raunak*, *Srinivas* and *others*; these made for refreshing restarts to even the most tiring of days.

I thank *Saranappa* for making coffee which makes most other coffees pale in comparison; a cup of this was a cure to most blues.

I give my heartfelt thanks to the JNC administration whose members have always been helpful. I specially thank Senior Administrative Officer, *Mr. A N Jayachandra* for his energy and sensitivity to students' needs. I also thank other *admin staff*; *library staff*; *hostel office staff*; *Princy* and *Sukanya* madam in the Academic sections for their help from time to time. My special thanks to the *JNC security staff* for their dedication and for making my late night walks to my room a bit less spooky. I wish to acknowledge *Department of Science and Technology (DST)*, *APS-DFD* and *Aspen Center for Physics* for providing me with financial support to attend conferences. I also thank *JNCASR* for all the infrastructural and financial support during my stay here.

Abstract

In this work we study two problems involving fluid flow and transport phenomena at small length scales. The first is concerned with solving the fundamental problem of heat or mass transfer from neutrally buoyant drops in an ambient shearing flow, where the rate of heat or mass transfer is calculated by a boundary layer analysis in the strong convection limit. In the second, we investigate through numerical simulations, the conditions for the onset of collective motion in a micro-scale swimmer suspension. This thesis is organized in two distinct parts with the drop heat transfer problem appearing first followed by the study on micro-scale swimmers.

Heat Transfer from Drops in Shearing Flows

The transport of heat or mass from suspensions of solid particles or drops is ubiquitous in many industrial processes. We study the heat transfer problem for a suspension of drops of one liquid (dispersed phase) suspended in another liquid (suspending medium); a system formally termed as an emulsion. We consider the heat transfer problem in the dilute limit where each dispersed phase droplet may be regarded as isolated and suspended in an infinite ambient. The size of the drops is small, usually in the range of a few micrometres to millimetres, which in turn leads to viscous effects dominating over inertial ones. It is a general feature of fluid flow in the limit of zero inertia (the Stokesian regime), arising from the principle of reversibility, that freely suspended particles or drops in shearing flows are completely surrounded by a region of closed streamlines. This makes the transport of heat or mass diffusion limited. The diffusion limitation is manifested in the Nusselt number (Nu : the dimensionless rate of heat transfer measured in units of conduction) saturating to an $O(1)$ value even as the Peclet number (Pe : which measures the relative magnitudes of convective and diffusive transport) is increased to infinity. A small but finite amount of (fluid) inertia though, results in a vastly different picture, greatly enhancing transport by destroying the closed streamline configuration. In this work, we develop a theoretical formulation to study the effects of weak inertia on transport from a density-matched drop in a planar linear flow. This makes the heat transfer problem a function of two main parameters; α which is a flow parameter characterizing the relative magnitudes of extension and vorticity in the ambient linear flow and λ , the ratio of drop fluid to the ambient fluid viscosity. The aim is to determine the dependence of Nu on α and λ in the limit of weak inertia ($Re \ll 1$) and strong convection ($Pe \gg 1$). While our results apply equally well to both heat and mass transfer, we will restrict our discussion to heat transfer from hereon. There are some key points which serve to distinguish the flow and transport problem for drops from a solid particle. It is shown that, unlike a solid particle, the near-surface streamlines are closed only when the viscosity ratio exceeds a critical value, $\lambda_c = 2\alpha/(1 - \alpha)$. There exists a second critical

viscosity ratio $\lambda'_c = (5\alpha + 1)/(2(1 - \alpha))$, which is important for characterizing the flow topology in the drop interior and therefore does not directly affect the external heat transfer. The drop heat transfer problem thus presents a parameter space which is general and rich in physics due to the appearance of both open and closed-streamline regimes; one expects fluid inertia to play a non-trivial role in the latter regime. Further, we find that the near-field streamlines for a drop are not circular as for a solid particle, but are Jeffery orbits. Using this observation, we characterize the streamlines on the drop surface using a complex-valued analogue of the (C, τ) coordinate system originally used to describe Jeffrey orbits of an axisymmetric particle. We show that the shapes of the orbits are characterized by an effective aspect ratio (γ) analogous to the geometric aspect ratio of the original Jeffrey orbits, here γ being a function of the flow parameters α and λ . This effective aspect ratio serves as an elegant means of distinguishing the open and closed-streamline regimes. The open-streamline regime is characterized, rather intuitively, by a purely imaginary value of the aspect ratio since the surface streamlines are not true closed orbits. The closed-streamline regime, on the other hand, is characterized by a real-valued effective aspect ratio.

In the open-streamline regime ($\lambda < \lambda_c$, $\gamma \rightarrow \text{Imaginary}$), enhanced convective transport occurs even with zero inertia, and for large Peclet number, the Nusselt number is expected to scale as $\mathcal{F}(\alpha, \lambda)Pe^{1/2}$. In this regime the effect of small inertia is perturbative in nature and does not affect the heat transfer at leading order (except in a vanishingly small neighbourhood of the critical viscosity curve). We present a novel solution to this non-axisymmetric problem via a boundary layer analysis in the aforementioned (C, τ) coordinate system, and thereby, determine $\mathcal{F}(\alpha, \lambda)$.

In the closed-streamline regime ($\lambda > \lambda_c$, $\gamma \rightarrow \text{Real}$), similar to the solid particle, inertia plays a crucial role in the transport, and the Nusselt number is seen to scale as $\mathcal{G}(\alpha, \lambda)Re^{1/2}Pe^{1/2}$, in the limit $RePe \gg 1$. For this case, we develop a methodology to analyse convection due to spiralling streamlines in the (C, τ) coordinate system developed for the open streamline analysis. The method relies on the separation of time scales characterizing motion (nearly) along a Jeffery orbit, and that across Jeffery orbits (caused by the spiralling), and the boundary layer analysis is formulated in terms of a ‘Jeffery-orbit-averaged’ convection. Further, we show that, using a physically intuitive coordinate system, where the analogue of the radial coordinate corresponds to non-circular isothermal streamlines, leads to a crucial simplification of the analysis allowing us to proceed towards a closed-form solution. Interestingly we find that, for the drop, the thermal wake that arises due to the spiralling inertial convection shows a novel bifurcation. The wake, originally in the plane of symmetry (the flow-gradient plane), lifts off the flow-gradient plane in a certain region in the (α, λ) space. Finally, we also present some scaling analyses for the limit $\lambda \rightarrow \lambda_c$, which we term as an ‘intermediate regime’. In this limit there exists a thin region near the flow-vorticity plane where Stokes and inertial convection are comparable. This allows us to define the range of validity for the open and closed streamline analyses outlined above.

Collective Motion in Micro-scale Swimmer Suspensions

Recent experiments have shown that suspensions of swimming micro-organisms are characterized by complex dynamics involving large-scale correlated motions much greater than the size of the

microorganism, enhanced swimming speeds and enhanced tracer diffusion. On length scales of the order of the size of the microorganisms, viscous effects dominate inertial ones and the fluid flow is governed by the Stokes equations. This leads to an instantaneous balance between thrust and drag forces on the swimmer, making them force-free. We study two kinds of swimmers, pushers and pullers, which are so named due to the opposing signs of the intrinsic dipole that arises based on their swimming mechanism. It is in suspensions of pushers that the above phenomena associated with collective motion are observed. Pullers, on the other hand, do not show such behaviour, and therefore, serve as a valuable baseline for contrast. Our main goal is to characterize (numerically) the threshold governing the onset of collective motion. The threshold is expected to be a function of parameters intrinsic to the suspension, and that characterize the motion of the swimmers on the micro-scale.

Towards this end, we develop a particle-based computational model to study an infinite suspension of hydrodynamically interacting rod-like swimmers with the relation between the swimming velocity and intrinsic stress being enforced from slender body theory. Such an a priori specification reduces the computational cost since one now has a ‘kinematic’ simulation with a fixed interaction law between swimmers. The interaction law governs the rate of change of swimmer positions and orientations, and is again obtained from slender body theory. The kinematic nature of the simulations does not restrict our study of the dynamics since the destabilizing mechanism has been attributed to the intrinsic (rather than the induced) stress field. The long-ranged nature of the hydrodynamic interactions motivates the use of periodic boundary conditions to simulate an infinite system, and an Ewald summation based method to reduce the computational cost. Importantly, the model includes intrinsic de-correlation mechanisms found in bacteria such as rotary diffusion and tumbling whose effects have so far not been studied via simulations. Swimmers which do not have any intrinsic orientation de-correlation mechanisms are termed smooth swimmers, and collections of such swimmers have been explored previously by other researchers. For such swimmers, the only cause for orientation de-correlation is due to hydrodynamic interactions, that is, on account of the disturbance fields of other randomly positioned swimmers. In light of the availability of earlier results, we use our smooth-swimmer simulations as a proof-of-principle to demonstrate that a kinematic simulation is indeed sufficient in capturing the instability predicted for a suspension of pushers. The solution of the equations of motion and the resulting satisfaction of the no-slip boundary conditions via the induced forces is thus shown to be an inessential detail. The smooth swimmer results also show that the diffusivity of passive tracer particles is the most sensitive measure of the bifurcation between pushers and pullers. By calculating tracer diffusivities we go on to show that a suspension of smooth swimmers has a box-size-dependent stability threshold for the suspension concentration in agreement with linear stability theory. The finite size of the periodic box results in an artificial stabilization and the concentration threshold scales inversely with box size (the true threshold for an unbounded suspension being identically zero).

The main effect of adding orientation de-correlation mechanisms such as tumbling and rotary diffusion is to stabilize the suspension. Importantly, however, even in the presence of intrinsic de-correlation mechanisms, suspensions of pushers and pullers behave in a qualitatively different manner. To begin with, we validate our simulations by comparing our results for a suspension

of tumbling swimmers in the stable regime to theory, and use this to characterize the non-trivial effect of finite box size on the predicted tracer diffusivity. Next, we explore suspensions of swimmers which tumble and those that undergo rotary diffusion both as a function of the swimmer number density (n) and the intrinsic decorrelation time. Our study leads us to our main finding that a dimensionless parameter exists that characterizes the onset of instability in a suspension of pushers, and that depends only on intrinsic suspension parameters. These parameters include the swimming speed (U), swimmer length (L), mean run time (τ) and rotary diffusivity (D_r); thus, the stability in a suspension of tumblers is governed by $nUL^2\tau$, and that in a suspension of rotary diffusers is governed by nUL^2/D_r . Such a parameter is expected to be useful in understanding the dynamics of suspensions of swimming microorganisms as well as artificial micro-swimmers.

List of Figures

2.1	Schematic of the coordinate system used showing the flow, gradient and vorticity axes for the particular case where the ambient flow is a simple shear flow.	14
2.2	Streamlines and fixed point locations interior and exterior to the drop at a fixed value of $\alpha = 0.25$ as a function λ . The arrows indicate the direction of movement of the fixed points lying on the $x_3 = 0$ plane with increasing λ	16
2.3	The two critical curves for the viscosity ratio λ . Solid red curve : λ_c and the green dashed curve : λ'_c	16
2.4	Plots of $\hat{F}_1(r)$ and $\hat{F}_2(r)$ with respect to r in the interior region, horizontal lines denote different values of the streamline label \hat{E} . There are three classes of interior streamlines (in general) which are labelled (i), (ii) and (iii). The green dashes depict the allowed range in r of a given class of streamlines. Black arrows connect each of the green hashed lines to the corresponding class of streamlines. Red(dashed) arrows connect the red dashed lines to the separatrix streamlines which separate two different classes of streamlines.	21
2.5	Plots of $F_1(r)$ and $F_2(r)$ with respect to r in the exterior region, horizontal lines depict various cases for the streamline label E . There are three classes of exterior streamlines (in general) which are labelled (i), (ii) and (iii). The green dashes depict the allowed range in r of a given class of streamlines. Black arrows connect each of the green hashed lines to the corresponding class of streamlines. Red(dashed) arrows connect the red dashed lines to the separatrix streamlines which separate two different classes of streamlines.	24
2.6	In-plane and off-plane closed streamlines along with in-plane open streamlines for a drop. The in-plane separatrix is shown as a red dashed curve	26
2.7	(a) Plots of the unit vectors and metrics of the (C, τ) coordinate system. (b) Depiction of the coordinate system on the drop surface showing mapping to spherical polar coordinates	34
2.8	The surface streamlines on a drop for distinct cases (a) Open streamline regime ($\lambda < \lambda_c$), (b) Intermediate regime ($\lambda \rightarrow \lambda_c$) (c) Closed streamline regime ($\lambda > \lambda_c$) and (d) Solid particle ($\lambda \rightarrow \infty$)	35
2.9	Figure showing a spiralling trajectory of a fluid element around a solid particle. Flow parameters: $\alpha = 0.1$, $Re = 0.5$ (a) A 3D view, (b) projection on the flow-gradient plane and (c) projection on the flow-vorticity plane.	39

2.10	Figure showing a spiralling trajectory of a fluid element around a drop in the single wake regime for $\lambda > \lambda_{bif}$. Flow parameters: $\alpha = 0.1$, $\lambda = 0.5$, $\lambda_c = 0.222$, $\lambda_{bif} = 0.3458$, $Re = 0.1$. (a) A 3D view, (b) projection on the flow-gradient plane and (c) projection on the flow-vorticity plane. Note that the neutral curve in this case lies at the equatorial plane.	40
2.11	Figure showing a spiralling trajectory of a fluid element around a drop in the bifurcated wake regime for a λ value close to λ_c ($\lambda_c < \lambda < \lambda_{bif}$). Flow parameters: $\alpha = 0.1$, $\lambda = 0.23$, $\lambda_c = 0.222$, $\lambda_{bif} = 0.3458$, $Re = 0.1$. (a) A 3D view, (b) projection on the flow-gradient plane and (c) projection on the flow-vorticity plane. The black dashed curve in (a) shows the neutral curve as predicted by Eq. B.1. . . .	41
2.12	Figure showing a spiralling trajectory of a fluid element around a drop in the bifurcated wake regime for a λ value close to λ_{bif} ($\lambda_c < \lambda < \lambda_{bif}$). Flow parameters: $\alpha = 0.1$, $\lambda = 0.34$, $\lambda_c = 0.222$, $\lambda_{bif} = 0.3458$, $Re = 0.1$. (a) A 3D view, (b) projection on the flow-gradient plane and (c) projection the flow-vorticity plane. The black dashed curve in (a) shows the neutral curve as predicted by Eq. B.1. Note how the neutral curve is closer to the equatorial plane compared to Fig. 2.11a.	42
2.13	Region in (α, λ) space showing the single and bifurcated wake regime along with wake location.	43
2.14	The variation of the orbit constant at which the wake occurs with viscosity ratio	43
3.1	Schematic representations of the thermal boundary layer (a) near a solid particle and (b) near a drop or liquid interface. The scalings of the boundary layer thickness and hence the dimensionless heat transfer with Peclet number can be inferred by taking a ratio of the time scales of convection and diffusion	47
3.2	Depiction of the (C, τ) coordinate system on the drop surface in the open streamline regime. The four regions are marked I through IV, where regions (I, III) and (II, IV) are equivalent. The streamline trajectories begin and culminate at one of four stagnation points which lie on the equatorial plane. The phase variable for the position along a given trajectory is given by $\hat{\tau}$ and varies from $-\infty$ at the inlet to $+\infty$ at the outlet. The trajectory itself is parametrized by the trajectory constants, C and \hat{C} , in region I and II respectively. These vary from 0 at the poles to ∞ at the equatorial plane	49
3.3	Plots of two prefactors to the Nusselt number (a) $Nu/Pe^{1/2}$ as a function of α and λ for $\lambda < \lambda_c$ and (b) $Nu/(1 - \alpha)^{1/2}$ as a function of the effective-aspect-ratio $\hat{\gamma}$. .	58
3.4	Surface streamlines plots for drop in an extensional flow (a) General three-dimensional extensional flow $E_1 \neq E_2$, (b) Axisymmetric (about x_1 axis) extensional flow with $E_1 = E_2$ and (c) Planar extensional flow $E_2 = 0$, $E_1 \neq 0$ (plane of the flow is the x_2x_3 plane.	63
3.5	Plot of the prefactor to the Nusselt number given in Eq. 3.100 as a function of ϵ for $0 \leq \epsilon \leq 1$. The end points correspond to planar extensional flow and axisymmetric extensional flow (about x_1 axis).	66

4.1	Depiction of a body at temperature T_0 in an ambient fluid of temperature T_∞ . The body is completely surrounded by a region of closed streamlines, which at steady state are isotherms. Convection is rendered ineffective in transporting heat, which is transported only through diffusion across these isotherms.	71
4.2	Figure showing the inertial surface streamlines for a drop in the single wake regime, $\alpha = 0.2$, $\lambda = 2$ ($\lambda_{bif} = 0.547$)	72
4.3	A schematic depiction of a near-field Stokes streamline, showing the varying radial distance from the drop surface. We see that these streamlines can be described by the equations $y_m = C_1$ and $C = C_2$, where C_1 and C_2 are constants. To satisfy the continuity constraint a fluid element moving along such a streamline has a volume which is independent of τ	77
4.4	Figures showing the inertial surface streamlines for a drop in the single wake regime, $\alpha = 0.2$, $\lambda = 2$ ($\lambda_{bif} = 0.547$), $Re = 0.1$ (a) three-dimensional view (b) projection on x_2x_3 plane (gradient-vorticity plane). The thickness and growth of the thermal boundary layer is schematically represented as the shaded portion. Note the existence of a single wake at the equatorial plane	84
4.5	Figures showing the inertial surface streamlines for a drop in the bifurcated wake regime, $\alpha = 0.2$, $\lambda = 0.52$ ($\lambda_{bif} = 0.547$), $Re = 0.1$ (a) three-dimensional view (b) projection on x_2x_3 plane (gradient-vorticity plane). The thickness and growth of the thermal boundary layer is schematically represented as the shaded portion. Note the existence of a bifurcated wake lifted off from the equatorial plane and at an intermediate C orbit.	85
4.6	A surface plot of the prefactor multiplying the scaling factor $Re^{1/2}Pe^{1/2}$ to give the Nusselt number. Note that the surface is plotted in the region $\lambda > \lambda_c$ on the (α, λ) plane corresponding to the closed streamline regime with inertia. The scaling with γ is clearly visible with the prefactor increasing with increasing γ (as one approaches the λ_c curve). The inset shows an expanded view of the bifurcated wake regime (shaded portion). α_{bif} and λ_{bif} serves as the upper bounds below which we see the bifurcated wake regime for $\lambda > \lambda_c$	89
4.7	Plot of the tangential velocity scale as a function of the inverse of the orbit constant C	90
4.8	A surface plot of the prefactor multiplying the scaling factor $Pe^{1/2}$ to give the Nusselt number in the open and closed streamline regimes for $Re = 0.1$. Notice the kink in the surface due to the divergence of the Nu predicted close to the $\lambda = \lambda_c$ curve from the closed streamline side.	90
4.9	Figure showing the inertia-less Stokes streamlines on the surface of the drop in the intermediate region ($\lambda \rightarrow \lambda_c$). Here $\alpha = 0.5$ and $\lambda = 2.001$ ($\lambda_c = 2$). The streamlines have a meridional character and converge and diverge away near the flow-vorticity plane.	94

4.10	A schematic of the extent of the annular region of closed (spiralling) streamline adjacent to the drop surface in the limit of large γ (intermediate regime on the closed streamline side). The asymptotically different radial extents near the flow-vorticity plane compared to the rest of the drop region is shown. Also shown is the radial extent of the fixed-circle which gives the maximal radial extent of the separatrix surface.	94
4.11	Inertial surface streamlines in the intermediate regime ($\alpha = 0.2$, $\lambda_c = 0.5$, $\lambda_{bif} = 0.547$, $Re = 0.1$) for (a) single wake ($\lambda = 0.6$) and (b) bifurcated wake ($\lambda = 0.501$) regimes. The large drift during a given turn is apparent from the small number of turns taken to drift across a large portion of the drop surface. Note the different drift direction in the two regimes even though the inertia-less streamlines in both cases have the same character (see Fig. 4.9)	95
4.12	The (α, λ) plane showing the open and closed streamline regimes separated by the critical viscosity ratio curve.	96
6.1	Experiemntal observations of collective bahviour. (a) Collective motion onin a sessile drop containing a suspension of <i>Bacillus subtilis</i> . (b) Instantaneous flow pattern in a plane of the drop. Reproduced from Dombrowski et al. (2004)	108
7.1	Electron micrographs of (a) <i>E. Coli</i> and (b) <i>Chlamydomonas reinhardtii</i> , two micro-scale swimmers which display pusher and puller-type swimming mechanisms, respectively. As model organisms, they motivate our study of suspensions of general pushers and pullers.	118
7.2	Schematic of a pusher-type swimmer. (a) The Stokeslet distribution used to model a pusher is shown along with the variation of the force density with the coordinate along the swimmer axis in (b). (c) Shows the disturbance velocity due to a pusher at large length scales which is that due to an extensile dipole	119
7.3	Schematic of a puller-type swimmer. (a) The Stokeslet distribution used to model a puller is shown along with the variation of the force density with the coordinate along the swimmer axis in (b). (c) Shows the disturbance velocity due to a puller at large length scales which is that due to a contractile dipole	119
7.4	(a)The simulation box with its nearest neighbours in the same plane. The swimmers are represented as arrows along their orientation vectors. Each swimmer has an infinite number of images repeated at the sites of a simple cubic lattice. The periodicity applies into and out of the page as well since we have implemented a periodic boundary condition in three dimensions. (b) The coordinate system used in the simulations where the geometric centre of each swimmer is used to track its position relative to a lab-fixed reference frame. The coordinate system on the swimmer measures the location of points along the swimmer axis with respect to this geometric centre.	122
7.5	A schematic of the run-and-tumble motion executed by peritrichously flagellated swimmers such as <i>E. Coli</i> . Reproduced in part from Subramanian & Nott (2012)	131

7.6	A schematic of the rotary diffusion model used. We see a section of a unit sphere on which the tip of the swimmer's orientation vector executes a two-dimensional random walk. The step size is denoted by $\Delta\theta$ and can occur with equal probability in any ϕ direction.	133
7.7	Comparison of simulations with theory of three time-dependent statistical quantities for swimmers which tumble. (i) The ratio of mean-square-displacement to time, $\langle r^2(t)/6t \rangle$, plotted with respect to time; (ii) orientation de-correlation measure $\langle \hat{\mathbf{p}}(t) \cdot \hat{\mathbf{p}}(0) \rangle$ and (iii) $\langle (\hat{\mathbf{p}}(t) \cdot \hat{\mathbf{p}}(0))^2 \rangle$ for (a) $\tau = 1$ and $\Delta t = 0.05$ and (b) $\tau = 10$ and $\Delta t = 0.2$	135
7.8	Comparison of simulations with theory of two time-dependent statistical quantities for rotary diffusing swimmers. (i) The ratio of mean-square-displacement to time, $\langle r^2(t)/6t \rangle$, plotted with respect to time and (ii) orientation de-correlation measure $\langle \hat{\mathbf{p}}(t) \cdot \hat{\mathbf{p}}(0) \rangle$ for (a) $D_r = 0.02$ and $\Delta t = 0.05$ and (b) $D_r = 0.5$ and $\Delta t = 0.01$	136
7.9	Simulation flow chart	138
7.10	Runge-Kutta second order time stepping scheme	139
8.1	Modal digram for a suspension for smooth swimming pushers. Reproduced from Subramanian <i>et al.</i> (2011a)	144
8.2	Variation of critical volume fraction for onset of instability ν_{crit} with the simulation box size	144
8.3	Schematic depiction of the response of three types of slender particles to a velocity wave perturbation (Fourier mode) (a) passive rods, (b) puller-type swimmers and (c) pusher-type swimmers.	145
8.4	Projections on the x_1x_2 plane of fluid velocity vectors lying on a plane at half the height (in x_3 direction) of the simulation box for (a) $\nu = 0.05$ and (b) $\nu = 0.5$ for pushers and pullers. The simulation box size is 10 swimmer lengths ($L_{box} = 10L$).	147
8.5	Fluid velocity statistics. (a) The probability distribution function of the fluid disturbance velocity plotted for (i)pushers and (ii)pullers for four volume fractions. (b) The probability distribution function of the fluid disturbance velocity magnitude for (i) pushers and (ii) pullers. (c) Mean fluid kinetic energy plotted with respect to ν for pushers and pullers for three box sizes (5, 10 and 15 swimmer lengths)	149
8.6	Fluid velocity correlations (a) Fluid velocity autocorrelation function $F(t)$ defined in Eq. 8.5 plotted for pushers and pullers at different volume fractions. (b) The correlation times for pushers and pullers plotted with respect to ν for three different simulation box sizes (5, 10 and 15 swimmer lengths)	150
8.7	Power spectrum of the fluid velocity field, as defined in Eq. 8.6, plotted with respect to the non-dimensional wavenumber $\hat{k} = L_{box}k$ (simulation box size: 10 swimmer lengths)	153

8.8	Swimmer statistics. (a) The probability distribution function for the swimmer velocity plotted for (i)pushers and (ii) pullers for four volume fractions. The top-hat profile corresponding to uncorrelated swimmers swimming at a speed of unity is also shown. (b) The probability distribution function for the swimmer speed for (i) pushers and (ii) pullers. (c) Mean swimming speed plotted with respect to ν for pushers pullers for three box sizes (5, 10 and 15 swimmer lengths)	155
8.9	Plot of pair correlation function as a function of distance from the swimmer for three volume fractions (a) $\nu = 0.1$ (b) $\nu = 0.5$ (c) $\nu = 1.0$ and (d) a combined plot with all three volume fraction. The distance from the swimmer is expressed in non-dimensional form in units of half the swimmer length $L/2$. The results are for simulation box of size 10 swimmer lengths.	157
8.10	Two local measures, (a) the local volume fraction and (b) local order parameter plotted as a function of the swimmer speed (simulation box size:10 swimmer lengths).	158
8.11	A measure of the swimmer alignment with the local extensional axis of the rate-of-strain tensor \mathbf{E} , given by the scalar $\mathbf{E} : \hat{\mathbf{p}}\hat{\mathbf{p}}$. A positive value indicates a tendency for the swimmers to orient parallel to the local extensional axis (simulation box size:10 swimmer lengths).	159
8.12	Swimmer transport. (a) Mean-square-displacement with respect to time for (i) pushers and (ii) pullers. (b) Translational diffusivities of the swimmers plotted with respect to ν for pushers pullers for three box sizes (5, 10 and 15 swimmer lengths).	161
8.13	Evolution of the orientation decorrelation function $\langle \hat{\mathbf{p}}(t) \cdot \hat{\mathbf{p}}(0) \rangle$ with time. The results are for a simulation box of size 10 swimmer lengths.	162
8.14	The swimmer diffusivity calculated using three methods (i) long-time mean-square-displacement (ii) swimmer orientation decorrelation using a generalized Taylor dispersion theory (iii) swimmer velocity auto-correlation (simulation box size: 10 swimmer lengths).	162
8.15	164
8.15	Simulation snapshots showing the swimmers' positions and the fluid disturbance velocity vectors on the left side column and trajectories of tracer particles on the right column. The simulation box size is 10 swimmer lengths and the volume fraction is $\nu = 0.5$, which for pushers lies in the unstable regime. The blue circles represent the geometric centres of the swimmers and the red arrows correspond to the swimmers' orientation vectors. The black arrows depict the fluid velocity vectors. In the right column, the red circles represent the positions of the tracer particles. (a) Puller suspension near the start of the simulation and (b) puller suspension at long times. (c) Pusher suspension near the start of the simulation, (b) pusher suspension at long times. We only display swimmers and tracers which lie in a slab of size 20203 in the x_1 , x_2 and x_3 directions, respectively, centred at the midpoint of the simulation box in the x_3 direction. The fluid velocity vectors lie on the plane at the midpoint of the simulation box in the x_3 direction.	165

8.16	Tracer transport. (a) Mean-square displacements for the tracer particles plotted with respect to time for (i) pushers and (ii) pullers. (b) Diffusivities of the tracer particles plotted with respect to ν for pushers pullers for three box sizes (5, 10 and 15 swimmer lengths). The vertical lines indicate the box-size-dependent theoretical prediction for the instability threshold given by Eq. 8.4.	166
9.1	Modal digram for a suspension of pushers with tumbling as the intrinsic orientation relaxation mechanism. Reproduced from Subramanian <i>et al.</i> (2011a)	170
9.2	Plot of the critical value of $nUL^2\tau$ for a periodic swimmer array as a function of L/L_{box} for $\nu = 0.05$. The red dashed line represents the result for an unbounded suspension ($L/L_{box} \rightarrow \infty$). The simulation box sizes for which we present results: 10, 15, 25 and 40 swimmer lengths, are marked on the abscissa.	171
9.3	Theoretical predictions for the tracer diffusivity in an unbounded suspension, and in an infinite periodic swimmer array. Note that in an unbounded suspension (solid black curve) the diffusivity monotonically increases with a well defined large τ asymptote. The periodic box results show a non-monotonic trend, with large τ asymptote which is $\sim O(1/\tau)$. The small τ asymptotes of the periodic swimmer array are also shown.	177
9.4	Fluid velocity statistics for a suspension of tumblers with $\tau = 1$. (a) The probability distribution function for the fluid disturbance velocity plotted for (i) pushers and (ii) pullers for three volume fractions. (b) The probability distribution for the fluid disturbance velocity magnitude plotted for (i) pushers and (ii) pullers for three volume fractions. (c) Mean fluid kinetic energy plotted with respect to ν for pushers and pullers. The simulation box sizes are 10 and 15 swimmer lengths.	179
9.5	Fluid velocity power spectrum, normalized by the number of swimmers, for a suspension of tumblers where the mean-run-time is fixed at $\tau = 1$; and for two different volume fractions: $\nu = 0.05$ and 0.5. Simulation box size: 10 swimmer lengths.	180
9.6	Fluid velocity correlation function (Eulerian) for a suspension of tumblers where the mean-run-time is fixed at $\tau = 1$ and for two different volume fractions of 0.05 and 0.5. Simulation box size: 10 swimmer lengths.	180
9.7	Swimmer statistics for a suspension of tumblers with $\tau = 1$. (a) The probability distribution function for the swimmer velocity plotted for (i) pushers and (ii) pullers for three volume fractions. (b) The probability distribution function for the swimmer velocity magnitude plotted for (i) pushers and (ii) pullers for three volume fractions. (c) Mean swimming speed plotted with respect to ν for pushers pullers. The simulation box sizes are 10 and 15 swimmer lengths	182
9.8	Tracer diffsuivities plotted as a function of volume fraction. Plots are shown for both smooth swimmers and tumblers with mean-run-time $\tau = 1$. Simulation box size: 10 swimmer lengths.	183

9.9	Two independent methods of predicting the stability threshold for a suspension of tumblers. (a) Tracer diffusivity as a function of volume fraction for a fixed mean-run-time $\tau = 1$ for two different box sizes (10 and 15 swimmer lengths). (b) Tracer diffusivity as a function of τ for a fixed volume fraction and a box size of 10 swimmer lengths. Symbols represent a mean over simulations run with different initial conditions and the error bars represent the standard deviation.	184
9.10	188
9.10	Non-dimensional tracer diffusivity for a suspension of tumblers, at a volume fraction of $\nu = 0.05$, for different values of τ . (a), (c), (e) and (g) show the results of interactions-off simulations for box sizes of 10, 15, 25 and 40 swimmer lengths, respectively. (b), (d), (f) and (h) show the results of interactions-on simulations for box sizes of 10, 15, 25 and 40 swimmer lengths, respectively. Symbols represent a mean over simulations run with different initial conditions and the error bars represent the standard deviation.	189
9.11	Fluid velocity power spectrum, normalized by number of swimmers, for a suspension of tumblers with fixed volume fraction of $\nu = 0.05$ and two different values of τ ($\tau = 0.5$ and $\tau = 5$). Simulation box size: 25 swimmer lengths.	189
9.12	Fluid velocity correlation function for a suspension of tumblers with fixed volume fraction of $\nu = 0.05$ and two different values of τ ($\tau = 0.5$ and $\tau = 5$). Simulation box size: 25 swimmer lengths.	190
9.13	Tracer diffusivity as a function of volume fraction for a suspension of rotary diffusers with $D_r = 0.5$ (simulation box size: 10 swimmer lengths)	192
9.14	Non-dimensional tracer diffusivity for a suspension of rotary diffusers at a volume fraction of $\nu = 0.05$ for different values of $1/D_r$. (a), (c) and (e) show the results for interactions-off simulations for box sizes of 10, 15 and 30 swimmer lengths respectively. (b), (d) and (f) show the results for interactions-on simulations for box sizes of 10, 15 and 30 swimmer lengths respectively. Symbols represent a mean over simulations run with different initial conditions and the error bars represent the standard deviation.	193

L i s t o f T a b l e s

2.1	Combined analysis of interior and exterior streamlines for a drop.	30
4.1	The inlet and outlet values of the C orbits for different regimes in the (α, λ) space	84

Contents

Abstract	vii
List of Figures	xviii
List of Tables	xix
I Heat Transfer from Drops in Shearing Flows	1
1 Introduction	3
1.1 Transport from Solid Particles	4
1.2 Transport from Drops	7
1.3 Our Work	8
2 Flow Topology	11
2.1 Governing Equations and Boundary Conditions	12
2.2 Streamline Topology: Fixed Point Analysis	14
2.3 Streamline Topology: Characterization using Streamsurfaces	17
2.3.1 Interior Streamlines	17
2.3.2 Exterior Streamlines	20
2.3.3 Combined Analysis of Interior and Exterior Streamlines	26
2.4 The Surface Streamlines at Zero Re - The (C, τ) Coordinate System	30
2.5 Streamline Topology with Small but Non-zero Inertia	34
3 Open Streamline Heat Transfer	45
3.1 Introduction	45
3.2 Preliminaries	46
3.2.1 Governing Equations	47
3.3 Drop in a Planar Linear Flow: $(\lambda < \lambda_c)$	48
3.3.1 (C, τ) Coordinate System	48
3.3.2 Boundary Layer Analysis	52
3.3.3 The Nusselt Number	55
3.4 Drop in a 3D Extensional Flow	60
3.4.1 (C, τ) Coordinate System	60
3.4.2 Boundary Layer Analysis	62

3.4.3	Nusselt Number Calculation	64
4	Closed Streamline Heat Transfer: Inertial Effects	69
4.1	Introduction	69
4.2	Governing Equations	71
4.3	Solution Approach and Coordinate System	72
4.4	Boundary layer analysis	76
4.4.1	Solution to the boundary layer thickness equation	82
4.5	Nusselt number calculation	84
4.5.1	Single wake regime	85
4.5.2	Bifurcated wake regime	86
4.5.3	Discussion	87
4.6	The intermediate regime	88
4.6.1	Flow topology for $\lambda \rightarrow \lambda_c$	91
4.6.2	Heat transfer in the intermediate regime	93
4.6.3	Connecting the Nu -surface across the open and closed streamline regimes	97
5	Conclusions and Future Work	101
II	Simulation of Collective Motion in Micro-scale Swimmers	105
6	Introduction	107
6.1	Experimental Work	107
6.2	Theory and Continuum Models	110
6.3	Simulations	112
6.4	Our Work	114
7	Simulation Model and Theory	117
7.1	Introduction	117
7.2	Single Swimmer Model	118
7.3	Hydrodynamic Interactions in a Swimmer Suspension	121
7.3.1	Ewald Summation Method	126
7.3.2	Ewald Summation Implementation	127
7.4	Swimmer Kinematics	128
7.5	Tumbling and Rotary Diffusion Models	130
7.5.1	Tumbling	130
7.5.2	Rotary Diffusion	132
7.5.3	Validation of Tumbling and Rotary Diffusion Models	134
7.6	Simulation Algorithm	137
8	Results and Discussion: Smooth Swimmers	141
8.1	Introduction	141
8.2	Theory for Smooth Swimmers	142
8.3	Simulation Results and Discussion	146

8.3.1	Fluid Velocity Statistics	146
8.3.2	Swimmer Statistics	152
8.3.3	Tracer Transport	160
9	Results and Discussion: Tumblers and Rotary Diffusers	167
9.1	Introduction	167
9.2	Theory	167
9.2.1	Stability Theory: Swimmers with Intrinsic Orientation Decorrelation Mechanisms	167
9.2.2	Theory: Tracer Transport in Swimmer Suspensions	170
9.3	Results and Discussions: Tumblers	177
9.3.1	Comparison between Tumblers and Smooth Swimmers: Volume Fraction Variation	177
9.3.2	Identifying the Stability Threshold Based on Varying Tumble Rate	183
9.3.3	Estimating the Instability Threshold for Tumblers	187
9.4	Results and Discussion: Rotary Diffusers	187
10	Conclusions and Future Work	195
Appendices		
A	$O(Re)$ Velocity and Pressure Field Constants for a Drop	199
B	$O(Re)$ Neutral Curve (wake) Location on Drop Surface	201
C	Ewald summation method	203
D	Equivalence of the formulations by Hasimoto and Beennakker	205
	References	209

Part I

Heat Transfer from Drops in Shearing Flows

Chapter 1

Introduction

The transport of heat or mass from solid particles or liquid drops, freely suspended in a fluid medium is a problem in transport phenomena which is both of fundamental and practical interest. Several industrial applications involve flows with suspended particles or drops undergoing chemical reactions which lead to both heat and mass transfer across the interface. A particular example is the process of suspension polymerization (Vivaldo-Lima *et al.* (1997), Brooks (2010)), where the process starts with the liquid monomer in the form of suspended drops in an ambient fluid. As the exothermic polymerization process progresses, heat is released from the drop which needs to be convected away efficiently. At the same time the viscosity ratio between the drop fluid and ambient increases as a function of time due to the polymerization reaction. Other problems involve vapourization of fuels in internal combustion engines which may have a direct impact on the efficiency and emission levels of the engine. Phenomenon in nature such as cloud formation where there is condensation of drops in an ambient turbulent flow also involve the transfer of heat from and mass to water drops (Beard & Pruppacher (1971), Duguid & Stampfer Jr (1971), Kinzer & Gunn (1951)). More recently, there have been applications such as drug release from porous polymer particles which involve such heat or mass transport from particles. Applications may also be found in bio-reactors using immobilized cells or cell aggregates.

In this thesis we study the problem of heat or mass transfer from single spherical drops in general shear flows under conditions where viscous effects dominate the momentum transport and convective effects dominate the transport of heat or mass. We will consider the case where the dominant resistance to the transport is from the region exterior to the drop. Importantly, we also study the effects of small but finite inertia of the ambient fluid on this transport. These conditions correspond to small values of the Reynolds number, defined based on the radius a of the drop as $Re = \dot{\gamma}a^2/\nu$, where $\dot{\gamma}$ is a scale for the ambient shear rate and ν is the kinematic viscosity of the ambient fluid. Strong convection, on the other hand, corresponds to large values of the Peclet number which is a relative measure of the importance of convective to diffusive transport, and is defined as $Pe = \dot{\gamma}a^2/D$, where D is the diffusivity of heat or mass in the ambient fluid. We note that $Pe = RePr$, where Pr is the Prandtl number (or the Schmidt number for mass transfer) and is defined as $Pr = \nu/D$. In order to set the stage for the work presented in this part of the thesis, we first provide a brief survey of relevant earlier work. We will only summarise efforts which have looked at the problem from a single particle or single drop viewpoint, and in doing so elucidate some aspects of the underlying physics. In general, these analyses, for purposes of simplicity, deal with transport from cylinders or spheres in various types of ambient flows. The main result in these efforts is an expression for the Nusselt number Nu (ratio of the overall heat transfer to that due to diffusion alone), as a function of Re and Pe , since the overall heat transfer is usually the primary quantity of interest. We focus here on

works which deal with Peclet numbers ranging from very small to large values, but in the limit of small Reynolds numbers. However, it is the large Pe limit which is relevant to this thesis.

1.1 Transport from Solid Particles

[Acrivos & Taylor \(1962\)](#) first solved the problem of heat transfer from a sphere in a uniform flow at small values of the Peclet number. They realized that in the limit of small Pe , the conduction approximation is not a uniformly valid one in an unbounded domain since, at large enough distances from the particle, convection effects will eventually dominate. Therefore, the analysis of the effect of small Pe requires a singular perturbation expansion about the pure conduction result. This expansion led to an $O(Pe)$ enhancement in the heat transfer. [Acrivos & Goddard \(1965\)](#) considered the heat transfer at low Reynolds and high Peclet number (implying $Pr \gg 1$), for heat transfer from an isothermal sphere held in a uniform flow. They found the Nusselt number as a function of Pe and showed that $Nu \sim Pe^{1/3} + O(1)$ for $Pe \gg 1$ and for $Re \ll 1$. This scaling arises because in the limit of large Pe , convective effects dominate everywhere in the flow except for a thin thermal boundary layer next to the surface of the body where they are comparable to diffusion. For a solid particle it is straightforward to show that the thickness of this thin layer scales as $Pe^{-1/3}$, thereby leading to $Nu \sim O(Pe^{1/3})$, since the temperature gradient driving the heat transfer scales inversely as the boundary layer thickness. Higher order contributions arise due to the fluid velocity outside the boundary layer and also from the thermal wake behind the body. In a related paper, [Goddard & Acrivos \(1966\)](#) considered the other case where Re is high with a fixed value of Pr . Here, the thermal and momentum boundary layers are comparable in thickness which is different from the earlier case where there was no momentum boundary layer due to Re being identically zero.

The problems discussed above involved particles in a uniform flow and typically arise when there is a density mismatch between the particle and the ambient fluid, leading to a non-zero relative velocity between the two phases. Another fundamentally distinct class of problems involve freely suspended density matched particles, in which case, the dominant heat transfer is due to the ambient shear flow. [Frankel & Acrivos \(1968\)](#) were the first to study, theoretically, the heat transfer from small spheres and cylinders freely rotating in a shear flow at both small and large Pe . In the low Pe limit they predicted that the Nusselt number for a cylinder increases as $O(\log Pe)^{-1}$ on account of the Stokes paradox in two dimensions, while for a sphere it increases by an amount $O(Pe^{1/2})$ over the pure diffusion value of order unity. We note that the $O(\log Pe)^{-1}$ Nu scaling for a cylinder holds both for a uniform flow as well as a shear flow. As for the case of uniform flow, these weak convective enhancements are obtained from a singular perturbation expansion that accounts for convective effects becoming important at leading order, at large distances from the particle. For the large Pe limit, in the case of a freely suspended cylinder in simple shear flow, [Yu-Fang & Acrivos \(1968\)](#) predicted the surprising result that the Nusselt number is independent of Pe , implying the absence of any boundary layer enhancement. Although a similar situation prevails for a sphere, owing again to the existence of closed streamlines, they were, however, unable to extend this method to the case of the sphere, to obtain a quantitative estimate of Nu , due to the more complicated and three-dimensional nature of the flow field. The result for cylinders was confirmed by [Robertson & Acrivos \(1970b\)](#)

who performed experiments on a freely rotating cylinder in a shear flow apparatus. They found that, for $Pe > 70$, the Nusselt number was indeed independent of Pe . On the other hand, when the cylinder was held fixed and not allowed to rotate, they found that the Nusselt number did scale with Pe as $Nu = 1.641Pe^{1/3}$ in agreement with the existence of a thermal boundary layer. The reason for this difference in scaling may be found by noting that the streamlines around a freely rotating cylinder in a shear flow are closed, as shown in experiments by [Robertson & Acrivos \(1970a\)](#), and in numerical simulations by [Kossack & Acrivos \(1974\)](#). The presence of closed streamlines makes even strong convection ineffective in carrying away heat from the body thereby making the transport diffusion limited, and leading to a Nusselt number which is independent of Pe .

Another set of experiments were carried out by [Poe & Acrivos \(1975\)](#), who considered freely rotating cylinders and spheres in a simple shear flow. Here they found that, just as in the case of a cylinder, a freely rotating sphere is again completely surrounded by a region of closed streamlines. Again, for a sphere that is held fixed, the streamlines adjacent to the body are open, and as we saw before, can contribute effectively to the transport through the formation of a thermal boundary layer. The result for freely rotating spheres implies that we expect the transport at high Pe to be diffusively limited and therefore independent of Pe . This was verified by [Acrivos \(1971\)](#) using an approximate method to calculate the heat transfer from a freely suspended sphere in a simple shear flow. He found that $Nu \approx 9$ at high Pe , which, according to the definition of the Nusselt number, is 4.5 times the pure diffusion value. This analysis was extended for a general planar linear flow by [Poe & Acrivos \(1976\)](#), who found that except in the case of an extensional flow for which the sphere is surrounded by open streamlines, the Nusselt number becomes independent of Pe , for sufficiently large Pe , due to the presence of closed streamlines surrounding the particle.

The presence of closed streamlines around cylinders and spheres in a general planar linear flow was originally shown by [Cox *et al.* \(1968\)](#) and [Kao *et al.* \(1977\)](#). Acrivos and co-workers used these results in their analysis of the heat transfer problem above. [Cox *et al.* \(1968\)](#) studied cylinders and spheres which were free to rotate in a simple shear and theoretically predicted that, in either case, there are regions of closed streamlines surrounding the body. This was then confirmed by experiments ([Cox *et al.* \(1968\)](#)). [Kao *et al.* \(1977\)](#) later extended this theoretical analysis for a general, one-parameter (denoted by α) family of planar linear flows, with the extremal members of this family consisting of purely rotational flow ($\alpha = -1$) and extensional flow ($\alpha = 1$), and with simple shear flow ($\alpha = 0$) as an intermediate case. They found that there were regions of both closed and open streamlines for flow regimes between simple shear and extensional flow whereas for flows between pure rotational and simple shear, all the streamlines were closed. They also derived an expression for the radial extent of the separatrix surface which separates regions of closed and open streamlines.

[Batchelor \(1979\)](#) analysed the problem of mass transfer from a sphere under fairly general assumptions for the ambient linear flow at both low and high Pe . In the high Pe calculation, of relevance to our work in this thesis, he considered two broad classes of problems. The first involved two flows in which the particle is stationary due to the absence of an ambient vorticity: a steady three-dimensional extensional flow and a two-dimensional extensional flow. For these

cases, he showed that, in the limit of large Pe , the transport is dictated by a thin thermal boundary layer adjacent to the particle. Batchelor used a flow-aligned orthogonal coordinate system along with a suitable transformation of the independent variables to derive a similarity solution for this boundary layer problem. By suitably defining the Peclet number based on the parameters of the linear flow, the Nusselt number for any arbitrary extensional flow was shown to be given by:

$$Nu = 0.90 \left(\frac{a^2 E}{D} \right)^{1/3}, \quad (1.1)$$

where E is a scale for the rate-of-strain tensor. The results for a spherical particle (and drop), in simpler limiting cases, had been obtained earlier. For instance, both a solid particle and a drop, in an axisymmetric extensional flow, had previously been considered by Gupalo & Riazantsev (1972). The analysis for a particle (and drop) in a planar extensional flow was done by Polyani (1984). Batchelor (1979) goes on to analyse a second class of linear flows with a vorticity vector aligned with one of the principal axes of the rate-of-strain tensor. For this case, a freely suspended sphere rotates with the angular velocity ($\omega/2$) of the vortical part of the flow. Unlike the case of a planar linear flow, where the streamlines adjacent to the sphere would be closed, here the contribution from the extensional component of the velocity gradient along the axis of rotation, causes the streamlines to become tightly wound spirals. Fluid elements therefore follow helical paths with a drift along the axis of the rotation. Thus, for the case of heat transfer at high Pe , Batchelor showed that it was only the component of the rate-of-strain tensor along the axis of rotation ($E_\omega = \mathbf{E}:\omega\omega$) which leads to this drift, and therefore, contributes to the heat transfer. Hence, for a fairly general class of linear flows the expression for the Nusselt number was found to be:

$$Nu = 0.968 \left(\frac{a^2 E_\omega}{D} \right)^{1/3}, \quad (1.2)$$

with the conditions that $|\omega|$ is not much smaller than E or that $|E_\omega|$ is not asymptotically small (in which case the spirals would cease to be tightly wound). When E_ω is zero, the drift which contributed to the heat transfer vanishes and we recover a closed streamline region near the sphere with the heat transfer becoming diffusion limited.

The above discussions have mainly looked at heat transfer in the low Reynolds number limit where the Stokes approximation is assumed valid. The Reynolds number entered, if at all, in the form of a regular perturbation about a leading order Stokesian contribution to the heat transfer. Subramanian & Koch (2006a) showed that, in the case of small spheres freely suspended in a planar linear flow, weak inertia has a fundamental effect on the heat transfer by destroying the region of closed streamlines which existed at $Re = 0$ (Acrivos (1971), Robertson & Acrivos (1970a), Poe & Acrivos (1975)). The streamlines become spirals, thereby opening up new channels of convection. Subramanian & Koch (2006a) showed that, in the limit of small but finite Re and for $Pe \gg 1$ and $RePe \gg 1$, when the near-surface streamlines are tightly wound spirals, the Nusselt number once again scales with Pe and is given by:

$$Nu = 0.33(RePe)^{1/3}, \quad (1.3)$$

for simple shear flow. Subramanian & Koch (2006b) extended this analysis for a general planar

linear flow and derived an expression for the Nusselt number which is given by:

$$Nu = 0.33(1 + \alpha)^{2/3}(RePe)^{1/3}. \quad (1.4)$$

Yang *et al.* (2011) have carried out simulations of heat transfer from spheres at finite Re which find good agreement in the relevant asymptotic limits of large Pe with the theoretical predictions by Subramanian & Koch (2006b).

1.2 Transport from Drops

While it is evident that the problem of transport from solid particles has received a great deal of attention, the analogous problem for drops in an ambient linear flow has been less widely studied, at least using a first-principles approach. Torza *et al.* (1971) analysed the streamlines in the interior and exterior of a drop in a simple shear flow. Their theoretical analysis predicted closed streamlines adjacent to the drop as well as open streamlines further away, and the existence of a limiting separatrix surface which separates regions of closed and open streamlines. The ratio of drop fluid to ambient fluid viscosity (λ) was found to influence the extent of this closed streamline region and the shape of the limiting separatrix surface. Additionally, Torza *et al.* (1971) performed experiments which confirmed their theoretical predictions and showed the presence of a closed streamline region. Importantly, their experiments showed that a closed streamline region also forms around a slightly deformed drop, implying that the deformation does not fundamentally modify this aspect of the flow. The theoretical analysis for streamlines interior and exterior to drops was extended to the case of a general one-parameter family of planar linear flows by Powell (1983), and equations were derived for the two families of streamsurfaces which intersect to give the streamlines. It was shown that extent of the closed streamline region and the limiting surface depended on both the linear flow parameter (α) as well as the viscosity ratio (λ). Interestingly, it was shown that, for any $\lambda < \infty$, there were values of α for which the region of closed streamlines around the drop was absent and only open streamlines were present. We note that $\lambda \rightarrow \infty$ corresponds to a solid particle, in which case, as seen earlier, all streamlines remain open only in the case of extensional flow. Thus, we have the important result that for a drop in a give planar linear flow, unlike a solid particle, we have two fundamentally distinct regimes with respect to the streamlines in the near-field. In turn, these regimes must reflect in the differing nature of the Nu -surface when plotted as a function of α and λ .

A first-principles solution of the problem of heat transfer from a neutrally buoyant, immiscible drop at high Pe has not received much attention in literature. The problem has only been solved for specific cases of the ambient flow, and a general expression for the Nusselt number, along the lines of that obtained by Batchelor (1979) for a solid particle, is not available. Among the problems which have been solved is the case of a drop in a uniform flow which is straightforward on account of the axisymmetric nature of the temperature field (Leal (2007)). The case of an ambient axisymmetric extensional flow, which is comparable in difficulty to the case of uniform flow was examined by Gupalo & Riazantsev (1972). Gupalo *et al.* (1975) have carried out the analysis for an ambient flow which is a sum of an axisymmetric extension and a uniform flow, again an axisymmetric problem. The only other example includes the case of a drop in a planar

extensional flow for which the drop is again surrounded by open streamlines and the approach used by [Batchelor \(1979\)](#) can be used. This calculation was done by [Polyanin \(1984\)](#). For all these cases, the flow field adjacent to the drop is entirely composed of open streamlines, and in the limit of high Pe , there is a thin thermal boundary layer which forms next to the drop whose thickness scales as $Pe^{-1/2}$. This results in the Nusselt number scaling as $Nu \sim O(Pe^{1/2})$. Note that this scaling implies that the heat transport from a drop is asymptotically larger than that from a solid particle at the same Pe , since the no-slip boundary condition in the latter case weakens convective effects. The problem for a general linear flow (planar or three-dimensional) has not been solved till date. Additionally, for the case of planar linear flows, the drop is surrounded by a region of closed streamlines and in this case inertia is expected to have a major effect on the heat transfer as seen for solid particles ([Subramanian & Koch \(2006a\)](#), [Subramanian & Koch \(2006b\)](#)). This problem has not received any attention in literature.

1.3 Our Work

The above literature survey motivates us to study, in this part of the thesis, the fundamental problem of heat transfer from single spherical drops in a general linear flow. We first consider drops in the one-parameter family of planar linear flows. Interestingly, for this case, depending on the flow parameter (α) and the viscosity ratio (λ), the streamline pattern may be classified into two distinct regimes. The first is an open-streamline regime which exists for viscosity ratios below a critical value ($\lambda_c = 2\alpha/(1 - \alpha)$), and where a boundary-layer-enhanced heat transfer leads to $Nu \sim O(Pe^{1/2})$ for large Pe , as seen above. In the other regime, which exists for $\lambda > \lambda_c$, the drop is completely surrounded by closed streamlines and the heat transfer is diffusion limited at $Re = 0$ even as $Pe \rightarrow \infty$. Recall that, for a solid particle in a planar linear flow, transport is always diffusion limited except when $\alpha = 1$ (extensional flow). The addition of inertia only has a perturbative effect in the open-streamline regime. Small but finite inertia however, leads to a widely different picture in the closed streamline regime. Thus, the drop heat transfer problem considered here consists of a rich parameter space, displaying both open and closed streamline patterns, which lead to fundamentally distinct transport characteristics. Our analytical study of this problem offers insights into the two limiting cases where the resistance to transport is entirely confined to either the open or closed streamline region, thus offering insights into the more general case which may involve resistances due to a combination of these.

The rest of this part of the thesis is organised as follows:

In chapter 2, we study the flow topology in both the interior and exterior of a spherical drop in a planar linear flow, first with the Stokes approximation ($Re = 0$) and then with small but finite inertia. Following the approach of [Kao *et al.* \(1977\)](#) and [Powell \(1983\)](#), we derive the equations for the two families of streamsurfaces which intersect to give the Stokesian streamline pattern. Importantly, we show through a graphical approach that allows for a unified analysis of both the interior and exterior streamline patterns. Using this, one may predict the nature of streamlines in the interior as well as exterior regions for given values of the flow parameter α and viscosity ratio λ . Through our analysis of the Stokesian streamline pattern, we make the important observation that the streamlines exterior to a drop show *two* distinct regimes namely the open and closed streamline regimes mentioned above. We then derive the important result

that the Stokesian surface streamlines for a drop are not circles (as for a solid particle) but are Jeffery orbits (Jeffery (1922)) with an aspect ratio which depends on the flow parameters α and the viscosity ratio λ . The original Jeffery orbits refer to the trajectories traced out by the orientation vector of an axisymmetric particle in a linear flow. Note that the Jeffery orbits, for a general axisymmetric particle, are describable in terms of an effective aspect ratio which differs from the true aspect ratio except for a spheroid. The above insight allows us to derive a flow-aligned non-orthogonal coordinate system which is used later in the heat transfer analysis. We then study the effect of a small amount of inertia on the external flow field which is relevant to the exterior heat transfer problem considered here. We show that, just as in the solid particle case, inertia breaks the region of closed streamlines, transforming them into spiralling ones. However, in contrast to the solid particle case, these are not circular as mentioned above implying that the heat transfer problem is non-axisymmetric and hence non-trivial. Further, we find a distinct regime, not observed in the case of solid particles, where the direction of spiralling near the plane of symmetry is reversed in a certain region in (α, λ) plane.

In chapter 3, we derive a solution for the heat transfer from a drop, in the open streamline regime for two families of linear flows: planar linear flows with viscosity ratios less than λ_c , and three-dimensional extensional flow. For this case inertia only plays a perturbative role, and does not enter the solution at leading order. We recast the Stokesian heat transfer problem in the non-orthogonal coordinate system derived in chapter 2. Next we derive a solution for the temperature field in the drop exterior, and thence, for the Nusselt number. This has the form:

$$Nu = \mathcal{F}(\alpha, \lambda) Pe^{1/2}, \quad (1.5)$$

where a closed form expression for the pre-factor $F(\alpha, \lambda)$ is derived in our analysis. We then proceed to solve the heat transfer equation for the case of a drop in a three-dimensional extensional flow with no vorticity. We show that we can derive a non-orthogonal coordinate for this case as well which is analogous to the one used for planar linear flows. Using this coordinate system we derive an expression for the Nusselt number which has the form:

$$Nu = \frac{\mathcal{G}(\epsilon)}{(1 + \lambda)^{1/2}} Pe^{1/2}, \quad (1.6)$$

where $\epsilon = E_2/E_1$ and E_1, E_2 are the principal rates of strain of the extensional flow. Our analysis recovers the known results for planar extensional flow and axisymmetric (uni-axial or bi-axial) extensional flow as special cases of the above general solution with $E_2 = 0$ and $E_1 = E_2$, respectively.

In chapter 4, we consider the regime $\lambda > \lambda_c$ for which the drop is completely surrounded by closed streamlines in the absence of inertia and for which the transport is diffusion limited for $Pe \rightarrow \infty$. We consider the case of small inertia in the flow and devise a method of solution using the coordinate system derived in chapter 2. The $O(Re)$ flow field for this case has been derived by Raja *et al.* (2010). Briefly, the spiralling streamlines, which arise at finite Re , open up new convective channels, and our method allows us to calculate the Jeffery-orbit-averaged drift due to inertia which contributes to the convective heat transfer. We solve the problem with the assumption that this inertial convection still dominates diffusion everywhere except in a thin

layer near the drop; the thickness of this thermal boundary layer is $O(Re^{-1/2} Pe^{-1/2})$. While the analysis is more intricate than the open-streamline analysis in chapter 3, we show that the three-dimensional heat transfer problem for this case can be simplified to a one-dimensional one using our coordinate system. We show that this coordinate system, in effect transforms the drop heat transfer problem which is non-axisymmetric to a much simpler axisymmetric one akin to the one solved for a solid particle (Subramanian & Koch (2006b)). The Nusselt number for this case is shown to be given by:

$$Nu = \mathcal{H}(\alpha, \lambda) Re^{1/2} Pe^{1/2} \quad (1.7)$$

in the limit of $Pe \gg 1$ and $RePe \gg 1$. The pre-factor $\mathcal{H}(\alpha, \lambda)$ is given by our analysis. We conclude the chapter by examining the connection between the open and closed streamline regimes which corresponds to λ near λ_c . In this so-called intermediate regime, there exist regions on the drop surface where both the inertial and Stokes velocity fields are comparable. Analysis of the intermediate regime via scaling arguments allows us to estimate the asymptotic region of validity of our open and closed(inertial) streamline solutions.

In chapter 5 we conclude and give some suggestions for future work.

Chapter 2

Flow Topology

In this chapter we study the interior and exterior flow fields for a neutrally buoyant drop of a given Newtonian fluid immersed in an ambient suspending medium which is again Newtonian. The ambient medium is assumed to be undergoing a general two-dimensional linear flow; these comprise a one-parameter family, the parameter being a certain ratio of vorticity to extension, where the requirement of two-dimensionality implies the vorticity vector is perpendicular to the plane of the extensional flow. We assume that the Reynolds number defined based on the drop radius is small such that viscous forces dominate inertial forces on the scale of the drop. The Reynolds number is defined as $Re = \dot{\gamma}a^2/\nu$, where, $\dot{\gamma}$ is a characteristic magnitude of the velocity gradient of the ambient flow, a the radius of the drop and ν is the kinematic viscosity of the suspending fluid. We note that the small length scale of the drop compared to the length scale over which the ambient velocity gradients vary, and also the fact that the drop is neutrally buoyant, are directly related to our assumption of an ambient linear flow. This is because, with the above assumptions, any complicated flow appears, in a frame of reference moving with the drop, as a linear flow at leading order. Further, we consider the case where surface tension forces dominate viscous forces leading to the drop interface remaining spherical at all times. This corresponds to a regime where the capillary number (Ca) is small, where $Ca = \mu\dot{\gamma}a/\Gamma$, and μ is the dynamic viscosity of the ambient fluid, Γ is the interfacial tension between the drop and ambient fluid. The onset of drop deformation at finite Ca will not qualitatively alter the conclusions of our analysis. For instance, the main objective of this first part of the thesis is to determine the Nusselt number as a function of the flow parameters and the drop-to-medium viscosity ratio. The key qualitative features of this Nusselt number surface will remain insensitive to the effects of small drop deformation. As we shall subsequently see, with these assumptions, we get a problem which is rich in physics and is also relevant in practical applications.

Beginning with the inertialess ($Re = 0$) flow topology we will move on to discussing the effects of inertia on the velocity field. Importantly, we will look at the flow from a geometrical perspective to best appreciate the spatial organization of the flow field around a spherical drop. Other than being of fundamental interest, this characterization will lay the foundation for the heat transfer analysis carried out in subsequent chapters. As we shall see, the flow topology for drops in an ambient planar linear flow shows two distinct regimes: the open and closed streamline regimes. The open streamline topology at $Re = 0$ will serve as a basis for the heat transfer analysis carried out in chapter 3, while the effects of inertia on the closed streamline topology will serve as a basis for the heat transfer analysis in chapter 4.

2.1 Governing Equations and Boundary Conditions

We denote the viscosities and densities of the fluids inside and outside the drop as $\hat{\mu}$, μ , $\hat{\rho}$ and ρ , with the variables with carets corresponding to the fluid within the drop. Neutral buoyancy implies that $\hat{\rho} = \rho$. The governing equations for fluid flow in the low-Reynolds-number limit are the Stokes equations given by:

$$\begin{aligned} -\nabla p + \mu \nabla^2 \mathbf{u} &= 0, \\ \nabla \cdot \mathbf{u} &= 0, \end{aligned} \quad (2.1)$$

where \mathbf{u} is the fluid velocity and p the associated pressure field. To convert these equations to dimensionless form, we use the radius of the undeformed drop as a characteristic length scale, $l_c = a$; the characteristic velocity based on the ambient flow, $u_c = \dot{\gamma}a$ for the velocity scale; and the viscous scalings for the interior and exterior pressure fields, $p_c = \mu u_c / l_c$ and $\hat{p}_c = \mu u_c / l_c$. Using these scalings, the governing equations in dimensionless form for the flow inside and outside the drop are, respectively, given by:

$$\left. \begin{aligned} -\nabla \hat{p} + \lambda \nabla^2 \hat{\mathbf{u}} &= 0 \\ \nabla \cdot \hat{\mathbf{u}} &= 0 \end{aligned} \right\} \text{interior problem,} \quad \left. \begin{aligned} -\nabla p + \nabla^2 \mathbf{u} &= 0 \\ \nabla \cdot \mathbf{u} &= 0 \end{aligned} \right\} \text{exterior problem,} \quad (2.2)$$

where $\lambda = \hat{\mu}/\mu$ is the drop to ambient fluid viscosity ratio. The ambient flow considered here will be a one-parameter family of two-dimensional linear flows which is defined by the velocity gradient tensor $\mathbf{\Gamma}$ given, in dimensionless form, by:

$$\mathbf{\Gamma} = \begin{bmatrix} 0 & -2 & 0 \\ -2\alpha & 0 & 0 \\ 0 & 0 & 0 \end{bmatrix}. \quad (2.3)$$

The second order tensor $\mathbf{\Gamma}$ can be written in terms of its symmetric and anti-symmetric components as:

$$\mathbf{\Gamma} = \mathbf{E} + \mathbf{\Omega}, \quad (2.4)$$

where \mathbf{E} is the rate-of-strain tensor and $\mathbf{\Omega}$ is the vorticity tensor. The parameter α in Eq. 2.3 measures the relative strengths of extension and vorticity, and is given by $\alpha = (E - \Omega)/(E + \Omega)$, where $2E/(E + \Omega)$ and $2\Omega/(E + \Omega)$ denote the normalized magnitudes of the rate-of-extension and vorticity, respectively. Therefore, $\alpha = -1$ ($E = 0$) represents pure vortical flow (solid body rotation); $\alpha = 0$ corresponds to simple shear flow ($E = \Omega$) and $\alpha = 1$ corresponds to two-dimensional extensional flow ($\Omega = 0$). In our coordinate system depicted in Fig. 2.1, x_1 , x_2 and x_3 are the flow, gradient and vorticity axis, respectively, of the ambient simple shear flow. We also note that the principal axes of the extensional flow are rotated by $\pi/4$ with respect to the x_1 and x_2 axes. While the flow, gradient and vorticity axes are specifically relevant to a simple shear flow, they will be used in this thesis to refer to the x_1 , x_2 and x_3 axes, respectively, for a general linear flow.

It is convenient to split the exterior velocity field for the drop as:

$$\mathbf{u} = \mathbf{\Gamma} \cdot \mathbf{x} + \mathbf{u}', \quad (2.5)$$

where \mathbf{u}' is the exterior disturbance velocity due to the drop. Since any linear flow (with a trivial pressure field) is a solution of the Stokes equations, the disturbance field also satisfies Eq. 2.2.

The other major parameter entering into the analysis is the viscosity ratio (λ), defined as ratio of drop to ambient fluid viscosity. The boundary conditions imposed on the flow inside and outside the drop are given by

$$\mathbf{u}' \rightarrow 0 \quad \text{as } r \rightarrow \infty \quad (\text{disturbance velocity decays off at infinity})$$

$$\hat{\mathbf{u}} = \mathbf{u}' + \mathbf{\Gamma} \cdot \mathbf{x} \quad \text{at } r = 1 \quad (\text{continuity of velocity at interface})$$

$$\mathbf{u} \cdot \hat{\mathbf{n}} = \hat{\mathbf{u}} \cdot \hat{\mathbf{n}} = 0 \quad r = 1 \quad (\text{stationary spherical interface}),$$

$$(\boldsymbol{\sigma} \cdot \hat{\mathbf{n}}) \cdot (\mathbf{I} - \hat{\mathbf{n}}\hat{\mathbf{n}}) = (\hat{\boldsymbol{\sigma}} \cdot \hat{\mathbf{n}}) \cdot (\mathbf{I} - \hat{\mathbf{n}}\hat{\mathbf{n}}) \quad \text{at } r = 1 \quad (\text{continuity of tangential stress at the interface})$$

where $\hat{\mathbf{n}}$ is the unit radial vector and $\boldsymbol{\sigma}$, $\hat{\boldsymbol{\sigma}}$ are the stress tensors in the exterior and interior fluid, respectively. Also we note that the condition of normal stress balance at $r = 1$ is not required to solve the system of equations for the velocity and pressure fields due to the assumed spherical shape of the interface. Based on the velocity and stress fields obtained at leading order, the normal stress balance would be used to determine the small, $O(Ca)$, drop deformation on account of viscous stresses. In turn, one may use this $O(Ca)$ interfacial deformation to determine the $O(Ca)$ correction to the velocity and stress fields; the normal stress balance may then be used to calculate the $O(Ca^2)$ deformation, and so on, in what is essentially an asymptotic expansion for small Ca .

The Stokes equations (Eq. 2.2) subject to the above boundary conditions can be solved to yield the well-known result for the velocity field in the drop interior and exterior (Leal (2007), Cox (1969)). In spherical polar coordinates with the polar axis aligned along the vorticity direction of the ambient flow, the components of the velocity field are given by:

$$u_r = -(1 + \alpha)r[A(r; \lambda)r^2 + B(r; \lambda)] \sin^2 \theta \sin 2\phi, \quad (2.6)$$

$$u_\theta = -\frac{(1 + \alpha)}{2}rB(r; \lambda) \sin 2\theta \sin 2\phi, \quad (2.7)$$

$$u_\phi = -(1 + \alpha)r \sin \theta [B(r; \lambda) \cos 2\phi - \beta], \quad (2.8)$$

where $A(r; \lambda)$ and $B(r; \lambda)$ are functions of r and λ which take different forms in the interior and exterior of the drop and $\beta = (1 - \alpha)/(1 + \alpha)$. $A(r; \lambda)$ and $B(r; \lambda)$ are given by:

$$\left. \begin{aligned} A(\lambda) &= -\frac{1}{1 + \lambda}, \\ B(r; \lambda) &= \frac{5r^2 - 3}{2(1 + \lambda)} \end{aligned} \right\} \text{interior} \quad (2.9)$$

$$\left. \begin{aligned} A(r; \lambda) &= -\frac{5\lambda + 2}{2(\lambda + 1)r^5} + \frac{5\lambda}{2(1 + \lambda)r^7}, \\ B(r; \lambda) &= 1 - \frac{\lambda}{(1 + \lambda)r^5}. \end{aligned} \right\} \text{exterior} \quad (2.10)$$

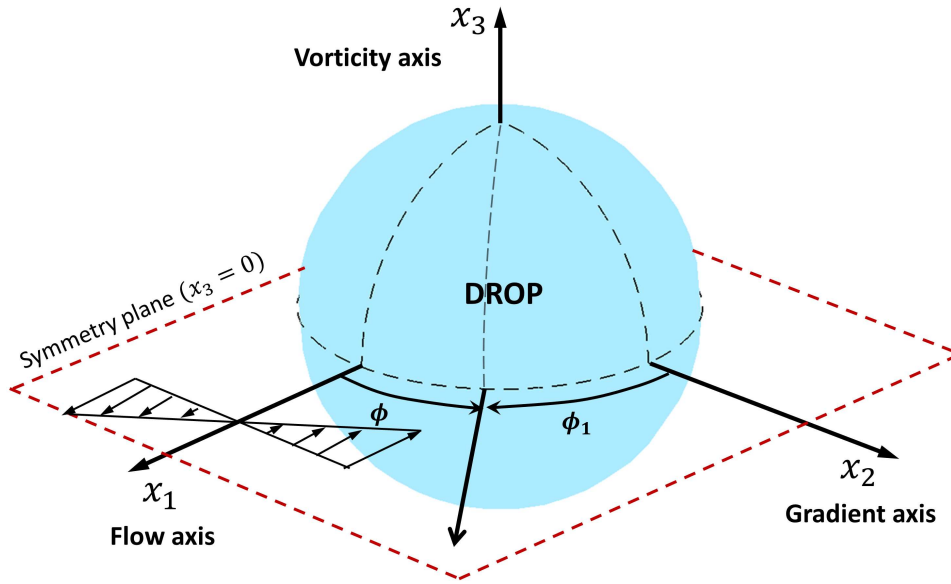


Figure 2.1: Schematic of the coordinate system used showing the flow, gradient and vorticity axes for the particular case where the ambient flow is a simple shear flow.

2.2 Streamline Topology: Fixed Point Analysis

Based on the expressions for the interior and exterior velocity fields given earlier, we now analyze the topology of streamlines in the interior and exterior regions. To help orient oneself, the position of the drop and direction of the base flow with respect to the coordinate system is shown in Figure 2.1. The x_1x_2 plane corresponds to the plane of the base linear flow. For simple shear flow, in particular, x_1 , x_2 and x_3 denote the flow, gradient and vorticity directions, respectively. We will study the behaviour of the fixed points with respect to the (α, λ) parameter space to gain insight into different regimes which exist which regard to the flow topology.

To obtain the location of the fixed points we solve the equations $\mathbf{u} = 0$ and $\hat{\mathbf{u}} = 0$. Keeping α fixed, from Fig. 2.2a we see that at a small value of the viscosity ratio(λ), there are *eight* fixed points on the symmetry plane ($x_3 = 0$) excluding the origin, which is always (trivially) a fixed point. Two pairs lie on the $x_1 = 0$ and $x_2 = 0$ axes within the unit circle, while another two pairs are at an intermediate ϕ location between the axes, but on the unit circle. The location of the first pair is found to be $\{\hat{r}_0^1, \hat{\theta}_0^1, \hat{\phi}_0^1\} = \{[3/5 + (2/5)\beta(1 + \lambda)]^{1/2}, \theta, (0, \pi)\}$ and that of the second is $\{\hat{r}_0^2, \hat{\theta}_0^2, \hat{\phi}_0^2\} = \{[3/5 - (2/5)\beta(1 + \lambda)]^{1/2}, \theta, (\pi/2, 3\pi/2)\}$. The fact that θ is arbitrary means that the first two pairs of fixed points on the $x_3 = 0$ plane are actually parts of fixed circles of radii \hat{r}_0^1 and \hat{r}_0^2 , inside the drop, and lying on the flow-vorticity and flow-gradient planes, respectively. It is interesting to note that these two circles will, in general, not intersect, but do so for the special case of $\alpha = 1$. The other two pairs of fixed points are true points lying on the symmetry plane at the surface of the drop, two of which are given by $(\hat{r}_0^3, \hat{\theta}_0^3, \hat{\phi}_0^3) = (1, \pi/2, (1/2)\cos^{-1}[\beta(1 + \lambda)])$ and $(\hat{r}_0^4, \hat{\theta}_0^4, \hat{\phi}_0^4) = (1, \pi/2, -(1/2)\cos^{-1}[\beta(1 + \lambda)])$. The respective pair for each is at a π separated location given by $(1, \pi/2, \pi - (1/2)\cos^{-1}[\beta(1 + \lambda)])$ and $(1, \pi/2, \pi + (1/2)\cos^{-1}[\beta(1 + \lambda)])$, respectively.

All eight of these fixed points exist on or within the drop, as shown in Fig. 2.2a, when λ is below a certain critical value denoted by λ_c . As one increases λ from below λ_c , the first pair

of fixed points moves radially outwards along the x_1 axis while the second pair moves radially inwards along the x_2 axis. From a three-dimensional perspective, this is because the fixed circle of radius \hat{r}_0^1 expands with increasing λ , while the fixed circle of radius \hat{r}_0^2 shrinks. The third and fourth pairs of fixed points move along the drop surface towards $\phi = 0$ and $\phi = \pi$ locations (see the arrows in Fig. 2.2a). At the first critical point, λ_c , the first, third and fourth pairs merge together at the $\phi = 0$ and $\phi = \pi$ points (Fig. 2.2b). Again, in a three-dimensional picture, this corresponds to the fixed circle of radius \hat{r}_0^1 expanding to lie on the drop surface. Thus λ_c can be calculated by solving the equation, $\hat{r}_0^1 = 1$, yielding:

$$\lambda_c = \frac{2\alpha}{(1-\alpha)}. \quad (2.11)$$

For λ values greater than λ_c , the fixed circle resulting from the merger of the third and fourth pairs of fixed points with the fixed circle of radius \hat{r}_0^1 moves outside the drop. At a second critical viscosity ratio λ'_c , the second pair of critical points merge and become coincident with the origin and remain so for all higher viscosity ratios (see Fig. 2.2c). In a three dimensional picture this corresponds to the fixed circle of radius \hat{r}_0^2 shrinking to a point. This second critical viscosity ratio can therefore be calculated by solving $\hat{r}_0^2 = 0$ giving:

$$\lambda'_c = \frac{5\alpha + 1}{2(1-\alpha)}. \quad (2.12)$$

The two critical viscosity ratio curves with respect to α are plotted in Fig. 2.3.

We now return to the first critical viscosity ratio λ_c which, as we show later, is important in the exterior heat transfer problem. As mentioned above, with an increase in λ beyond λ_c , the fixed-circle moves outside the drop interior, and its radius is given by

$$r_0^1 = \left[\frac{(1+\alpha)\lambda}{2\alpha(1+\lambda)} \right]^{1/5}, \quad (2.13)$$

where $r_0^1 > 1$ for $\lambda > \lambda_c$. Thus the only fixed points in the exterior flow lie on a circle and are given by $(r_0^1, \theta, \phi = 0, \pi)$. Importantly, these lie on a separatrix surface which lies at the interface between closed and open streamline regions, the projection of which is shown in Fig. 2.2c. The exact three-dimensional nature of the closed streamline region will be elucidated in the following sections. To summarize, the fixed point analysis has shown us that, with respect to the exterior flow field, there are two regions of interest in the (α, λ) plane separated by the critical viscosity ratio curve $\lambda = \lambda_c(\alpha)$: (1) An open streamline regime for $\lambda < \lambda_c(\alpha)$ where the drop is surrounded by open streamlines only. (2) A closed streamline regime for $\lambda > \lambda_c(\alpha)$, where the drop is completely surrounded by closed streamlines. The second critical viscosity ratio, while important in the context of the interior flow, will not directly play a role in the exterior heat transfer problem. The latter is the focus of this work.

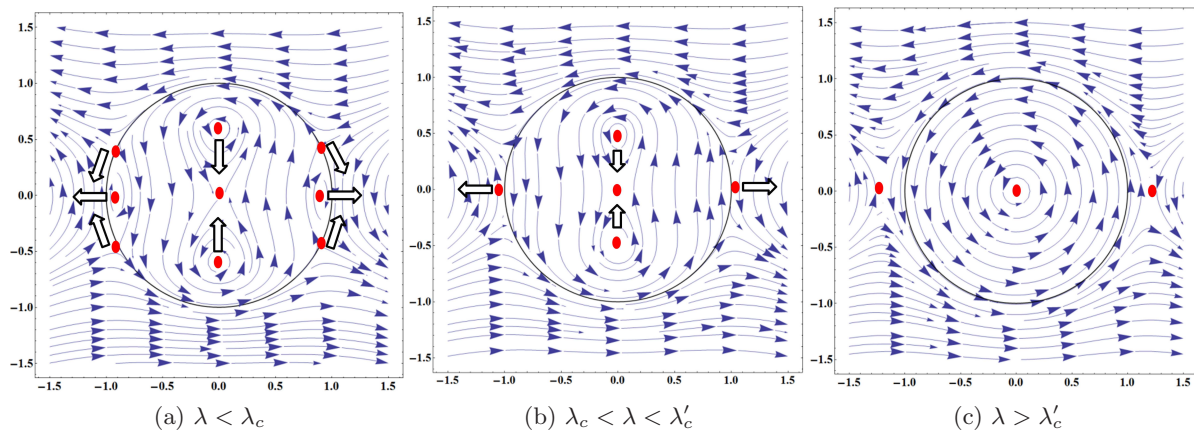


Figure 2.2: Streamlines and fixed point locations interior and exterior to the drop at a fixed value of $\alpha = 0.25$ as a function λ . The arrows indicate the direction of movement of the fixed points lying on the $x_3 = 0$ plane with increasing λ

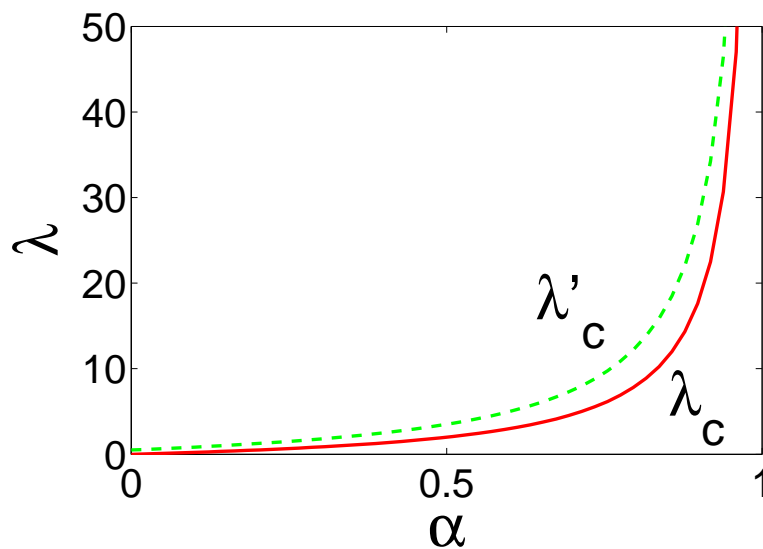


Figure 2.3: The two critical curves for the viscosity ratio λ . Solid red curve : λ_c and the green dashed curve : λ'_c

2.3 Streamline Topology: Characterization using Streamsurfaces

In this section, we derive the equations of the streamlines interior and exterior to the drop. The streamlines will be characterized as curves resulting from the intersections of two families of streamsurfaces. By calculating the relevant bounds on the streamline coordinates, we distinguish between regions of closed and open streamlines and also analyse their three-dimensional topology. This analysis will closely follow that of [Kao *et al.* \(1977\)](#) and [Powell \(1983\)](#). We first derive the equations separately in the interior and exterior regions and later go on to present a systematic and unified analysis valid in both regions. We also make connections to the fixed point analysis presented earlier.

Our starting point is the velocity field equations for the drop given by Eqs. [2.6](#) - [2.8](#). By definition ([Batchelor \(2000\)](#)), the equations that define a streamline, in spherical coordinates, are given by:

$$\frac{dr}{u_r} = \frac{rd\theta}{u_\theta} = \frac{r \sin \theta d\phi}{u_\phi} \quad (2.14)$$

2.3.1 Interior Streamlines

We first derive the equations for the interior streamlines. Substituting for u_r and u_θ from Eqs. [2.6](#), [2.7](#) and [2.9](#) in Eq. [2.14](#), and upon integrating, one obtains:

$$\cos \theta = \hat{D}r^{-1}(1 - r^2)^{-1/3}, \quad (2.15)$$

where \hat{D} is a constant of integration and characterizes a one-parameter family of invariant streamsurfaces in the drop interior ($r \leq 1$). Similarly, considering the second relation in Eq. [2.14](#) and substituting for u_θ and u_ϕ from Eqs. [2.7](#) and [2.8](#), one obtains:

$$\frac{d\theta}{(1 + \alpha) \sin \theta \cos \theta \sin 2\phi B(r; \lambda)} = \frac{d\phi}{(1 + \alpha)B(r; \lambda) \cos 2\phi - (1 - \alpha)}, \quad (2.16)$$

and, upon rearranging, we get:

$$\sin \theta \cos \theta \sin 2\phi \frac{d\phi}{d\theta} = \cos 2\phi - \frac{\beta}{B(r; \lambda)}, \quad (2.17)$$

$$\sin \theta \cos \theta \sin 2\phi \frac{d\phi}{d\theta} + 2 \sin^2 \phi = 1 - \frac{\beta}{B(r; \lambda)}, \quad (2.18)$$

where, recall that $\beta = (1 - \alpha)/(1 + \alpha)$. This is a linear first-order differential equation and the integrating factor is found to be $\sin \theta / (\cos^3 \theta)$. Multiplying both sides by the integrating factor, one obtains:

$$\frac{d(\tan^2 \theta \sin^2 \phi)}{d\theta} = \left[1 - \frac{\beta}{B(r; \lambda)} \right] \frac{\sin \theta}{\cos^3 \theta}. \quad (2.19)$$

Substituting for $B(r, \lambda)$ from Eq. 2.9 (corresponding to the interior flow), rewriting the RHS and integrating both sides with respect to θ , one obtains:

$$\tan^2 \theta \sin^2 \phi = [1 - \beta(1 + \lambda)] \int \frac{\sin \theta}{\cos^3 \theta} d\theta + 5\beta(1 + \lambda) \int \frac{(r^2 - 1) \sin \theta}{(5r^2 - 3) \cos^3 \theta} d\theta. \quad (2.20)$$

Integrating the first term on the RHS, one obtains:

$$\tan^2 \theta \sin^2 \phi = \frac{1 - \beta(1 + \lambda)}{2 \cos^2 \theta} + \hat{F} + 5\beta(1 + \lambda) \int \frac{(r^2 - 1) \sin \theta}{(5r^2 - 3) \cos^3 \theta} d\theta, \quad (2.21)$$

where \hat{F} is a constant of integration. Substituting for $\theta(r)$ from Eq. 2.15, and performing the second integration, one obtains:

$$\sin^2 \theta \sin^2 \phi = \frac{1 - \beta(1 + \lambda)}{2} + \hat{F} \hat{D}^2 r^{-2} (1 - r^2)^{-2/3} - \frac{\beta(1 + \lambda)}{2} r^{-2} (1 - r^2). \quad (2.22)$$

Simplifying the RHS further and denoting the combination $\hat{F} \hat{D}^2$ by the constant \hat{E} , we get the final expression for the second set of interior streamsurfaces, termed the “ \hat{E} surfaces”, as:

$$\sin \theta \sin \phi = \pm \left[\frac{1}{2} - \frac{\beta(1 + \lambda)}{2r^2} + \hat{E} r^{-2} (1 - r^2)^{-2/3} \right]^{1/2}. \quad (2.23)$$

We now use Eqs. 2.15 and 2.23 to comment on both the topology of the streamsurfaces and thence, their curves of intersection, the streamlines. Rewriting the Eqs. 2.15 and 2.23 for the interior region, one obtains:

$$x_2 = \pm r \left[\frac{1}{2} - \frac{\beta(1 + \lambda)}{2r^2} + \hat{E} r^{-2} (1 - r^2)^{-2/3} \right]^{1/2}, \quad (2.24)$$

$$x_3 = \hat{D} (1 - r^2)^{-1/3}. \quad (2.25)$$

Note that x_3 and x_2 in the above equations are functions of r alone. This implies that the \hat{D} and \hat{E} surfaces form one-parameter families of surfaces-of-revolution about the x_3 and x_2 axes, respectively. From Eq. 2.25 we see that the streamsurface identified by $\hat{D} = 0$ corresponds both to the surface $r = 1$, which is the drop surface and also the symmetry plane $\theta = \pi/2$ ($x_3 = 0$). The drop surface is also a limiting member of the “ \hat{E} surfaces” family and corresponds to the surface $\hat{E} = 0$. One consequence of the drop surface (unit sphere) being a member of both families is that the surface streamlines cannot be recovered as the curves of intersection from the present analysis. We consider these streamlines independently in section 2.4.

A streamline is thus defined by an intersection of a given \hat{D} and \hat{E} surface and can be uniquely identified by the labels (\hat{D}, \hat{E}) . To analyze the nature of the interior streamlines further, we make a note of the following bounds that exist for the streamline expressions. Since $0 \leq |x_2| \leq r$ we can write down the following relations for the \hat{E} surfaces:

$$\hat{E} \leq \frac{(1 - r^2)^{2/3}}{2} [\beta(1 + \lambda) + r^2] = \hat{F}_1(r), \quad (2.26)$$

$$\hat{E} \geq \frac{(1 - r^2)^{2/3}}{2} [\beta(1 + \lambda) - r^2] = \hat{F}_2(r). \quad (2.27)$$

Eqs. 2.26 - 2.27 allow us to study the nature and spatial extent of the streamlines. For a given streamline (identified by the pair of streamsurface labels, as mentioned above), we can calculate the interval in the spatial coordinates bounded by $(r_{min}, \theta_{min}, \phi_{min})$ and $(r_{max}, \theta_{max}, \phi_{max})$ for which the above relationships are satisfied. For instance, when the lower and upper bounds for the radial coordinate of a streamline are both finite, one can conclude that these are closed streamlines (in the $Re = 0$ limit). This lets us distinguish between open and closed streamlines. Open streamlines are characterized by an interval in the radial coordinate where the upper bound is at infinity, since an open streamline, by definition, comes from or goes to infinity relative to the drop position

To calculate the allowed intervals in r , we consider the behaviour of the RHS of Eqs. 2.26-2.27 as a function of r . Starting with the RHS of Eq. 2.26, given by $\hat{F}_1(r)$, we see that this function varies non-monotonically from $\beta(1 + \lambda)/2$ at $r = 0$ to zero at $r = 1$ with a single maximum at $r_1 = [3/5 - (2/5)\beta(1 + \lambda)]^{1/2}$. The location of this maxima is nothing but the second fixed circle derived for the interior flow given by $(\hat{r}_0^2, \hat{\theta}_0^2, \hat{\phi}_0^2)$ which was identified in section 2.2. Similarly, the RHS of Eq. 2.27, given by $\hat{F}_2(r)$, varies between the same two limits as $\hat{F}_1(r)$, but with an intermediate minimum at $r_2 = [3/5 + (2/5)\beta(1 + \lambda)]^{1/2}$. Again, this is the first fixed circle in the interior flow $(\hat{r}_0^1, \hat{\theta}_0^1, \hat{\phi}_0^1)$, which was identified in section 2.2. It is straightforward to see that $r_2 \geq r_1$. The curves $\hat{F}_1(r)$ and $\hat{F}_2(r)$ are plotted for the most general case, where the maxima of $\hat{F}_1(r)$ and minima of $\hat{F}_2(r)$ (and hence the two fixed circles) are found within the drop ($r \leq 1$), in Fig. 2.4.

In-plane Streamlines

It is possible, using the afore-mentioned curves (see Fig. 2.4), to comment on the geometry of the interior streamlines based on their streamline label for the most general behaviour of $\hat{F}_1(r)$ and $\hat{F}_2(r)$ (both fixed circle lying within the drop). We will first discuss streamlines lying on the symmetry plane ($x_3 = 0$), all of which have the $\hat{D} = 0$ label. This in turn helps one understand the three-dimensional topology of the interior streamlines. For different values of \hat{E} (horizontal lines in Fig. 2.4), we now derive the allowed ranges in the radial coordinate using Eqs. 2.26 - 2.27. The allowed ranges are depicted as hashed green lines in Fig. 2.4.

- $\hat{E} < \hat{F}_2(r_2)$: No interior streamlines are defined for this range of the streamline label since Eq. 2.27 is not satisfied for any value of $r \in [0, 1]$.
- $\hat{F}_2(r_2) \leq \hat{E} < 0$: For this range of the streamline label we have a closed streamline branch with an \hat{r}_{min2} and \hat{r}_{max2} which are solutions of $E = \hat{F}_2(r)$ (see Fig. 2.4 (i)). At $\hat{E} = \hat{F}_2(r_2)$ these maxima and minima coincide and the streamline label corresponds to the fixed points $(\hat{r}_0^1, \pi/2, \hat{\phi}_0^1)$ and $(\hat{r}_0^1, \pi/2, \pi - \hat{\phi}_0^1)$ (see Fig. 2.4 (i)). For off-plane streamlines for which $\hat{D} \neq 0$, this corresponds to the fixed circle given by $(\hat{r}_0^1, \hat{\theta}_0^1, \hat{\phi}_0^1)$.
- $0 \leq \hat{E} < \beta(1 + \lambda)/2$: We have a closed streamline branch with an \hat{r}_{min2} which is a solution of $E = \hat{F}_2(r)$, and an \hat{r}_{max1} arising from a solution of $E = \hat{F}_1(r)$ (see Fig. 2.4 (ii)). $\hat{E} = 0$ corresponds to a separatrix streamline separating two classes of interior streamlines ((i) and (ii) in Fig. 2.4) and is depicted by a red dashed curve in Fig. 2.4 (ii).

- $\beta(1 + \lambda)/2 \leq \hat{E} < \hat{F}_1(r_1)$: This corresponds to a closed streamline branch with an \hat{r}_{min1} and an \hat{r}_{max1} both of which are solutions of $E = \hat{F}_1(r)$ (see Fig. 2.4 (iii)). $\hat{E} = \beta(1 + \lambda)/2$ corresponds to a second eight-shaped separatrix streamline separating two classes of interior streamlines ((ii) and (iii) in Fig. 2.4) and is depicted by a red dashed curve in Fig. 2.4 (iii).
- $\hat{F}_1(r_1) \leq \hat{E}$: At $\hat{E} = \hat{F}_1(r_1)$, the minima and maxima of the closed streamline are coincident and correspond to the fixed points given by $(\hat{r}_0^2, \pi/2, \hat{\phi}_0^2)$ and $(\hat{r}_0^2, \pi/2, \pi - \hat{\phi}_0^2)$ (see Fig. 2.4 (iii)). In a three-dimensional picture for which $\hat{D} \neq 0$, this corresponds to the fixed circle given by $(\hat{r}_0^2, \hat{\theta}_0^2, \hat{\phi}_0^2)$. Greater values of \hat{E} do not correspond to interior streamlines.

One can also comment about the ϕ and θ locations where the streamlines attain their minima or maxima value in r . This in turn helps one deduce the three-dimensional structure of the streamlines. The roots of $E = \hat{F}_1(r)$, in light of Eqs. 2.23 and 2.26, give rise to the condition that $\sin \theta \sin \phi = 0$, which means that the streamline attains \hat{r}_{min2} and \hat{r}_{max2} at $(\theta, \phi = 0, \pi)$, where θ is arbitrary. Roots of $E = \hat{F}_2(r)$, using Eq. 2.23 and 2.27, give rise to the condition that $\sin \theta \sin \phi = \pm 1$. Thus, \hat{r}_{min1} and \hat{r}_{max1} occur at $(\theta = \pi/2, \phi = \pi/2, 3\pi/2)$.

Thus, in general, there are *three* distinct classes of interior streamlines. The first has an r_{min2} and an r_{max2} , both lying at $\phi = (0, \pi)$ (Fig. 2.4 (i)). The second has an r_{min2} and an r_{max1} at $\phi = (0, \pi)$ and $\phi = (\pi/2, 3\pi/2)$, respectively (Fig. 2.4 (ii)). The third has an r_{min1} and an r_{max1} , both at $\phi = (\pi/2, 3\pi/2)$ (Fig. 2.4 (iii)). As we comment later in the combined analysis of interior and exterior streamlines (2.3.3), all three types occur only when $\lambda < \lambda_c$. We note that the first and third classes of streamlines correspond to two in-plane closed streamlines for each value of the streamline label \hat{E} , while the second class corresponds to a single, in-plane, closed streamline per streamline label.

2.3.2 Exterior Streamlines

Next, we derive the streamline equations in the exterior region. As for the interior case, we first consider the streamline equation for the r and θ coordinates, to obtain:

$$\frac{B(r; \lambda) dr}{r [A(r; \lambda) r^2 + B(r; \lambda)]} = \tan \theta d\theta. \quad (2.28)$$

Substituting for $A(r; \lambda)$ and $B(r; \lambda)$ from Eq. 2.10 in Eq. 2.14 corresponding to the exterior, and upon performing the straightforward integration of Eq. 2.28, one obtains for the exterior flow field:

$$\cos \theta = Df(r), \quad (2.29)$$

$$f(r) = \left[r^3 - \frac{5\lambda + 2}{2(\lambda + 1)} + \frac{3\lambda}{2(\lambda + 1)r^2} \right]^{-1/3}, \quad (2.30)$$

where D is a constant of integration and characterizes the first set of streamsurfaces, the so-called “ D surfaces” in the drop exterior. Now, considering the equation relating θ and ϕ and proceeding as before, we get Eq. 2.19, where $B(r)$ is now for the exterior flow. As before the

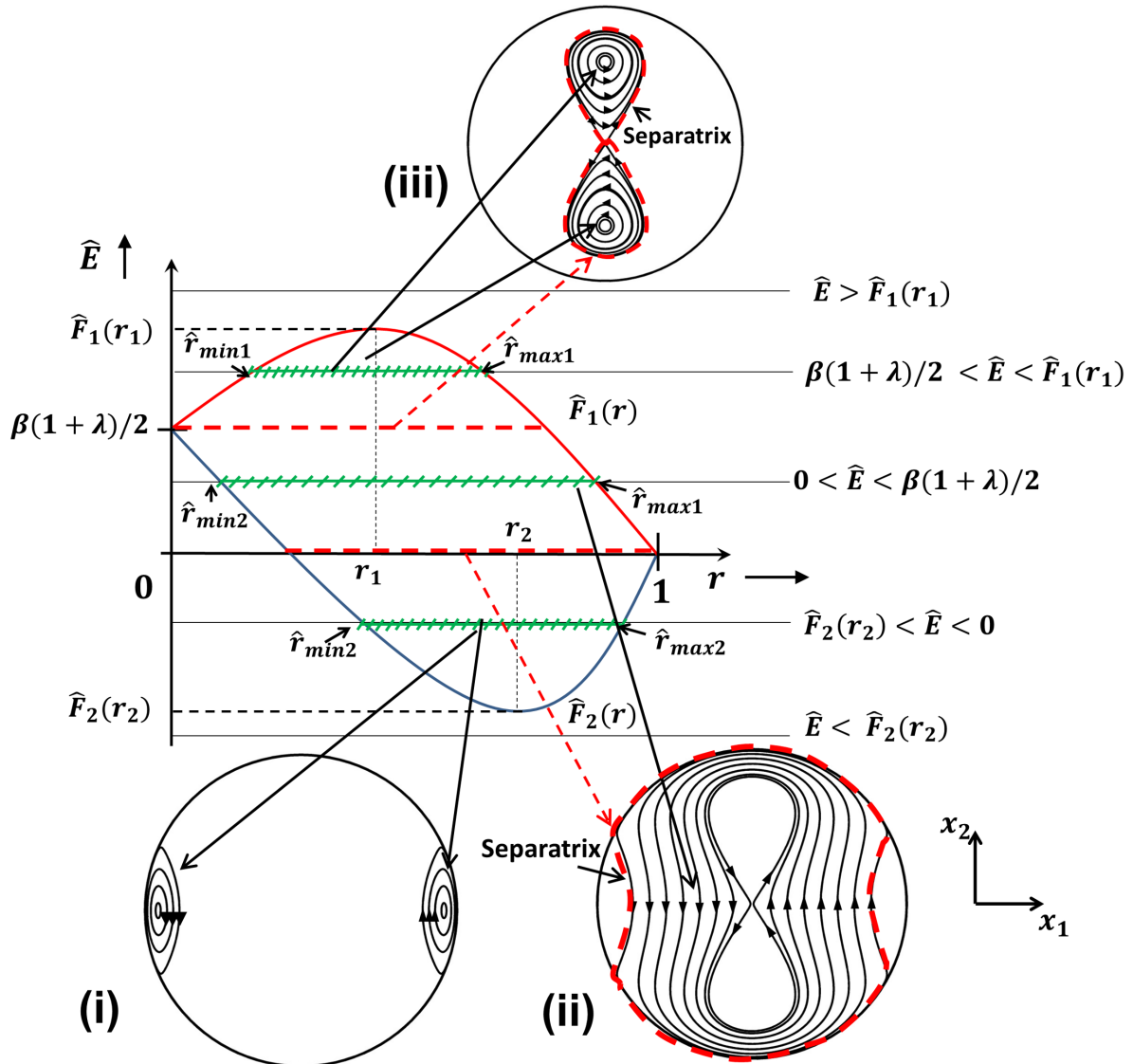


Figure 2.4: Plots of $\hat{F}_1(r)$ and $\hat{F}_2(r)$ with respect to r in the interior region, horizontal lines denote different values of the streamline label \hat{E} . There are three classes of interior streamlines (in general) which are labelled (i), (ii) and (iii). The green dashes depict the allowed range in r of a given class of streamlines. Black arrows connect each of the green hashed lines to the corresponding class of streamlines. Red(dashed) arrows connect the red dashed lines to the separatrix streamlines which separate two different classes of streamlines.

integrating factor is given by $\sin \theta / \cos^3 \theta$. Rearranging the RHS, and integrating both sides with respect to θ , gives:

$$\tan^2 \theta \sin^2 \phi = \int \left[\frac{2\alpha}{1+\alpha} - \frac{\beta\lambda}{(\lambda+1)r^5 - \lambda} \right] \frac{\sin \theta}{\cos^3 \theta} d\theta.$$

Integrating the first term, one obtains:

$$\tan^2 \theta \sin^2 \phi = \frac{\alpha}{\cos^2 \theta (1+\alpha)} + F - \int \left[\frac{\beta\lambda}{(\lambda+1)r^5 - \lambda} \right] \frac{\sin \theta}{\cos^3 \theta} d\theta,$$

where F is a constant of integration. Substituting for θ in terms of r from 2.29, and transforming the integral, one obtains:

$$\tan^2 \theta \sin^2 \phi = \frac{\alpha}{\cos^2 \theta (1+\alpha)} + F - \frac{\beta\lambda}{(1+\lambda)D^2} \int f(r)r^{-3} dr. \quad (2.31)$$

Rewriting the above and substituting for $\cos \theta$ from Eq. 2.29, one obtains:

$$\sin^2 \theta \sin^2 \phi = \frac{\alpha}{(1+\alpha)} + FD^2[f(r)]^2 + \frac{\beta\lambda}{(1+\lambda)}[f(r)]^2 \int_r^\infty f(y)y^{-3} dy \quad (2.32)$$

We note that $f(r)r^{-3}$ goes to zero as $r \rightarrow \infty$. Denoting the combination FD^2 by E , we have the final expression for the second set of stream-surfaces in the drop exterior which will henceforth be referred to as the “ E surfaces”:

$$\sin \theta \sin \phi = \pm \left[\frac{\alpha}{(1+\alpha)} + Ef(r)^2 + \frac{\beta\lambda}{(1+\lambda)}f(r)^2g(r) \right]^{1/2}, \quad (2.33)$$

where $g(r) = \int_r^\infty f(y)y^{-3} dy$.

As for the interior streamlines, we use Eqs. 2.29 and 2.33 to comment on the topology of the stream surfaces, and thence, the exterior streamlines. Rewriting Eqs. 2.29 and 2.33 for the exterior region, one obtains:

$$x_2 = \pm r \left[\frac{\alpha}{(1+\alpha)} + Ef(r)^2 + \frac{\beta\lambda}{(1+\lambda)}f(r)^2g(r) \right]^{1/2}, \quad (2.34)$$

$$x_3 = rDf(r). \quad (2.35)$$

Just as in the interior case, the D and E surfaces are surfaces of revolution about the x_3 and x_2 axes, respectively. In the exterior flow, the $D = 0$ label corresponds to the surface $r = 1$ and also $x_3 = 0$ (the symmetry plane), as seen from Eq. 2.35. Thus the near-field D surfaces hug the drop for the most part and become parallel to the symmetry plane near $x_3 = 0$. Further, the nature of the constant D surfaces can be deduced by noting that as $r \rightarrow \infty$ the equation for the D surface reduces to $x_3 = D$, implying that the D surfaces far away from the drop are parallel to the symmetry plane. From Eq. 2.35, surfaces with positive values of D leads to surfaces with $x_3 > 0$ while negative values of D lead to a surfaces which are mirrored across the $x_3 = 0$ plane. This symmetry implies that it is sufficient to restrict our attention to positive values of x_3 , and hence positive values of D .

Based on Eq. 2.34, we now write down the bounds that exist for the streamlines. Since $0 \leq |x_2| \leq r$, we can write down the following relations for the E surfaces:

$$E \leq \frac{1}{(1+\alpha)f(r)^2} - \frac{\beta\lambda g(r)}{1+\lambda} = F_1(r), \quad (2.36)$$

$$E \geq \frac{-\alpha}{(1+\alpha)f(r)^2} - \frac{\beta\lambda g(r)}{1+\lambda} = F_2(r). \quad (2.37)$$

We now proceed to use Eqs. 2.36 and 2.37 to study the nature and spatial extent of the exterior streamlines. The RHS of Eqs. 2.36, given by $F_1(r)$, is a strictly increasing function and has a value of $-\beta\lambda g(1)/(1+\lambda)$ at $r = 1$. The RHS of Eq. 2.37, given by $\hat{F}_2(r)$, is non-monotonic with a single maximum at a value of r given by:

$$r_0 = \left[\frac{\lambda(1+\alpha)}{(1+\lambda)2\alpha} \right]^{1/5}. \quad (2.38)$$

Note that this is the same radial location as the fixed circle in the exterior flow field which was calculated earlier and is given in Eq. 2.13 (section 2.2). The value of the streamline label corresponding to this maximum is given by $E_0 = F_2(r_0)$. The shape of the curves $F_1(r)$ and $F_2(r)$ are plotted with respect to r in Fig. 2.5 for the most general case, for which the maximum of $F_2(r)$ occurs at $r_0 \geq 1$, which corresponds to the aforementioned fixed circle.

In-plane Streamlines

We now comment on the nature of streamlines lying in the symmetry plane ($x_3 = 0$) by considering different values of the streamline label E . Note that for these streamlines, $D = 0$. We can further deduce the nature of the E surfaces by generating the surface of revolution of these streamlines about the x_2 axis.

- $E < -\beta\lambda g(1)/(1+\lambda)$: For this case the streamlines have a minimum r given by r_{min2} above which Eq. 2.37 is not satisfied. These are open streamlines since their maximum allowed radial distance is infinity (see Fig. 2.5 (i)).
- $-\beta\lambda g(1)/(1+\lambda) < E < E_0$: Here we have two streamline branches. The first of these corresponds to a closed streamline branch with an r_{min1} which is a solution of $F_1(r) = E$ and an r_{max2} which is a solution of $F_2(r) = E$ (see Fig. 2.5 (ii)). The second is an open streamline branch with an r_{min2} given by a second solution of $F_2(r) = E$ (see Fig. 2.5 (i)). Since $F_1(r) \geq F_2(r)$, we see that $r_{max2} > r_{min1}$ and $r_{min2} > r_{max2}$.
- $E = E_0$: For this case r_{max2} and r_{min2} are coincident and this corresponds to a separatrix which separate the region of closed and open streamlines. The separatrix consists of a closed portion with an r_{min1} from $F_1(r)$ and an r_{max2} from $F_2(r)$; it also consists of an open portion which has an $r_{min2} = r_0$. Both these are depicted as red, dashed curves in (ii) and (iii), respectively, in Fig. 2.5.
- $E > E_0$: For this case we have a single open streamline branch given by $F_1(r)$ with an r_{min1} (see Fig. 2.5 (iii)).

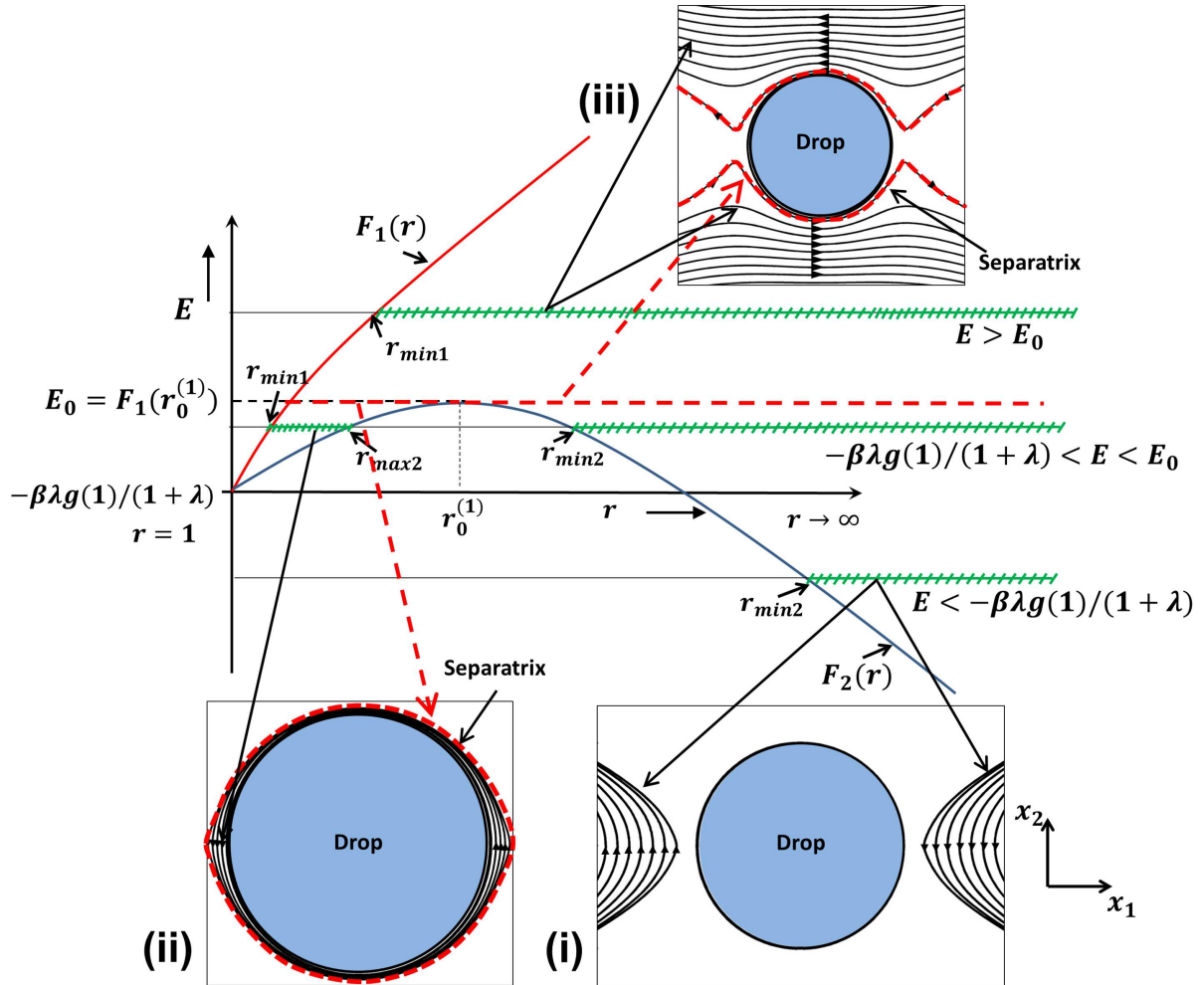


Figure 2.5: Plots of $F_1(r)$ and $F_2(r)$ with respect to r in the exterior region, horizontal lines depict various cases for the streamline label E . There are three classes of exterior streamlines (in general) which are labelled (i), (ii) and (iii). The green dashes depict the allowed range in r of a given class of streamlines. Black arrows connect each of the green hashed lines to the corresponding class of streamlines. Red(dashed) arrows connect the red dashed lines to the separatrix streamlines which separate two different classes of streamlines.

As for the interior flow we comment on the θ and ϕ locations where the streamlines achieve their maximum or minimum distance of approach to the drop. If we consider the r_{min1} limit imposed due to $F_1(r)$, it is clear that $E = F_1(r_{min1})$ also means that $\sin \theta \sin \phi = \pm 1$, as seen from Eqs. 2.33 and 2.36. Thus r_{min1} occurs at $(\theta = \pi/2, \phi = \pi/2, 3\pi/2)$. Similarly from Eqs. 2.33 and 2.37, we see that $E = F_2(r_{max2})$ and $E = F_2(r_{min2})$ is equivalent to $\sin \theta \sin \phi = 0$, meaning that the streamlines are at r_{min2} and r_{max2} at $(\theta, \phi = 0, \pi)$, where θ is arbitrary.

In summary, in the exterior flow field we have, in general, *three* classes of streamlines. There are *two* distinct classes of open streamlines, the first has an r_{min2} at $\phi = (0, \pi)$, while the second has an r_{min1} at $\phi = (\pi/2, 3\pi/2)$. These correspond to (i) and (iii) in Fig. 2.5. There is a single class of closed streamlines with an r_{min1} at $\phi = (\pi/2, 3\pi/2)$ and a r_{max2} at $\phi = (0, \pi)$ (see (ii) in Fig. 2.5). We note that streamline labels corresponding to the open streamline branches, correspond to two streamlines each (see (i) and (iii) in Fig. 2.5), while the closed streamline branches correspond to a single streamline per label (see (ii) in Fig. 2.5). There also exists a separatrix (with an open and closed portion) which separates the regions of closed and open streamline regions (depicted as red, dashed curves in (ii) and (iii) in Fig. 2.5).

Off-plane Streamlines

It is possible to use the streamline shapes on the symmetry plane along with our knowledge of the D surfaces to understand the nature of off-plane streamlines. Since the in-plane streamlines are a result of the intersection of E surfaces with the $D = 0$ surface ($x_3 = 0$), we can generate the three-dimensional E surfaces as surfaces-of-revolution of these streamlines about the x_2 axis.

The closed streamlines surrounding the drop, which exist when $\lambda > \lambda_c$ and $-\beta\lambda g(1)/(1+\lambda) < E < E_0$, lead to E surfaces which enclose a finite volume, since they are surfaces-of-revolution of a closed curve. These have the same minimum and maximum distance of approach to the drop (given by r_{min1} and r_{max2}) as the in-plane closed streamlines and may be likened to a saturn shape since they bulge out at the flow-vorticity plane (where their maximum radial distance r_{max2} occurs), and are flattened along the gradient axis (where they attain their minimum radial distance r_{min1}). The largest of these closed surfaces is a portion of the separatrix surface which is given by $E = E_0$. This surface is the limiting surface separating the region of closed streamlines adjacent to the drop from the open streamline region. The separatrix surface has a maximum radial distance r_0 and a minimum radial distance given by r_{min1} . The maximum radial distance can be used as a measure for the extent of the closed streamline region. As seen from the expression for r_0 this region is infinite in extent for simple shear flow ($\alpha = 0$). On the other hand, for planar extensional flow ($\alpha = 1$), this radial extent is smaller than the drop radius for any finite value of the viscosity ratio, indicating the absence of a closed streamline region in the drop exterior. For $E < -\beta\lambda g(1)/(1+\lambda)$ the E surfaces are topologically equivalent to one-sheeted hyperboloids of revolution about the x_2 axis with a minimum distance of approach given by r_{min2} and a maximum which is unbounded. Similarly, the second open streamline branch which occurs for $E > -\beta\lambda g(1)/(1+\lambda)$ leads to a set of surfaces are topologically equivalent to two-sheeted hyperboloids of revolution about the x_2 axis. The open portion of the separatrix surface $E = E_0$ is topologically like a distorted double cone along the x_2 axis with a unit sphere inserted at the origin.

The off-plane closed streamlines, which play a role in the $O(Re)$ heat transfer problem, are

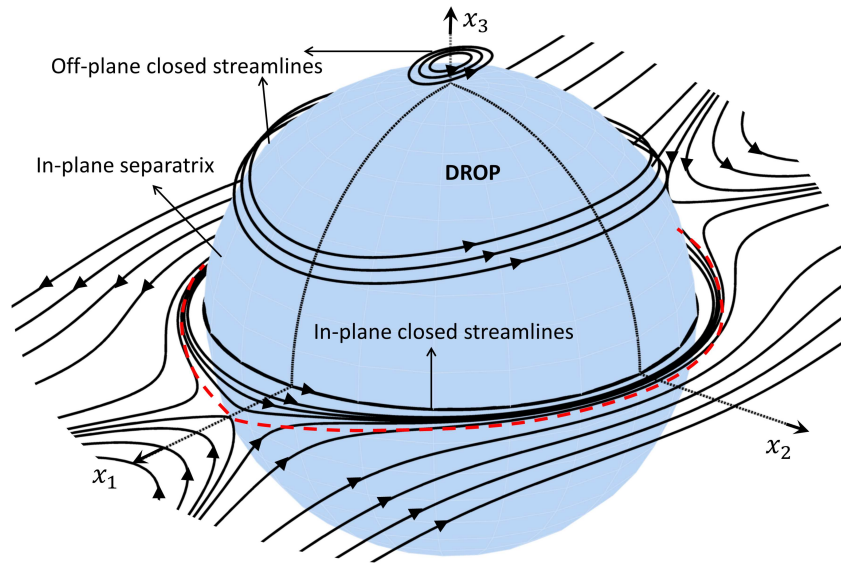


Figure 2.6: In-plane and off-plane closed streamlines along with in-plane open streamlines for a drop. The in-plane separatrix is shown as a red dashed curve

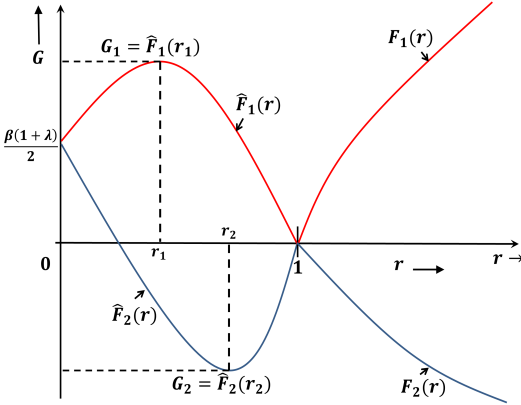
then given by intersection of the saturn shaped E surfaces for $(-\beta\lambda g(1)/(1+\lambda) < E \leq E_0)$ with the D surfaces for $D \neq 0$. From the shapes of the D and E surfaces, we see that the off-plane closed streamlines are nearest to the $x_3 = 0$ plane at $\phi = \pi/2, 3\pi/2$ and are farthest away at $\phi = 0, \pi$ (see Fig. 2.6). Also the separatrix, which is given by $E = E_0$, places a bound on the D surfaces which contribute to closed streamlines. The separatrix surface has an $r_{max2} = r_0$ and it intersects the largest D surface at a point at distance of r_0 along the x_3 axis. This corresponds to the value of the D surface satisfying $D^*f(r_0) = 1$, giving $D^* = 1/f(r_0)$. Thus the closed streamline region is bounded by $-D^* < D < D^*$ and $(-\beta\lambda g(1)/(1+\lambda) < E < E_0)$. Fig. 2.6 shows a plot of both in-plane and off-plane closed streamlines.

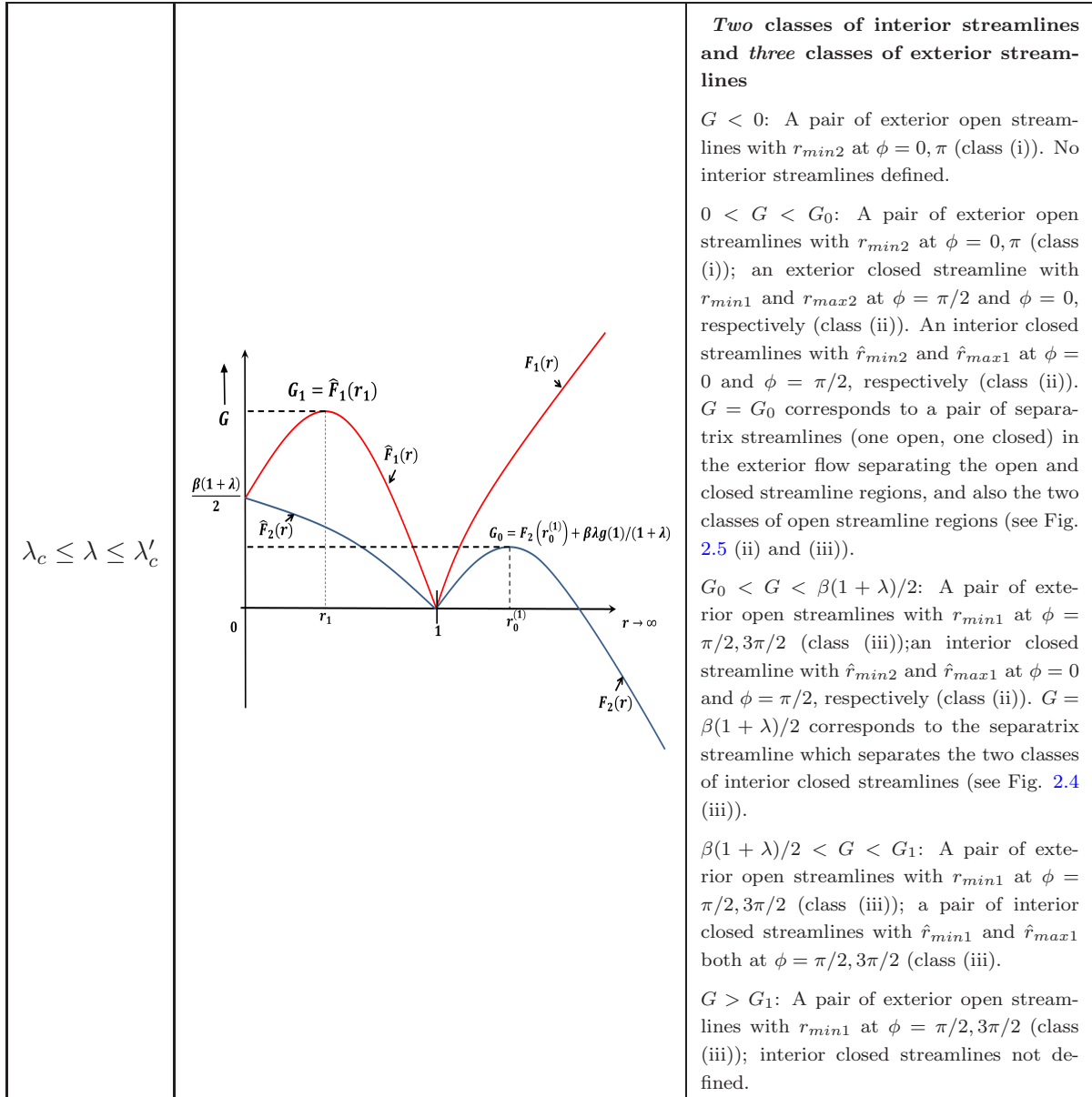
As we mentioned previously, a version of this analysis, involving the interior and exterior streamlines for a drop in a planar linear flow, has been carried out by [Kao *et al.* \(1977\)](#) (simple shear flow), [Powell \(1983\)](#) (general planar linear flows). However, our emphasis is on the implications of the streamline topology for the heat transfer and this has motivated us to independently carry out this analysis. For instance, our fixed point analysis enables us to distinguish between regimes where the drop is surrounded by open or closed streamlines, which is important for carrying out the heat transfer analysis. Further, in the next section, we present a unified picture of the interior and exterior streamlines which has not been done previously. Also, in a subsequent section (section 2.4), we derive a non-orthogonal coordinate system based on the streamlines on the drop surface, which, as we shall see in subsequent chapters, will play a crucial role in both the open streamline and closed streamline heat transfer analyses.

2.3.3 Combined Analysis of Interior and Exterior Streamlines

While the analysis presented above considers the most general behaviour of the RHS functions, their behaviour is a function of both α and λ as seen from Eqs. 2.26, 2.27, 2.36 and 2.37, and

need not always subscribe to the general scenario. Also these curves are not independent of each other with respect to α and λ . For instance, we note that for a given value of (α, λ) , $\hat{F}_2(r)$ cannot have a minimum in $r \in [0, 1]$, while $F_2(r)$ has a maximum in $r \in (1, \infty)$. In other words, there is a transition between monotonicity and non-monotonicity (in opposite directions for $\hat{F}_2(r)$ and $F_2(r)$) at the same critical value of λ . The flow field within the drop is therefore connected to the flow field outside. Apart from a theoretical understanding, there is also an important utility of doing such a combined analysis from an experimental view point. It is in general more challenging to study the flow inside a drop via experiments whereas the flow outside is more readily accessible (Torza *et al.* (1971)). Thus one can, by understanding the relationship between the interior and exterior flow, deduce the interior flow field using observations of the exterior field. This motivates the streamline classification in a unified manner for the interior and exterior regions using a single streamline label. In order to do this, we rewrite the streamline label E in the exterior coordinate as $G = E + \beta\lambda g(1)/(1 + \lambda)$. This allows $G = \hat{E}$, and the transformed variable $G = E + \beta\lambda g(1)/(1 + \lambda)$, to be the single streamline label describing both the interior and exterior flow since the RHS curves with respect to r for Eqs. 2.26, 2.27, 2.36 and 2.37 are now continuous across the drop interface ($r = 1$). We find that, as seen above in the fixed-point analysis, there are two critical values of the viscosity ratio λ_c and λ'_c resulting in three distinct regimes for the streamlines interior and exterior to the drop. A summary of this analysis is presented in Table. 2.1. This table is best understood in conjunction with Figs. 2.2, 2.4 and 2.5. We will use the labels (i), (ii) and (iii) to identify the three classes of interior and exterior streamlines depicted in Figs. 2.4 and 2.5, respectively.

Range in viscosity ratio	Behaviour of RHS functions Eqs. 2.26, 2.27, 2.36 and 2.37	Classification of streamlines
$0 \leq \lambda \leq \lambda_c$		<p>Three classes of interior streamlines and two classes of exterior streamlines</p> <p>$G < G_2$: A pair of exterior open streamlines with r_{min2} at $\phi = 0, \pi$</p> <p>$G_2 < G < 0$: A pair of exterior open streamlines with r_{min2} at $\phi = 0, \pi$ (class (i)); a pair of interior closed streamlines with \hat{r}_{min2} and \hat{r}_{max2} at $\phi = 0, \pi$ (class (i))</p> <p>$0 < G < \beta(1 + \lambda)/2$: A pair of exterior open streamlines with r_{min1} at $\phi = \pi/2, 3\pi/2$ (class (iii)); an interior closed streamline with \hat{r}_{min2} and \hat{r}_{max1} at $\phi = 0$ and $\phi = \pi/2$, respectively (class (ii)). $G = 0$ corresponds to a separatrix streamline, with $\hat{r}_{max2} = 1$, separating the first and second class of interior streamlines (see Fig. 2.4 (ii)). This also corresponds to the separatrix streamline in the exterior flow, with $r_{min2} = 1$, separating the two classes of exterior open streamlines (see Fig. 2.5 (iii)).</p> <p>$\beta(1 + \lambda)/2 < G < G_1$: A pair of exterior open streamlines with r_{min1} at $\phi = \pi/2, 3\pi/2$ (class (iii)); a pair of interior closed streamlines with \hat{r}_{min1} and \hat{r}_{max1} both at $\phi = \pi/2, 3\pi/2$ (class (iii)). $G = \beta(1 + \lambda)/2$ corresponds to the separatrix between the second and third class of interior streamlines (see Fig. 2.4 (iii)).</p> <p>$G > G_1$: A pair of exterior open streamlines with r_{min1} at $\phi = \pi/2, 3\pi/2$ (class (iii)); interior closed streamlines not defined.</p>



$\lambda'_c \leq \lambda \leq \infty$	<p style="text-align: center;"> $G_0 = F_2(r_0^{(1)}) + \beta\lambda g(1)/(1+\lambda)$ </p>	<p>One class of interior streamlines and three classes of exterior streamlines</p> <p>$G < 0$: A pair of exterior open streamlines with r_{min2} at $\phi = 0, \pi$ (class (i)). No interior streamlines defined.</p> <p>$0 < G < G_0$: A pair of exterior open streamlines with r_{min2} at $\phi = 0, \pi$ (class (i)), and a closed streamline branch with r_{min1} and r_{max2} at $\phi = \pi/2$ and $\phi = 0$, respectively (class (ii)). An interior closed streamline with \hat{r}_{min2} and \hat{r}_{max1} at $\phi = 0$ and $\phi = \pi/2$, respectively (class (ii)). $G = G_0$ corresponds to a pair of separatrix streamlines (one open and one closed) in the exterior which separate the closed and open streamline regions, and also separate the two classes of open streamlines (see Fig. 2.5 (ii) and (iii)).</p> <p>$G_0 < G < \beta(1+\lambda)/2$: A pair of exterior open streamlines with r_{min1} at $\phi = \pi/2, 3\pi/2$ (class (iii)); an interior closed streamline with \hat{r}_{min2} and \hat{r}_{max1} at $\phi = 0$ and $\phi = \pi/2$, respectively (class (ii)).</p> <p>$G > \beta(1+\lambda)/2$: A pair of exterior open streamlines with r_{min1} at $\phi = \pi/2, 3\pi/2$ (class (iii)); interior closed streamline not defined.</p>
---------------------------------------	--	--

Table 2.1: Combined analysis of interior and exterior streamlines for a drop.

2.4 The Surface Streamlines at Zero Re - The (C, τ) Coordinate System

It is of interest to separately analyze the streamlines on the surface of the drop, given the important role these play in the exterior heat transfer problem. Since our problem assumes the limit of small Ca , the deformation of the drop is small and therefore neglected. The radial velocity at the surface is thus identically zero, and the surface streamlines are trajectories on the unit sphere determined by the velocity components in the θ and ϕ directions. On the surface, these components reduce to:

$$u_\theta|_{r=1} = -\frac{(1+\alpha)}{2(1+\lambda)} \sin 2\theta \sin 2\phi_1 = \frac{d\theta}{ds}, \quad (2.39)$$

$$u_\phi|_{r=1} = \frac{(1+\alpha)}{(1+\lambda)} \sin \theta [\cos 2\phi_1 + \beta(1+\lambda)] = -\sin \theta \frac{d\phi_1}{ds}, \quad (2.40)$$

where we have used the transformation $\phi_1 = \pi/2 - \phi$, so that ϕ_1 is measured from the x_2 axis. Also, s is the dimensionless time (time measured in units of $\dot{\gamma}^{-1}$). We can rewrite the above

equations as:

$$\frac{d\theta}{ds} = -\frac{(1+\alpha)}{2(1+\lambda)} \sin 2\theta \sin 2\phi_1, \quad (2.41)$$

$$\frac{d\phi_1}{ds} = -\frac{(1+\alpha)}{(1+\lambda)} (\beta(1+\lambda) - 1) \left[\frac{\beta(1+\lambda) + 1}{\beta(1+\lambda) - 1} \cos^2 \phi_1 + \sin^2 \phi_1 \right], \quad (2.42)$$

where we have defined

$$\gamma = \left[\frac{(\beta(1+\lambda) + 1)}{(\beta(1+\lambda) - 1)} \right]^{1/2}. \quad (2.43)$$

Using this we can write the above equations in the form:

$$\frac{d\theta}{ds} = -\frac{(1-\alpha)(\gamma^2 - 1)}{2(\gamma^2 + 1)} \sin 2\theta \sin 2\phi_1, \quad (2.44)$$

$$\frac{d\phi_1}{ds} = -\frac{2(1-\alpha)}{\gamma^2 + 1} [\gamma^2 \cos^2 \phi_1 + \sin^2 \phi_1]. \quad (2.45)$$

We make the important observation by comparing the above equations to Eqs. 2(a) and 2(b) in [Leal & Hinch \(1971\)](#) that these have the exact same form as the equations for the Jeffery orbits of an axisymmetric particle in a shear flow. While in the original Jeffery orbits, the shape of the orbits depended on a geometric aspect ratio (this being the actual aspect ratio for the special case of spheroidal particles), in the present case of a drop, its place is taken by an effective-aspect-ratio γ which depends on the flow parameters α and λ as defined in Eq. 2.43¹. This insight allows us to define a new coordinate system on the drop surface to describe the surface streamlines. Proceeding as in [Leal & Hinch \(1971\)](#), and by integrating Eq. 2.45, one obtains:

$$\tan \phi_1 = \gamma \tan \frac{-2(1-\alpha)s}{\gamma + 1/\gamma}. \quad (2.46)$$

Introducing a new variable $\tau = (-2(1-\alpha)s)/(\gamma + 1/\gamma)$, we have the equation:

$$\tan \phi_1 = \gamma \tan \tau. \quad (2.47)$$

Similarly, we can integrate Eq. 2.44, after substituting for ϕ_1 in terms of τ , and one obtains:

$$\tan \theta = C[\cos^2 \tau + \gamma^2 \sin^2 \tau]^{1/2}. \quad (2.48)$$

Eqs. 2.47 and 2.48 form the basis of the (C, τ) coordinate system. This is a coordinate system where the coordinate lines C and τ are in general not orthogonal to one another. Physically, as seen in Fig. 2.7b, the C coordinate defines which orbit (or trajectory if the streamline is not closed) we are on while the τ coordinate gives the phase along that orbit (trajectory). Following [Leal & Hinch \(1971\)](#), the metrics of the coordinate system h and k and also the skewness angle

¹We note here that while we have highlighted the analogy between the surface streamlines on a drop and Jeffery orbits and a drop for the case of a planar linear flow, the same remains true for a general linear flow. This can be seen by noting that Jeffery orbit equations ([Hinch & Leal \(1972\)](#)) are given by $\dot{\mathbf{p}} = \boldsymbol{\Omega} \cdot \mathbf{p} + \frac{\gamma'^2 - 1}{\gamma'^2 + 1} [\mathbf{E} \cdot \mathbf{p} - \mathbf{p}(\mathbf{E} : \mathbf{p})]$, where γ' is the geometric aspect ratio of the particle. As we show in chapter 3, the drop surface streamlines obey the same equations but with an effective aspect ratio depending on the flow parameters.

α_1 (α_1 would be $\pi/2$ in an orthogonal coordinate system) are found to be given by:

$$h = g_{CC} = \theta_C, \quad (2.49)$$

$$k = g_{\tau\tau} = (\theta_\tau^2 + \sin^2 \theta \phi_{1\tau}^2)^{1/2}, \quad (2.50)$$

$$g_{C\tau} = \theta_C \theta_\tau, \quad (2.51)$$

$$\sin \alpha_1 = \phi_{1\tau} \sin \theta (\theta_\tau^2 + \sin^2 \theta \phi_{1\tau}^2)^{-1/2}, \quad (2.52)$$

where θ_C, θ_τ etc, denote derivatives with respect to the subscript variable, and $g_{CC}, g_{\tau\tau}$ and $g_{C\tau}$ are the components of the metric tensor of the (C, τ) coordinate system on the unit sphere surface, as per the conventional notation (Aris (2012)). The contravariant unit vectors of the (C, τ) coordinate system (i.e the unit vectors along the coordinate lines) in terms of the conventional spherical coordinates unit vectors are given by:

$$\hat{\mathbf{C}} = \hat{\boldsymbol{\theta}}, \quad (2.53)$$

$$\hat{\boldsymbol{\tau}} = \cos \alpha_1 \hat{\boldsymbol{\theta}} + \sin \alpha_1 \hat{\boldsymbol{\phi}}_1, \quad (2.54)$$

where $\hat{\boldsymbol{\phi}}_1 = \cos \phi_1 \hat{\boldsymbol{x}}_1 - \sin \phi_1 \hat{\boldsymbol{x}}_2$ and is the unit vector in the $\hat{\boldsymbol{\phi}}_1$ direction where ϕ_1 is measured in a clockwise sense from x_2 axis. We note that $\hat{\mathbf{C}}$ is still along the meridional direction, but $\hat{\boldsymbol{\tau}}$ is along the streamline/Jeffery orbit, rather than along the azimuth, which leads to the non-orthogonality. The (C, τ) coordinate system is depicted in Fig. 2.7a. The components of the velocity field on the drop surface, in the (C, τ) coordinate system are given by

$$\mathbf{u} = u_C \hat{\mathbf{C}} + u_\tau \hat{\boldsymbol{\tau}}, \quad (2.55)$$

where

$$u_C = u_\theta - \frac{u_{\phi_1} \theta_\tau}{\phi_{1\tau} \sin \theta}, \quad (2.56)$$

$$u_\tau = \frac{k u_{\phi_1}}{\phi_{1\tau} \sin \theta}. \quad (2.57)$$

For the case of Stokes flow, we can show that the velocity along $\hat{\mathbf{C}}$ is:

$$u_C^{(0)} = 0, \quad (2.58)$$

where we have used the expressions for u_θ and u_ϕ given in Eqs. 2.39 and 2.40, respectively. The above result is because the τ coordinate is aligned along the surface streamlines of the Stokes velocity field. This simplification of the velocity field in the (C, τ) coordinate system (i.e the reduction of \mathbf{u} @ $r = 1$ to a one-dimensional field), is helpful in proceeding towards a solution of the heat transfer problem, both in the open and closed streamline regimes, which we solve in Chapters 3 and 4.

The surface streamlines for the open and closed streamline regimes are shown in Fig. 2.8. We now show that our definition of the (C, τ) coordinate system, enables a natural means of distinguishing the presence or absence of closed streamlines in the exterior flow. When closed

streamlines are present, the surface streamlines are true closed orbits, and in this case, they must be characterized by a real valued effective-aspect-ratio γ (as for the case of the original axisymmetric particle). This can be easily seen by noting from Eq. 2.43 that, for $\lambda > \lambda_c$, $\gamma^2 > 0$. On the other hand, for $\lambda < \lambda_c$, for which the drop is surrounded by open streamlines, we see that $\gamma^2 < 0$ leading to a purely imaginary value of γ . This makes intuitive sense since, for the open streamline case, the surface streamlines are not true closed orbits but are trajectories which begin and end at the fixed points on the symmetry plane (see Fig. 2.8a). Thus the value of γ gives us an elegant method to distinguish the closed and open streamline regimes. Another, equally important feature of the parameter γ is that the open streamline heat transfer analysis (discussed in chapter 3), to within a multiplicative factor $(1 - \alpha)$, only depends on γ . Thus, instead of studying a single linear flow and varying the viscosity ratios, we can study at a range of linear flows and viscosity ratios corresponding to a given value of γ .

The mapping from the (C, τ) coordinate system to the spherical polar coordinate system is clear from Eqs. 2.48 and 2.47 at least for the closed streamline regime where γ is real and positive. For the open streamline regime, the imaginary value of γ means that both C and τ describing the surface streamlines are in general complex valued. We elucidate this further while solving the open streamline heat transfer problem in Chapter 3, where an understanding of this complex-valued coordinate system is essential. Here we comment only on the simpler case of the closed streamline regime. The (C, τ) coordinate system and the physical mappings are depicted in Fig. 2.7b. From Eq. 2.48, we see that $\theta = 0$ corresponds to $C = 0$ with τ arbitrary, and $\theta = \pi/2$ corresponds to $C = \infty$ with τ again arbitrary. The τ mapping can be inferred from Eq. 2.47 and we see that as ϕ_1 varies from 0 to 2π ,

τ varies between the same limits. Importantly however, the rates of variation of ϕ_1 and τ along a streamline are not the same and differ by a factor which depends on α and γ . Indeed, we will see in subsequent chapters that τ varies with the dimensionless time s at a constant rate along a surface streamline which only depends on α and γ . This fact, as we shall see later, plays a crucial role in simplifying the heat transfer analysis when the problem is cast in terms of the (C, τ) coordinate system. In effect, the choice of the (C, τ) coordinate system allows for the problem of heat transfer from a drop to be analysed in a manner similar to the solid particle (due to τ along a surface streamline changing at a constant rate).

Thus, the surface streamlines on a drop in both the open and closed streamline regimes can be regarded as generalized Jeffery orbits. This is in contrast to the streamlines near a solid particle (Kao *et al.* (1977)) in a planar linear flow which are circles owing to the fluid elements being dragged along by the rotating solid particle (the no-slip boundary condition). In addition, unlike the case of a drop, the near field streamlines for a solid particle are always closed (Subramanian & Koch (2006b)) in the presence of any amount of finite vorticity in the ambient linear flow. This can be inferred from the principle of reversibility of the Stokes equations which exclude spiralling streamlines at $Re = 0$. The effect of varying the viscosity ratio while keeping α constant is shown in Fig. 2.8. For viscosity ratios below λ_c (Fig. 2.8a), we have the open streamline regime where the surface streamlines are trajectories that begin and end at fixed points on the symmetry plane. For viscosity ratios close to λ_c , the surface streamlines are nearly meridional in nature (Fig. 2.8b). The surface streamlines become closed orbits for viscosity

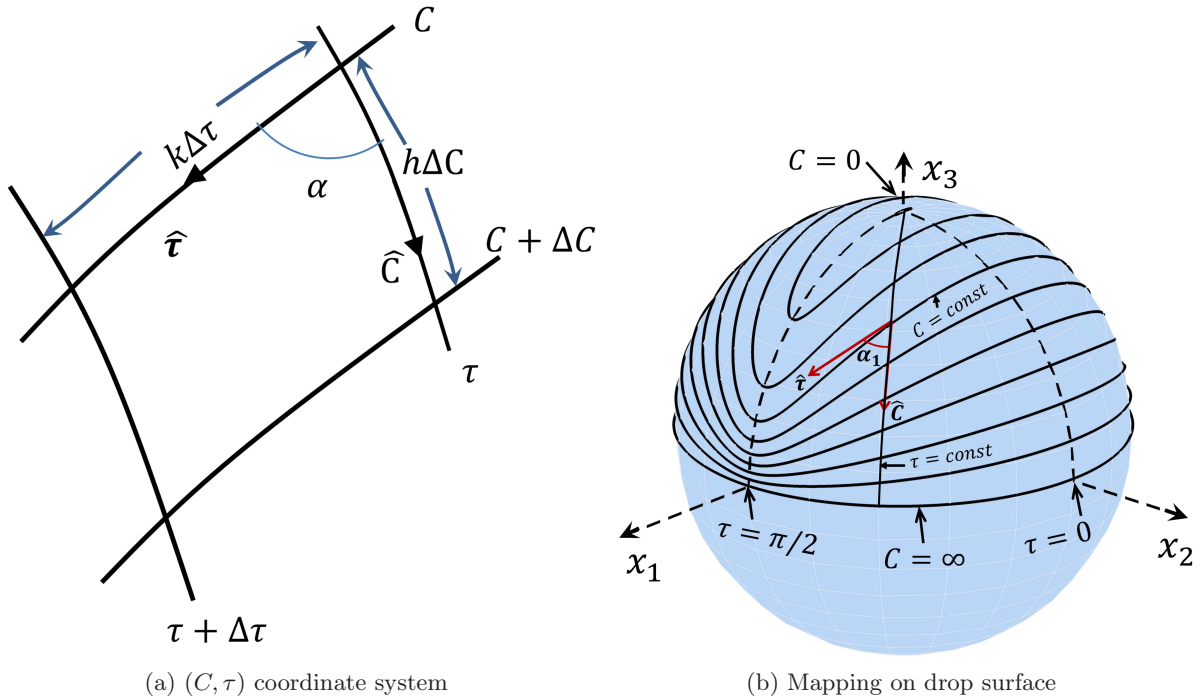


Figure 2.7: (a) Plots of the unit vectors and metrics of the (C, τ) coordinate system. (b) Depiction of the coordinate system on the drop surface showing mapping to spherical polar coordinates

ratios greater than λ_c (Fig. 2.8c. It can be clearly seen that for $\lambda \rightarrow \infty$ the surface streamlines reduce to circles as expected for a solid particle (Fig. 2.8d).

2.5 Streamline Topology with Small but Non-zero Inertia

In this section we discuss the effects of small but non-zero inertia on the streamline topology. The inertial velocity field, to $O(Re)$, may be written as

$$\mathbf{u} = \mathbf{u}^{(0)} + Re\mathbf{u}^{(1)} + O(Re^{3/2}), \quad (2.59)$$

where $\mathbf{u}^{(1)}$ is the $O(Re)$ correction to the Stokes velocity field for a drop in a linear flow calculated by Raja *et al.* (2010) and reproduced in appendix A. We note that the above correction is restricted in its validity to the viscous dominated region at distances (from the drop) smaller than the inertial screening length of $O(aRe^{-1/2})$ (Raja *et al.* (2010)). However, we will be interested mainly in heat transfer at small and finite Re in the strong convection limit, and the above lack of a uniform validity of the velocity field is hardly a restriction. In the context of the heat transfer problem, only the form of the velocity field in a thin thermal boundary layer region near the drop is of consequence. The form of the $O(Re^{3/2})$ field, close to the drop, is known (Subramanian *et al.* (2011b)), but its addition is only expected to alter the heat transfer results by a small amount of $O(Re^{1/2})$. We therefore do not consider it any further in the analysis that follows. The discussion of the streamline topology is based on the $O(Re)$ velocity field.

In the case of a solid sphere, for any ambient planar linear flow with non-zero vorticity, we

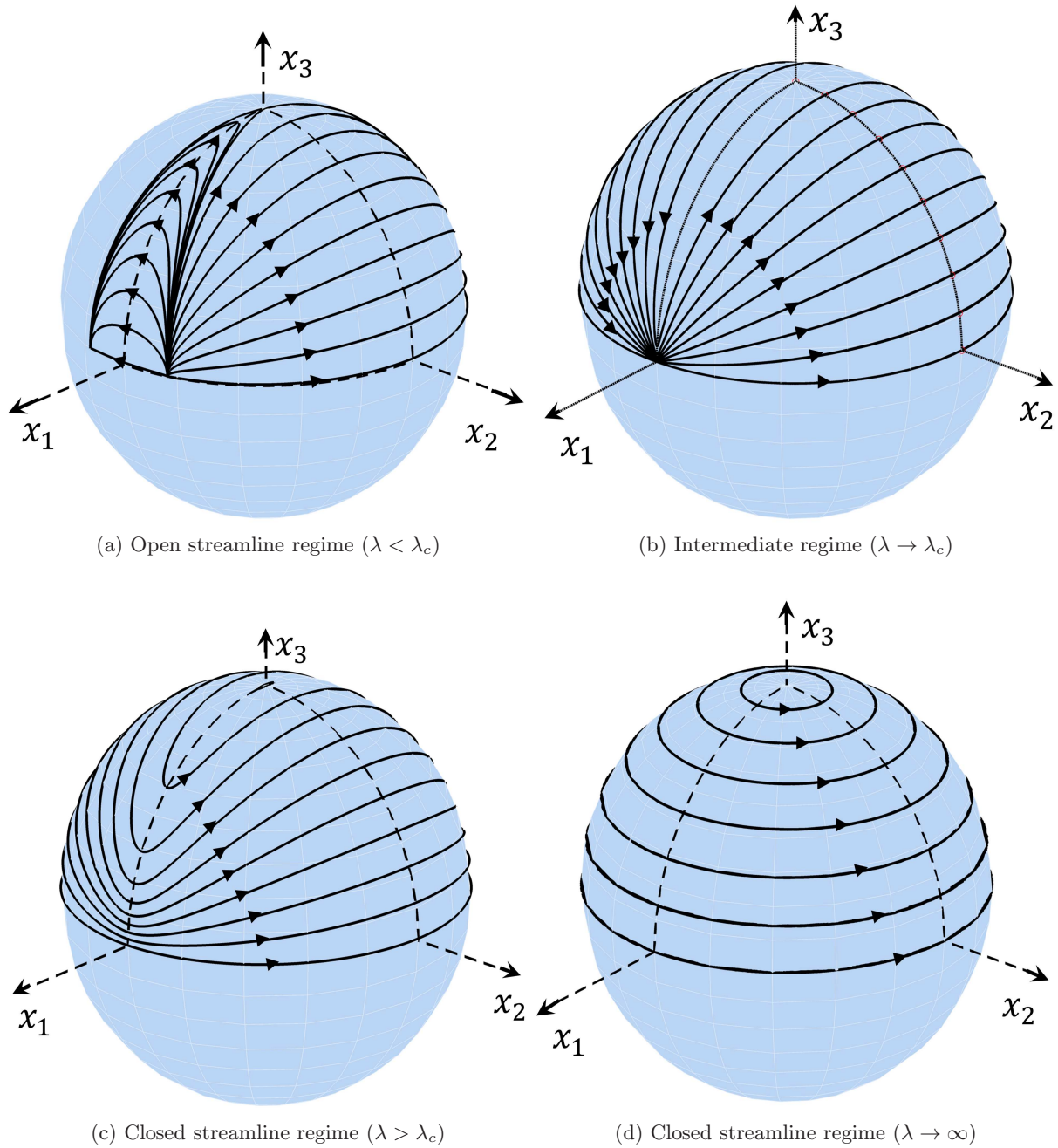


Figure 2.8: The surface streamlines on a drop for distinct cases (a) Open streamline regime ($\lambda < \lambda_c$), (b) Intermediate regime ($\lambda \rightarrow \lambda_c$) (c) Closed streamline regime ($\lambda > \lambda_c$) and (d) Solid particle ($\lambda \rightarrow \infty$)

always have a fore-aft symmetric region of closed streamlines surrounding the particle [Subramanian & Koch \(2006b\)](#). This is similar to the two-dimensional case of a cylinder in a linear flow which also exhibits such a region of closed streamlines ([Robertson & Acrivos \(1970a\)](#)). Addition of inertia in the two-dimensional case however does not lead to any qualitative changes to the flow (although the streamlines lose their fore-aft symmetry) since the centrifugal forces which are present due to small inertia are exactly balanced by pressure forces ([Subramanian & Koch \(2006b\)](#)). However, in the three-dimensional case of a sphere in a linear flow it was shown by ([Subramanian & Koch \(2006a\)](#), [Subramanian & Koch \(2006b\)](#)) that inertia breaks the degenerate region of closed streamlines. In this case, unbalanced centrifugal forces along a streamline lead to the streamlines within the separatrix region no longer being closed.

For the case of drops the effect of inertia is very different based on whether one is in the open streamline or closed streamline regimes. In the open streamline regime ($\lambda < \lambda_c$), the effect of inertia is merely perturbative in nature, except in the vicinity of $\lambda = \lambda_c$. On the hand, in the closed streamline regime ($\lambda > \lambda_c$), inertia fundamentally alters the streamline topology, and just as in the case of a solid particle, leads to a disappearance of the closed streamlines which now become finite- Re spiralling streamlines. From a heat transfer perspective, inertia therefore opens up new channels for convection, and fundamentally alters the nature of the heat transport. We will present a solution to this transport problem in chapter 4.

In the case of a solid sphere the velocity disturbance and hence the centrifugal forces are strongest at the equatorial plane leading to convective channels which carry heat away from the particle. The mass conservation constraint implies that to compensate for this efflux, fluid is drawn in from the polar regions. A distant fluid parcel in effect, moves towards the solid particle at a certain value of the vorticity coordinate (x_3), spirals around the sphere and finally exits via an outgoing channel, closer to the plane of symmetry ([Subramanian & Koch \(2006b\)](#)).

However, for a drop, the spiralling behaviour is more interesting with the presence of two regimes based on the direction of the spiralling. The first is a regime similar to a solid particle where the direction of spiralling is towards the equatorial plane (see Fig. 2.9 and 2.10). The second is a regime where the direction of spiralling reverses close to the equatorial plane. As a result, spiralling trajectories from close to the equatorial plane ($C = \infty$), and those from close to the poles ($C = 0$), converge onto an intermediate location $0 < C < \infty$, from where they spiral away from the drop (see Figs. 2.11 and 2.12). Thus for a drop, a fluid parcel moves near the drop via an incoming channel, spirals towards the intermediate C location and then exits through an outgoing channel. A few representative trajectories for the single wake and bifurcated wake regimes are plotted in Fig. 2.10 , 2.11 and 2.12 . From a heat transfer perspective, the first of these regimes corresponds to the thermal wake being located at the equatorial plane, henceforth called the “single-wake” regime. This is similar to what is seen for a solid particle ([Subramanian & Koch \(2006b\)](#)). The second regime corresponds to the thermal wake being located at an intermediate value of C for each of the symmetric hemispheres of the drop. This regime will be henceforth termed the “bifurcated-wake” regime.

We now present a method to determine the location of the wake based on the averaged drift velocity of the streamlines. The Stokes and $O(Re)$ velocity in terms of the (C, τ) coordinate

system, at the drop surface, are given in what follows:

$$u_C^{(0)}|_{r=1} = 0, \quad (2.60)$$

$$u_\tau^{(0)}|_{r=1} = -\frac{\sqrt{2}C\sqrt{1+(1+2C^2)\gamma^2+(-1+\gamma^2)\cos 2\tau}}{\gamma(1+\lambda)(-2-C^2(1+\gamma^2)+C^2(-1+\gamma^2)\cos 2\tau)} \\ ((-2+(-1+\alpha)\lambda)\cos^2\tau+\gamma^2(-\lambda+\alpha(2+\lambda))\sin^2\tau). \quad (2.61)$$

We note that:

$$\frac{u_\tau^{(0)}}{k}\bigg|_{r=1} = \frac{-2\gamma(1+\alpha)}{(1+\lambda)(\gamma^2-1)} = \frac{d\tau}{ds}, \quad (2.62)$$

which is a constant independent of C and τ . This implies, as mentioned in the previous section that the rate of change of τ along a surface orbit/trajectory is a constant in the (C, τ) coordinate system. The Stokes streamlines ($Re = 0$) are closed orbits each denoted by an orbit constant C for $\lambda > \lambda_c$ (the closed streamline regime). Being closed orbits, the net displacement of a fluid element over a complete orbit is identically zero. However, the addition of a small amount of inertia causes these orbits to become spiralling trajectories that have a net displacement over an orbital period. In the limit of $Re \ll 1$, this drift is small over a given orbit and we can think of the spiralling streamlines as a set of closely spaced Stokes(Jeffery) orbits. Expressing the $O(Re)$ velocity field along the unit vectors of the (C, τ) coordinate system, one obtains:

$$\mathbf{u}^{(1)} = u_C^{(1)}\hat{\mathbf{C}} + u_\tau^{(1)}\hat{\boldsymbol{\tau}}. \quad (2.63)$$

The expression for the $O(Re)$ drift along the C direction is given by:

$$\frac{u_C^{(1)}}{h} = \\ (C(1+C^2(\cos^2\tau+\gamma^2\sin^2\tau))((14C^2(1+\alpha)^2(1032+3718\lambda+2145\lambda^2) \\ (\cos^4\tau-6\gamma^2\cos^2\tau\sin^2\tau+\gamma^4\sin^4\tau)+\frac{1}{5+2\lambda}(\cos^2\tau+\gamma^2\sin^2\tau)(1+C^2(\cos^2\tau+\gamma^2\sin^2\tau)) \\ (-256256(-1+\alpha^2)(1+\lambda)(3+8\lambda+3\lambda^2)(\cos^2\tau-\gamma^2\sin^2\tau))/(\cos^2\tau+\gamma^2\sin^2\tau) \\ + (2(1+\alpha)^2(5+2\lambda)(4(7896+27742\lambda+19305\lambda^2)+3C^2(8120+28314\lambda+20735\lambda^2)\cos^2\tau+3C^2\gamma^2 \\ (8120+28314\lambda+20735\lambda^2)\sin^2\tau))/(1+C^2\cos^2\tau+C^2\gamma^2\sin^2\tau)))/(1+C^2(\cos^2\tau+\gamma^2\sin^2\tau))^2 \\ - (28(1+\alpha)(-1+\gamma^2)\cos\tau\sin\tau(9152(-1+\alpha)(3+11\lambda+11\lambda^2+3\lambda^3)+C^2(-14312-70990\lambda \\ -73073\lambda^2-18018\lambda^3+\alpha(3992+29682\lambda+36751\lambda^2+9438\lambda^3))\cos^2\tau+C^2\gamma^2(-3992-29682\lambda \\ -36751\lambda^2-9438\lambda^3+\alpha(14312+70990\lambda+73073\lambda^2+18018\lambda^3))\sin^2\tau)\sin 2\tau)/((5+2\lambda) \\ (1+C^2\cos^2\tau+C^2\gamma^2\sin^2\tau)^2)))/(576576(1+\lambda)^3(\cos^2\tau+\gamma^2\sin^2\tau)). \quad (2.64)$$

Instead of the detailed inertial drift at every τ , one may also determine the net inertial drift across Jeffery orbits. This implies integrating the $O(Re)$ velocity field with respect to τ , with C

held fixed, which gives us the net inertial drift across the orbit C . This can be written as:

$$\mathbf{u}_{drift}(C) = \int_0^{2\pi} \left(\frac{u_C^{(1)}}{h} \hat{\mathbf{C}} + \frac{u_\tau^{(1)}}{k} \hat{\boldsymbol{\tau}} \right) d\tau. \quad (2.65)$$

Now, the velocity along the τ direction, by definition does not lead to a net displacement across a Jeffery orbit, since it is always tangential to the orbit. Thus the only remaining contribution is from the component $u_C^{(1)}$, which leads to drift across Jeffery orbits in the $\hat{\mathbf{C}}$ direction, whose magnitude is given by:

$$u_{drift}(C) = \int_0^{2\pi} \frac{u_C^{(1)}}{h} d\tau. \quad (2.66)$$

At the location on the drop surface where the fluid elements spiral away from the drop, the above drift goes to zero. Furthermore, this occurs at an intermediate location $0 < C < \infty$, in a certain region in the (α, λ) plane. To determine this region in the (α, λ) plane and to find the neutral curve C^* (the location of the thermal wake from a heat transfer perspective) where the fluid elements spiral away from the drop, we solve the equation $u_{drift}(C) = 0$ using the symbolic computing software MATHEMATICA. We find that the neutral curve(wake) is always at the equatorial plane for $\alpha > \alpha_{bif}$ where $\alpha_{bif} \approx 0.35$. For $\alpha < \alpha_{bif}$, the neutral curve(wake) is at the equatorial plane for $\lambda > \lambda_{bif}$, but for $\lambda < \lambda_{bif}$ lies at an intermediate C orbit. λ_{bif} is found to be given to be the largest positive root of the following polynomial equation in λ :

$$\begin{aligned} & -7274042944 - 10390640512\alpha - 7274042944\alpha^2 + (-12278826336 - 170633994048\alpha \\ & - 12278826336\alpha^2) \lambda + (86362141836 - 746700261976\alpha + 86362141836\alpha^2) \lambda^2 + (363709811676 \\ & - 1527740177528\alpha + 363709811676\alpha^2) \lambda^3 + (588400542515 - 1737399173366\alpha + 588400542515\alpha^2) \\ & \lambda^4 + (488697797302 - 1165205754284\alpha + 488697797302\alpha^2) \lambda^5 + (215692744839 - 455237203278 \\ & \alpha + 215692744839\alpha^2) \lambda^6 + (46799172420 - 93598344840\alpha + 46799172420\alpha^2) \lambda^7 \\ & + (3736032300 - 7472064600\alpha + 3736032300\alpha^2) \lambda^8 = 0 \end{aligned} \quad (2.67)$$

The Jeffery orbit (neutral curve) satisfying $u_{drift}(C) = 0$ and denoted by C^* is plotted in Fig. 2.14. The expression for the same is given in appendix B.

The region in the (α, λ) plane showing this bifurcated wake region is depicted in Fig. 2.13. We now study the location of the neutral curve (wake) as a function of α and λ by plotting the streamlines of the $O(Re)$ velocity field in the exterior of the drop. For a fixed $\alpha < \alpha_{bif}$ as we increase λ from zero, we first cross the open streamline regime, where the effect of inertia is perturbative. At $\lambda = \lambda_c$ the neutral curve is at the poles ($C_{neutral} = 0$) and the spiralling is from the equator to the poles (Fig. 2.11). As we increase λ further the wake location moves towards the equator (Fig. 2.12) so that at $\lambda = \lambda_{bif}$ the wake is at the equator and remains there for all greater values of λ (Fig. 2.10). The dashed curve in Figs. 2.11 and 2.12 show the neutral curve as determined by solving Eq. 2.66, and we see that it is indeed the C orbit where the fluid elements spiral away from the drop. The location of the wake in terms of the C orbit where Eq. 2.66 is satisfied is plotted with respect to the viscosity ratio in Fig. 2.14.

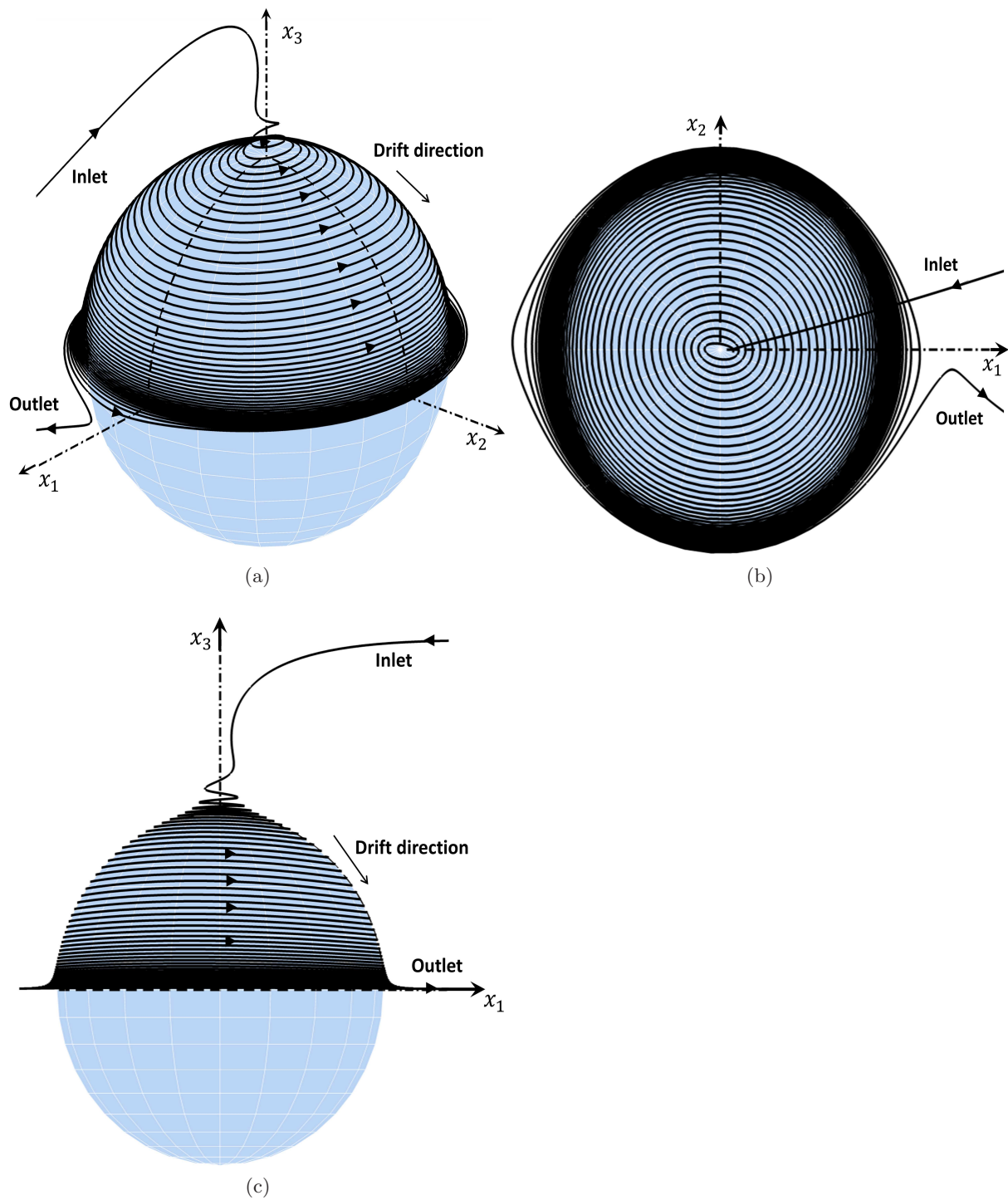


Figure 2.9: Figure showing a spiralling trajectory of a fluid element around a solid particle. Flow parameters: $\alpha = 0.1$, $Re = 0.5$ (a) A 3D view, (b) projection on the flow-gradient plane and (c) projection on the flow-vorticity plane.

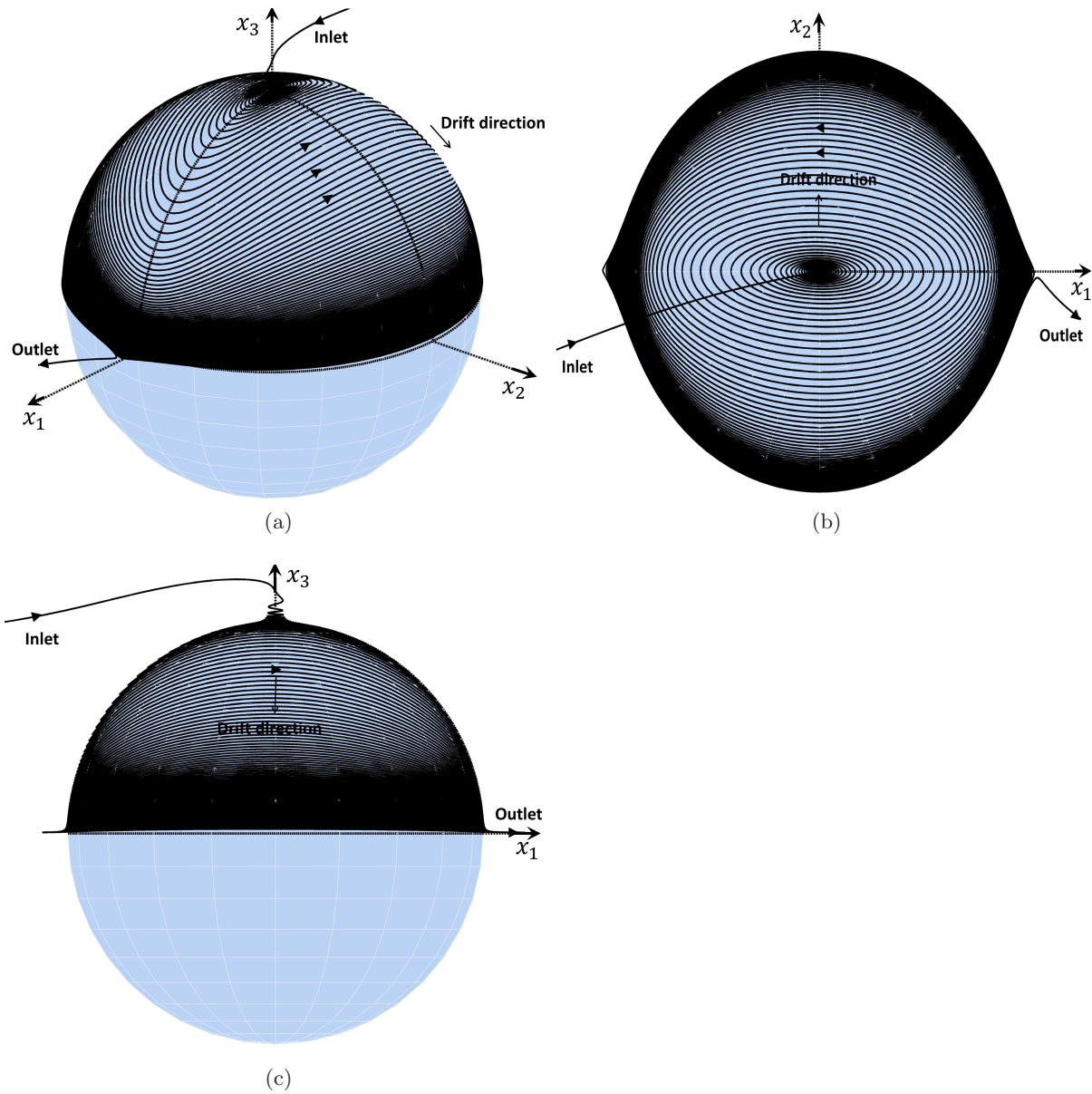


Figure 2.10: Figure showing a spiraling trajectory of a fluid element around a drop in the single wake regime for $\lambda > \lambda_{bif}$. Flow parameters: $\alpha = 0.1$, $\lambda = 0.5$, $\lambda_c = 0.222$, $\lambda_{bif} = 0.3458$, $Re = 0.1$. (a) A 3D view, (b) projection on the flow-gradient plane and (c) projection on the flow-vorticity plane. Note that the neutral curve in this case lies at the equatorial plane.

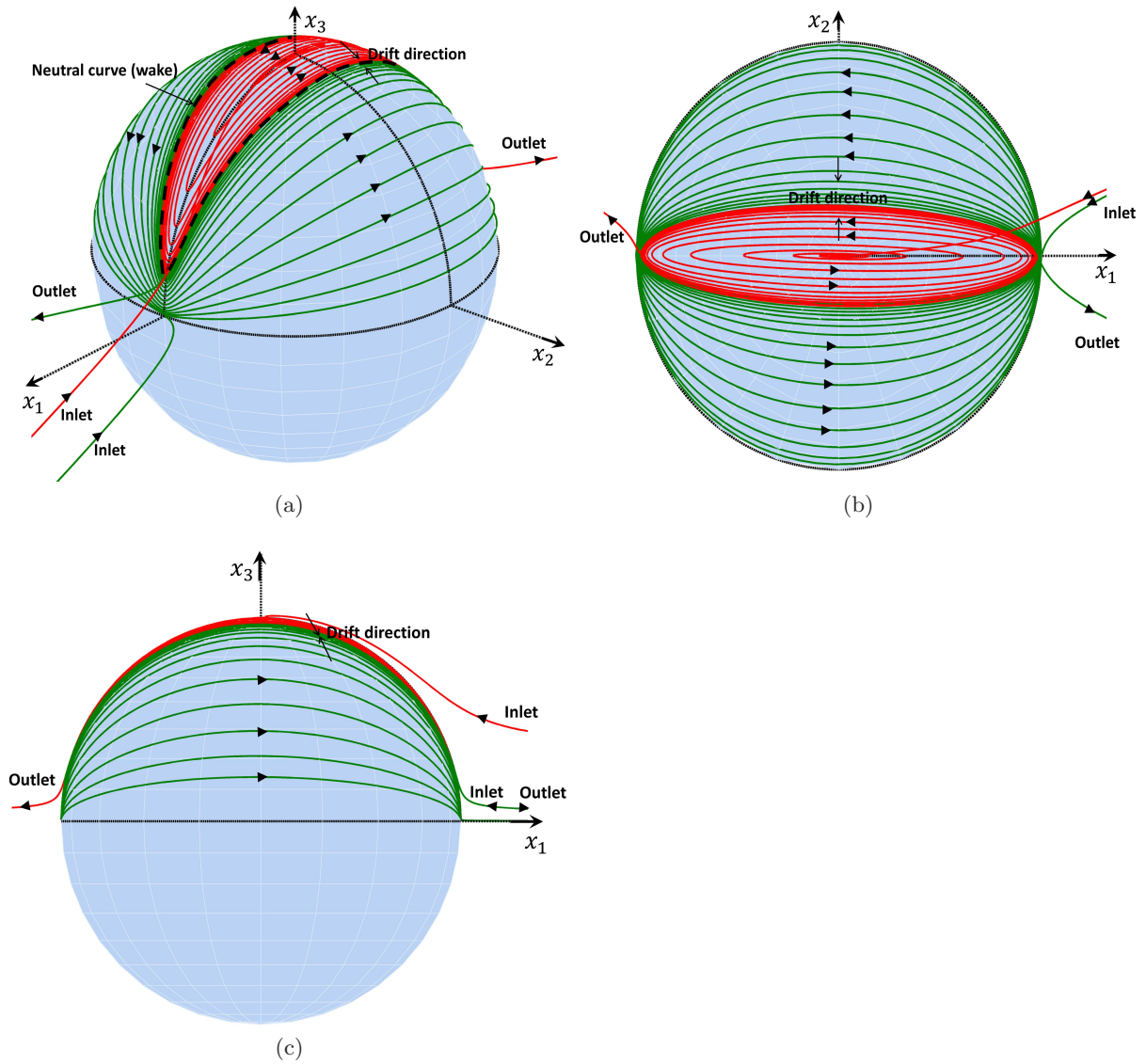


Figure 2.11: Figure showing a spiraling trajectory of a fluid element around a drop in the bifurcated wake regime for a λ value close to λ_c ($\lambda_c < \lambda < \lambda_{bif}$). Flow parameters: $\alpha = 0.1$, $\lambda = 0.23$, $\lambda_c = 0.222$, $\lambda_{bif} = 0.3458$, $Re = 0.1$. (a) A 3D view, (b) projection on the flow-gradient plane and (c) projection on the flow-vorticity plane. The black dashed curve in (a) shows the neutral curve as predicted by Eq. B.1.

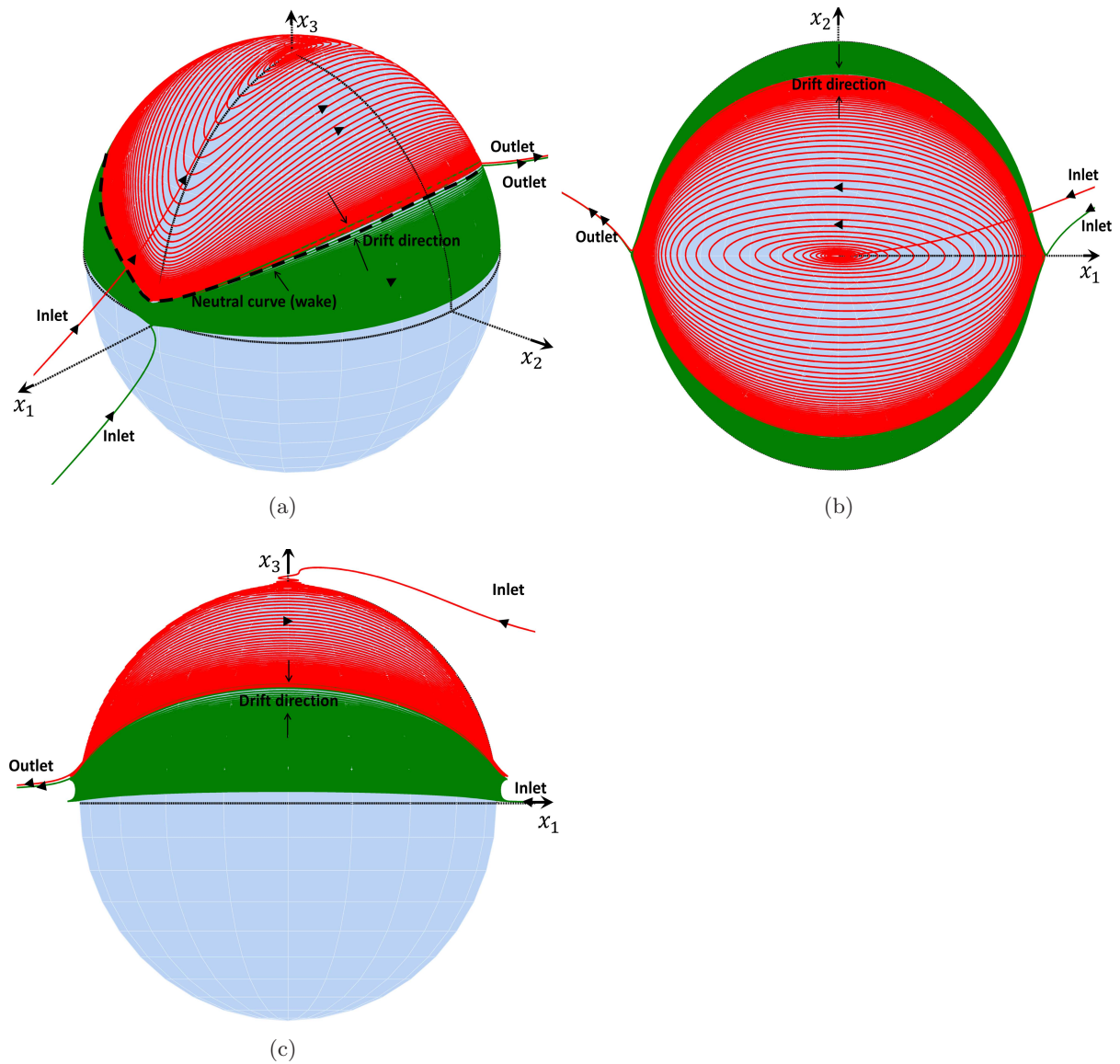


Figure 2.12: Figure showing a spiraling trajectory of a fluid element around a drop in the bifurcated wake regime for a λ value close to λ_{bif} ($\lambda_c < \lambda < \lambda_{bif}$). Flow parameters: $\alpha = 0.1$, $\lambda = 0.34$, $\lambda_c = 0.222$, $\lambda_{bif} = 0.3458$, $Re = 0.1$. (a) A 3D view, (b) projection on the flow-gradient plane and (c) projection the flow-vorticity plane. The black dashed curve in (a) shows the neutral curve as predicted by Eq. B.1. Note how the neutral curve is closer to the equatorial plane compared to Fig. 2.11a.

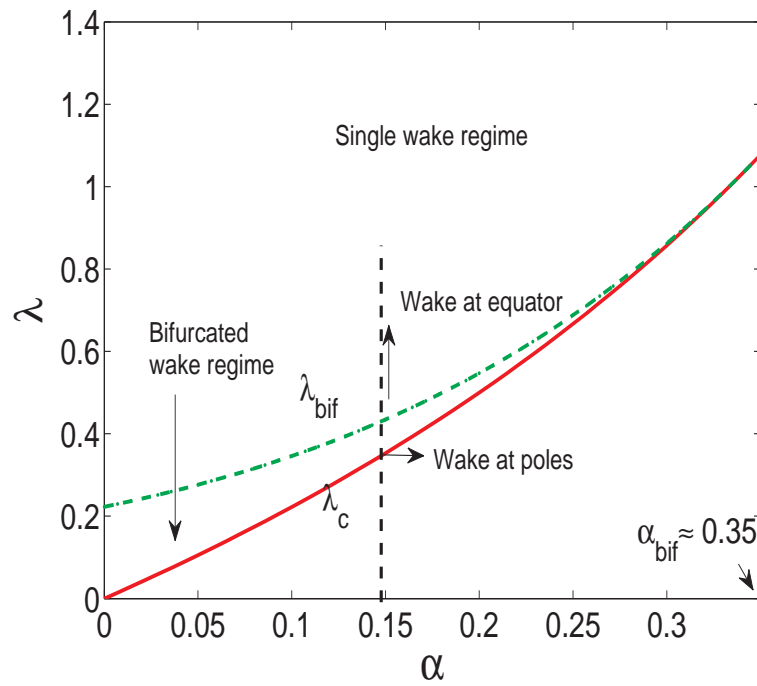


Figure 2.13: Region in (α, λ) space showing the single and bifurcated wake regime along with wake location.

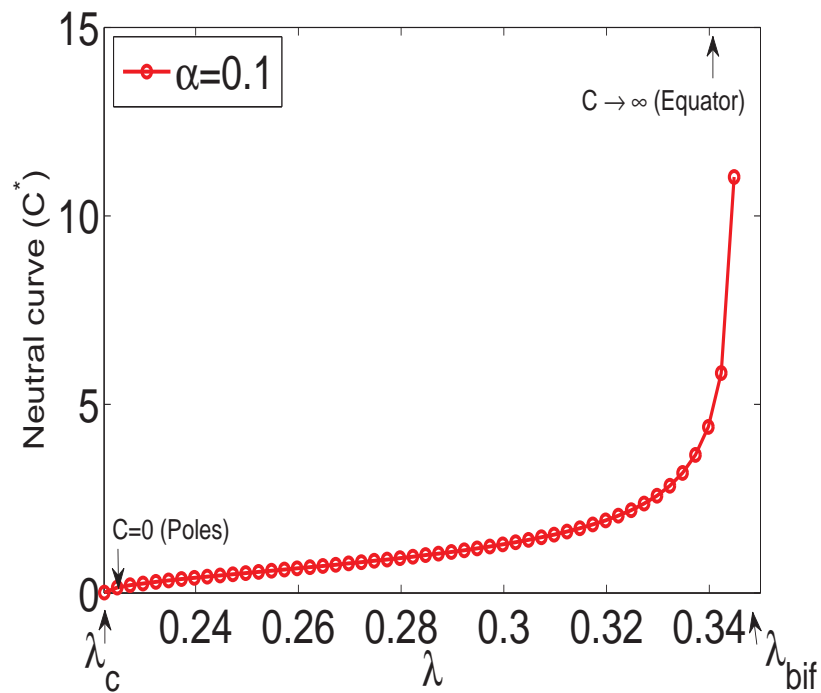


Figure 2.14: The variation of the orbit constant at which the wake occurs with viscosity ratio

Chapter 3

Open Streamline Heat Transfer

3.1 Introduction

In the last chapter we studied in detail the flow topology inside and outside a drop in an ambient planar linear flow. These flows constitute a one-parameter family, where the parameter α denotes the ratio $(E - \Omega)/(E + \Omega)$, where $2E/(E + \Omega)$ and $2\Omega/(E + \Omega)$ denote the dimensionless magnitudes of the rate-of-extension and vorticity, respectively. We saw, based on the parameters in the problem (α, λ) , that there were two topologically distinct regimes with respect to the exterior flow field. We found that for viscosity ratios below a certain critical, α -dependent value ($\lambda_c = 2\alpha/(1 - \alpha)$), the drop was exposed only to open streamlines. In other words, the drop surface is accessed by streamlines which are not confined to a bounded domain and ensure convectively enhanced transport from and to the ambient fluid at large distances from the drop when the Peclet number is sufficiently large. On the other side of the critical viscosity ratio curve, we had a region of closed streamlines surrounding the drop; as a result, transport even at large Peclet numbers, remains diffusion limited.

Before moving on to the heat transfer problem for specific families of linear flows, it is instructive to paint a broader picture of the heat transfer from a drop in a general linear flow in terms of the parametric dependence of the Nusselt number (Nu). An incompressible linear flow is characterized by a traceless velocity gradient tensor, and therefore has *eight* independent pieces of information defining the flow. But, if we factor out the magnitude of the velocity gradient tensor (i.e the shear rate), then we are left with *seven* dimensionless pieces of information. For the special case of irrotational (purely extensional) linear flows, after factoring out the magnitude, and accounting for the zero trace constraint, there are only *four* pieces of information remaining since the relevant rate-of-strain tensor is symmetric. *Three* of these are used in considering a principal-axes-aligned coordinate system. The remaining piece then enters as the parameter which measures departure from axisymmetry in the rate-of-strain tensor. In our analysis this will be the ratio $\epsilon = E_2/E_1$, where E_2 and E_1 are the magnitudes of the rate-of-strain tensor along two of the principal axes. This is the second one-parameter family of flows we consider in this chapter. For a general linear flow, there are *four* pieces of information remaining after we have chosen a principal-axes-aligned coordinate system. One of them would be the ratio E_2/E_1 mentioned above and a second would measure the relative magnitudes of vorticity and extension. The remaining two would help fix the orientation of the vorticity vector relative to any two of the principal axes. In the case of a planar linear flow, which is the first family we consider for the heat transfer analysis, the vorticity vector is constrained to lie along one of the principal axes, along which, additionally, there is no extensional component (so as to impose planarity). Thus *three* pieces of information are specified (two angles to fix the orientation of the vorticity vector and one of the rate-of-strain components). This leaves *one*

piece of information. Thus, a planar linear flow can be reduced to a one-parameter family where the parameter signifies the relative magnitudes of extension and vorticity. This parameter in our analysis is α , which is defined above.

Having gained a broad outlook of the different classes of linear flows, we now move on to our heat transfer analysis. In this chapter we present the solution to the heat transfer problem for a drop in two one-parameter families of linear flows: (1) planar linear flows in the open streamline regime and (2) three-dimensional extensional flows with zero vorticity (which always correspond to open streamlines). We will consider the limit of small Reynolds numbers and large Peclet numbers. The Peclet number quantifies the relative importance of convective to diffusive transport, and in our case is defined as $Pe = \dot{\gamma}a^2/D$, where $\dot{\gamma}$ is the shear rate (a characteristic magnitude of the velocity gradient), a the drop radius and D the diffusivity of heat or mass. The limit of large Pe implies that the transport is dominated by convection and in this convectively dominated regime, for the first family of flows, we determine the Nusselt number, as a function of α and λ ¹. As we have seen before (chapter 2), in the open streamline regime the effects of inertia do not fundamentally alter the streamline topology and therefore are not expected to alter the transport at leading order. Thus for small but finite Re , one only expects a small $O(Re)$ correction to the Nu obtained in the Stokesian regime; this is no longer true in the vicinity of the critical viscosity curve ($\lambda \rightarrow \lambda_c^-$), but this aspect is beyond the scope of this work. Our approach will use the (C, τ) coordinate system as defined in the last chapter (chapter 2) to simplify what is, in essence, a non-trivial heat transfer calculation owing to the absence of axisymmetry. We show that our approach based on this natural albeit non-orthogonal coordinate system has several advantages and offers a simple and elegant method of solution. In particular, a modified C, τ coordinate system may also be used to solve the heat transfer problem for the second family of flows mentioned above, whereby Nu is obtained as a function of ϵ

3.2 Preliminaries

In this section we will set up the heat transfer problem for a drop in a general linear flow in the open streamline regime. We consider a drop whose surface is maintained at a constant temperature T_0 and is suspended in an ambient fluid of temperature T_∞ . The presence of open streamlines near the drop surface implies that in the limit of large Peclet ($Pe \gg 1$), there is formation of a thin thermal boundary layer across which almost the entire temperature drop occurs. We measure the efficiency of the transport using the Nusselt number, which is the dimensionless rate of heat transfer (measured in conduction units), and is defined as the ratio of total heat transfer rate to the transfer rate due to conduction alone (the Nusselt number is defined such that $Nu = 1$ for purely conductive heat transfer):

$$Nu = \frac{Ql}{kA(T_0 - T_\infty)}, \quad (3.1)$$

¹We note here that our analysis is equally applicable for heat or mass transfer, and we henceforth restrict ourselves to the former. The large Pe limit, however, naturally pertains to mass transfer since the Schmidt number ($Sc = \nu/D$) (specially for liquids) is much larger than unity.

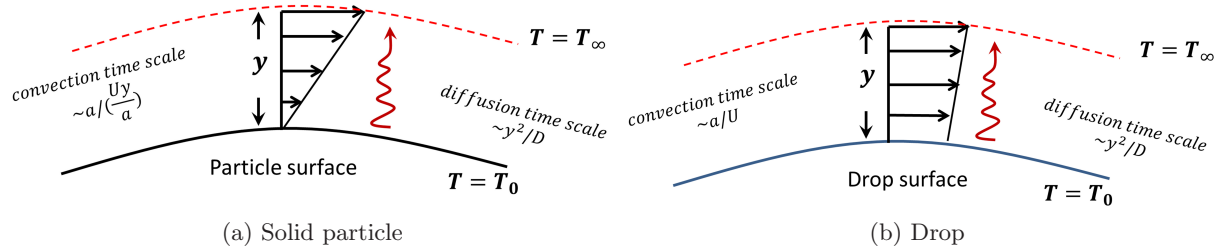


Figure 3.1: Schematic representations of the thermal boundary layer (a) near a solid particle and (b) near a drop or liquid interface. The scalings of the boundary layer thickness and hence the dimensionless heat transfer with Peclet number can be inferred by taking a ratio of the time scales of convection and diffusion

where Q is the total heat transfer rate, k the thermal conductivity of the ambient fluid, l is a relevant length scale and A is a scale for the area across which the heat transfer occurs. In our problem the length scale will be the drop radius and the scale for the area will be the surface area (of $O(a^2)$) of the drop. For a thermal boundary layer near a solid surface, the boundary layer thickness scales as $Pe^{-1/3}$. This can be seen by comparing the time scales of convective transport given by $a^2/(Uy)$ and diffusive transport given by y^2/D as shown in Fig. 3.1a. The convective time scale has this form since the no-slip boundary condition for the velocity at the solid surface makes the flow inside the thermal boundary layer appear locally linear (a simple shear flow). This scaling for the boundary layer thickness leads to the Nusselt number scaling as $Nu \sim Pe^{1/3}$ (Goddard & Acrivos (1966), Acrivos (1971), Acrivos (1980), Batchelor (1979)). For a drop, on the other hand, the thermal boundary layer forms at a fluid-fluid interface. The convective time scale in this case is just a/U , since a no-slip condition is absent. The diffusive time scale for a drop is again given by y^2/D , giving us a boundary layer thickness scaling as $Pe^{-1/2}$, and the Nusselt number scaling as $Nu \sim Pe^{1/2}$ (see Fig. 3.1b)². Schematic representations of the thermal boundary layer for the case of a solid particle and drop along with the related convective and diffusive time scales of the transport are depicted in Fig. 3.1. Clearly, the absence of a no-slip boundary condition implies that the Nu for a drop is asymptotically larger than that for a solid particle at the same (large) Pe .

3.2.1 Governing Equations

The heat transfer problem is governed by the convection-diffusion equation for the energy conservation with the convection being driven by the Stokesian velocity field. For purposes of simplicity and in order to highlight the underlying physics, we assume that the heat transfer is decoupled from the momentum conservation equations and that the changes in temperature do not cause variations in the fluid properties. This is usually a sound assumption when the temperature differences are not large. The convection-diffusion equation can be written in dimensionless

²In the scaling arguments above, the Nusselt number is related to the inverse of the thermal boundary layer thickness, because the dominant heat transfer from the drop occurs across the thin boundary layer. This is no longer true in the vicinity of certain points or singular curves where the boundary layer approximation breaks down, implying the presence of a thermal wake. Unlike the large Re momentum wake, the thermal wake at large Pe occupies a vanishingly small portion of the drop's surface, and therefore, contributes negligibly to the heat/mass transfer.

form as:

$$Pe(\mathbf{u} \cdot \nabla \Theta) = \nabla^2 \Theta, \quad (3.2)$$

where we have used the non-dimensional temperature $\Theta = (T - T_\infty)/(T_0 - T_\infty)$. As mentioned earlier, we will solve these equations in the limit of $Pe \gg 1$. The boundary conditions for the heat transfer are given by:

$$\Theta = 1 \quad \text{at} \quad r = 1 \text{ (Isothermal drop surface with temperature } T_0), \quad (3.3)$$

$$\Theta \rightarrow 0 \quad \text{as} \quad r \rightarrow \infty \quad \text{(Ambient temperature is } T_\infty \text{ at infinity)}. \quad (3.4)$$

Having setup the general open streamline heat transfer problem for a drop, we now present the solutions for two families of linear flows. In section 3.3, we consider the one parameter family of planar linear flows followed by general three-dimensional extensional flows in section 3.4.

3.3 Drop in a Planar Linear Flow: ($\lambda < \lambda_c$)

The flow field for this class of linear flows was derived in chapter 2 and will be used here to solve the heat transfer problem. We begin by setting up the (C, τ) coordinate system for the flow field in the open streamline regime which corresponds to viscosity ratios smaller than λ_c .

3.3.1 (C, τ) Coordinate System

Having described the (C, τ) coordinate system for the closed streamline regime in chapter 2 section 2.4), we now do so for the open streamline regime in which the form of the (C, τ) equations remain the same. The details of the (C, τ) coordinate system are nevertheless reproduced here for convenience. The equations relating the (C, τ) and (θ, ϕ_1) coordinate systems on the drop surface are given by:

$$\tan \theta = C(\cos^2 \tau + \gamma^2 \sin^2 \tau)^{1/2}, \quad (3.5)$$

$$\tan \phi_1 = \gamma \tan \tau. \quad (3.6)$$

We also saw that the metrics and the angle between the contravariant unit vectors for this coordinate system are given by:

$$h = \theta_C, \quad (3.7)$$

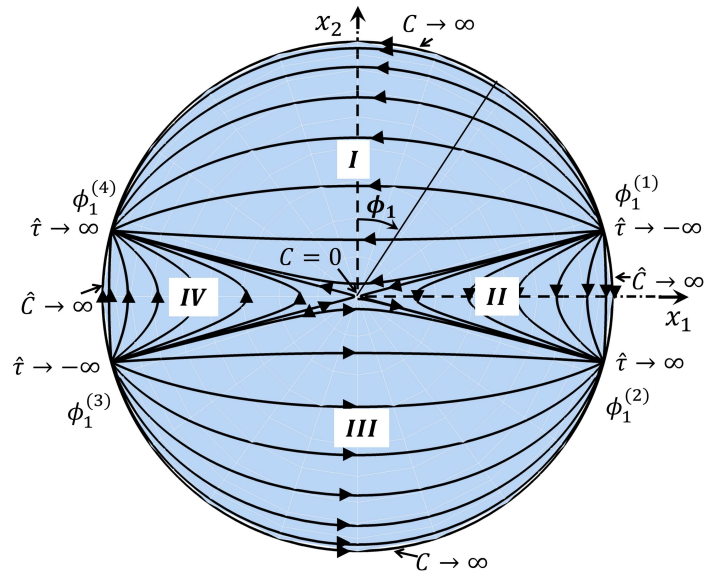
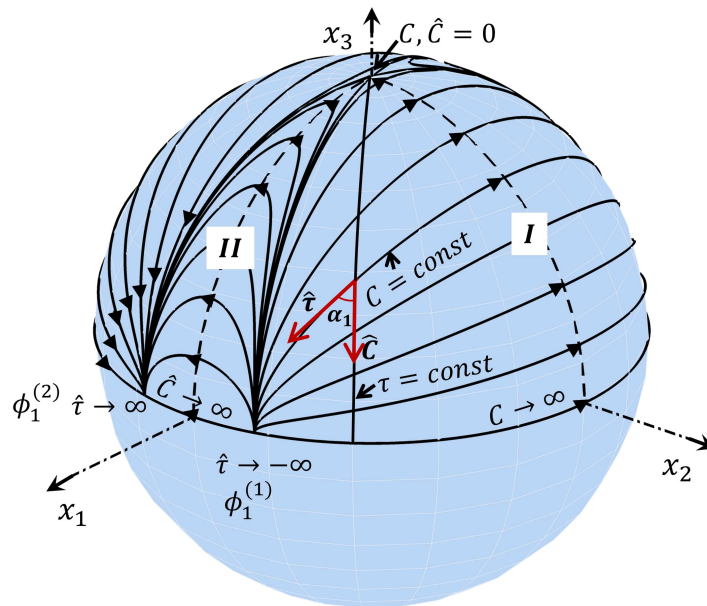
$$k = (\theta_\tau^2 + \sin^2 \theta \phi_{1\tau}^2)^{1/2}, \quad (3.8)$$

$$\sin \alpha_1 = \phi_{1\tau} \sin \theta (\theta_\tau^2 + \sin^2 \theta \phi_{1\tau}^2)^{-1/2}, \quad (3.9)$$

and the unit vectors are given by:

$$\hat{C} = \hat{\theta}, \quad (3.10)$$

$$\hat{\tau} = \cos \alpha_1 \hat{\theta} + \sin \alpha_1 \hat{\phi}_1. \quad (3.11)$$

(a) Projection of trajectories on x_1x_2 plane

(b) Trajectories on the unit sphere

Figure 3.2: Depiction of the (C, τ) coordinate system on the drop surface in the open streamline regime. The four regions are marked I through IV, where regions (I, III) and (II, IV) are equivalent. The streamline trajectories begin and culminate at one of four stagnation points which lie on the equatorial plane. The phase variable for the position along a given trajectory is given by $\hat{\tau}$ and varies from $-\infty$ at the inlet to $+\infty$ at the outlet. The trajectory itself is parametrized by the trajectory constants, C and \hat{C} , in region I and II respectively. These vary from 0 at the poles to ∞ at the equatorial plane

In the open streamline regime, the surface streamlines are not true orbits, hence we interpret the orbit constant C as a trajectory constant instead. For the open streamline case, the effective aspect ratio γ is purely imaginary (recall that γ is purely real for the closed streamline regime) and it is therefore convenient to define:

$$\gamma = i\hat{\gamma}, \quad (3.12)$$

where $\hat{\gamma}$ is purely real and

$$\hat{\gamma}^2 = \frac{1 + \beta(1 + \lambda)}{1 - \beta(1 + \lambda)}, \quad (3.13)$$

where $\beta = (1 - \alpha)/(1 + \alpha)$. Noting that ϕ_1 corresponds to a physical coordinate and is therefore real valued, we have by rearranging Eq. 3.6:

$$\tau = -i \tanh^{-1}(\tan \phi_1 / \hat{\gamma}). \quad (3.14)$$

Using the well known form of the inverse hyperbolic tangent in terms of the logarithm function, one obtains:

$$\tau = \frac{i}{2} \log \left(\frac{\hat{\gamma} - \tan \phi_1}{\hat{\gamma} + \tan \phi_1} \right). \quad (3.15)$$

Similarly, we can rearrange Eq. 3.5 to get:

$$C = \frac{\tan \theta (\hat{\gamma}^2 - \tan^2 \phi_1)^{1/2}}{|\sec \phi_1| \hat{\gamma}}. \quad (3.16)$$

The branch points of the logarithm in Eq. 3.15 are to be found at $\tan \phi_1 = \pm \hat{\gamma}$. For $\phi_1 \in [0, 2\pi]$, this corresponds to four values distinct values of ϕ_1 (see Fig. 3.2a). These values in our coordinate system are given by:

$$\phi_1^{(1)} = \tan^{-1}(\hat{\gamma}), \quad (3.17)$$

$$\phi_1^{(2)} = \tan^{-1}(-\hat{\gamma}), \quad (3.18)$$

$$\phi_1^{(3)} = \pi + \phi_1^{(1)}, \quad (3.19)$$

$$\phi_1^{(4)} = \pi + \phi_1^{(2)} = -\phi_1^{(1)}. \quad (3.20)$$

It is interesting to note that these values of ϕ_1 correspond to the four stagnation points which were seen to exist on the drop surface at the equatorial plane for the open streamline regime (see Section 2.2 of chapter 2). The $\phi_1 = \text{const}$ lines corresponding to these four stagnation points separate the drop surface into four regions I-IV, where the pairs (I,III) and (II, IV) are equivalent, and merely separated by π in the azimuthal coordinate (see Fig. 3.2). This arises due to the underlying symmetry (to a π rotation) of the one-parameter family of linear flows which we are considering. Therefore, it is sufficient to confine our analysis to two of these regions (I and II).

We see that the logarithm in Eq. 3.15 is purely real for $\tan^2 \phi_1 < \hat{\gamma}^2$, which corresponds to $-\phi_1^{(1)} < \phi_1 < \phi_1^{(1)}$ and $\phi_1^{(2)} < \phi_1 < \phi_1^{(3)}$, making τ purely imaginary in these two regions (I and III). Also, from Eq. 3.16 we see that the trajectory constant C is purely real in these regions. The other two regions, II and IV, lie in the range $\phi_1^{(1)} < \phi_1 < \phi_1^{(2)}$ and $\phi_1^{(3)} < \phi_1 < \phi_1^{(4)}$, respectively. In these regions, we see that the combination $(\hat{\gamma} - \tan \phi_1)/(\hat{\gamma} + \tan \phi_1) < 0$, implying

the logarithm is complex valued. In these regions, we rewrite the equation for τ as:

$$\tau = \frac{i}{2} \log \left[\frac{\tan \phi_1 - \hat{\gamma}}{\tan \phi_1 + \hat{\gamma}} \exp(i\pi) \right], \quad (3.21)$$

where $(\tan \phi_1 - \hat{\gamma})/(\tan \phi_1 + \hat{\gamma}) > 0$. Expanding this we have:

$$\tau = \frac{i}{2} \log \left[\frac{\tan \phi_1 - \hat{\gamma}}{\tan \phi_1 + \hat{\gamma}} \right] - \frac{\pi}{2}, \quad (3.22)$$

where $\tau + \pi/2$ is now purely imaginary. This motivates the introduction of a new variable:

$$\tau' = \tau + \frac{\pi}{2}, \quad (3.23)$$

where τ' is purely imaginary. In regions II and IV we see from Eq. 3.16 that the trajectory constant C is purely imaginary.

Thus in both regions we have redefined the τ coordinate such that the phase variable along a trajectory is purely imaginary, and we further define:

$$\tau = i\hat{\tau}, \quad (3.24)$$

$$\tau' = i\hat{\tau}, \quad (3.25)$$

in the regions I and II, respectively, such that $\hat{\tau}$ is real. Since the original 'trajectory' constant C is real in regions I and III, and is purely imaginary in regions II and IV, this motivates us to define

$$C = i\hat{C}, \quad (3.26)$$

where \hat{C} like $\hat{\tau}$, is purely real in all regions concerned. The above relation is valid in regions II and IV. In summary, $(C, \tau) \equiv (C, i\hat{\tau})$ in regions I and III, and $(C, \tau) \equiv (i\hat{C}, i\hat{\tau} - \pi/2)$ in regions II and IV. Fig. 3.2 depicts the (C, τ) coordinate mapping on the drop surface.

From Fig. 3.2 we see that the surface streamlines on the drop surface begin and end at these stagnation points and are therefore entirely confined to one of the four regions. Focussing our attention to region I and II, we see that the stagnation point corresponding to $\phi_1 = \phi_1^{(1)}$ is an inlet since fluid outside the drop moves radially inwards towards the drop (see Fig. 3.2). This inlet location corresponds to $\hat{\tau} = -\infty$ in both regions (regardless of the particular value of C). The $\phi_1 = \phi_1^{(2)}$ and $\phi_1 = \phi_1^{(4)}$ locations are outlets, as can be seen from Fig. 3.2. These outlet points correspond to $\hat{\tau} = \infty$ for both the regions (regardless of the particular value of C). Thus along a surface streamline, as it moves from an inlet to outlet location, the phase variable along the trajectory, $\hat{\tau}$ varies from $-\infty$ to $+\infty$ (for any non-zero value of C).

The trajectory constants C and \hat{C} are mapped as follows: From Eq. 3.16, the $C = 0$ and $\hat{C} = 0$ trajectories in regions I and II respectively correspond to the constant ϕ_1 lines corresponding to the inlet and outlet stagnation points and thus also include the intersection of these lines at $\theta = 0$ (see Fig. 3.2b). Thus the $C = 0$ and $\hat{C} = 0$ trajectories for the open streamline case are fundamentally different from the closed streamline case since they are the intersection of two meridional trajectories corresponding to the inlet and outlet values of ϕ_1 . We recall that in the closed streamline case the $C = 0$ coordinate was just the pair of points

corresponding to the poles of the unit sphere (see Fig. 2.7b in chapter 2). As we increase C or \hat{C} , these trajectories move closer to the equatorial plane such that the $C \rightarrow \infty$ and $\hat{C} \rightarrow \infty$ correspond to trajectories in the plane $\theta = \pi/2$.

3.3.2 Boundary Layer Analysis

We now write down the convection-diffusion equation in the (C, τ) coordinate system which has the form:

$$u_r^{(0)} \frac{\partial \Theta}{\partial r} + \frac{u_C^{(0)}}{h} \frac{\partial \Theta}{\partial C} + \frac{u_\tau^{(0)}}{k} \frac{\partial \Theta}{\partial \tau} = \frac{\nabla^2 \Theta}{Pe}, \quad (3.27)$$

where $u_r^{(0)}$ is the velocity along the radial direction; $u_C^{(0)}$ and $u_\tau^{(0)}$ are the velocities in the C and τ directions respectively and are given by Eqs. 2.56 and 2.57 in chapter 2. In the above equation $u_C^{(0)}$ is identically zero by definition of the coordinate C . Thus the equation simplifies to:

$$u_r^{(0)} \frac{\partial \Theta}{\partial r} + \frac{u_\tau^{(0)}}{k} \frac{\partial \Theta}{\partial \tau} = \frac{1}{Pe} \frac{\partial^2 \Theta}{\partial r^2}, \quad (3.28)$$

where we have assumed the radial derivatives in the diffusion terms to be dominant since, in the limit of large Pe , there is formation of a thin thermal boundary layer next to the drop surface. Since the thickness of this boundary layer is small (scaling as $O(aPe^{-1/2})$ for a drop; see below) compared to the drop radius for large Pe , it is only the velocity field near the drop surface which is relevant in the heat transfer analysis. Defining the boundary layer coordinate, $y = r - 1$ and expanding the velocity field (expressed in the (C, τ) coordinate system) near the drop surface, we get from Eqs. 2.6 and 2.57, respectively, in chapter 2:

$$u_r^{(0)} = \left[-\frac{3C^2(1+\alpha)\gamma \sin 2\tau}{(1+\lambda)(1+C^2(\cos^2 \tau + \gamma^2 \sin^2 \tau))} \right] y + O(y^2), \quad (3.29)$$

$$= h_r(C, \tau, \alpha, \lambda) y + O(y^2), \quad (3.30)$$

$$\frac{u_\tau^{(0)}}{k} = \frac{-2\gamma(1+\alpha)}{(1+\lambda)(\gamma^2 - 1)} + O(y), \quad (3.31)$$

$$= h_\tau(\alpha, \lambda) + O(y). \quad (3.32)$$

We note that the dependence of $h_r(C, \tau; \alpha, \lambda)$ and $h_\tau(\alpha, \lambda)$ on α and λ has a specific form; there is an implicit dependence via the effective aspect ratio γ and an explicit dependence via the factor $(1+\alpha)/(1+\lambda)$. As a result, we will see later that one may include the dependence on $(1+\alpha)/(1+\lambda)$ into the Peclet number so that the residual dependence of the heat transfer is solely a function of the effective aspect ratio γ . Rescaling the boundary layer coordinate as $Y = Pe^m y$, where m is an exponent which gives the boundary layer thickness scale and Y is $O(1)$, we get:

$$h_r(C, \tau, \alpha, \lambda) Y \frac{\partial \Theta}{\partial Y} + h_\tau(\alpha, \lambda) \frac{\partial \Theta}{\partial \tau} = \frac{Pe^{2m}}{Pe} \frac{\partial^2 \Theta}{\partial Y^2}, \quad (3.33)$$

where the leading order balance implies $m = 1/2$ giving the expected the boundary layer thickness scaling as $y \sim Pe^{-1/2} Y$. Note that the use of a non-orthogonal (C, τ) coordinate system has led to a major simplification with the rate of convection in the ‘tangential’ τ direction being independent of both C and τ . We note that the (C, τ) coordinate system has allowed us to

establish parallels between the analysis for a drop and that for a rotating solid particle for which u_ϕ is a constant (Subramanian & Koch (2006b)). Therefore, τ plays the role of ϕ in the solid particle case. From here on the analysis is standard (Leal (2007)). Defining a similarity variable $\eta = Y/g(C, \tau)$, where $g(C, \tau)$ characterizes the dependence of the boundary layer thickness on the position on the drop surface, the non-dimensional temperature is found to satisfy:

$$\frac{d^2\Theta}{d\eta^2} + 2\eta \frac{d\Theta}{d\eta} = 0, \quad (3.34)$$

where

$$h_\tau g \frac{dg}{d\eta} - h_r g^2 = 2. \quad (3.35)$$

The boundary conditions for the non-dimensional temperature are given by:

$$\Theta = 1 \quad @ \quad r = 1, \quad (3.36)$$

$$\Theta \rightarrow 0 \quad \text{as} \quad r \rightarrow \infty. \quad (3.37)$$

Solving Eq. 3.34 and using Eqs. 3.36 and 3.37, we get:

$$\Theta(\eta) = 1 - \frac{2}{\sqrt{\pi}} \int_0^\eta \exp(-t^2) dt. \quad (3.38)$$

Next, we solve the equation for the boundary layer thickness given by Eq. 3.35. Introducing a new variable $f = g^2/2$, we get:

$$h_\tau \frac{df}{d\eta} - 2h_r f = 2 \quad (3.39)$$

Substituting for h_r and h_τ the equation has the form:

$$\frac{df}{d\eta} - \frac{3C^2(\gamma^2 - 1) \sin 2\tau}{[1 + C^2(\cos^2 \tau_1 + \gamma^2 \sin^2 \tau_1)]} f = -\frac{(1 + \lambda)(\gamma^2 - 1)}{(1 + \alpha)\gamma}. \quad (3.40)$$

It is simple to show that the integrating factor is given by $[1 + C^2(\cos^2 \tau + \gamma^2 \sin^2 \tau)]^{-3}$, and upon integrating we get the expression for the boundary layer thickness as:

$$g = \left[-\frac{2(1 + \lambda)(\gamma^2 - 1)[1 + C^2(\cos^2 \tau + \gamma^2 \sin^2 \tau)]^3}{(1 + \alpha)\gamma} \int_{\tau_{inlet}}^\tau [1 + C^2(\cos^2 \tau_1 + \gamma^2 \sin^2 \tau_1)]^{-3} d\tau_1 \right]^{1/2}, \quad (3.41)$$

where the boundary condition on Eq. 3.35 is the constraint that the boundary layer thickness remains finite at the inlet stagnation points located at $\phi_1 = \phi_1^{(1)}$ and $\phi_1 = \phi_1^{(3)}$ on the symmetry plane ($\theta = \pi/2$). It is instructive to note that the boundary layer thickness $g(C, \tau)$ has the form:

$$g(C, \tau) = \left[-\frac{2(1 + \lambda)(\gamma^2 - 1)}{(1 + \alpha)\gamma} Q(C, \tau) \mathcal{I}(C, \tau) \right]^{1/2}, \quad (3.42)$$

$$\mathcal{I}(C, \tau) = \int_{\tau_{inlet}}^\tau Q(C, \tau_1)^{-1} d\tau_1, \quad (3.43)$$

where $Q(C, \tau) = [1 + C^2(\cos^2 \tau + \gamma^2 \sin^2 \tau)]^3$.

We can now proceed to write down the form of the boundary layer thicknesses in the two distinct regions which exist on the drop surface in the open streamline regime (regions (I,III) and (II,IV) in Fig. 3.2). The forms of γ and τ in regions (I,III) are given by Eqs. 3.12 and 3.24, and we further note that C is purely real in this region. The integral appearing in the boundary layer thickness equation now has the form:

$$\mathcal{I}_I(C, \hat{\tau}) = \int_{-\infty}^{\hat{\tau}} Q_I(C, \hat{\tau}_1)^{-1} d\hat{\tau}_1, \quad (3.44)$$

where $Q_I(C, \hat{\tau}) = [1 + C^2(\cosh^2 \hat{\tau} + \hat{\gamma}^2 \sinh^2 \hat{\tau})]^3$. Using this, we get the boundary layer thickness expressions in region I(and III) as:

$$g_I(C, \hat{\tau}) = \left[\frac{2(1 + \lambda)(\hat{\gamma}^2 + 1)}{(1 + \alpha)\hat{\gamma}} Q_I(C, \hat{\tau}) \mathcal{I}_I(C, \hat{\tau}) \right]^{1/2}. \quad (3.45)$$

It is possible to perform the integration involved in Eq. 3.45 analytically, and $\mathcal{I}_I(C, \hat{\tau})$ in regions (I,III) is given by:

$$\begin{aligned} \mathcal{I}_I(C, \hat{\tau}) = & \frac{1}{(C^2\hat{\gamma}^2 - 1)^3 A^5} \left[\frac{3A^4 - 2A^2 + 3}{8} \{ \tan^{-1}(\tanh \hat{\tau}/A) - \tan^{-1}(-1/A) \} \right. \\ & + \frac{A(1 - A^4) \tanh \hat{\tau}}{2(A^2 + \tanh^2 \hat{\tau})} + \frac{A(1 + A^2)^2 (A^2 - \tanh^2 \hat{\tau}) \tanh \hat{\tau}}{8(A^2 + \tanh^2 \hat{\tau})^2} \\ & \left. - \frac{3A(A^2 - 1)}{8} \right], \end{aligned} \quad (3.46)$$

where $A = [(1 + C^2)/(C^2\hat{\gamma}^2 - 1)]^{1/2}$.

We now show that the boundary layer thickness is finite at the inlet stagnation point $\phi^{(1)}$. As mentioned earlier, The inlet stagnation point, expressed in (C, τ) coordinates, is given by $\hat{\tau} \rightarrow -\infty$ and C arbitrary. Applying the inlet condition $\hat{\tau} \rightarrow -\infty$ to Eq. 3.45, and noting that as $\hat{\tau} \rightarrow -\infty$, $Q(C, \hat{\tau}) \sim e^{-6\hat{\tau}}$ and $\mathcal{I}_I(C, \hat{\tau}) \sim e^{6\hat{\tau}}$, we see that the boundary layer thickness is indeed finite at the inlet stagnation point and is given by:

$$g_I(\hat{\tau}_{inlet}) = \left[\frac{(1 + \lambda)(1 + \hat{\gamma}^2)}{3(1 + \alpha)\hat{\gamma}} \right]^{1/2}. \quad (3.47)$$

The outlet of the surface trajectories corresponds to $\hat{\tau} \rightarrow \infty$ and C arbitrary. We note that for $\hat{\tau} \rightarrow \infty$, $Q(C, \hat{\tau}) \sim e^{6\hat{\tau}}$ and from Eq. 3.46 we see that $\mathcal{I}_I(C, \hat{\tau})$ is a function of C only. Thus the boundary layer thickness is divergent in the limit $\hat{\tau} \rightarrow \infty$, indicating the presence of a thermal wake.

Now, in regions (II,IV), we saw that the τ coordinate has the form given by Eq. 3.23 and we can define $\hat{\tau}$ using Eq. 3.25. Further, the C coordinate in this region is purely imaginary and a new variable \hat{C} can be defined using Eq. 3.26. Using these transformations the integral appearing in the boundary layer thickness equation in region II(and IV) has the form:

$$\mathcal{I}_{II}(C, \hat{\tau}) = \int_{-\infty}^{\hat{\tau}} Q_{II}(\hat{C}, \hat{\tau}_1)^{-1} d\hat{\tau}_1, \quad (3.48)$$

where $Q_{II}(\hat{C}, \hat{\tau}) = [1 + \hat{C}^2(\hat{\gamma}^2 \cosh^2 \hat{\tau} + \sinh^2 \hat{\tau})]^3$. Using Eq. 3.48, we get the boundary layer thickness expressions in region II (and IV) as:

$$g_{II}(C, \hat{\tau}) = \left[\frac{2(1 + \lambda)(\hat{\gamma}^2 + 1)}{(1 + \alpha)\hat{\gamma}} Q_{II}(\hat{C}, \hat{\tau}) \mathcal{I}_{II}(C, \hat{\tau}) \right]^{1/2}. \quad (3.49)$$

Again, performing the integration with respect to $\hat{\tau}$ analytically, we see that the integral $\mathcal{I}_{II}(C, \hat{\tau})$ in region II (and IV) takes the form:

$$\begin{aligned} \mathcal{I}_{II}(C, \hat{\tau}) = & \frac{1}{(\hat{C}^2 - 1)^3 \hat{A}^5} \left[\frac{3\hat{A}^4 - 2\hat{A}^2 + 3}{8} \{ \tan^{-1}(1/\hat{A} \tanh \hat{\tau}) - \tan^{-1}(-1/\hat{A}) \} \right. \\ & + \frac{\hat{A}(1 - \hat{A}^4) \tanh \hat{\tau}}{2(\hat{A}^2 \tanh^2 \hat{\tau} + 1)} + \frac{\hat{A}(1 + \hat{A}^2)^2 (\hat{A}^2 \tanh^2 \hat{\tau} - 1) \tanh \hat{\tau}}{8(\hat{A}^2 \tanh^2 \hat{\tau} + 1)^2} \\ & \left. - \frac{3\hat{A}(\hat{A}^2 - 1)}{8} \right], \end{aligned} \quad (3.50)$$

where $\hat{A} = [(1 + \hat{C}^2 \hat{\gamma}^2)/(\hat{C}^2 - 1)]^{1/2}$. We note that, as expected, since regions (I,III) and (II,IV) share a common inlet and outlet (see Fig. 3.2), the boundary layer thickness given by Eq. 3.49 has a finite value given by Eq. 3.47 at the inlet ($\hat{\tau} \rightarrow -\infty$) and is divergent at the outlet, indicating the presence of a thermal wake.

3.3.3 The Nusselt Number

Having calculated the boundary layer thickness as a function of (C, τ) on the drop surface, we can now proceed to calculate the dimensionless rate of heat transfer. The Nusselt number in our case is given by:

$$\begin{aligned} Nu &= -\frac{1}{4\pi} \int_S \left. \frac{\partial \Theta}{\partial y} \right|_{y=0} dS, \\ &= -\frac{Pe^{1/2}}{4\pi} \int_S \left. \frac{\partial \Theta}{\partial Y} \right|_{y=0} dS, \end{aligned} \quad (3.51)$$

where S denotes the surface area of the drop. Rewriting this in terms of the similarity variable η , we get:

$$Nu = -\frac{1}{4\pi} \int_S \left. \frac{1}{g} \frac{d\Theta}{d\eta} \right|_{\eta=0} dS \quad (3.52)$$

$$= \frac{Pe^{1/2}}{2\pi^{3/2}} \int_S \frac{dS}{g(C, \tau)} \quad (3.53)$$

In the (C, τ) coordinate system the differential area element is given by:

$$dS = hk \sin \alpha_1 dC d\tau. \quad (3.54)$$

Since the boundary layer thickness has different forms in regions (I,III) and (II,IV), we write them out separately as:

$$\begin{aligned} Nu &= (4) \frac{Pe^{1/2}}{2\pi^{3/2}} \left[\int_{S_I} \frac{dS_I}{g_I} + \int_{S_{II}} \frac{dS_{II}}{g_{II}} \right], \\ &= Nu_I + Nu_{II}, \end{aligned} \quad (3.55)$$

where the prefactor of *four* is included since, in our analysis, the drop surface is divided into eight regions, four which are equivalent to region I and four to region II (Note that Fig. 3.2a depicts only one hemisphere); the integrals S_I , S_{II} denote integration over regions I and II, respectively. At this point we show that it is always possible to perform the integration with respect to the $\hat{\tau}$ variable analytically. Considering the Nusselt number contribution to regions (I,III), and substituting for the boundary layer thickness from Eq. 3.45, we get:

$$Nu_I = \frac{2Pe^{1/2}}{\pi^{3/2}} \int_{S_I} \left[\frac{(1+\alpha)\hat{\gamma}}{2(1+\lambda)(\hat{\gamma}^2+1)Q_I(C,\hat{\tau})\mathcal{I}_I(C,\hat{\tau})} \right]^{1/2} dS_I, \quad (3.56)$$

$$= \frac{(2(1+\alpha)\hat{\gamma})^{1/2} Pe^{1/2}}{\pi^{3/2}(1+\lambda)^{1/2}(1+\hat{\gamma}^2)^{1/2}} \int_0^\infty \int_{-\infty}^\infty \left[\frac{1}{Q_I(C,\hat{\tau})\mathcal{I}_I(C,\hat{\tau})} \right]^{1/2} hk \sin \alpha_1 dC d\hat{\tau}. \quad (3.57)$$

From Eqs. 3.7, 3.8 and 3.9, we see that combination $hk \sin \alpha_1$ in terms of C and τ is given by

$$\begin{aligned} hk \sin \alpha_1 &= \frac{C\hat{\gamma}}{[1+C^2(\cosh^2 \hat{\tau} + \hat{\gamma}^2 \sinh^2 \hat{\tau})]^{3/2}}, \\ &= \frac{C\hat{\gamma}}{Q_I(C,\hat{\tau})^{1/2}}. \end{aligned} \quad (3.58)$$

Substituting this expression in Eq. 3.57, we get:

$$Nu_I = \frac{[2(1+\alpha)\hat{\gamma}]^{1/2} Pe^{1/2}}{\pi^{3/2}(1+\lambda)^{1/2}(1+\hat{\gamma}^2)^{1/2}} \int_0^\infty \int_{-\infty}^\infty \frac{1}{[\mathcal{I}_I(C,\hat{\tau})]^{1/2} Q_I(C,\hat{\tau})} dC d\hat{\tau}, \quad (3.59)$$

where, upon noting from Eq. 3.44 that $\partial \mathcal{I}_I(C,\hat{\tau})/\partial \hat{\tau} = 1/Q_I(C,\hat{\tau})$, we see that the integral over $\hat{\tau}$ is in the form of an exact differential. Carrying out this integration, we get:

$$Nu_I = \frac{2^{3/2}(1+\alpha)^{1/2}\hat{\gamma}^{3/2} Pe^{1/2}}{\pi^{3/2}(1+\lambda)^{1/2}(1+\hat{\gamma}^2)^{1/2}} \int_0^\infty C [\mathcal{I}_I(C,\infty)^{1/2} - \mathcal{I}_I(C,-\infty)^{1/2}] dC, \quad (3.60)$$

where $\mathcal{I}_I(C,-\infty) = 0$ from Eq. 3.44. This gives the Nusselt number for a drop in an ambient linear flow in terms of a single integral over the C coordinate. Physically, this form for Nu implies that one may first calculate the heat transfer along a given streamline ($\hat{\tau}$ integration) and then calculate the average across streamlines (C integration). Substituting for $\mathcal{I}_I(C,\infty)$ from Eq. 3.46, the final expression for the Nusselt number in region I is given by:

$$Nu_I = \frac{2^{1/2}\hat{\gamma}^{3/2}(1+\alpha)^{1/2}}{\pi^{3/2}(1+\lambda)^{1/2}(1+\hat{\gamma}^2)^{1/2}} F_I(\hat{\gamma}) Pe^{1/2}, \quad (3.61)$$

$$F_I(\hat{\gamma}) = \int_0^\infty C \left[\frac{(3A^4 - 2A^2 + 3) \tan^{-1}(1/A) - 3A(A^2 - 1)}{(C^2\hat{\gamma}^2 - 1)^3 A^5} \right]^{1/2} dC. \quad (3.62)$$

Similarly, we find the Nusselt number for regions equivalent to region II is given by:

$$Nu_{II} = \frac{2^{1/2}\hat{\gamma}^{3/2}(1+\alpha)^{1/2}}{\pi^{3/2}(1+\lambda)^{1/2}(1+\hat{\gamma}^2)^{1/2}} F_{II}(\hat{\gamma}) Pe^{1/2}, \quad (3.63)$$

$$F_{II}(\hat{\gamma}) = \int_0^\infty \hat{C} \left[\frac{(3\hat{A}^4 - 2\hat{A}^2 + 3) \tan^{-1}(1/\hat{A}) - 3\hat{A}(\hat{A}^2 - 1)}{(\hat{C}^2 - 1)^3 \hat{A}^5} \right]^{1/2} d\hat{C}, \quad (3.64)$$

where $A = [(1 + C^2)/(C^2\hat{\gamma}^2 - 1)]^{1/2}$ and $\hat{A} = [(1 + \hat{C}^2\hat{\gamma}^2)/(\hat{C}^2 - 1)]^{1/2}$. Thus, we have the expression for the Nusselt number in terms of a one-dimensional integral which can be carried out numerically. The total Nusselt number is then given by the sum of Nu_I and Nu_{II} :

$$Nu = \frac{2^{1/2}\hat{\gamma}^{3/2}(1+\alpha)^{1/2}}{\pi^{3/2}(1+\lambda)^{1/2}(1+\hat{\gamma}^2)^{1/2}} (F_I(\hat{\gamma}) + F_{II}(\hat{\gamma})) Pe^{1/2}. \quad (3.65)$$

We can absorb the prefactor $[(1 + \alpha)/(1 + \lambda)]^{1/2}$ into the Peclet number so as to define an effective Peclet number \tilde{Pe} given by:

$$\tilde{Pe} = \frac{(1 + \alpha)Pe}{1 + \lambda}. \quad (3.66)$$

The Nusselt number expressed in terms of \tilde{Pe} now has a prefactor which only depends on $\hat{\gamma}$ and is given by:

$$Nu = \frac{2^{1/2}\hat{\gamma}^{3/2}}{\pi^{3/2}(1+\hat{\gamma}^2)^{1/2}} (F_I(\hat{\gamma}) + F_{II}(\hat{\gamma})) \tilde{Pe}^{1/2}. \quad (3.67)$$

Discussion

A surface plot of $Nu/Pe^{1/2}$ in the (α, λ) plane, confined to the open streamline region, is shown in Fig 3.3a. We observe a decreasing trend of the Nu prefactor with the viscosity ratio, with the highest heat transfer rates corresponding to that of a bubble ($\lambda = 0$) in purely extensional flow ($\alpha = 1$).

In Eq. 3.65, we can see that the prefactor appearing in the Nusselt number expressions can be alternatively written in terms of $\hat{\gamma}$. The resulting Nu is given by:

$$Nu = \frac{2^{1/2}\hat{\gamma}^{3/2}(1-\alpha)^{1/2}}{\pi^{3/2}(\hat{\gamma}^2 - 1)^{1/2}} (F_I(\hat{\gamma}) + F_{II}(\hat{\gamma})) Pe^{1/2}. \quad (3.68)$$

We also see from Eq. 3.68 that $Nu/(1-\alpha)^{1/2}$ is purely a function of $\hat{\gamma}$. The variation of Nusselt number with respect to $\hat{\gamma}$ is shown in Fig. 3.3b. We can show from Eq. 3.13 that $\hat{\gamma}$ lies in the interval $[1, \infty]$ for (α, λ) in the open streamline regime. It is clear from Fig. 3.3b that $Nu/(1-\alpha)^{1/2}$ is a rather weak function of $\hat{\gamma}$ for even moderately large values of $\hat{\gamma}$. We can thus conclude that the dependence on $(1-\alpha)^{1/2}$ is sufficient to capture the behaviour of the Nusselt number in the open streamline regime. For purely extensional flows, for which case $\hat{\gamma} = 1$, we write the expression for Nu in the earlier form (Eq. 3.65). In this case, we see that dependence of Nu on the viscosity ratio is captured solely by the $(1 + \lambda)^{-1/2}$ term. We see later in section 3.4 that this scaling of Nu with the viscosity ratio seems to be a general feature of any purely

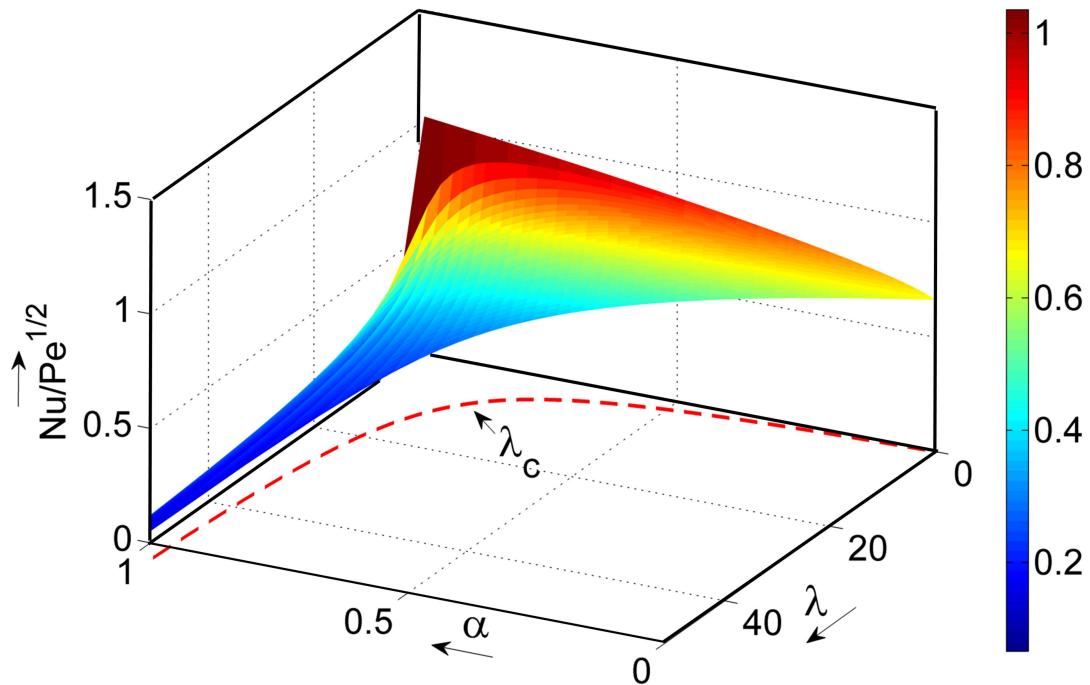
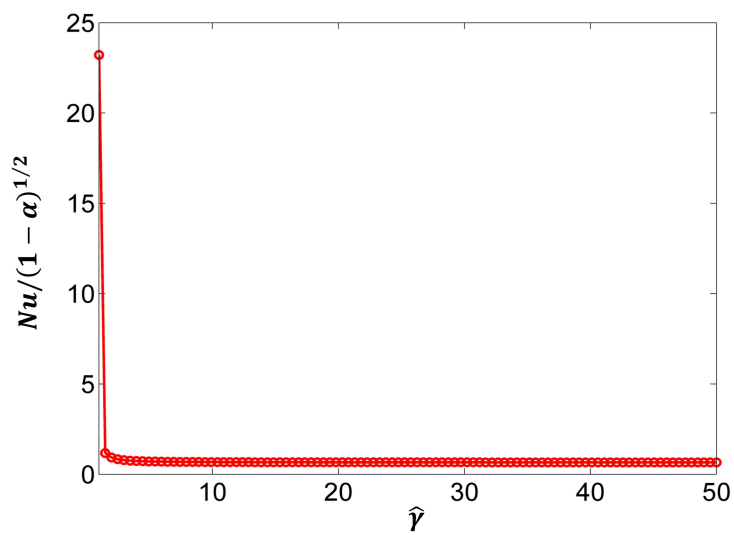
(a) Variation of the prefactor to the Nusselt number with α and λ (b) Variation of Nusselt prefactor with $\hat{\gamma}$

Figure 3.3: Plots of two prefactors to the Nusselt number (a) $Nu/Pe^{1/2}$ as a function of α and λ for $\lambda < \lambda_c$ and (b) $Nu/(1-\alpha)^{1/2}$ as a function of the effective-aspect-ratio $\hat{\gamma}$.

extensional flow. For other values of α we see that the dependence on the viscosity ratio is more complicated since for these cases $\hat{\gamma}$ remains a function of λ .

Special Cases

- $\alpha = 1$: This corresponds to planar extensional flow, and the stagnation points on the drop surface lie at odd multiples of $\pi/4$, since $\hat{\gamma} = 1$. In this case the regions I and II are equivalent with the Nusselt number expressions in the two regions reducing to the same form. The total Nusselt number is now given by eight times the integral over a single region (now an octant):

$$Nu = \frac{2^{3/2}}{\pi^{3/2}(1+\lambda)^{1/2}} F_I(1) Pe^{1/2} \quad (3.69)$$

$$F_I(1) = \int_0^\infty C \left[\frac{(3A^4 - 2A^2 + 3) \tan^{-1}(1/A) - 3A(A^2 - 1)}{(C^2 - 1)^3 A^5} \right]^{1/2} dC \quad (3.70)$$

$$A = \left(\frac{C^2 + 1}{C^2 - 1} \right)^{1/2}. \quad (3.71)$$

Evaluating the definite integral numerically, we find:

$$Nu = \frac{1.0380}{(1+\lambda)^{1/2}} Pe^{1/2}. \quad (3.72)$$

Note that, here, Peclet is defined as $Pe = \dot{\gamma} a^2 / D$. In terms of an effective Peclet number \tilde{Pe} , defined above, the Nusselt number is given by:

$$Nu = 1.0380 \tilde{Pe}^{1/2}. \quad (3.73)$$

Alternatively, if the Peclet number is defined based on the actual component of the velocity gradient tensor (Eq. 2.3 in chapter 2) as $Pe_D = \dot{\gamma}(1+\alpha)a^2/D$, then the Nusselt number for the case of $\alpha = 1$ is given by:

$$Nu_D = \frac{0.734}{(1+\lambda)^{1/2}} Pe_D^{1/2}. \quad (3.74)$$

This agrees well with the prefactor of 0.737 derived by [Polyanin \(1984\)](#) for transport from a drop in a planar extensional flow. We note, however, that their approach used an orthogonal coordinate system and is therefore more involved than the approach presented above (in addition to being less elegant and, more importantly, less general).

- $\hat{\gamma} \rightarrow \infty$: This corresponds to the limit $\lambda \rightarrow \lambda_c^-$. In this case the streamlines on the drop surface have a meridional nature and the region II and IV are vanishingly small. This is because the pairs of stagnation points lying on the drop surface as well as the symmetry plane at $\phi_1^{(1)}$, $\phi_1^{(2)}$ and $\phi_1^{(3)}$, $\phi_1^{(4)}$, are almost coincident, and now lie near the flow axis at $\phi_1 = \pi/2$ and $\phi_1 = -\pi/2$. We now estimate the Nu in this limit, which only has contributions from regions I and III. Taking the limit $\hat{\gamma} \rightarrow \infty$ in Eqs. 3.61 and 3.62, and

noting that $A \sim O(1/\hat{\gamma})$ in this limit, the expression for the Nu simplifies to:

$$Nu_I = \frac{3^{1/2}}{\pi} \left(\frac{1+\alpha}{1+\lambda} \right)^{1/2} Pe^{1/2} \int_0^\infty \frac{C^{1/2} dC}{(1+C^2)^{5/4}}. \quad (3.75)$$

We note that, in the above simplification, we assume that the dominant contribution to the Nu from region I still comes from $O(1)$ values of C (justified posteriori). Evaluating the integral over C numerically, we get:

$$Nu_I = 0.66 \left(\frac{1+\alpha}{1+\lambda} \right)^{1/2} Pe^{1/2}. \quad (3.76)$$

It is straightforward to show that $Nu_{II} \rightarrow 0$ as $\hat{\gamma} \rightarrow \infty$. Thus, the above expression gives the total Nu in this limit. We note that this matches very well with our numerical evaluation of Nu near λ_c using Eq. 3.65. The above analysis has resulted in a finite estimate for Nu even as $\hat{\gamma} \rightarrow \infty$, however, this is expected to change with the inclusion of weak inertia. Inertia is expected to have a singular effect in this limit, and we explore this further in chapter 4.

3.4 Drop in a 3D Extensional Flow

Next we consider the one-parameter family of three-dimensional extensional flows. For these flows the vorticity is identically zero, thus leading to open streamlines in the drop exterior for all values of the viscosity ratio unlike the planar linear flow case. This family of linear flows is characterized by the rate-of-strain tensor (the vorticity tensor being identically zero), which, when expressed in a principal-axis-aligned coordinate system, has the following form:

$$\mathbf{E} = \begin{bmatrix} E_1 & 0 & 0 \\ 0 & E_2 & 0 \\ 0 & 0 & -(E_1 + E_2) \end{bmatrix}, \quad (3.77)$$

where E_1 and E_2 are magnitudes of the rates-of-strain along two of the principal axes. We can factor out a characteristic magnitude of the velocity gradient and express the rate-of-strain tensor in dimensionless form as:

$$\mathbf{E} = \begin{bmatrix} 1 & 0 & 0 \\ 0 & \epsilon & 0 \\ 0 & 0 & -(1 + \epsilon) \end{bmatrix}, \quad (3.78)$$

where $\epsilon = E_2/E_1$ and we have used E_1 as a scale for the rate-of-strain tensor. Thus, the Peclet number for this case is defined as $Pe = E_1 a^2/D$.

3.4.1 (C, τ) Coordinate System

For purposes of our analysis using a (C, τ) coordinate system, in order to have a clear mapping between the (C, τ) coordinates and the (θ, ϕ) coordinates on the unit sphere, we find it simpler to

move to a coordinate system where the surface streamlines begin and end at distinct ϕ locations. This merely involves a rearrangement of the principal axes of the rate-of-strain tensor such that the new rate-of-strain tensor is given by:

$$\mathbf{E} = \begin{bmatrix} -(1 + \epsilon) & 0 & 0 \\ 0 & 1 & 0 \\ 0 & 0 & \epsilon \end{bmatrix}. \quad (3.79)$$

Such a choice of coordinate system is counter-intuitive, and we can see this by considering the simple case of uni-axial extensional flow ($\epsilon = 1$). The usual way of analyzing the heat transfer problem for such an ambient flow would be to use a spherical coordinate system with the polar axis along the axis of symmetry, but in this case the streamlines do not migrate along ϕ , which is necessary for us to use the (C, τ) coordinate system. Our choice of coordinate system for this case does not exploit the axisymmetry of the problem, but this is for the additional benefit that accrues for all non-axisymmetric extensional flows.

Now to simplify our analysis we assume, without loss of generality, that $E_1 \geq E_2$ ($\epsilon \leq 1$) and $E_1, E_2 \geq 0$ ($\epsilon \geq 0$). It is straightforward to see that if one or both of E_1 and E_2 are negative, a rearrangement of the principal axes of the rate-of-strain tensor will ensure the surface streamlines begin and end at distinct ϕ locations, as required. Also, a reversal in the direction of the trajectories between two ϕ locations will be shown to not affect the heat transfer result which is consistent with similar predictions by [Batchelor \(1979\)](#), [Brenner \(1963\)](#) in the context of a solid particle. This result implies that the Nu remains the same despite the temperature field, over the entire drop, being very different for the reversed flow. This is because, in the absence of tangential diffusion, all that matters to the rate of heat transfer is the cumulative distribution of boundary layer thicknesses along a single surface streamline, and this remains unaltered even on flow reversal. The velocity field expressions in the drop exterior, expressed in the spherical coordinate system (with x_3 as the polar axis), are given by:

$$u_r = r(A(r)r^2 + B(r))\left[\epsilon \cos^2 \theta - \frac{1}{2}(\epsilon + (2 + \epsilon) \cos 2\phi) \sin^2 \theta\right], \quad (3.80)$$

$$u_\theta = -\frac{1}{4}B(r)r[3\epsilon + (2 + \epsilon) \cos 2\phi] \sin 2\theta, \quad (3.81)$$

$$u_\phi = B(r)(2 + \epsilon)r \sin \theta \sin \phi \cos \phi, \quad (3.82)$$

where $A(r)$ and $B(r)$ have the same definition as in the planar linear flow case (see [Chapter 2 section 2.1](#)). On the drop surface $u_r = 0$, while u_θ and u_ϕ reduce to:

$$u_\theta|_{surface} = -\frac{1}{4(1 + \lambda)}[3\epsilon + (2 + \epsilon) \cos 2\phi] \sin 2\theta = \frac{d\theta}{ds}, \quad (3.83)$$

$$u_\phi|_{surface} = \frac{1}{(1 + \lambda)}(2 + \epsilon) \sin \theta \sin \phi \cos \phi = \sin \theta \frac{d\phi}{ds}, \quad (3.84)$$

where s is the dimensionless time coordinate (which is measured in units of E_1^{-1}). Proceeding as for the planar linear flow case, we integrate [Eqs. 3.83](#) and [3.84](#) in order to obtain the streamline

equations. From Eq. 3.84 we get:

$$\tan \phi = \exp(\tau), \quad (3.85)$$

$$\tau = \frac{(2 + \epsilon)s}{1 + \lambda}. \quad (3.86)$$

Similarly, integrating Eq. 3.83, we get:

$$\tan \theta = C(1 + \exp 2\tau)^{1/2} \exp -\frac{(1 + 2\epsilon)\tau}{2 + \epsilon}, \quad (3.87)$$

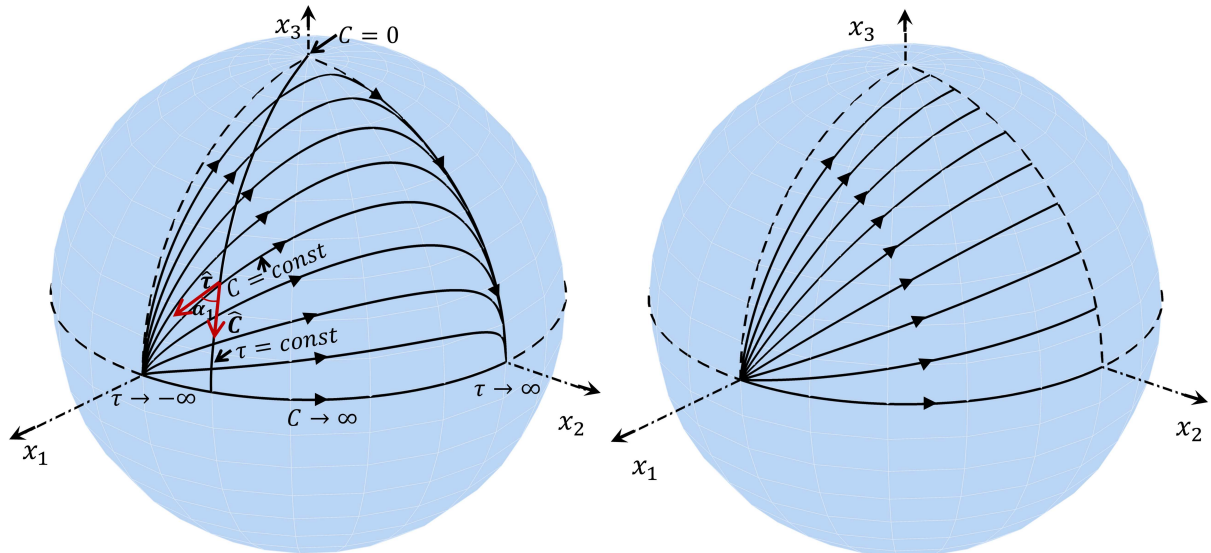
where C is a constant of integration. Eqs. 3.85 and 3.87 constitute the (C, τ) equations for a drop in a general three-dimensional extensional flow.

Defining the metrics of this coordinate system just as we did for the planar linear flow case, we see that they have the same form. Thus the metrics in the C, τ directions and the non-orthogonal angle are still given by Eqs. 3.7, 3.8 and 3.9, respectively, while the unit vectors in the C and τ directions are given by Eqs. 3.10 and 3.11, respectively. We note that \hat{C} still points in the θ since for the new (C, τ) coordinate system ϕ is independent of C .

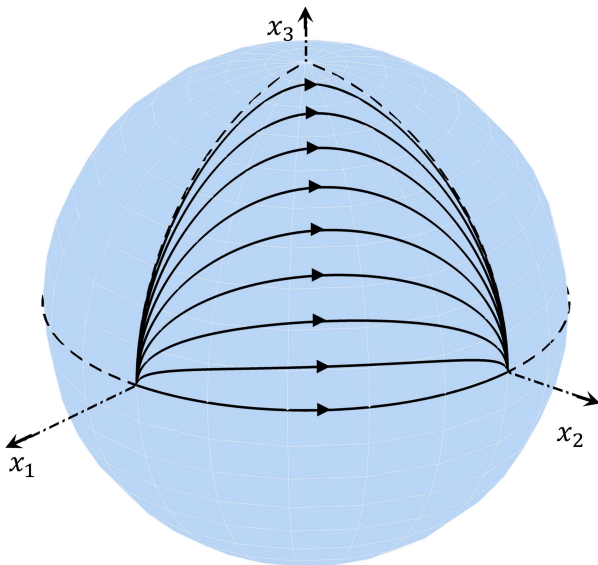
A physical picture of the new (C, τ) coordinate system and its mapping to the spherical coordinate system follows. As we have seen before, the surface streamlines begin and terminate at one of the surface stagnation points. In this case, these stagnation points lie at $\phi = 0, \pi/2, \pi, 3\pi/2$ and $\theta = \pi/2$ as seen from Eqs. 3.83, 3.84 and shown in Fig. 3.4a. The drop surface is thus divided into *eight* equivalent octants and we can therefore confine our attention to one of these octants. We note that this division into eight octants is no longer true for $\epsilon = 1$ ($E_1 = E_2$), for which case the inlet(outlet) for $E_1, E_2 > 0$ ($E_1, E_2 < 0$) is a stagnation ring lying on the x_2x_3 plane (see Fig. 3.4b). Nonetheless, we show later that this flow may be analyzed as a limit of the general case. Another limit we consider is when $\epsilon = 0$ ($E_2 = 0$), which corresponds to a planar extensional flow already analyzed above, and where the plane of the ambient flow is the x_2x_3 plane (see Fig. 3.4c). For the general case, the stagnation points at $\phi = 0, \pi$ act as inlets while those at $\phi = \pi/2, 3\pi/2$ are outlets (see Fig. 3.4a). The mapping of the τ coordinate is thus immediately apparent from Eq. 3.85. At the inlet points $\tau \rightarrow -\infty$ and $\tau \rightarrow \infty$ at the outlet. Similarly, $C = 0$ corresponds to the poles ($\theta = 0$) as well as $\phi = 0, \pi/2$ for arbitrary θ , and $C \rightarrow \infty$ is the equatorial plane ($\theta = \pi/2$). These mappings are depicted in Fig. 3.4a.

3.4.2 Boundary Layer Analysis

The boundary layer analysis for this case closely follows the one presented for the planar linear flows. The convection-diffusion equation expressed in the (C, τ) coordinate system is given by Eq. 3.27, and as before, u_C is identically zero. In the limit of $Pe \gg 1$, it is the velocity field near the drop surface (within the thin thermal boundary layer) which contributes to the leading order heat transfer. Expanding the radial and tangential velocities expressed in (C, τ) coordinates in



(a) Non-axisymmetric extensional flow: $\epsilon = 1/2$ ($E_1 = 2$, $E_2 = 1$) (b) Axisymmetric extensional flow: $\epsilon = 1$ ($E_1 = E_2$)



(c) Planar extensional flow: $\epsilon = 0$ ($E_2 = 0$)

Figure 3.4: Surface streamlines plots for drop in an extensional flow (a) General three-dimensional extensional flow $E_1 \neq E_2$, (b) Axisymmetric (about x_1 axis) extensional flow with $E_1 = E_2$ and (c) Planar extensional flow $E_2 = 0$, $E_1 \neq 0$ (plane of the flow is the x_2x_3 plane).

terms of the boundary layer coordinate $y = r - 1$, we get:

$$u_r = \left\{ \frac{3 \left[C^2 ((\exp(2\tau) - 1) - \epsilon) + \exp \left[\frac{2(1+2\epsilon)\tau}{2+\epsilon} \right] \epsilon \right]}{\left[\exp \left[\frac{2(1+2\epsilon)\tau}{2+\epsilon} \right] + C^2 (1 + \exp(2\tau)) \right] (1 + \lambda)} \right\} y + O(y^2), \quad (3.88)$$

$$= h_r(C, \tau, \epsilon, \lambda) y + O(y^2), \quad (3.89)$$

$$u_\tau/k = \frac{2 + \epsilon}{1 + \lambda} + O(y), \quad (3.90)$$

$$= h_\tau(\epsilon, \lambda). \quad (3.91)$$

We note that, as a consequence of the (C, τ) coordinate system, the convective term in the τ direction is independent of C and τ ; again mimicking the much simpler case of a solid particle in a vortical linear flow wherein the surface velocity is independent of both θ and ϕ . Substituting the above in the convection-diffusion equation and defining a scaled boundary layer coordinate $Y = Pe^m y$, we find, as expected, that $m = 1/2$. Defining a similarity variable $\eta = Y/g(C, \tau)$, where $g(C, \tau)$ denotes the boundary layer thickness, we see that the non-dimensional temperature satisfies Eq. 3.34 and the boundary conditions are given by Eqs. 3.36 and 3.37. The non-dimensional temperature is therefore given by Eq. 3.38. The boundary layer thickness satisfies Eq. 3.35, and proceeding as in the earlier case, we get the final expression for the boundary layer thickness as:

$$g(C, \tau) = \left[\frac{4(1 + \lambda)}{2 + \epsilon} Q(C, \tau) \mathcal{I}(C, \tau) \right]^{1/2} \quad (3.92)$$

where

$$Q(C, \tau) = \exp \left[-\frac{6(1 + \epsilon)\tau}{2 + \epsilon} \right] \left\{ \exp \left[\frac{2(1 + 2\epsilon)\tau}{2 + \epsilon} \right] + (1 + \exp(2\tau)) C^2 \right\}^3, \quad (3.93)$$

and

$$\mathcal{I}(C, \tau) = \int_{-\infty}^{\tau} Q(C, \tau_1)^{-1} d\tau_1. \quad (3.94)$$

It is interesting to note that the boundary layer has the same form as in the planar linear flow case (see Eq. 3.45). Also just as in the previous case, it is straightforward to see that the boundary layer thickness is finite at the inlet $\tau \rightarrow -\infty$. This is because $Q(C, \tau) \sim \exp \left[-\frac{6(1+\epsilon)\tau}{2+\epsilon} \right]$ as $\tau \rightarrow -\infty$ and $\mathcal{I}(C, \tau) \sim \exp \left[\frac{6(1+\epsilon)\tau}{2+\epsilon} \right]$, so that their product is finite.

3.4.3 Nusselt Number Calculation

The dimensionless heat transfer rate is given by:

$$Nu = (8) \frac{Pe^{1/2}}{2\pi^{3/2}} \int_0^\infty \int_{-\infty}^\infty \frac{hk \sin \alpha_1}{g(C, \tau)} dC d\tau, \quad (3.95)$$

where the prefactor of *eight* appears since the total drop surface consists of eight equivalent octants (see Fig. 3.4a which depicts only one octant). The combination $hk \sin \alpha_1$ for this case

is given by:

$$hk \sin \alpha_1 = \frac{C \exp \left[\frac{3(E_1 + E_2)\tau}{2E_1 + E_2} \right]}{\left\{ \exp \left[\frac{2(E_1 + 2E_2)\tau}{2E_1 + E_2} \right] + C^2(1 + \exp(2\tau)) \right\}^{3/2}}, \quad (3.96)$$

$$= CQ(C, \tau)^{-1}. \quad (3.97)$$

Substituting from Eqs. 3.92 and 3.97 in Eq. 3.95, we see that the integration with respect to τ is in the form of an exact differential and can therefore be readily carried out. Since $\mathcal{I}(C, -\infty) = 0$, we get:

$$Nu = Pe^{1/2} \frac{4(2 + \epsilon)^{1/2}}{\pi^{3/2}(1 + \lambda)^{1/2}} \int_0^\infty C[\mathcal{I}(C, \infty)]^{1/2} dC, \quad (3.98)$$

where $\mathcal{I}(C, \tau)$ is given by Eq. 3.94. Thus, we have the expression for the Nusselt number in terms of a one-dimensional integral which can be carried out numerically. The above expression can be rewritten by defining an effective Peclet number:

$$\tilde{Pe} = \frac{(2 + \epsilon)Pe}{(1 + \lambda)}, \quad (3.99)$$

using which the expression for the Nusselt number becomes:

$$Nu = \tilde{Pe}^{1/2} \frac{4}{\pi^{3/2}} \int_0^\infty C[\mathcal{I}(C, \infty)]^{1/2} dC, \quad (3.100)$$

Thus making the prefactor to the Nusselt number purely a function of ϵ . This prefactor is plotted in Fig. 3.5 as a function ϵ , for ϵ varying between 0 and 1, where the end points correspond to planar extensional flow and axisymmetric extensional flow (about x_1 axis).

Special Cases

- $\epsilon = 1$ ($E_1 = E_2$): This corresponds to the axisymmetric extensional flow (with respect to x_1 axis), and $\mathcal{I}(C, \tau)$ reduces to:

$$\mathcal{I}(C, \tau) = \int_{-\infty}^\tau \frac{\exp(4\tau_1) d\tau_1}{[\exp(2\tau_1) + (1 + \exp(2\tau_1))C^2]^3}, \quad (3.101)$$

which can be integrated to yield:

$$\mathcal{I}(C, \tau) = \frac{\exp(4\tau)}{4C^2[C^2 + (1 + C^2)\exp(2\tau)]^2}, \quad (3.102)$$

and

$$\mathcal{I}(C, \infty) = \frac{1}{4C^2(1 + C^2)^2}. \quad (3.103)$$

The rather simple expression for $\mathcal{I}(C, \tau)$ allows an entirely analytical estimate of the Nusselt number. Substituting this in Eq. 3.98, we can evaluate the resulting integral with

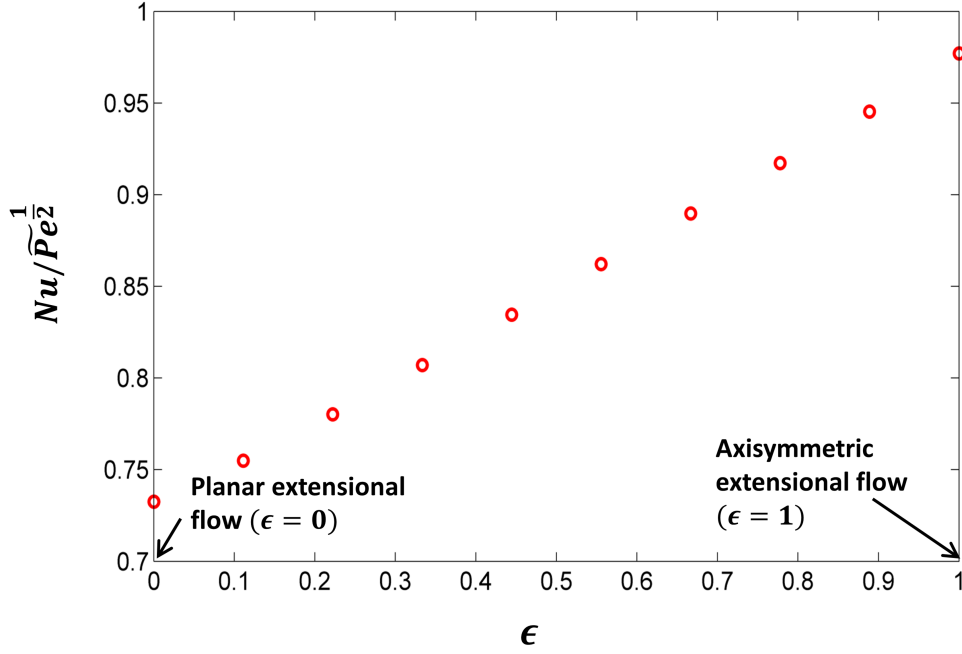


Figure 3.5: Plot of the prefactor to the Nusselt number given in Eq. 3.100 as a function of ϵ for $0 \leq \epsilon \leq 1$. The end points correspond to planar extensional flow and axisymmetric extensional flow (about x_1 axis).

respect to C to give:

$$Nu = \left[\frac{3}{\pi(1+\lambda)} \right]^{1/2} Pe^{1/2}, \quad (3.104)$$

where the Peclet number is defined as $Pe = E_1 a^2/D$. We remark that this agrees exactly with the expression derived by Gupalo & Riazantsev (1972) for the case of a drop in an axisymmetric extensional flow, thus serving as a validation for our approach. In terms of the effective Peclet number this becomes:

$$Nu = \left(\frac{3}{\pi} \right)^{1/2} \tilde{Pe}^{1/2}. \quad (3.105)$$

- $\epsilon = 0 (E_2 = 0)$: This gives us back the planar extensional flow ($\alpha = 1$) for which we derived the Nusselt number in section 3.3, only here, the plane of the ambient flow is the x_2x_3 plane. Evaluating the definite integral in Eq. 3.98 for this case, we find:

$$Nu = \frac{0.734}{(1+\lambda)^{1/2}} Pe^{1/2} \quad (3.106)$$

where the Peclet number is defined as $Pe = E_1 a^2/D$. The equivalence with the earlier analysis can be seen by noting that $E_1 = \dot{\gamma}(1+\alpha)$. As expected, this is the same result we reported previously, though here we have used a different version of the (C, τ) coordinate system. This internal consistency provides a valuable validation of our (C, τ) coordinate system approach.

Although not shown here, the (C, τ) method used here may be used to analyze non-axisymmetric heat transfer problems involving a solid particle, for instance, those analyzed by [Batchelor \(1979\)](#). For the three-dimensional extensional flows considered here, where the particle is stationary, the $\hat{\boldsymbol{\tau}}$ vector would be along the surface tangential stress vector (referred to by Batchelor as ‘surface streamlines’).

Chapter 4

Closed Streamline Heat Transfer: Inertial Effects

4.1 Introduction

In the previous chapter, we explored the heat transfer from a neutrally buoyant drop immersed, in certain classes of ambient linear flows driven by open streamlines in the Stokes limit. In this chapter, we move to a fundamentally distinct regime where the drop is completely surrounded by a region of closed streamlines in the limit of zero Reynolds number. In the case of a drop in a planar linear flow, we saw that this regime exists for viscosity ratios greater than a critical value which depends on the flow parameter α . We now focus on this “closed streamline” regime and the associated heat transfer problem for drops.

The presence of closed streamlines surrounding a body suspended in a fluid has important consequences for heat transport. Since the streamlines are closed and confined to a bounded region next to the body, they cannot transport heat away from the drop by convection (Yu-Fang & Acrivos (1968), Poe & Acrivos (1975), Poe & Acrivos (1976), Subramanian & Koch (2006b)). As a result, transport in a flow field with closed streamlines remains limited by the rate of diffusion across isothermal closed streamlines (see Fig. 4.1).

The above statement that the closed streamlines, at steady state, are isotherms is a non-trivial result worthy of some attention (see Rhines & Young (1983)). Consider an initially stationary sphere in a quiescent ambient fluid with an arbitrary temperature field. Once the sphere begins to rotate there is a region of closed streamlines formed as a consequence of the no-slip boundary condition at the sphere surface. However, there exist temperature differences along these closed streamlines arising from the initial temperature field which cannot be wiped out due to convection alone. Therefore, a naive explanation of the isothermal nature of these streamlines based $\mathbf{u} \cdot \nabla T = 0$ is misleading at best. To understand the mechanism, let us consider two closed streamlines separated by a small distance Δy , which have a relative velocity of $O(\dot{\gamma}\Delta y)$. Portions of these streamlines with different temperatures will be brought next to each other in a time $O(a/(\dot{\gamma}\Delta y))$. Diffusion then wipes out the temperature differences in a time scale of $O(\Delta y^2/D)$. Equating the above two time scales, one obtains $\Delta y/a \sim O(Pe^{-1/3})$. Using this, we can estimate the time scale for the temperature differences to be wiped out as $t_a \sim O(\Delta y^2/D) \sim O(Pe^{-2/3}a^2/D)$. Thus shear-enhanced diffusion is crucially important for removing the temperature differentials along a closed streamline leading to isothermal closed streamlines at steady state. The heat transfer analysis in this chapter involves inertial transport on time scales which is $O([(PeRe)^{-1/2}]^2)a^2/D$ for a drop and $O([(PeRe)^{-1/3}]^2)a^2/D$ for a solid particle (this is the time scale for diffusion of heat across the thermal boundary layer). In both cases, the time scales are much larger than the time scale for the closed streamlines to

become isotherms, since $Pe^{-2/3} \ll (RePe)^{-1}$ and $Pe^{-2/3} \ll (RePe)^{-2/3}$ when $Re \ll 1$. Thus, our assumption that the closed streamlines are isotherms at the time scale of our heat transfer analysis is consistent.

The transport at zero Reynolds, for times much longer than the time taken for the closed streamlines to become isothermal, is therefore due to diffusion across these isotherms. This is manifested in the Nusselt number, in the limit of large Pe , plateauing out to an $O(1)$ value. While this is the scenario in the Stokes limit ($Re = 0$), things are vastly different with the addition of a small but finite amount of inertia. Even weak inertia leads to a breakdown of the degenerate region of closed streamlines, transforming them into tightly spiralling ones at small Re . Physically, this is because fluid elements moving around the drop now experience an additional centrifugal force which leads to a net displacement during a complete orbit, and every fluid element now comes from and goes to infinity. Since the inertial streamlines are no longer limited to a finite region next to the immersed body, heat can be transported effectively. These newly formed ‘convective channels’ due to inertia, lead to the Nusselt number increasing with Pe at large Pe ; for any Re , however small, the Nu far exceeds the geometrical limit (diffusion limited regime) attained in the limit $Re = 0$, $Pe \rightarrow \infty$. Therefore, unlike the open streamline regime, where the effects of inertia were perturbative in nature, in the closed streamline regime, inertia has a dramatic effect and modifies the heat transport at leading order. This provides general motivation for the study of heat transfer from suspended bodies at small but finite inertia.

The inertial heat transfer calculation for solid particles immersed in a planar linear flow was carried out by [Subramanian & Koch \(2006a\)](#), [Subramanian & Koch \(2006b\)](#), who found that the Nusselt number scales as $Nu \sim Re^{1/3} Pe^{1/3}$, in the limit of $Re \ll 1$, $Pe \gg 1$, $RePe \gg 1$. We note that for the solid particle case, there is always an annular region of closed streamlines present for any non-zero vorticity in the ambient linear flow. In this chapter, we carry out the heat transfer analysis for drops, which pose several novel and interesting features when compared to solid particles. For instance, as discussed in chapter 2, drops in a planar linear flow are surrounded by closed streamlines only when $\lambda > \lambda_c = 2\alpha/(1 - \alpha)$. Further, we have shown that, unlike a solid particle, the near-field and surface streamlines for a drop are not circles, but are Jeffery orbits (see chapter 2). Therefore, the streamline geometry is inherently non-axisymmetric and requires use of the (C, τ) coordinate system developed earlier for the closed streamline regime (section 2.4 in chapter 2). We show that the simplifications resulting from the use of this coordinate system are crucial in solving this non-axisymmetric heat transfer problem. After writing down the governing equations in section 4.2, we revisit, in section 4.3, the streamline topology in the closed streamline region, first at $Re = 0$ and then at finite Re , to get a sense of the spatial organization of the streamlines near the drop surface. This understanding will help us set up the relevant equations and boundary conditions for the heat transfer problem using the (C, τ) coordinate system in section 4.4. Our final result, just as in the open streamline case, is an expression for the Nusselt number as a function of the flow parameters for the region $\lambda > \lambda_c$ in the (α, λ) space which we give in section 4.5. We conclude this chapter with a brief discussion of the so-called “intermediate regime” in section 4.6, which corresponds to λ close to λ_c , where we show that both the inertial and Stokes velocities become comparable (as far as their contribution to convection is concerned) over certain regions on the drop surface.

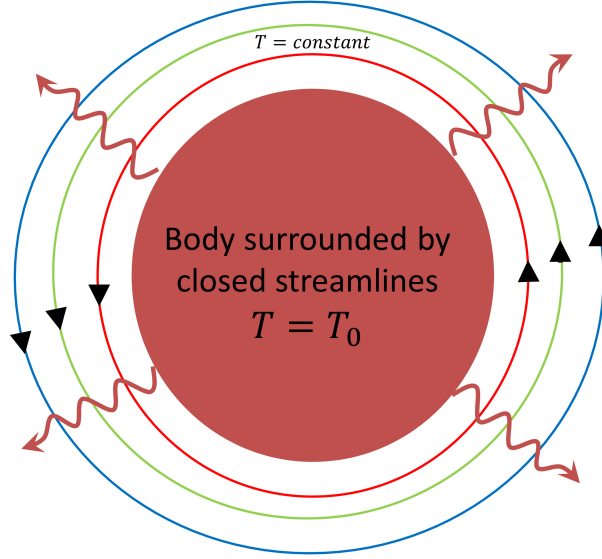


Figure 4.1: Depiction of a body at temperature T_0 in an ambient fluid of temperature T_∞ . The body is completely surrounded by a region of closed streamlines, which at steady state are isotherms. Convection is rendered ineffective in transporting heat, which is transported only through diffusion across these isotherms.

4.2 Governing Equations

The governing equations in dimensionless form for the fluid motion outside the drop, in the presence of inertia, are given by:

$$Re \mathbf{u} \cdot \nabla \mathbf{u} = -\nabla p + \nabla^2 \mathbf{u}, \quad (4.1)$$

$$\nabla \cdot \mathbf{u} = 0. \quad (4.2)$$

The velocity field in the drop exterior, which we will utilize in our heat transfer analysis, was derived by [Raja *et al.* \(2010\)](#) using a regular perturbation procedure. To $O(Re)$, the exterior velocity field around the spherical drop may be written as:

$$\mathbf{u} = \mathbf{u}^{(0)}(\mathbf{r}; \alpha, \lambda) + Re \mathbf{u}^{(1)}(\mathbf{r}; \alpha, \lambda) + O(Re^{3/2}), \quad (4.3)$$

where, for a planar linear flow $\mathbf{u}^{(0)}$ is given in Eqs. 2.6 to 2.8 in chapter 2. The expressions for the $O(Re)$ velocity field are given in $\mathbf{u}^{(1)}$ is given in [Raja *et al.* \(2010\)](#) and reproduced in appendix A. ¹

We will consider the limit of small but finite Re , since we are interested in studying the leading order effect of inertia on the heat transfer. Further, we will consider the large convection limit ($Pe \gg 1$ and $RePe \gg 1$), such that convection due to the finite Re spiralling flow dominates diffusion everywhere except in a thin thermal boundary layer near the drop surface and in a wake, which however does not contribute to the leading order heat transfer. Using our analysis,

¹Note that $\mathbf{u}^{(1)}$ arises from inertial forces acting in a region around the drop of the order of its own size. The next correction, at $O(Re^{3/2})$, arises from distances of $O(Re^{-1/2})$ (and thus, has a singular origin), and was considered by [Subramanian *et al.* \(2011b\)](#) in the context of the exterior streamline topology (especially at large distances). It is not considered here, since it would only lead to an $O(Re^{1/2})$ correction to the leading order $O(RePe)^{1/2}$ estimate for the Nusselt number.

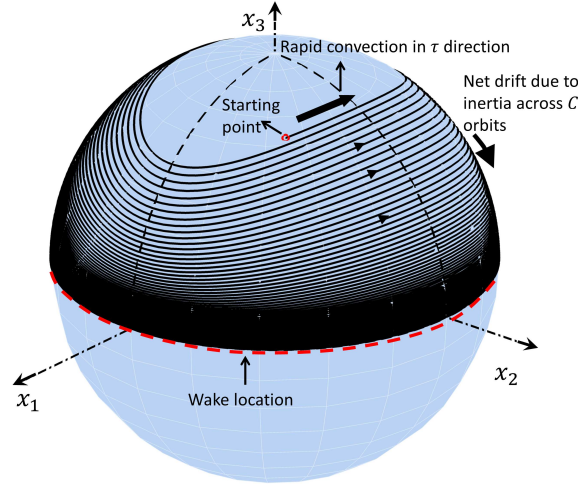


Figure 4.2: Figure showing the inertial surface streamlines for a drop in the single wake regime, $\alpha = 0.2$, $\lambda = 2$ ($\lambda_{bif} = 0.547$)

we obtain an asymptotic solution for the temperature field which is valid when $PeRe \gg 1$, and arises from a balance of the convective and diffusive terms in the thermal boundary layer mentioned above.

The heat transfer is governed by the convection-diffusion equation, written here in non-dimensional form:

$$Pe(\mathbf{u} \cdot \nabla \Theta) = \nabla^2 \Theta, \quad (4.4)$$

where $\Theta = (T - T_\infty)/(T_0 - T_\infty)$ and $Pe = \dot{\gamma}a^2/D$. This is subject to the boundary conditions:

$$\Theta = 1 \quad \text{at} \quad r = 1 \quad (\text{Isothermal drop surface with temperature } T_0), \quad (4.5)$$

$$\Theta \rightarrow 0 \quad \text{as} \quad r \rightarrow \infty \quad (\text{Ambient temperature is } T_\infty \text{ at infinity}). \quad (4.6)$$

Having set up the governing equations, we now proceed to describe the coordinate system which will be used in the analysis. Beginning with the tangential coordinates (C, τ) on the drop surface, described in chapter 2, we show the need for a modified radial coordinate only for the case of drops (for solid particles, as shown by Subramanian & Koch (2006b), the usual radial coordinate suffices for the large Pe boundary layer analysis).

4.3 Solution Approach and Coordinate System

We begin by writing down the convection-diffusion equation expressed in the (r, C, τ) coordinate system:

$$(u_r^{(0)} + Reu_r^{(1)}) \frac{\partial \Theta}{\partial r} + \frac{(u_C^{(0)} + Reu_C^{(1)})}{h} \frac{\partial \Theta}{\partial C} + \frac{(u_\tau^{(0)} + Reu_\tau^{(1)})}{k} \frac{\partial \Theta}{\partial \tau} = \frac{\nabla^2 \Theta}{Pe}, \quad (4.7)$$

where the (C, τ) components of the velocity field, in terms of the (θ, ϕ) components, are given by Eqs. 2.56 and 2.57 in chapter 2. By definition of the (C, τ) coordinate system, the Stokes velocity component in the C direction is identically zero. Since we are interested in the transport in a thin thermal boundary layer adjacent to the drop, it is the near-field form of the velocity

field which enters into the analysis. The near-field form of the Stokes velocity field is given by:

$$u_r^{(0)} = h_r^{(0)}(C, \tau; \alpha, \lambda)y, \quad (4.8)$$

$$u_C^{(0)} = 0, \quad (4.9)$$

$$\frac{u_\tau^{(0)}}{k} = h_\tau^{(0)}(\alpha, \lambda), \quad (4.10)$$

and the $O(Re)$ field has the form:

$$u_r^{(1)} = h_r^{(1)}(C, \tau; \alpha, \lambda)y, \quad (4.11)$$

$$\frac{u_C^{(1)}}{h} = h_C^{(1)}(C, \tau; \alpha, \lambda), \quad (4.12)$$

$$\frac{u_\tau^{(1)}}{k} = h_\tau^{(1)}(C, \tau; \alpha, \lambda). \quad (4.13)$$

Here, $y = r - 1$ and y is expected to be of the order of the boundary layer thickness at large Pe . The expressions for $h_r^{(0)}$ and $h_\tau^{(0)}$ are the same as those given in section 3.3.2 of chapter 3. $h_r^{(1)}$, $h_C^{(1)}$ and $h_\tau^{(1)}$ are found to be given by:

$$\begin{aligned} h_r^{(1)}(C, \tau; \alpha, \lambda) = & \\ & \left(1 / \left(288288 (\lambda + 1)^3\right)\right) \left((\alpha + 1) \left(- \left(4C^2 (\gamma^2 \sin^2 \tau + \cos^2 \tau) \left(- \left(32032 (\alpha - 1) \right. \right. \right. \right. \right. \right. \\ & \left. \left. \left. \left. \left. (\lambda + 1) (3\lambda + 1) (\gamma^2 \tan \tau - 1) \right) / (\gamma^2 \tan \tau + 1) \right) - 2(\alpha + 1) (36465\lambda^2 + 54626\lambda + 15456) \right) \right) \right. \\ & \left. / \left(C^2 (\gamma^2 \sin^2 \tau + \cos^2 \tau + 1) \right) - \left(35C^4 (\alpha + 1) \gamma^2 (4290\lambda^2 + 7436\lambda + 2064) \sin^2 2\tau \right) \right. \\ & \left. / \left(C^2 (\gamma^2 \sin^2 \tau + \cos^2 \tau) + 1 \right)^2 - 8(\alpha + 1) (19305\lambda^2 + 27742\lambda + 7896) \right) \right), \quad (4.14) \end{aligned}$$

$$\begin{aligned} h_C^{(1)}(C, \tau; \alpha, \lambda) = & \\ & \left(C \left(1 + C^2 (\cos^2 \tau + \gamma^2 \sin^2 \tau) \right) \left(\left(14C^2 (1 + \alpha)^2 (1032 + 3718\lambda + 2145\lambda^2) \right. \right. \right. \\ & \left. \left. \left(\cos^4 \tau - 6\gamma^2 \cos^2 \tau \sin^2 \tau + \gamma^4 \sin^4 \tau \right) + \frac{1}{5 + 2\lambda} (\cos^2 \tau + \gamma^2 \sin^2 \tau) (1 + C^2 (\cos^2 \tau + \gamma^2 \sin^2 \tau)) \right) \right. \\ & \left. \left(- (256256 (-1 + \alpha^2) (1 + \lambda) (3 + 8\lambda + 3\lambda^2) (\cos^2 \tau - \gamma^2 \sin^2 \tau)) / (\cos^2 \tau + \gamma^2 \sin^2 \tau) \right. \right. \\ & \left. \left. + (2(1 + \alpha)^2 (5 + 2\lambda) (4 (7896 + 27742\lambda + 19305\lambda^2) + 3C^2 (8120 + 28314\lambda + 20735\lambda^2) \cos^2 \tau + 3C^2 \gamma^2 \right. \right. \right. \\ & \left. \left. \left. (8120 + 28314\lambda + 20735\lambda^2) \sin^2 \tau) \right) / (1 + C^2 \cos^2 \tau + C^2 \gamma^2 \sin^2 \tau) \right) \right) / (1 + C^2 (\cos^2 \tau + \gamma^2 \sin^2 \tau))^2 \\ & - (28(1 + \alpha) (-1 + \gamma^2) \cos \tau \sin \tau (9152(-1 + \alpha) (3 + 11\lambda + 11\lambda^2 + 3\lambda^3) + C^2 (-14312 - 70990\lambda \\ & - 73073\lambda^2 - 18018\lambda^3 + \alpha (3992 + 29682\lambda + 36751\lambda^2 + 9438\lambda^3)) \cos^2 \tau + C^2 \gamma^2 (-3992 - 29682\lambda \\ & - 36751\lambda^2 - 9438\lambda^3 + \alpha (14312 + 70990\lambda + 73073\lambda^2 + 18018\lambda^3)) \sin^2 \tau) \sin 2\tau) / ((5 + 2\lambda) \\ & \left. \left. \left. \left. \left. (1 + C^2 \cos^2 \tau + C^2 \gamma^2 \sin^2 \tau)^2 \right) \right) \right) / (576576(1 + \lambda)^3 (\cos^2 \tau + \gamma^2 \sin^2 \tau)), \quad (4.15) \end{aligned}$$

$$\begin{aligned}
h_\tau^{(1)}(C, \tau; \alpha, \lambda) = & \\
& ((1 + \alpha) (9152(-1 + \alpha)(1 + \lambda)(3 + \lambda(8 + 3\lambda)) + C^2 ((-14312 - \lambda(70990 + 1001\lambda \\
& (73 + 18\lambda)) + \alpha(3992 + \lambda(29682 + 143\lambda(257 + 66\lambda)))) \cos^2 \tau + \gamma^2(-3992 \\
& -\lambda(29682 + 143\lambda(257 + 66\lambda)) + \alpha(14312 + \lambda(70990 + 1001\lambda(73 + 18\lambda)))) \sin^2 \tau)) \sin 2\tau) \\
& / (20592(1 + \lambda)^3(5 + 2\lambda) (1 + C^2 (\cos^2 \tau + \gamma^2 \sin^2 \tau))). \tag{4.16}
\end{aligned}$$

It is important to note that the radial velocity is $O(y)$, while the tangential velocities are $O(1)$ near the surface. Also, as we saw in the open streamline analysis, the combination $h_\tau^{(0)}/k$ is independent of both C and τ . This is analogous to a rotating solid particle for which u_ϕ is independent of both θ and ϕ (Subramanian & Koch (2006b)). The Stokes velocity in the drop exterior, allowed us to derive the flow-aligned and non-orthogonal (C, τ) coordinate which we described in chapter 2. The details of the coordinate system, for the closed streamline regime, are given in chapter 2 section 2.4.

From Fig. 4.2 we see that the inertial streamlines are tightly wound spirals for small Re , with each turn closely resembling an inertia-less Jeffery orbits. The trajectories are, of course, not closed, since there is a net displacement along the drop surface during a given revolution. The rapid convection due to the Stokes velocity along the orbit compared to the slow drift due to the $O(Re)$ velocity field means that, for the purposes of the heat transfer analysis, these spiralling streamlines can be approximated as a series of inertia-less Jeffery orbits. The condition that drift across the orbits is slow is met when $Re \ll 1$. In this limit, the inertial convection may now be interpreted in a τ -averaged sense, where the inertial drift is given by the τ average of the $O(Re)$ velocity field along a Jeffery orbit. This is analogous to the much simpler ϕ -averaged used for a solid particle by Subramanian & Koch (2006b). Recall that this τ -averaged approach was earlier used by us to calculate the location of the wake on the drop surface (chapter 2). Using this estimate for the inertial convection, we can estimate the scale of the boundary layer thickness in the limit $RePe \gg 1$. The convective time scale is $O[a/(Rea\dot{\gamma}^{-1})]$, while the diffusive time scales is $O(y^2/D)$, where y is a scale for the boundary layer thickness. Equating these time scales, we obtain $y \sim O(RePe)^{-1/2}$.

As already discussed at the beginning of this chapter, a consequence of the rapid convection along an orbit is that the leading order temperature field is independent of τ . Physically, this τ -independence, of course, corresponds to isothermal streamlines. For large Pe , the heat transfer depends on the nature of the near-field streamlines. These streamlines are circular for the case of a solid particle, while for the drop, these near-surface streamlines are close to being Jeffery orbits (curves of constant C in the (C, τ) coordinate system). In both cases of a solid particle and a drop, the radial distance along a streamline remains unchanged at leading order. This distance varies by an amount $O(y^2)$ for a solid particle, and by $O(y)$ for a drop as can be deduced by the scaling for the Stokes radial velocity in each case (see Subramanian & Koch (2006b) and Eq. 4.8). This difference in the order of variation, however, proves to be crucial. This is because, for a drop, this radial distance varies by an amount of order the boundary layer thickness. Holding the radial coordinate constant while averaging over an orbit, will lead to an $O(1)$ error in the estimate of the temperature field. This is because in our rescaling, the temperature varies by an $O(1)$ amount over a distance of $O(y)$. This is unlike the solid particle case, where integration

along the azimuthal coordinate in order to compute the averaged inertial drift, can be carried out at a constant radial distance from the particle surface, leading only to an asymptotically small error in the estimate of temperature (see [Subramanian & Koch \(2006b\)](#)).

Thus, in the case of a drop, we need to define a new radial coordinate which takes into account the radial displacements of the inertia-less streamlines, displacements that are of the same order as the boundary layer thickness. The “D surfaces” and “E surfaces”, which were derived while analysing the exterior streamlines in chapter 2, serve as natural candidates for the constant coordinate surfaces in the radial direction (instead of spheres as was the case for the solid particle). However, of these, we choose the “E surfaces”, since these do not exhibit a singularity at the equatorial plane shown by the “D surfaces”. The latter family of surfaces become parallel to the plane of symmetry (see the discussion in section 2.3.2, chapter 2). This causes the normal to the surfaces, that is in the radial direction for most of the drop surface, to become tangential close to the plane of symmetry. In turn, this leads to a spurious dominance of tangential diffusion close to the plane of symmetry.

We now derive the near-field form of the D and E surfaces. Writing down the near-field Stokes velocity in a spherical coordinate system, we have:

$$u_r = -\frac{3(1+\alpha)}{1+\lambda} \sin^2 \theta \sin 2\phi_1 y = \frac{dy}{ds}, \quad (4.17)$$

$$u_\theta = -\frac{(1+\alpha)}{2(1+\lambda)} \sin 2\theta \sin 2\phi_1 = \frac{d\theta}{ds}, \quad (4.18)$$

$$u_\phi = -\frac{(1+\alpha)}{1+\lambda} \sin \theta (\cos 2\phi_1 + \beta) = \sin \theta \frac{d\phi_1}{ds}. \quad (4.19)$$

Recall that $\phi_1 = \pi/2 - \phi$. Dividing Eq. 4.17 by Eq. 4.18, we get:

$$\frac{dy}{d\theta} = \frac{3y \sin \theta}{\cos \theta}. \quad (4.20)$$

Upon integrating this, we get the near-field form of the D surfaces, denoted here by ψ , as:

$$\psi = \cos^3 \theta y. \quad (4.21)$$

Note that ψ and D (derived in chapter 2) can be shown to be related as follows:

$$\psi = D^3 \left[\frac{3(\lambda+2)}{2(\lambda+1)} \right]^{-1}. \quad (4.22)$$

Similarly dividing Eq. 4.19 and 4.18, we get:

$$\sin \theta \cos \theta \sin 2\phi \frac{d\phi}{d\theta} = \cos 2\phi + \beta(1+\lambda). \quad (4.23)$$

Upon rearranging, this becomes:

$$\frac{d(\tan^2 \theta \cos^2 \phi_1)}{d\theta} = [1 - \beta(1+\lambda)] \frac{\sin \theta}{\cos^2 \theta}. \quad (4.24)$$

Dividing Eq. 4.24 by 4.20, we get:

$$\frac{d(\tan^2 \theta \cos^2 \phi_1)}{dy} = \frac{[1 - \beta(1 + \lambda)]}{\cos^2 \theta}. \quad (4.25)$$

Integrating from y_m to y and substituting for $\cos \theta$ from Eq. 4.21, we have:

$$\int_{y_m}^y \frac{d(\tan^2 \theta \cos^2 \phi_1)}{dy} dy = \frac{[1 - \beta(1 + \lambda)]}{3\psi^{2/3}} \int_{y_m}^y y^{-1/3}. \quad (4.26)$$

Imposing that $\tan^2 \theta \cos^2 \phi = 0$ at $y = y_m$, we get after some algebra:

$$y_m = y \left[1 - \frac{2 \sin^2 \theta \cos^2 \phi_1}{1 - \beta(1 + \lambda)} \right]^{3/2}, \quad (4.27)$$

where y_m is the required new radial coordinate which characterizes the near-field inertia-less orbits. We note that the constant y_m surfaces are the near-field form of the constant E surfaces derived in chapter 2. Writing this in terms of the (C, τ) coordinate system, we have the expression for the new radial coordinate as:

$$y_m = M(C, \tau)y, \quad (4.28)$$

in terms of the original radial coordinate, where:

$$M(C, \tau) = \left[\frac{1 + C^2 \gamma^2}{1 + C^2 (\cos^2 \tau + \gamma^2 \sin^2 \tau)} \right]^{3/2}. \quad (4.29)$$

We see that this new radial coordinate is a rescaled version of the spherical radial coordinate y , where the scaling prefactor being a function of C and τ . As we show later, physically this prefactor is related to the radial extent of a fluid element in the near-field; the prefactor changes as a function of τ in such a manner as to enforce the incompressibility constraint for the fluid element as it moves around the drop in a Jeffery orbit. Thus, a near-field streamline is defined by a constant value of y_m and C . Also, $y_m = y$ at $\tau = \pi/2$, which corresponds to $\phi_1 = \pi/2$ (see Fig. 4.3).

4.4 Boundary layer analysis

Having characterized the coordinate system required for the analysis, we now transform the convection-diffusion equation from the (y, C, τ) coordinate system to a (y_m, C, τ) coordinate system. Using the chain rule for differentiation, we can write:

$$\frac{\partial \Theta}{\partial y} \Big|_{C, \tau} = \frac{\partial \Theta}{\partial y_m} \Big|_{C, \tau} \frac{\partial y_m}{\partial y} \Big|_{C, \tau}, \quad (4.30)$$

$$\frac{\partial \Theta}{\partial C} \Big|_{y, \tau} = \frac{\partial \Theta}{\partial y_m} \Big|_{C, \tau} \frac{\partial y_m}{\partial C} \Big|_{y, \tau} + \frac{\partial \Theta}{\partial C} \Big|_{y_m, \tau}, \quad (4.31)$$

$$\frac{\partial \Theta}{\partial \tau} \Big|_{y, C} = \frac{\partial \Theta}{\partial y_m} \Big|_{C, \tau} \frac{\partial y_m}{\partial \tau} \Big|_{y, C} + \frac{\partial \Theta}{\partial \tau} \Big|_{y_m, C}. \quad (4.32)$$

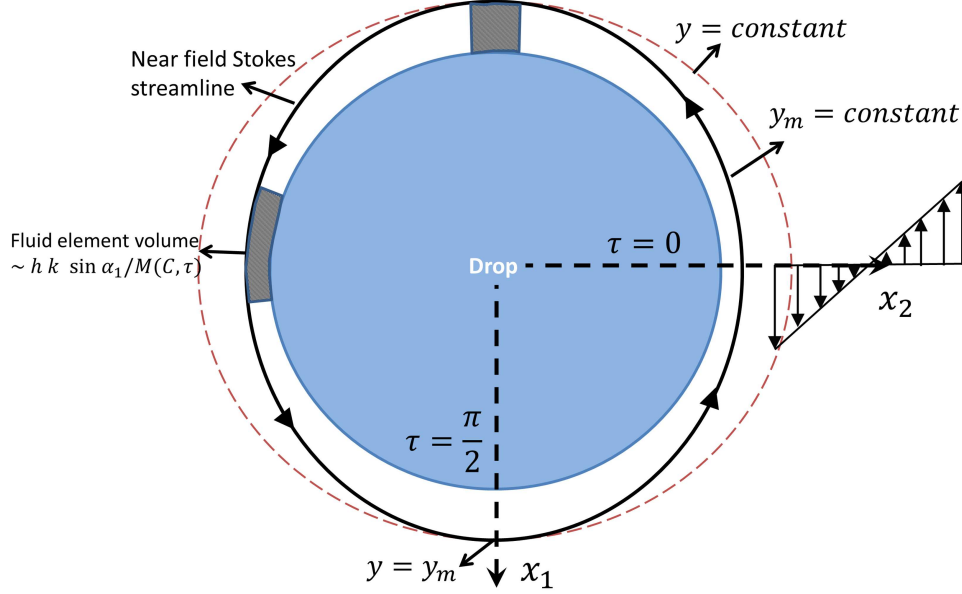


Figure 4.3: A schematic depiction of a near-field Stokes streamline, showing the varying radial distance from the drop surface. We see that these streamlines can be described by the equations $y_m = C_1$ and $C = C_2$, where C_1 and C_2 are constants. To satisfy the continuity constraint a fluid element moving along such a streamline has a volume which is independent of τ .

Note that in the derivative with respect to the radial coordinate, we have not included terms which involve changes to the C and τ coordinates with respect to y . Such terms will, in general, be non-zero since the (C, τ) coordinate system is defined at the drop surface and therefore, in principle, we need to consider a perturbation to this coordinate system when we are at a radial distance of $O(y)$ from the drop surface. However, for the purposes of the heat transfer analysis, it is straightforward to show that this perturbation to the (C, τ) coordinate system does not contribute at leading order since it is $O(y)$ and is therefore of order the boundary layer thickness. The physical significance of Eqs. 4.31 and 4.32 can be understood from Fig. 4.3. As we move across Jeffery orbits (across constant- C curves) at a constant y , we also end up moving across constant- y_m surfaces in the process. A similar argument applies for Eq. 4.32 with respect to τ . These, therefore, appear as additional ‘radial’ velocity contributions in our (y_m, C, τ) coordinate system.

Using the above expressions, the convection-diffusion equation in the (y_m, C, τ) coordinate system is given by:

$$\left(u_r \frac{\partial y_m}{\partial y} + \frac{u_C}{h} \frac{\partial y_m}{\partial C} + \frac{u_\tau}{k} \frac{\partial y_m}{\partial \tau} \right) \frac{\partial \Theta}{\partial y_m} + \frac{u_C}{h} \frac{\partial \Theta}{\partial C} \Big|_{y_m, \tau} + \frac{u_\tau}{k} \frac{\partial \Theta}{\partial \tau} \Big|_{y_m, C} = \frac{1}{Pe} \frac{\partial^2 \Theta}{\partial y_m^2} \left(\frac{\partial y_m}{\partial y} \right)^2, \quad (4.33)$$

where considering only the Stokes velocity contribution to the convection terms, to begin with, we get:

$$\left(u_r^{(0)} \frac{\partial y_m}{\partial y} + \frac{u_C^{(0)}}{h} \frac{\partial y_m}{\partial C} + \frac{u_\tau^{(0)}}{k} \frac{\partial y_m}{\partial \tau} \right) \frac{\partial \Theta}{\partial y_m} + \frac{u_C^{(0)}}{h} \frac{\partial \Theta}{\partial C} + \frac{u_\tau^{(0)}}{k} \frac{\partial \Theta}{\partial \tau} = \frac{1}{Pe} \frac{\partial^2 \Theta}{\partial y_m^2} \left(\frac{\partial y_m}{\partial y} \right)^2, \quad (4.34)$$

where $u_C^{(0)} = 0$. The term $(\partial y_m / \partial y)^2$, physically, captures the variation of the diffusion term which is larger in regions where the constant- y_m surfaces (isotherms at zero Re) are squeezed close together and smaller when they are far apart. Near the surface of the drop, the above equation becomes:

$$\left(h_r^{(0)} y \frac{\partial y_m}{\partial y} + h_\tau^{(0)} \frac{\partial y_m}{\partial \tau} \right) \frac{\partial \Theta}{\partial y_m} + h_r^{(0)} \frac{\partial \Theta}{\partial \tau} = \frac{1}{Pe} \frac{\partial^2 \Theta}{\partial y_m^2} \left(\frac{\partial y_m}{\partial y} \right)^2. \quad (4.35)$$

Further, if we look at the rate of convection in the y_m direction, we see that:

$$h_r^{(0)} y \frac{\partial y_m}{\partial y} + h_\tau^{(0)} \frac{\partial y_m}{\partial \tau} = 0. \quad (4.36)$$

This is simply a mathematical statement of the fact that the Stokes velocity, by definition, cannot lead to convection across the constant- y_m surfaces, which are the invariant streamsurfaces of the Stokes velocity field. Thus, at leading order, in the limit of $Pe \gg 1$, we have:

$$\frac{\partial \Theta^{(0)}}{\partial \tau} = 0, \quad (4.37)$$

which implies that the leading order temperature field is independent of the τ coordinate. Note our earlier argument which shows that this statement is only valid for times much longer than $O(Pe^{-2/3})a^2/D$. This is true in our case since the time scale for inertial convection which is $O([(RePe)^{-1/2}]^2)a^2/D$. Evidently, the transformation to the new radial coordinate system has helped us see directly that the Stokes streamlines, on account of being closed orbits, must be isothermal. Mathematically, in the chosen coordinate system, this leads to a temperature field independent of τ . Also, we see that the isotherms, even at leading order, are constant- y_m (and constant- C) curves and not constant- y curves. Expanding the temperature field in a perturbation series:

$$\Theta = \Theta^{(0)}(y_m, C) + f(Re, Pe)\Theta^{(1)}(y_m, C, \tau), \quad (4.38)$$

where $f(Re, Pe)$ is a small parameter, proportional to the boundary layer thickness, which will be determined by the balance of terms within the thermal boundary layer. Writing the convection-diffusion equation to $O(Re)$ in the velocity field, and making use of Eqs. 4.36 and 4.37, we get:

$$\begin{aligned} \left(Re u_r^{(1)} \frac{\partial y_m}{\partial y} + Re \frac{u_C^{(1)}}{h} \frac{\partial y_m}{\partial C} + Re \frac{u_\tau^{(1)}}{k} \frac{\partial y_m}{\partial \tau} \right) \frac{\partial \Theta^{(0)}}{\partial y_m} + Re \frac{u_C^{(1)}}{h} \frac{\partial \Theta^{(0)}}{\partial C} \\ + Re f(Re, Pe) \frac{u_\tau^{(0)}}{k} \frac{\partial \Theta^{(1)}}{\partial \tau} = \frac{1}{Pe} \frac{\partial^2 \Theta^{(0)}}{\partial y_m^2} \left(\frac{\partial y_m}{\partial y} \right)^2. \end{aligned} \quad (4.39)$$

Since $u_\tau^{(0)}/k$ is a constant, we can average the above equation over τ , to get:

$$\begin{aligned} Re \left[\int_0^{2\pi} \left(u_r^{(1)} \frac{\partial y_m}{\partial y} + \frac{u_C^{(1)}}{h} \frac{\partial y_m}{\partial C} + \frac{u_\tau^{(1)}}{k} \frac{\partial y_m}{\partial \tau} \right) d\tau \right] \frac{\partial \Theta^{(0)}}{\partial y_m} + Re \left[\int_0^{2\pi} \left(\frac{u_C^{(1)}}{h} \right) d\tau \right] \frac{\partial \Theta^{(0)}}{\partial C} \\ = \frac{1}{Pe} \left[\int_0^{2\pi} \left(\frac{\partial y_m}{\partial y} \right)^2 d\tau \right] \frac{\partial^2 \Theta^{(0)}}{\partial y_m^2}. \end{aligned} \quad (4.40)$$

Expanding the inertial velocity components in the near-field using Eqs. 4.11 to 4.13 we get:

$$\begin{aligned} & Re \left[\int_0^{2\pi} \left(h_r^{(1)} y \frac{\partial y_m}{\partial y} + h_C^{(1)} \frac{\partial y_m}{\partial C} + h_\tau^{(1)} \frac{\partial y_m}{\partial \tau} \right) d\tau \right] \frac{\partial \Theta^{(0)}}{\partial y_m} + Re \left[\int_0^{2\pi} h_C^{(1)} d\tau \right] \frac{\partial \Theta^{(0)}}{\partial C} \quad (4.41) \\ &= \frac{1}{Pe} \left[\int_0^{2\pi} \left(\frac{\partial y_m}{\partial y} \right)^2 d\tau \right] \frac{\partial^2 \Theta^{(0)}}{\partial y_m^2}. \end{aligned}$$

The τ -average used above points to a crucial difference between the particle and drop cases. In the particle case, the uniform angular velocity implies that one just has an integral with respect to ϕ . On the other hand, for a drop, the weighting is not uniform (since u_τ is a function of τ along a Jeffery orbit), and the non-trivial relation between τ and ϕ implies that, when written as an average over ϕ , the parts of the orbit where the fluid elements are moving slower have a greater weightage since inertia, acting over a longer time, leads to a greater drift; and vice versa.

From the above equation, clearly, it is the τ -averaged inertial velocity which leads to a net convection, implying that the scale for the boundary layer thickness is $O(Re^{-1/2} Pe^{-1/2})$. Indeed, on postulating a rescaling for the modified radial coordinate y_m of the form $Y_m = m(Re, Pe)y_m$, where Y_m is strictly $O(1)$, we see that the leading order balance gives $m(Re, Pe) = Re^{1/2} Pe^{1/2}$. In terms of this rescaled coordinate, the τ -averaged convection-diffusion equation is now given by:

$$\begin{aligned} & \left[\int_0^{2\pi} \left(h_r^{(1)} Y_m + h_C^{(1)} \frac{\partial Y_m}{\partial C} + h_\tau^{(1)} \frac{\partial Y_m}{\partial \tau} \right) d\tau \right] \frac{\partial \Theta^{(0)}}{\partial Y_m} + \left[\int_0^{2\pi} h_C^{(1)} d\tau \right] \frac{\partial \Theta^{(0)}}{\partial C} \quad (4.42) \\ &= \left[\int_0^{2\pi} \left(\frac{\partial y_m}{\partial y} \right)^2 d\tau \right] \frac{\partial^2 \Theta^{(0)}}{\partial Y_m^2}. \end{aligned}$$

Using Eq. 4.28 the above equation can be rewritten as:

$$\begin{aligned} & Y_m \left[\int_0^{2\pi} \left(h_r^{(1)} + \frac{h_C^{(1)}}{M} \frac{\partial M}{\partial C} + \frac{h_\tau^{(1)}}{M} \frac{\partial M}{\partial \tau} \right) d\tau \right] \frac{\partial \Theta^{(0)}}{\partial Y_m} + \left[\int_0^{2\pi} h_C^{(1)} d\tau \right] \frac{\partial \Theta^{(0)}}{\partial C} \quad (4.43) \\ &= \left[\int_0^{2\pi} \left(\frac{\partial y_m}{\partial y} \right)^2 d\tau \right] \frac{\partial^2 \Theta^{(0)}}{\partial Y_m^2}, \end{aligned}$$

which is of the form:

$$Y_m \mathcal{A}(C) \frac{\partial \Theta^{(0)}}{\partial Y_m} + \mathcal{B}(C) \frac{\partial \Theta^{(0)}}{\partial C} = \mathcal{D}(C) \frac{\partial^2 \Theta^{(0)}}{\partial Y_m^2}, \quad (4.44)$$

where

$$\mathcal{A}(C) = \int_0^{2\pi} \left(h_r^{(1)} + \frac{h_C^{(1)}}{M} \frac{\partial M}{\partial C} + \frac{h_\tau^{(1)}}{M} \frac{\partial M}{\partial \tau} \right) d\tau, \quad (4.45)$$

$$\mathcal{B}(C) = \int_0^{2\pi} h_C^{(1)} d\tau, \quad (4.46)$$

$$\mathcal{D}(C) = \int_0^{2\pi} \left(\frac{\partial y_m}{\partial y} \right)^2 d\tau. \quad (4.47)$$

It is noteworthy that a three-dimensional non-axisymmetric heat transfer problem has been reduced, through the use of a suitable coordinate system and an averaging procedure, to a one-

dimensional problem in the C variable. The physical interpretations of the three terms $\mathcal{A}(C)$, $\mathcal{B}(C)$ and $\mathcal{D}(C)$ follow naturally. $\mathcal{A}(C)$ represents the convective flux across the constant- y_m surfaces due to the τ -averaged inertial velocity. $\mathcal{B}(C)$ is a quantity which we already encountered in chapter 2, when determining the location of the wake on the drop surface. This represents the τ -averaged convective flux across inertia-less orbits, which leads to a net convection tangential to the drop surface; the thermal wake is the location (a constant- C Jeffery orbit to the order considered) at which this tangential convection vanishes. $\mathcal{D}(C)$ is the scaling parameter for the diffusion term, and physically, it represents the fact that the near-field isotherms, in the absence of inertia are not at a constant radial distance from the drop surface. This is a consequence of the displacement, of the order of a boundary layer thickness, undergone by the near-field closed orbits as was shown previously. When inertia is added, we showed that leading order temperature field still satisfies $\partial\Theta^{(0)}/\partial\tau|_{y_m,C} = 0$, implying that the constant y_m surfaces are still the isotherms. Since heat must diffuse across these isotherms, which are at a scaled radial distance from the drop surface, we have the emergence of the scaling factor $\mathcal{D}(C)$ multiplying the diffusion term. This term is larger in regions where the constant- y_m surfaces are squeezed together and is smaller in regions where they are farther apart from one another. It is important to note that this scaling factor arises due to the topology of the near-field streamlines and is present over and above the conventional scaling terms with respect to the boundary layer thickness.

We now introduce a similarity variable of the form $\eta = Y_m/g(C)$, where $g(C)$ characterises the dependence of the boundary layer thickness on the position on the drop surface. Note that, unlike the open streamline regime, the boundary layer thickness on account of τ averaging is only a function of C . Transforming Eq. 4.44, we find that the non-dimensional temperature satisfies:

$$\frac{d^2\Theta}{d\eta^2} + 2\eta\frac{d\Theta}{d\eta} = 0, \quad (4.48)$$

and the boundary layer thickness is governed by:

$$\frac{df}{dC} - \frac{2\mathcal{A}(C)}{\mathcal{B}(C)}f = \frac{2\mathcal{D}(C)}{\mathcal{B}(C)}, \quad (4.49)$$

where $f = g^2/2$. The boundary conditions for the non-dimensional temperature are given by:

$$\Theta = 1 \quad \text{at} \quad r = 1, \quad (4.50)$$

$$\Theta \rightarrow 0 \quad \text{as} \quad r \rightarrow \infty. \quad (4.51)$$

Solving Eq. 4.48 and using Eqs. 4.50 and 4.51, we get:

$$\Theta(\eta) = 1 - \frac{2}{\sqrt{\pi}} \int_0^\eta \exp(-t^2) dt \quad (4.52)$$

In order to proceed towards a solution for the boundary layer thickness, and thence, the Nusselt number, we rewrite the convective term involving the ‘radial’ velocity $\mathcal{A}(C)$. From the continuity equation written for the Stokes velocity field, expressed in the (y, C, τ) coordinate system, we get:

$$\frac{\partial(hk \sin \alpha_1 u_r^{(0)})}{\partial y} + \frac{\partial(k \sin \alpha_1 u_C^{(0)})}{\partial C} + \frac{\partial(h \sin \alpha_1 u_\tau^{(0)})}{\partial \tau} = 0, \quad (4.53)$$

where $u_C^{(0)} = 0$ by definition. In terms of the velocity field near the drop surface, the remaining two terms take the form:

$$\frac{\partial(hk \sin \alpha_1 h_r^{(0)} y)}{\partial y} + \frac{\partial(hk \sin \alpha_1 h_\tau^{(0)})}{\partial \tau} = 0. \quad (4.54)$$

Noting that the term $h_r^{(0)}$ is independent of both C and τ and that the metric factor $hk \sin \alpha_1$ is independent of the radial coordinate, we can write the above equation as:

$$hk \sin \alpha_1 h_r^{(0)} + h_\tau^{(0)} \frac{\partial(hk \sin \alpha_1)}{\partial \tau} = 0. \quad (4.55)$$

From Eq. 4.28 and 4.36, we see that the radial Stokes velocity may be written as:

$$h_r^{(0)} = -\frac{1}{M} \frac{\partial M}{\partial \tau} h_\tau^{(0)}, \quad (4.56)$$

where $M(C, \tau)$ is given by Eq. 4.29. Substituting for $h_r^{(0)}$ in Eq. 4.55, we get the relation:

$$\frac{1}{M} \frac{\partial M}{\partial \tau} = \frac{1}{hk \sin \alpha_1} \frac{\partial(hk \sin \alpha_1)}{\partial \tau}. \quad (4.57)$$

Physically, this is a statement of the fact that the volume of a fluid element (the element being a column sandwiched between the drop surface and the near-field constant y_m surface) as it moves along an inertia-less Stokes orbits is conserved as required by continuity (see Fig. 4.3). This can be seen by noting that the volume of an infinitesimal fluid element is given by $\Delta V = hk \sin \alpha_1 \Delta C \Delta \tau y_m / M(C, \tau)$ and the above equation is the same as the condition that:

$$\partial(\Delta V) / \partial \tau|_{y_m, C} = 0. \quad (4.58)$$

The variation of the shape of this element can be understood by considering a fluid element moving along a constant- y_m trajectory lying on the plane of symmetry ($C \rightarrow \infty$). We see that $M(C, \tau) = [(1 + C^2 \gamma^2) / (1 + C^2)]^{3/2} > 1$ at $\tau = 0, \pi$ and $M(C, \tau) = 1$ at $\tau = \pi/2, 3\pi/2$. From the expression for ΔV given above, this implies that a fluid element is compressed in the radial direction near the gradient axis ($x_2, \tau = 0, \pi$), while it is stretched in the radial direction near the flow axis ($x_1, \tau = \pi/2, 3\pi/2$) as shown in Fig. 4.3.

Next, the continuity equation, at $O(Re)$ expressed in a (y, C, τ) coordinate system, is given by:

$$hk \sin \alpha_1 \frac{\partial u_r^{(1)}}{\partial y} + \frac{\partial(k \sin \alpha_1 u_C^{(1)})}{\partial C} + \frac{\partial(h \sin \alpha_1 u_\tau^{(1)})}{\partial \tau} = 0. \quad (4.59)$$

Rewriting this equation for the near-field inertial velocity, we have:

$$h_r^{(1)} + \frac{1}{hk \sin \alpha_1} \frac{\partial(hk \sin \alpha_1 h_C^{(1)})}{\partial C} + \frac{1}{hk \sin \alpha_1} \frac{\partial(hk \sin \alpha_1 h_\tau^{(1)})}{\partial \tau} = 0, \quad (4.60)$$

$$h_r^{(1)} + \frac{1}{hk \sin \alpha_1} \frac{\partial(hk \sin \alpha_1 h_C^{(1)})}{\partial C} + \frac{h_\tau^{(1)}}{hk \sin \alpha_1} \frac{\partial(hk \sin \alpha_1)}{\partial \tau} + \frac{\partial(hk \sin \alpha_1)}{\partial \tau} = 0. \quad (4.61)$$

Using the relation given by Eq. 4.57, we get:

$$h_r^{(1)} + \frac{h_\tau^{(1)}}{M} \frac{\partial M}{\partial \tau} = - \left[\frac{\partial h_\tau^{(1)}}{\partial \tau} + \frac{1}{hk \sin \alpha_1} \frac{\partial(hk \sin \alpha_1 h_C^{(1)})}{\partial C} \right]. \quad (4.62)$$

We note that the LHS of the above equation contains the first and third terms in the integrand in the expression for $\mathcal{A}(C)$ (see Eq. 4.45). Upon substituting, we get:

$$\mathcal{A}(C) = \int_0^{2\pi} \left[-\frac{\partial h_\tau^{(1)}}{\partial \tau} - \frac{1}{hk \sin \alpha_1} \frac{\partial(hk \sin \alpha_1 h_C^{(1)})}{\partial C} + \frac{h_C^{(1)}}{M} \frac{\partial M}{\partial C} \right] d\tau. \quad (4.63)$$

The first term in the above expression is in the form of an exact differential and hence is zero when integrated from 0 to 2π . Upon rearranging the expression further, we have the following:

$$\mathcal{A}(C) = \int_0^{2\pi} \left[\left(\frac{1}{M} \frac{\partial M}{\partial C} - \frac{1}{hk \sin \alpha_1} \frac{\partial(hk \sin \alpha_1)}{\partial C} \right) h_C^{(1)} - \frac{\partial h_C^{(1)}}{\partial C} \right] d\tau. \quad (4.64)$$

We see that the term:

$$\frac{1}{M} \frac{\partial M}{\partial C} - \frac{1}{hk \sin \alpha_1} \frac{\partial(hk \sin \alpha_1)}{\partial C} = \frac{2C^2\gamma^2 - 1}{C(1 + C^2\gamma^2)}, \quad (4.65)$$

which is independent of τ and can therefore be pulled out of the integral. The remaining terms can be expressed in terms of $\mathcal{B}(C)$, leaving us with the final expression for $\mathcal{A}(C)$ as:

$$\mathcal{A}(C) = \frac{2C^2\gamma^2 - 1}{C(1 + C^2\gamma^2)} \mathcal{B}(C) - \frac{d\mathcal{B}(C)}{dC} \quad (4.66)$$

Physically, the above expression is a statement of the τ -averaged continuity equation for the $O(Re)$ velocity field. The τ averaging trivially excludes any convection in the τ direction, even at $O(Re)$, which leaves only the convection in the radial direction (across constant- y_m surfaces) and in the C direction (across constant- C orbits) denoted by $\mathcal{A}(C)$ and $\mathcal{B}(C)$, respectively. The continuity equation dictates that these two must be related and that relation is given by Eq. 4.66.

4.4.1 Solution to the boundary layer thickness equation

Substituting Eq. 4.66 in Eq. 4.49, we get:

$$\frac{df}{dC} - 2 \left[\frac{2C^2\gamma^2 - 1}{C(1 + C^2\gamma^2)} - \frac{1}{\mathcal{B}(C)} \frac{d\mathcal{B}(C)}{dC} \right] f = \frac{2\mathcal{D}(C)}{\mathcal{B}(C)}, \quad (4.67)$$

which can be rewritten to give:

$$\frac{d}{dC} \left[\frac{f\mathcal{B}(C)^2 C^2}{(1 + C^2\gamma^2)^3} \right] = \frac{2\mathcal{D}(C)\mathcal{B}(C)^2 C^2}{(1 + C^2\gamma^2)^3}. \quad (4.68)$$

Integrating this between the limits C_{inlet} to C , we get:

$$f(C) = \frac{2(1 + C^2\gamma^2)^3}{\mathcal{B}(C)^2 C^2} \int_{C_{inlet}}^C \left[\frac{\mathcal{D}(C')\mathcal{B}(C')^2 C'^2}{(1 + C'^2\gamma^2)^3} \right] dC', \quad (4.69)$$

$$g(C) = \left[\frac{4(1 + C^2\gamma^2)^3}{\mathcal{B}(C)^2 C^2} \mathcal{I}(C) \right]^{1/2}, \quad (4.70)$$

where

$$\mathcal{I}(C) = \int_{C_{inlet}}^C \frac{\mathcal{D}(C')\mathcal{B}(C')^2 C'^2}{(1 + C'^2\gamma^2)^3} dC'. \quad (4.71)$$

The detailed expressions for $\mathcal{B}(C)$ and $\mathcal{D}(C)$ are found to be given by:

$$\begin{aligned} \mathcal{B}(C) = & - \left(\pi(1 + \alpha) \left(14 \left(-1 + \sqrt{(1 + C^2)(1 + C^2\gamma^2)} \right) (13144 + 29682\lambda + 27599\lambda^2 + 9438\lambda^3 \right. \right. \\ & - \gamma^2 (23464 + 70990\lambda + 63921\lambda^2 + 18018\lambda^3) + \alpha (-23464 - 70990\lambda - 63921\lambda^2 - 18018\lambda^3 + \gamma^2 \\ & (13144 + 29682\lambda + 27599\lambda^2 + 9438\lambda^3)) \left. \right) + C^2 (-170968 - 516778\lambda - 497211\lambda^2 - 143286\lambda^3 + 6\gamma^2 \\ & (38360 + 151194\lambda + 143715\lambda^2 + 35750\lambda^3) + \gamma^4 (85288 + 187926\lambda + 143429\lambda^2 + 48906\lambda^3) \\ & + \alpha (85288 + 187926\lambda + 143429\lambda^2 + 48906\lambda^3 + 6\gamma^2 (38360 + 151194\lambda + 143715\lambda^2 + 35750\lambda^3) \\ & \left. - \gamma^4 (170968 + 516778\lambda + 497211\lambda^2 + 143286\lambda^3)) \right) \left. \right) / \left(72072C (-1 + \gamma^2)^2 (1 + \lambda)^3 (5 + 2\lambda) \right), \end{aligned} \quad (4.72)$$

and

$$\mathcal{D}(C) = \frac{\pi \sqrt{1 + C^2\gamma^2} (8 + 8C^2 (1 + \gamma^2) + C^4 (3 + 2\gamma^2 + 3\gamma^4))}{4(1 + C^2)^{5/2}}. \quad (4.73)$$

The boundary conditions above are specified such that the boundary layer thickness is finite at the inlet. The value of C_{inlet} is decided by which regime we are on in the (α, λ) plane. C_{inlet} is always at $C = 0$ (poles) for the single wake regime, where the inertial flow has a bi-axial extensional character, whereas it can be at both the poles and the equator for the bifurcated regime. The values of C_{inlet} in both these regimes is given in Table. 4.1. $g(C)$ gives the thickness variation of the boundary layer with C . We now consider the boundary layer thickness at the outlet, which corresponds to the $C \rightarrow \infty$ in the single wake regime or to an intermediate orbit C^* in the bifurcated wake regime. In both cases, we note that C value at the outlet satisfies the equation $\mathcal{B}(C) = 0$ (see our analysis of the neutral curve C^* in 2.5, chapter 2). Now, in the expression for the boundary layer thickness, the denominator which is proportional to $C\mathcal{B}(C)$, goes to zero at the outlet C orbit, whereas the numerator remains finite. This is true even in the case of the single wake regime where $(1 + C^2\gamma^2)^{3/2}/C\mathcal{B}(C) \rightarrow \infty$ as $C \rightarrow \infty$, while $\mathcal{I}(C)$ remains finite. This divergence of $g(C)$ at the outlet indicates the presence of a thermal wake at this location.

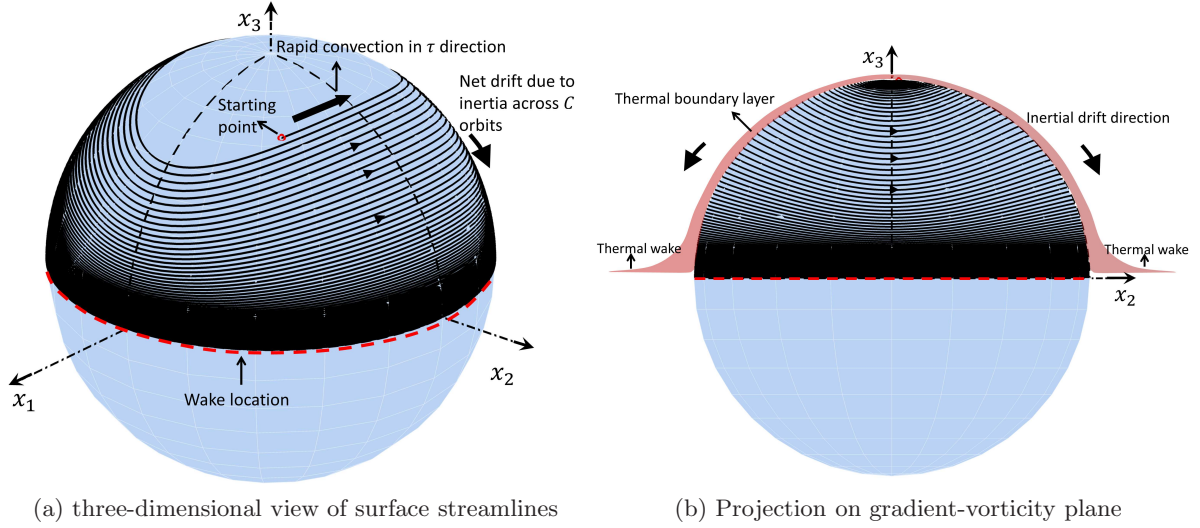


Figure 4.4: Figures showing the inertial surface streamlines for a drop in the single wake regime, $\alpha = 0.2$, $\lambda = 2$ ($\lambda_{bif} = 0.547$), $Re = 0.1$ (a) three-dimensional view (b) projection on x_2x_3 plane (gradient-vorticity plane). The thickness and growth of the thermal boundary layer is schematically represented as the shaded portion. Note the existence of a single wake at the equatorial plane

α, λ	C_{inlet} and C_{outlet}
$\alpha < \alpha_{bif}$ and $\lambda < \lambda_{bif}$	$C_{inlet} = 0, \infty, C_{outlet} = C^*$
$\alpha < \alpha_{bif}$ and $\lambda > \lambda_{bif}$	$C_{inlet} = 0, C_{outlet} = \infty$
$\alpha > \alpha_{bif}$ and any λ	$C_{inlet} = 0, C_{outlet} = \infty$

Table 4.1: The inlet and outlet values of the C orbits for different regimes in the (α, λ) space

4.5 Nusselt number calculation

Using the expression for the boundary layer thickness derived above, we can proceed to calculate the dimensionless heat transfer defined as:

$$\begin{aligned}
 Nu &= -\frac{1}{4\pi} \int_S \frac{\partial \Theta}{\partial y} dS, \\
 &= -\frac{Re^{1/2} Pe^{1/2}}{4\pi} \int_S \frac{\partial \Theta}{\partial Y_m} \frac{\partial y_m}{\partial y} dS,
 \end{aligned} \tag{4.74}$$

where S denotes the surface area of the drop. Rewriting this in terms of the similarity variable η , we get

$$Nu = -\frac{Re^{1/2} Pe^{1/2}}{4\pi} \int_S \frac{1}{g} \frac{d\Theta}{d\eta} \frac{\partial y_m}{\partial y} dS \tag{4.75}$$

$$= \frac{Re^{1/2} Pe^{1/2}}{2\pi^{3/2}} \int_S \frac{\partial y_m}{\partial y} \frac{dS}{g} \tag{4.76}$$

The limits of integration for calculating the Nusselt number are different in the single wake and bifurcated wake regimes and are given in table. 4.1. As we have shown in chapter 2, in the single wake regime, which exists for two distinct regions in (α, λ) space, (1) $\alpha > \alpha_{bif}$ or for (2) $\alpha < \alpha_{bif}$ and $\lambda > \lambda_{bif}$, the spiralling is from the poles towards the equator.

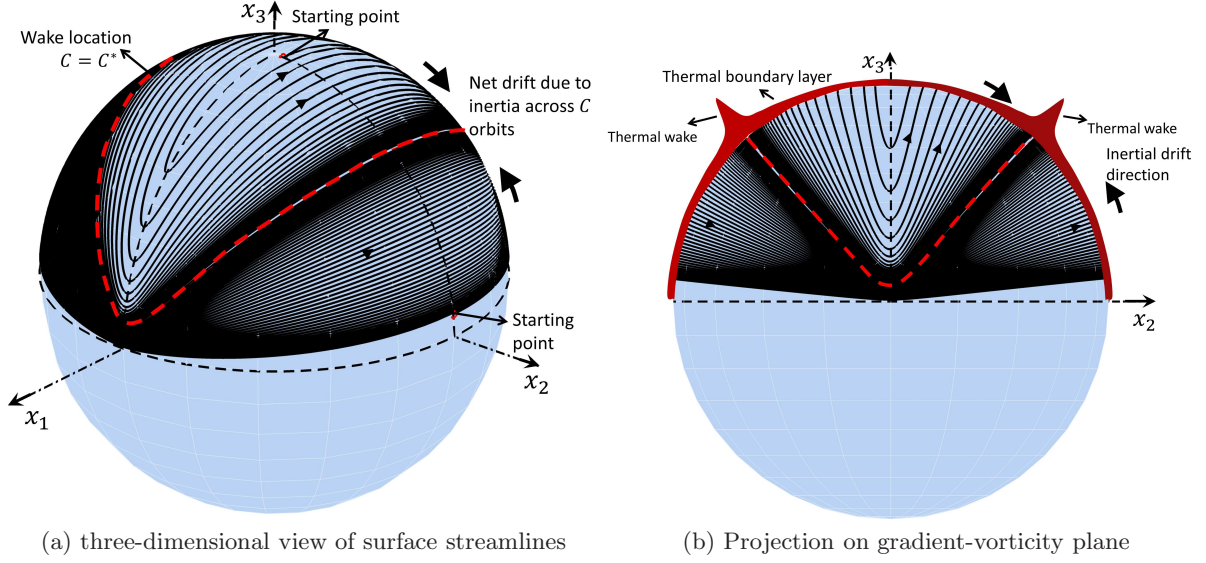


Figure 4.5: Figures showing the inertial surface streamlines for a drop in the bifurcated wake regime, $\alpha = 0.2$, $\lambda = 0.52$ ($\lambda_{bif} = 0.547$), $Re = 0.1$ (a) three-dimensional view (b) projection on x_2x_3 plane (gradient-vorticity plane). The thickness and growth of the thermal boundary layer is schematically represented as the shaded portion. Note the existence of a bifurcated wake lifted off from the equatorial plane and at an intermediate C orbit.

4.5.1 Single wake regime

In this regime, the wake exists at the equator, corresponding to $C \rightarrow \infty$ and the inlet is at the poles ($C = 0$) (see Fig. 4.4). Using these limits, and noting that $dS = hk \sin \alpha_1 dC d\tau$, the Nusselt number in this region is given by:

$$Nu = (2) \frac{Re^{1/2} Pe^{1/2}}{2\pi^{3/2}} \int_0^\infty \int_0^{2\pi} \frac{\partial y_m}{\partial y} \frac{hk \sin \alpha_1}{g(C)} dC d\tau, \quad (4.77)$$

where the prefactor of *two* denotes that the total heat transfer occurs over two symmetric hemispheres on either side of the symmetry plane, only one of which is described by the above limits. Substituting for $\partial y_m / \partial y$ from Eq. 4.28, we get:

$$Nu = \frac{Re^{1/2} Pe^{1/2}}{\pi^{3/2}} \int_0^\infty \frac{dC}{g(C)} \int_0^{2\pi} d\tau M(C, \tau) hk \sin \alpha_1, \quad (4.78)$$

We note that the term:

$$hk \sin \alpha_1 = \frac{C\gamma}{[1 + C^2(\cos^2 \tau + \gamma^2 \sin^2 \tau)]^{3/2}}. \quad (4.79)$$

Substituting for $hk \sin \alpha_1$ and for $M(C, \tau)$ from Eq. 4.29, we get:

$$Nu = \frac{Re^{1/2} Pe^{1/2}}{\pi^{3/2}} \int_0^\infty \frac{dC}{g(C)} \int_0^{2\pi} d\tau \frac{C\gamma(1 + C^2\gamma^2)^{3/2}}{[1 + C^2(\cos^2 \tau + \gamma^2 \sin^2 \tau)]^3}, \quad (4.80)$$

which can be rewritten to give:

$$Nu = \frac{Re^{1/2} Pe^{1/2}}{\pi^{3/2}} \int_0^\infty \frac{dC}{g(C)} \frac{C\gamma}{(1 + C^2\gamma^2)^{3/2}} \int_0^{2\pi} d\tau \frac{(1 + C^2\gamma^2)^3}{[1 + C^2(\cos^2 \tau + \gamma^2 \sin^2 \tau)]^3}. \quad (4.81)$$

Using Eq. 4.47, we can rewrite the above equation as:

$$Nu = \frac{Re^{1/2} Pe^{1/2}}{\pi^{3/2}} \int_0^\infty \frac{dC}{g(C)} \frac{C\gamma \mathcal{D}(C)}{(1 + C^2\gamma^2)^{3/2}}. \quad (4.82)$$

where $\mathcal{D}(C)$ is given by Eq. 4.73. Substituting for the boundary layer thickness from Eq. 4.70, and noting that in the single-wake regime the inlet occurs at $C = 0$, we have:

$$Nu = \frac{Re^{1/2} Pe^{1/2} \gamma}{2\pi^{3/2}} \int_0^\infty dC \frac{\mathcal{D}(C)\mathcal{B}(C)C^2}{(1 + C^2\gamma^2)^3 \mathcal{I}(C)^{1/2}}, \quad (4.83)$$

where, we see that the integral is in the form of an exact differential, because:

$$\frac{d\mathcal{I}(C)}{dC} = \frac{\mathcal{D}(C)\mathcal{B}(C)C^2}{(1 + C^2\gamma^2)^3}. \quad (4.84)$$

Using the above, we get:

$$Nu = \frac{Re^{1/2} Pe^{1/2} \gamma}{\pi^{3/2}} \left[\mathcal{I}(\infty)^{1/2} - \mathcal{I}(0)^{1/2} \right], \quad (4.85)$$

where $\mathcal{I}(0) = 0$, since $C_{inlet} = 0$. Simplifying, we get the final expression for the Nusselt number as:

$$Nu = \frac{Re^{1/2} Pe^{1/2} \gamma}{\pi^{3/2}} \left[\int_0^\infty \frac{\mathcal{D}(C)\mathcal{B}(C)^2 C^2}{(1 + C^2\gamma^2)^3} dC \right]^{1/2}. \quad (4.86)$$

Thus we have the expression for the Nusselt number in terms of a one-dimensional integral which can be carried out numerically. Unlike the open streamline case, here it is not possible to define an effective Pe such that the prefactor to Nu is solely a function of γ . This is so because of the nature of the inertial velocity field which is a complicated function of α and λ .

4.5.2 Bifurcated wake regime

As we saw in chapter 2, there exists a bifurcated wake regime in which the wake exists at an intermediate location between the poles and equator (see Fig. 4.5). The bifurcated wake regime occurs for $\alpha < \alpha_{bif}$ and $\lambda_c < \lambda < \lambda_{bif}$. Denoting the C orbit where the wake occurs as C^* , we now have two convective branches (I and II) in each hemisphere of the drop (see Fig. 4.5). In the first, the fluid spirals from the pole towards the equator, before exiting at the wake location C^* . In the second branch, the spiralling causes a drift from the equator towards the poles with the outlet again at C^* . The Nusselt number is therefore the sum of contributions from each of these branches. The τ integral remains identical to the single-wake case. Thus, starting from

Eq. 4.82 we have, for the case of a bifurcated wake:

$$Nu = \frac{Re^{1/2} Pe^{1/2}}{\pi^{3/2}} \left[\int_0^{C^*} dC \frac{1}{g_I(C)} \frac{\mathcal{D}(C)C\gamma}{(1+C^2\gamma^2)^{3/2}} + \int_{C^*}^{\infty} dC \frac{1}{g_{II}(C)} \frac{\mathcal{D}(C)C\gamma}{(1+C^2\gamma^2)^{3/2}} \right], \quad (4.87)$$

where

$$g_I(C) = \left[\frac{4(1+C^2\gamma^2)^3}{\mathcal{B}(C)^2 C^2} \mathcal{I}_I(C) \right]^{1/2}, \quad (4.88)$$

$$\mathcal{I}_I(C) = \int_0^C \frac{\mathcal{D}(C')\mathcal{B}(C')^2 C'^2}{(1+C'^2\gamma^2)^3} dC', \quad (4.89)$$

$$g_{II}(C) = \left[\frac{4(1+C^2\gamma^2)^3}{\mathcal{B}(C)^2 C^2} \mathcal{I}_{II}(C) \right]^{1/2}, \quad (4.90)$$

$$\mathcal{I}_{II}(C) = \int_{\infty}^C \frac{\mathcal{D}(C')\mathcal{B}(C')^2 C'^2}{(1+C'^2\gamma^2)^3} dC'. \quad (4.91)$$

Substituting in the expression for the Nusselt number and carrying out the integration as before, we get:

$$Nu = \frac{Re^{1/2} Pe^{1/2} \gamma}{\pi^{3/2}} \left[\mathcal{I}_I(C^*)^{1/2} + \mathcal{I}_{II}(C^*)^{1/2} \right], \quad (4.92)$$

$$Nu = \frac{Re^{1/2} Pe^{1/2} \gamma}{\pi^{3/2}} \left[\left(\int_0^{C^*} \frac{\mathcal{D}(C)\mathcal{B}(C)^2 C^2}{(1+C^2\gamma^2)^3} dC \right)^{1/2} + \left(\int_{\infty}^{C^*} \frac{\mathcal{D}(C)\mathcal{B}(C)^2 C^2}{(1+C^2\gamma^2)^3} dC \right)^{1/2} \right]. \quad (4.93)$$

The location of the neutral curve C^* , which is the location of the thermal wake from a heat transfer perspective, was derived in chapter 2. The variation of C^* with λ in the bifurcated wake regime is depicted in Fig. 2.14 in chapter 2. At a fixed $\alpha < \alpha_{bif}$, for λ close to λ_c , we have the wake near the poles corresponding to C^* close to zero (the inertia flow now having predominantly a uni-axial character), so that the first term in 4.93 has a small contribution to the heat transfer. As the viscosity ratio is further increased the value of C^* increases and we have contributions to the heat transfer from both the convective branches. As one approaches $\lambda = \lambda_{bif}$, the value of C^* is very large and the contribution from the second term in 4.93 diminishes and finally for $\lambda \geq \lambda_{bif}$, the wake is at equator and we recover the single wake regime. We remark here that the bifurcated wake region is a finite one and is depicted in (α, λ) space in Fig. 4.6 (inset). We also have a single wake regime with the wake at the equator for $\alpha > \alpha_{bif}$ and any λ .

4.5.3 Discussion

Fig. 4.6 shows the variation of the prefactor multiplying the scaling term $Re^{1/2} Pe^{1/2}$ with α and λ in both the single and bifurcated wake regimes. The part of the Nu -prefactor-surface plotted corresponds to the closed streamline region, where inertia plays a critical role ($\lambda > \lambda_c$). The strong dependence of the prefactor on γ is clearly noticeable as we approach the λ_c curve since γ increases as one approaches λ_c . However, as we commented previously, it is not possible in this case to isolate an effective Pe such that the remaining Nu prefactor is a sole function of γ , as we did in the open streamline case. In the closed streamline regime, the complicated nature

of the inertial velocity field leads to a complicated dependence of the Nu prefactor on α and λ .

In the bifurcated wake region ($\alpha < \alpha_{bif}$ and $\lambda < \lambda_{bif}$) we see a minimum in the Nu -prefactor-surface (see Fig. 4.6). This appears to be due to the presence of the bifurcated wake, where a greater area of the drop surface is occupied by the wake region consisting of slowly moving fluid, thereby making the heat transfer less efficient. This can be shown by considering the scaling of the τ -averaged tangential inertial velocity component $u_C^{(1)}|_{\tau\text{-averaged}} = \int_0^{2\pi} u_C^{(1)} d\tau$ near the plane of symmetry ($C \rightarrow \infty$). This scaling can be estimated from the scaling of $\mathcal{B}(C)$ by noting that the metric factor $h \sim O(1/C^2)$ as $C \rightarrow \infty$. Thus $u_C^{(1)}|_{\tau\text{-averaged}} \sim \mathcal{B}(C)/C^2$. Using this, we find that:

$$u_C^{(1)}|_{\tau\text{-averaged}} \sim O(1/C) \quad \text{for } \lambda > \lambda_{bif},$$

while

$$u_C^{(1)}|_{\tau\text{-averaged}} \sim O(1/C^3) \quad \text{for } \lambda \rightarrow \lambda_{bif}.$$

This means that the tangential velocity near the wake ($C \rightarrow \infty$) falls away asymptotically faster in the vicinity of the curve $\lambda = \lambda_{bif}$ compared to $\lambda > \lambda_{bif}$. This is depicted in Fig. 4.7, where the term $\mathcal{B}(C)/C^2$ is plotted as a function of $1/C$. We find that the tangential velocity near the wake ($C \rightarrow \infty$ and $1/C \rightarrow 0$) is indeed smaller when we are near $\lambda = \lambda_{bif}$. This explains the minimum observed in the Nu -prefactor-surface (plotted in Fig. 4.6) in the vicinity of the $\lambda = \lambda_{bif}$ curve.

Fig. 4.8 shows the Nu prefactor to $Pe^{1/2}$ in both the open and closed streamline regimes. The Reynolds number in the closed streamline regime is chosen to be $Re = 0.1$. The kink in the surface near $\lambda = \lambda_c$ approaching from the closed-streamline regime is clearly visible. This is due to the divergence of the prefactor as $O(\gamma)$ as $\gamma \rightarrow \infty$ near $\lambda = \lambda_c$. Although not present in the Stokesian estimate (see Eq. 3.67 in chapter 3, a similar divergence is expected in the open streamline side when the $O(Re)$ correction terms are added to the analysis. The reasons for the breakdown of our analysis close to $\lambda = \lambda_c$ will be considered in section 4.6. Thus, we see that the leading order analyses in the open and closed streamline regimes fails to predict a smooth connection between these regions. This motivates us to study the intermediate regime corresponding to a thin band of viscosity ratios close to $\lambda = \lambda_c$ to better understand the connection between the portions of the Nu -surface corresponding to the two regimes.

4.6 The intermediate regime

In chapter 3, we looked at the flow topology and heat transfer in the open streamline regime ($\lambda < \lambda_c$). In this regime, we found that the Stokes velocity field was the main agent of convective heat transfer with inertia having only a perturbative effect, so that the Nusselt number scaled as $Nu \sim Pe^{1/2}$ for $Pe \gg 1$. On the other side of the critical curve ($\lambda > \lambda_c$), we saw that the Stokes streamlines were closed orbits, incapable of transporting heat from the drop, leading to a Nusselt number that is independent of Pe for $Pe \gg 1$. Addition of a small amount of inertia, however, fundamentally modified the nature of the closed streamlines. Inertia opens

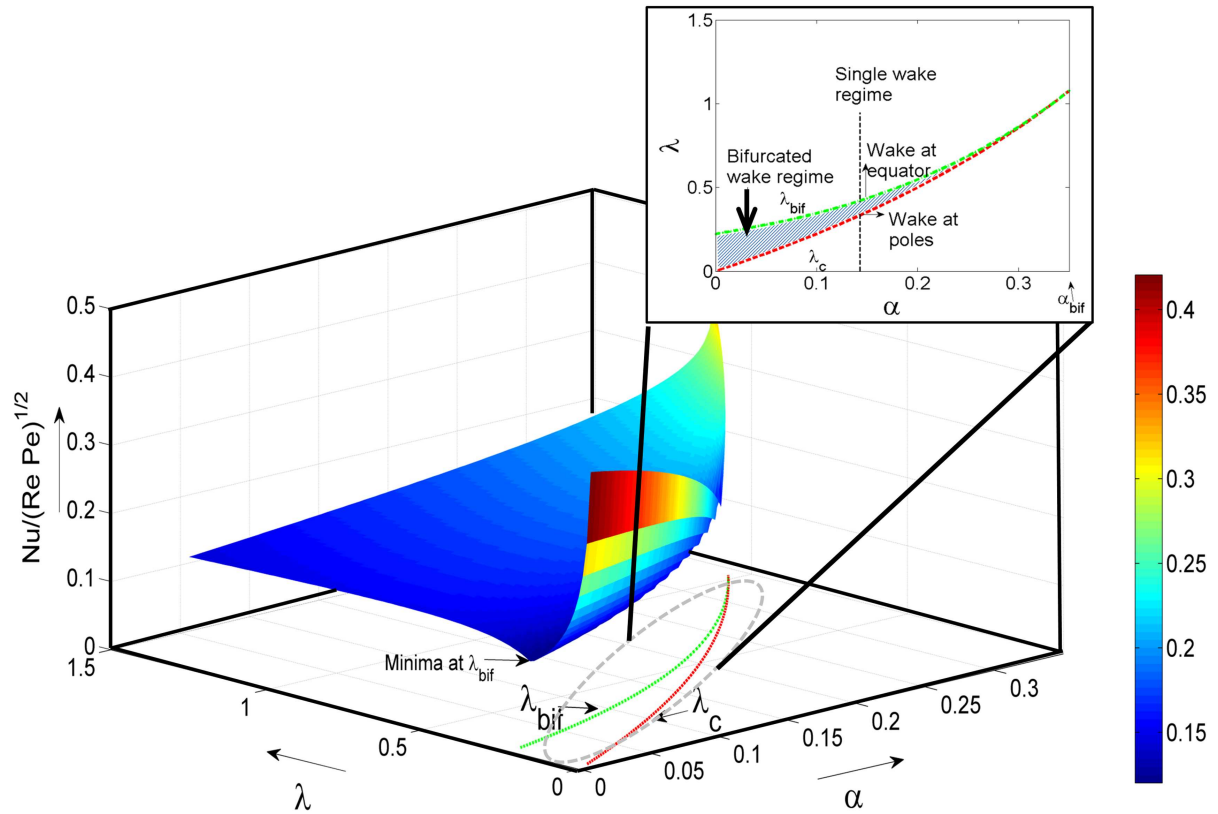


Figure 4.6: A surface plot of the prefactor multiplying the scaling factor $Re^{1/2} Pe^{1/2}$ to give the Nusselt number. Note that the surface is plotted in the region $\lambda > \lambda_c$ on the (α, λ) plane corresponding to the closed streamline regime with inertia. The scaling with γ is clearly visible with the prefactor increasing with increasing γ (as one approaches the λ_c curve). The inset shows an expanded view of the bifurcated wake regime (shaded portion). α_{bif} and λ_{bif} serves as the upper bounds below which we see the bifurcated wake regime for $\lambda > \lambda_c$.

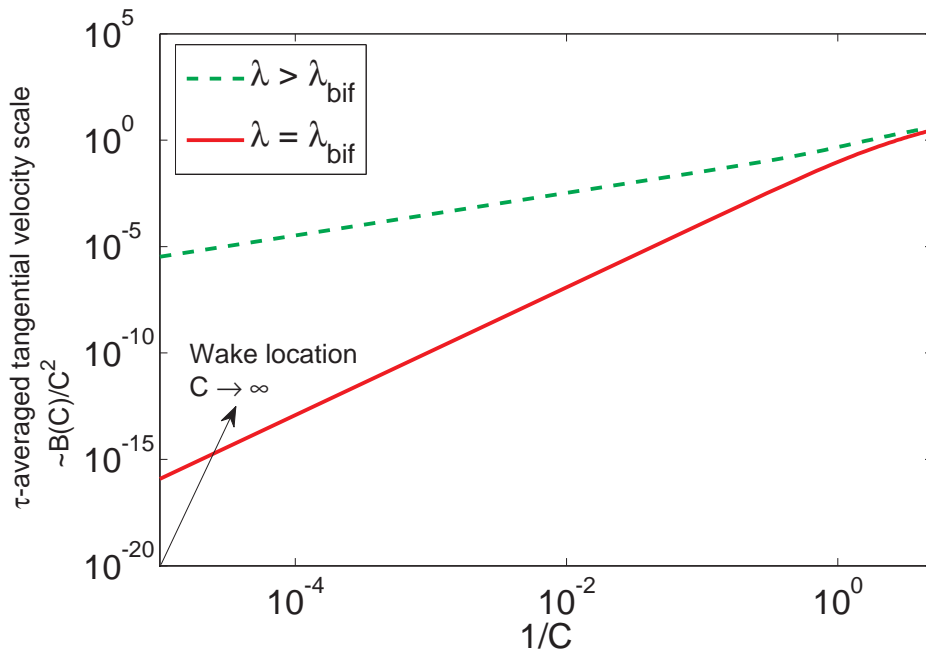


Figure 4.7: Plot of the tangential velocity scale as a function of the inverse of the orbit constant C .

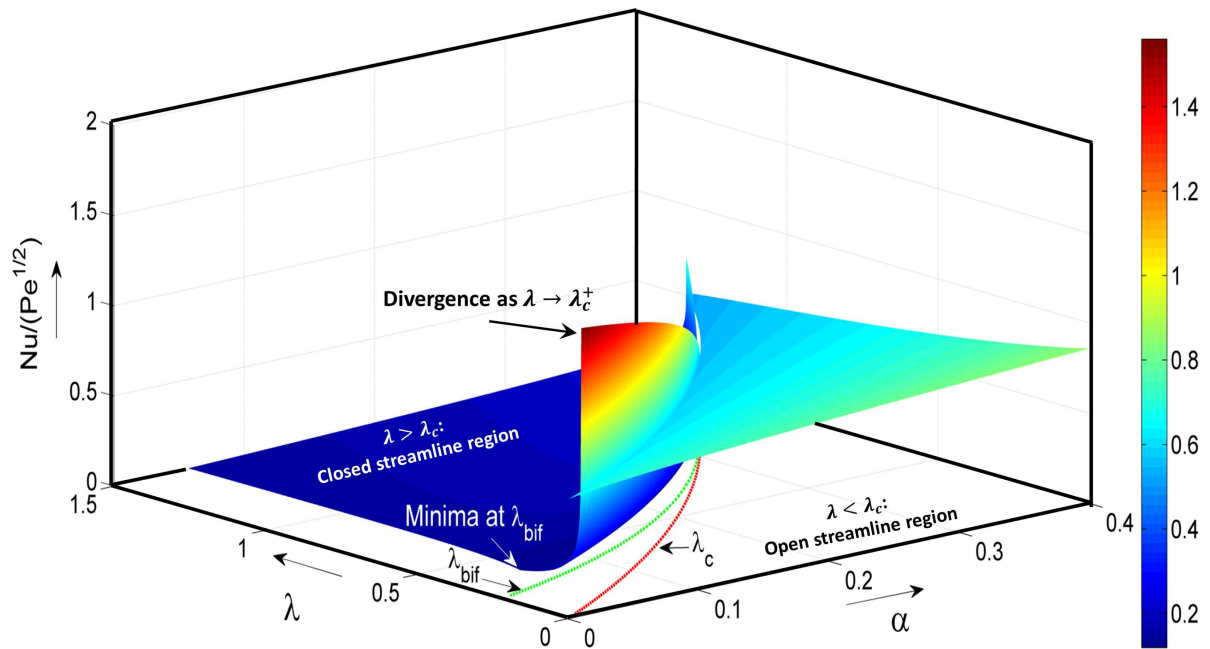


Figure 4.8: A surface plot of the prefactor multiplying the scaling factor $Pe^{1/2}$ to give the Nusselt number in the open and closed streamline regimes for $Re = 0.1$. Notice the kink in the surface due to the divergence of the Nu predicted close to the $\lambda = \lambda_c$ curve from the closed streamline side.

up convective channels, causing the Nusselt number to scale as $Re^{1/2} Pe^{1/2}$ for $RePe \gg 1$. In this case, the convective enhancement of heat transfer was due to the $O(Re)$ inertial velocity field. We now analyse what we call the “intermediate regime” ($\lambda \rightarrow \lambda_c$), where both the Stokes and inertial velocity fields are comparable in certain regions on the drop surface. While the $\lambda = \lambda_c$ curve can be approached from either the open-streamline or closed-streamline sides, we consider here first the approach from the closed-streamline side. We look at the flow topology near the critical viscosity ratio curve and then move on to making scaling estimates for the heat transfer. We find that this scaling analysis allows us to define the regions of validity for our open streamline and closed streamline heat transfer analyses. In particular, a scaling analysis of the intermediate regime allows us to understand the connection between the open and closed streamline regimes across the critical viscosity curve as regards the heat transfer. To reiterate, such an understanding is essential because the leading order analysis in the two regimes fails to predict a smooth transition across $\lambda = \lambda_c$.

4.6.1 Flow topology for $\lambda \rightarrow \lambda_c$

It is instructive to first study the flow topology without inertia. Fig. 4.9 shows the surface streamlines for $\lambda \rightarrow \lambda_c$. The surface streamlines in this case have a nearly meridional character, there being a radial convergence in the vicinity of the intersection of the flow axis with the unit sphere (these points serve as the ‘poles’ of the meridians). Further, the circle of fixed points in the exterior flow is now close to the drop surface. The radius of this fixed-circle, which is also the maximum radial extent of the separatrix surface is given by r_0 , and for $\lambda \rightarrow \lambda_c$, has the form:

$$r_0 - 1 \sim \frac{(\lambda - \lambda_c)(1 - \alpha)^2}{10\alpha(1 + \alpha)}. \quad (4.94)$$

Therefore, as $\lambda \rightarrow \lambda_c$, the separatrix surface lies very close to the drop surface and the extent of the closed streamline region diminishes. At $\lambda = \lambda_c$, the separatrix surface is coincident with the drop surface and there are no closed streamlines in the drop exterior. The parameter γ diverges when $\lambda \rightarrow \lambda_c$ as:

$$\gamma^2 = \frac{2(1 + \lambda_c)}{\lambda - \lambda_c} \sim O(\lambda - \lambda_c)^{-1}. \quad (4.95)$$

Using Eqs. 4.94 and 4.95, we have the scaling of the fixed-circle radius as $r_0 - 1 \sim \frac{1 - \alpha}{5\gamma^2\alpha}$. Thus, near the flow-vorticity plane, the radial extent of the closed streamline region scales as $y \sim 1/\gamma^2$. From Eq. 4.28, we see that this scaling is only valid in a $\phi \sim O(1/\gamma)$ angular region measured from the flow-vorticity plane. While this gives us the scaling of the maximum extent of the closed separatrix surface, which occurs at the flow-vorticity plane, we are also interested in the extent of the separatrix for the remaining portion of the drop (this would determine the scaling of the geometrically-limited estimate of Nu for $Pe \rightarrow \infty$). This can be inferred using the equation for the constant y_m surfaces (Eq. 4.28), of which the separatrix is radially the outermost closed surface. From Eq. 4.28, in the limit $\gamma \gg 1$, we see that scaling is indeed different for the rest of the drop and we have $y \sim y_m/\gamma^3$ for $\phi \sim O(1)$. However, we have shown that at the flow vorticity plane $y = y_m = 1/\gamma^2$, which implies that for the remaining portion of the drop we must have $y \sim 1/\gamma^5$. Thus, the extent of closed streamline region over most of the drop is

asymptotically thinner by a factor of $1/\gamma^3$, compared to the $O(1/\gamma)$ angular region near the flow-vorticity plane. Fig. 4.10 shows the extent of the closed streamline envelope on the drop surface along with the scalings. This small extent of the closed streamline region has important consequences to the heat transport which we consider in the next section.

Recalling our original observation that the surface streamlines for a drop in a linear flow are described by exactly the same equations as those describing the Jeffery orbits of an axisymmetric particle in simple shear flow (Leal & Hinch (1971), Hinch & Leal (1972)), we note that the limit of $\gamma \rightarrow \infty$ corresponds to the Jeffery orbits of an infinitely slender rod. The orientation of such a rod changes very quickly, on a time scale of order the inverse shear rate, when not aligned with the flow axis, while changing very slowly in the nearly aligned orientation. This is exactly true for the drop surface streamlines as $\lambda \rightarrow \lambda_c$. A given fluid element moves very rapidly between the two fixed points lying on the flow axis, while spending a large amount of time in the vicinity of the flow-vorticity plane (see Fig. 4.9). These statements can be made precise by considering the scalings for the near-field velocity along τ direction, and the coordinate metrics:

$$\left. \begin{aligned} u_\tau^{(0)} \Big|_{r \rightarrow 1} &\sim O(1/\gamma^2), \\ k &\sim O(1/\gamma) \end{aligned} \right\} \text{Near flow-vorticity plane} \quad (4.96)$$

Recalling the definition of the τ coordinate, we can write:

$$\frac{d\tau}{ds} = \frac{u_\tau^{(0)}}{k} = h_\tau^{(0)} \sim O(1/\gamma), \quad (4.97)$$

where s is the non-dimensional time. From the definition of τ in chapter 2, we see that it is $O(1)$ near the flow-vorticity plane. Therefore, we must have the time t scaling as $O(\gamma)$. Away from the flow vorticity plane, we have the following scaling relations:

$$\left. \begin{aligned} u_\tau^{(0)} \Big|_{r \rightarrow 1} &\sim O(1), \\ k &\sim O(\gamma). \end{aligned} \right\} \text{Away from flow-vorticity plane} \quad (4.98)$$

Once again $d\tau/ds \sim O(1/\gamma)$, however in this region $\tau \sim O(1/\gamma)$, leading to t being $O(1)$. Thus, a fluid element spends a time of $O(\gamma\dot{\gamma}^{-1})$ near the flow vorticity plane and a time of $O(\dot{\gamma}^{-1})$, for the rest of its orbit, where $\dot{\gamma}$ is the shear rate.

On the addition of weak inertia, the originally closed trajectories become spirals just as before. Now, however, inertia has an $O(\gamma\dot{\gamma}^{-1})$ time to act on the Stokes trajectories near the flow-vorticity plane with $\gamma \rightarrow \infty$. For Re however small, for $\gamma \rightarrow \infty$, weak inertia leads to a drift across several Jeffery orbits, close to the flow vorticity plane (since the Jeffery orbits are tightly bunched close to the flow-vorticity plane). Having crossed several Jeffery orbits, the Stokes velocity is dominant away from the flow-vorticity plane and this leads to the inertial streamline rapidly traversing the drop surface before again starting to drift on reaching the π separated flow-vorticity plane. Clearly, for Re finite and with $\gamma \rightarrow \infty$, the near-surface inertial streamlines are no longer expected to be tight spirals as was implicitly assumed in the analysis presented earlier in section 4.4.

A typical trajectory of an inertial streamline, in the intermediate regime, is shown in Fig.

4.11 for $\lambda \rightarrow \lambda_c$ in both single ($\alpha > \alpha_{bif}$) and bifurcated wake ($\alpha < \alpha_{bif}$) regimes. That the drift is across several orbits is apparent since, in a very few number of turns, the trajectory has drifted a sizeable distance on the drop surface. The following simple scaling argument confirms this. We note that the inertial velocity field scales as $O(Re)$, apart from the scaling due to other flow parameters. Writing down the scaling for the inertial velocity along C direction, near and away from the flow-vorticity plane, we have:

$$\left. \begin{aligned} u_C^{(1)}|_{r \rightarrow 1} &\sim O(Re/\gamma) \\ h &\sim O(1/\gamma) \end{aligned} \right\} \text{Near the flow-vorticity plane,} \quad (4.99)$$

$$\left. \begin{aligned} u_C^{(1)} &\sim O(Re), \\ h &\sim O(1). \end{aligned} \right\} \text{Away from the flow-vorticity plane.} \quad (4.100)$$

So that, in both regions, the drift across orbits can be written as:

$$\frac{dC}{ds} = \frac{u_C^{(1)}}{h} \sim O(Re). \quad (4.101)$$

However, since the time spent near the flow-vorticity plane is $O(\gamma)$, we must have $dC \sim O(\gamma Re)$ in this region, implying the drift occurs across a large number of orbits when one is close enough to the critical viscosity ratio such that $\gamma \sim O(1/Re)$ for $Re \ll 1$. The change in orbits in the region away from the flow-vorticity plane, remains $O(Re)$, so that these portions still look like sections of Jeffery orbits. This picture is clearly corroborated by the trajectories in Fig. 4.11. A fluid element enters the region near the flow-vorticity plane and undergoes a large shift in orbits, leaving along a trajectory which is very different from the one it entered on. The portion of the trajectory away from the flow-vorticity plane is close to an inertia-less trajectory and does not undergo any significant drift. In summary, with the addition of inertia, we have the emergence of a spatial boundary layer near the flow-vorticity plane, where the Stokes and inertial velocities are comparable. Although the above discussion has been in the context of the closed streamline regime, a similar situation prevails even on the other side of the critical viscosity ratio curve. On the open streamline side, for λ sufficiently close to λ_c , the streamline is expected to undergo a significant inertial drift after it enters and before it leaves the boundary layer on the drop surface.

4.6.2 Heat transfer in the intermediate regime

We now consider the heat transfer in the intermediate regime. The two characteristic features of this regime namely, the drift across a large number of orbits and the small extent of the closed streamline region, both restrict the validity of our heat transfer analysis presented earlier. Consideration of inertial effects enables one to explicitly see the breakdown of the analysis on the closed streamline side as $\lambda \rightarrow \lambda_c$, while seeing such a breakdown on the open streamline side requires inclusion of an $O(Re)$ correction. Therefore, a useful result of the ensuing scaling analysis is a clear idea of the regions in the (α, λ) plane where the open and closed streamline (inertial) analyses, given in earlier sections, are valid; specifically, the narrow interval of viscosity ratios around $\lambda = \lambda_c$ which requires a separate analysis. Also, we comment on the changes in

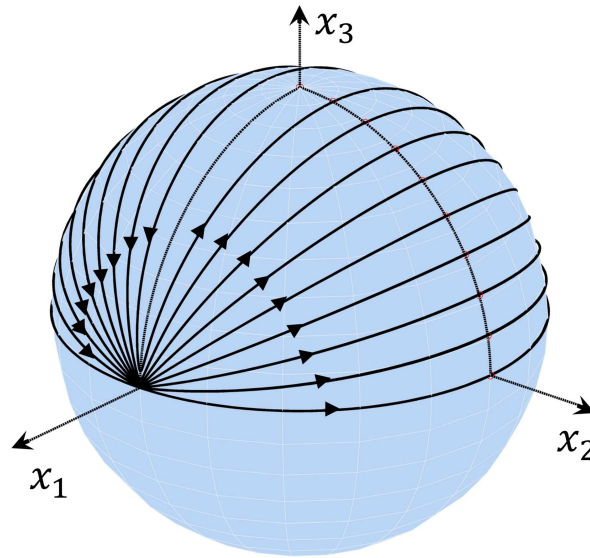


Figure 4.9: Figure showing the inertia-less Stokes streamlines on the surface of the drop in the intermediate region ($\lambda \rightarrow \lambda_c$). Here $\alpha = 0.5$ and $\lambda = 2.001$ ($\lambda_c = 2$). The streamlines have a meridional character and converge and diverge away near the flow-vorticity plane.

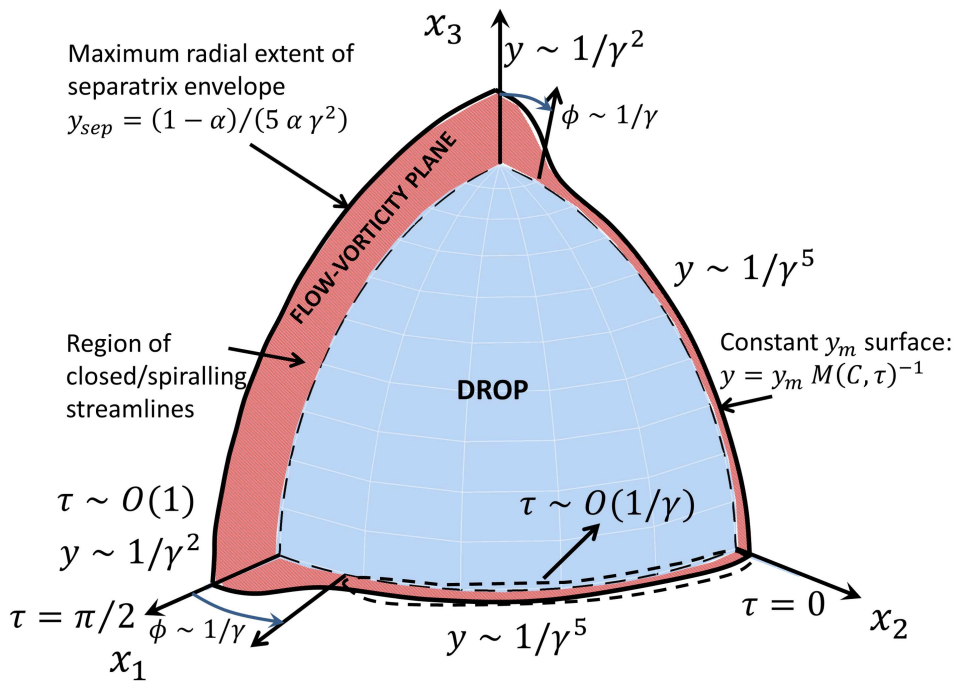


Figure 4.10: A schematic of the extent of the annular region of closed (spiralling) streamline adjacent to the drop surface in the limit of large γ (intermediate regime on the closed streamline side). The asymptotically different radial extents near the flow-vorticity plane compared to the rest of the drop region is shown. Also shown is the radial extent of the fixed-circle which gives the maximal radial extent of the separatrix surface.

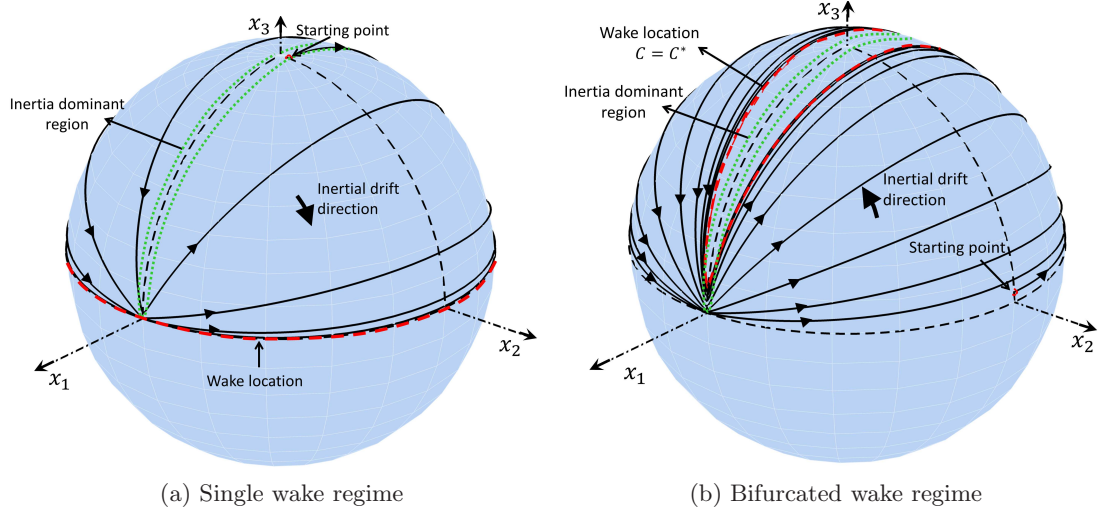


Figure 4.11: Inertial surface streamlines in the intermediate regime ($\alpha = 0.2$, $\lambda_c = 0.5$, $\lambda_{bif} = 0.547$, $Re = 0.1$) for (a) single wake ($\lambda = 0.6$) and (b) bifurcated wake ($\lambda = 0.501$) regimes. The large drift during a given turn is apparent from the small number of turns taken to drift across a large portion of the drop surface. Note the different drift direction in the two regimes even though the inertia-less streamlines in both cases have the same character (see Fig. 4.9)

the nature of the heat transport (that is, the nature of the Nu surface) as one moves from the open streamline regime, across the critical viscosity ratio curve and into the closed streamline regime.

We begin by rescaling the convection-diffusion equation, keeping in mind that γ is large. In the (y_m, C, τ) coordinate system, after the simplification due to Eq. 4.36, we have:

$$\begin{aligned}
 & \underbrace{Re \left(u_r^{(1)} \frac{\partial y_m}{\partial y} + \frac{u_C^{(1)}}{h} \frac{\partial y_m}{\partial C} + \frac{u_\tau^{(1)}}{k} \frac{\partial y_m}{\partial \tau} \right)}_1 \frac{\partial \Theta}{\partial y_m} + \underbrace{Re \frac{u_C^{(1)}}{h} \frac{\partial \Theta}{\partial C}}_2 \\
 & \quad + \underbrace{\frac{u_\tau^{(0)}}{k} \frac{\partial \Theta}{\partial \tau}}_3 + \underbrace{Re \frac{u_\tau^{(1)}}{k} \frac{\partial \Theta}{\partial \tau}}_4 = \underbrace{\frac{1}{Pe} \frac{\partial^2 \Theta}{\partial y_m^2} \left(\frac{\partial y_m}{\partial y} \right)^2}_5. \tag{4.102}
 \end{aligned}$$

For $\gamma \sim O(1)$, the term (3) was the dominant one on the LHS and this relation gave us the result that the leading order temperature field is independent of τ for large Pe . However for $\gamma \gg 1$ (relevant to the region $\gamma \gg 1$), we see that the scaling of the terms imposes further constraints. Near the flow-vorticity plane, the scalings of the different terms are:

$$\underbrace{RePe}_1 \quad \underbrace{RePe}_2 \quad \underbrace{\frac{Pe}{\gamma}}_3 \quad \underbrace{RePe}_4 \quad \underbrace{\gamma^4}_5 \quad \text{Near flow-vorticity plane.} \tag{4.103}$$

Now, for $\gamma \gg 1$, the balance between the terms is no longer obvious and depends on the relative magnitudes of γ , Re and Pe . Thus for $\gamma \ll Pe^{1/5}$ and $\gamma \ll Re^{-1}$, we have the dominance of term (3) and, in this region, we have the leading order temperature field being independent of τ . For larger values of γ , this assumption is no longer valid and there are temperature variations

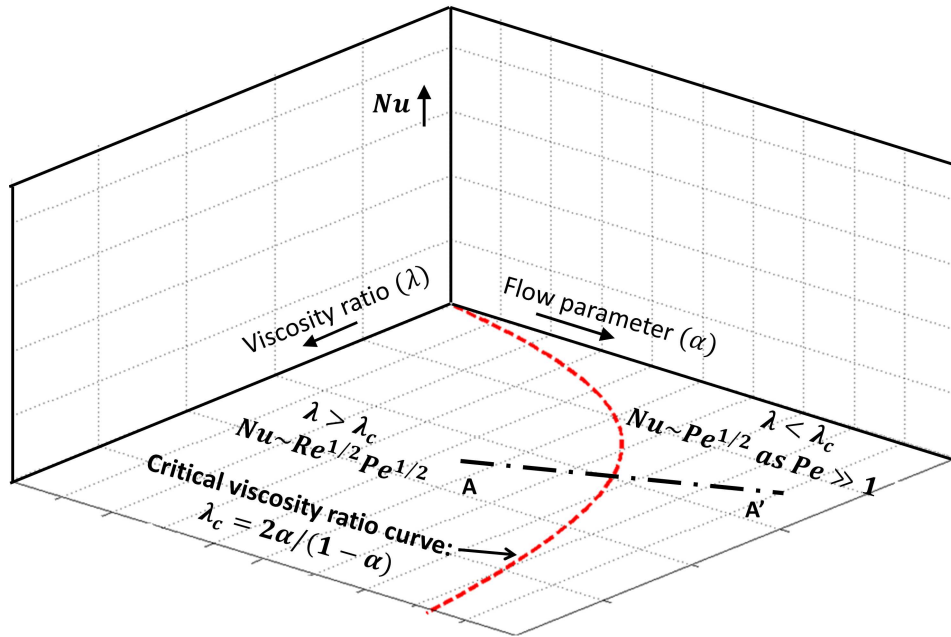


Figure 4.12: The (α, λ) plane showing the open and closed streamline regimes separated by the critical viscosity ratio curve.

even along a Stokes streamline. Away from the flow-vorticity plane, the scaling for the different terms in Eq. 4.102 are given by:

$$\underbrace{RePe}_1 \quad \underbrace{RePe}_2 \quad \underbrace{Pe}_3 \quad \underbrace{RePe}_4 \quad \underbrace{\gamma^{10}}_5 \quad \text{Away from flow-vorticity plane.} \quad (4.104)$$

This region places a stricter constraint on the values of γ for which our analysis is valid. For term (3) to be dominant, we have the relation $\gamma \ll Pe^{1/10}$ and $Re \ll 1$. We note that in this region, the constraint related to Re is not strict since as we have shown, inertia is mainly dominant in a thin region near the flow-vorticity plane.

A second assumption implicit in our heat transfer calculation is that the thermal boundary layer due to inertial convection is the dominant resistance to the heat transfer. In other words, most of the temperature drop is assumed to occur across the thermal boundary layer. However, in the intermediate regime, we have seen that the radial extent of the closed streamline region is asymptotically small (scaling as $O(1/\gamma^5)$ for most of the drop). Thus, the restriction that the thermal boundary layer be much thinner than the already thin closed (or spiralling) streamline region becomes increasingly restrictive. For the extent of the thermal boundary layer to be much smaller than the extent of closed streamlines over most of the drop, we must therefore have $Re^{-1/2} Pe^{-1/2} \ll 1/\gamma^5 \ll 1/\gamma^2$. Rewriting, this gives the condition that $\gamma \ll (RePe)^{1/10}$. Therefore for our analysis to be valid in the closed streamline region, we have the constraint $\gamma \ll (RePe)^{1/10}$, which also ensures $\gamma \ll Pe^{1/10}$ and for small Re , $\gamma \ll Re^{-1}$.

Having described the region of validity of analysis in the closed streamline region, we now consider the nature of the connection between the open and closed streamline regimes across the critical viscosity curve (λ_c).

4.6.3 Connecting the Nu -surface across the open and closed streamline regimes

We saw in Fig. 4.8, that the Nu -surface, obtained from the leading order analysis, exhibits a discontinuity along the critical viscosity curve. This is because of the divergence of Nu as $O(\gamma)$ for $\lambda \rightarrow \lambda_c$ from the closed streamline side. The open streamline analysis is also expected to develop a similar divergence if $O(Re)$ correction terms are included in the analysis. However, physically, there must exist a smooth connection between these two regimes. In this section, we attempt, via a scaling analysis, to connect the Nu surfaces in the open and closed streamline regimes across the $\lambda = \lambda_c$ curve.

Consider a path AA' on the (α, λ) plane which starts from the open streamline side of the critical viscosity ratio curve, crosses this curve and ends inside the closed streamline regime (see Fig. 4.12). Starting from the open-streamline side, the parameter $\hat{\gamma}$ increases, as we approach λ_c , as $\hat{\gamma} \sim (\lambda_c - \lambda)^{-1/2}$, becoming infinite at λ_c . Once we cross λ_c , the parameter in the closed streamline region is γ , which decreases from infinity at λ_c as $\gamma \sim (\lambda - \lambda_c)^{-1/2}$. We now consider various asymptotic regimes of the parameters $\hat{\gamma}$ and γ in the open and closed streamline regimes, respectively, to better understand the transition of the Nu -surface.

- $\hat{\gamma} \sim O(1)$ ($\hat{\gamma} \ll 1/Re$): The original open streamline analysis (chapter 3) is valid.
- $\hat{\gamma} \gg 1$ and $\infty \gg \gamma \gg Pe^{1/4}$: We are in a thin region near the $\lambda = \lambda_c$ curve, where inertial effects are expected to play a role even in the open streamline regime. As in the closed streamline case, inertia is dominant near the flow-vorticity plane and causes a given streamline to drift by a sizeable amount before moving across the drop surface towards the wake. However, most of the temperature drop still occurs across a thermal boundary layer whose thickness scales as $Pe^{-1/2}$, leading to the Nusselt number scaling as $Pe^{1/2}$; although the prefactor is no longer given by the analysis in chapter 3, since inertia modifies the open streamline geometry. Continuing across the $\lambda = \lambda_c$ curve, very close to λ_c on the closed streamline side, the radial extent of the closed(spiralling, with inertia) streamlines is very small everywhere on the drop and is also smaller than the thermal boundary layer. This corresponds to the scaling $1/\gamma^2 \ll Pe^{-1/2}$, which gives $\gamma \gg Pe^{1/4}$, where $1/\gamma^2$ is the maximum radial extent of the separatrix envelope (see section 4.6.1 and the scaling estimates therein). Note that, with this condition, we automatically have that the closed(spiralling) streamline extent in the region away from the flow-vorticity plane, which scales as $1/\gamma^5$, is also asymptotically thinner compared to the boundary layer. Diffusion is dominant on the length scale of the spiralling streamline envelope, which is therefore at practically the same temperature as the drop surface. The outer extent of the spiralling streamline region can be thought of as a new isothermal surface whose temperature is very close to T_0 . This surface, which envelopes the drop surface very closely, is accessed by open streamlines, so that the controlling resistance is still in the open streamline thermal boundary layer, and we expect a Nusselt number scaling as $Pe^{1/2}$, again with the inertia-modified prefactor mentioned above.
- $\gamma \ll Pe^{1/4}$ and $\gamma \gg Pe^{1/10}$: Diffusion is dominant for most of the drop surface except for a thin region near the flow-vorticity plane. The transport in this region involves a balance

of Stokes convection and diffusion thus making the temperature distribution and the heat transfer analysis complicated in this region. Due to the small extent of this region, which is only $\phi \sim O(1/\gamma)$, the controlling resistance to the heat transfer is still in the $O(Pe^{-1/2})$ boundary layer for most of the drop and therefore Nu is expected to scale as $Pe^{1/2}$ in this regime as well.

- $\gamma \ll Pe^{1/10}$ and $\gamma \gg (RePe)^{1/10}$: In this regime, the spiralling streamline envelope everywhere on the drop is asymptotically larger than the $O(Pe^{-1/2})$ boundary layer thickness. Indeed, the concept of an $O(Pe^{-1/2})$ boundary layer here ceases to have relevance since it has receded within the spiralling streamline envelope. The condition that $\gamma \gg (RePe)^{1/10}$ means that this diffusion time scale is much smaller than the time scale for inertial convection. Thus, this is a geometrically limited regime where the resistance to the heat transfer is due to diffusion across a closed (spiralling) streamline envelope in the presence (absence) of inertia; as first analyzed by Acrivos and co-workers. The precise geometrical limited Nu value requires a calculation along the lines of Yu-Fang & Acrivos (1968), who carried out the analysis for a cylinder freely rotating in a shear flow in the absence of inertia. A scaling estimate for large γ can be obtained as follows. The value of y_m corresponding to the separatrix surface can be calculated by using the maximum extent of the separatrix surface which occurs at the flow-vorticity plane, and noting that $y = y_m$ here (see Fig. 4.10). This gives from Eq. 4.94:

$$y_m = \frac{(1 - \alpha)}{5\alpha\gamma^2}, \quad (4.105)$$

so that the equation of the separatrix surface is (using Eq. 4.28):

$$y_{sep} = \frac{(1 - \alpha)}{5\alpha\gamma^2} M(C, \tau)^{-1}. \quad (4.106)$$

The Nusselt number can therefore be approximated by:

$$Nu \approx \frac{1}{4\pi} \int_S \frac{hk \sin \alpha_1}{y_{sep}} dC d\tau, \quad (4.107)$$

where S denotes the surface area of the drop. This expression implicitly assumes that the temperature varies linearly through the closed streamline envelope from T_0 on the drop to T_∞ at the separatrix. Only when such a functional form for the temperature difference is specified can the Nu be related to the inverse thickness in the manner shown above. The linearity above ensures that the temperature gradient everywhere within the closed streamline region is the same, and in particular, equal to its surface value. Physically, the above integral is the surface average of the inverse thickness of the closed streamline region over the unit sphere. Writing in terms of the C and τ limits and substituting for y_{sep} and the metric factors, we have:

$$Nu \approx \frac{5\alpha\gamma^3}{2\pi(1 - \alpha)} \int_0^\infty dC C (1 + C^2\gamma^2)^{3/2} \int_0^{2\pi} d\tau \frac{1}{[1 + C^2(\cos^2 \tau + \gamma^2 \sin^2 \tau)]^3}. \quad (4.108)$$

Carrying out the integration one finds (using Eq. 4.95) that:

$$Nu \approx \frac{5\alpha\gamma^5}{4(1-\alpha)}. \quad (4.109)$$

Thus, we see that it is the $O(1/\gamma^5)$ scaling of the spiralling streamline envelope which provides the leading order scaling for the Nusselt number. This is expected since for large γ , the separatrix surface over most of the drop surface has y_{sep} scaling as $O(\gamma^5)$, while an $O(1/\gamma)$ regions has y_{sep} scaling as $O(1/\gamma^2)$ (see section 4.6.1) implying that the former region contributes to the heat transfer at leading order.

- $\gamma \ll (RePe)^{1/10}$ and $\gamma \ll Re^{-1}$: All the assumptions implicit in our inertial heat transfer analysis, given earlier in this chapter, are satisfied. The thermal boundary layer due to inertial convection is much thinner than the extent of spiralling streamlines and is the dominant resistance to the heat transfer. While this seems rather restrictive, we note the scaling analysis above is in the limit of large γ .

In light of the small exponents (1/10) obtained via the above scaling arguments, the above regimes will appear in a well separated manner only if Pe is unrealistically large. So, the scenario we have painted will hold only in theory, and in practice, many of these regimes will no longer be well separated.

Chapter 5

Conclusions and Future Work

In this part of the thesis we have studied the rate of convective heat or mass transfer from neutrally buoyant drops in shearing flows. We have solved the heat transfer problem and derived the dimensionless heat transfer rate (Nusselt number) for a drop in a fairly general set of ambient linear flows. We have also elucidated the significant role played by weak inertia towards the transport in one region of the parameter space (corresponding to the closed-streamline regime), and have obtained a solution to the heat transfer problem for this case. To do this we have made use of a novel non-orthogonal coordinate system, leading to major simplifications and an elegant method of solution.

As we have shown, in chapter 2, the flow field for drops has several distinguishing features when compared to the case of solid particles. We first considered drops freely suspended in a one-parameter family of planar linear flows defined by the parameter α . For this case solid particles are surrounded by a region of closed streamlines for any finite amount of vorticity in the ambient flow. However, for drops we showed that closed streamlines exist only when the ratio of drop to ambient fluid viscosity (λ) exceeds a critical value $\lambda_c = 2\alpha/(1 - \alpha)$. There exists a second critical viscosity ratio given by $\lambda'_c = 5\alpha + 1/(2(1 - \alpha))$, which affects the topology of the interior streamlines and therefore does not affect the external heat transfer. In chapter 2, we studied the flow field interior and exterior to a drop in a planar linear flow in detail and derived the equations for the streamlines. For the surface streamlines, we have the interesting result that these are Jeffery orbits. This latter terminology was originally used to describe the trajectories of an axisymmetric rigid particle in a linear flow and the shape of the orbits is defined by an effective aspect ratio related to the actual aspect ratio. In the case of a drop in a planar linear flow, the surface streamlines are Jeffery orbits defined by an aspect ratio (γ) which is a function of the parameters α and λ . Rather intuitively, we find that this aspect ratio is purely imaginary in the open streamline regime since the trajectories on the drop surface are not true orbits. For the closed streamline regime, the surface trajectories are true orbits, and as expected, γ is real. This insight into the nature of the surface streamlines allowed us to define a non-orthogonal (C, τ) coordinate system, where C is the orbit constant and τ is the phase along each orbit; this coordinate system is used for the subsequent heat transfer analysis. With the addition of weak inertia, the flow field for the closed streamline regime shows a fundamental change with closed Stokesian streamlines transformed into finite- Re spiralling ones. These streamlines spiral towards a neutral curve (constant- C curve) lying on the drop surface at which point fluid elements move radially away from the drop. From a heat transfer perspective, this neutral curve corresponds to the location of the thermal wake on the drop surface. While the wake brackets the plane of symmetry over most of the (α, λ) , we also find a novel bifurcation, where this wake is lifted off the plane of symmetry for a certain region on the (α, λ) plane.

For planar linear flows, the open and closed streamline regimes identified in chapter 2 lead to

fundamentally different transport characteristics. At large Pe , the transport is diffusion limited in the closed streamline regime in the absence of inertia, while being convectively enhanced in the open streamline regime. In chapter 3 we considered the open streamline heat transfer problem. Recasting the problem in the (C, τ) coordinate system, which is complex-valued in this case, leads to major simplifications in the analysis and allowed us to derive a closed-form solution. We find that the Nusselt number for this case was given by $Nu = \mathcal{F}(\alpha, \lambda)Pe^{1/2}$, where $\mathcal{F}(\alpha, \lambda)$ is given in closed form. We have also extended our method to solve the heat transfer problem for a drop in a three-dimensional extensional flow which again involves open streamlines adjacent to the drop. The (C, τ) coordinate system may be defined for an arbitrary linear flow, and for the three-dimensional extensional flow, use of such a coordinate system leads to a Nusselt number of the form $Nu = \mathcal{G}(\epsilon)Pe^{1/2}/(1 + \lambda)^{1/2}$, where $\epsilon = E_2/E_1$, and E_1 and E_2 define the principal rates of strain for the extensional flow. This allowed us to validate our results against earlier work for axisymmetric and planar extensional flow which are specific cases of our general analysis. Though we do not include it as part of this thesis, we mention here that our approach is readily extendable to the case of a solid particle, and yields the same results as those obtained by Batchelor (1979) using an orthogonal coordinate system.

In the closed streamline heat transfer problem considered in chapter 4, the addition of inertia opens up new convective channels via the spiralling streamlines. We have developed a methodology to analyse convection, due to spiralling streamlines, in a modified version of the (C, τ) coordinate system developed for the open streamline analysis, one with a real-valued aspect ratio. The method relies on the separation between the time scales characterizing the rapid motion (nearly) along a Jeffery orbit, and the slow drift across Jeffery orbits (caused by the spiralling), and allows for the boundary layer analysis to be formulated in terms of a Jeffery-orbit-averaged convection. Further, we show that using a physically intuitive coordinate system, where the analogue of the radial coordinate corresponds to non-circular isothermal streamlines, leads to a crucial simplification of the analysis allowing us to proceed towards a closed-form solution. The three-dimensional, non-axisymmetric problem was simplified to a one-dimensional one using our method. In the limit where the inertial convection dominates diffusion ($RePe \gg 1$), we find the Nusselt number to have the form $Nu = \mathcal{H}(\alpha, \lambda)Re^{1/2}Pe^{1/2}$, where $\mathcal{H}(\alpha, \lambda)$ is given in closed form. Finally, we examined, via scaling arguments, the so-called intermediate regime for λ near λ_c , for which there are regions on the drop surface near the flow-vorticity plane where the inertial and Stokes velocities are comparable. The analysis of the intermediate region mainly lets us define the regions of validity of our asymptotic solutions presented above.

The theoretical results from this thesis provide a good starting point for estimating heat transfer in suspensions of drops, due to convective effects, which was lacking until now. Our results for the heat transfer in the limits of either the open-streamline or closed (or spiralling) streamline regions contributing dominantly to the external resistance provides the tools to understand general heat transfer problems which may involve the boundary-layer-resistance spread across regions of both open and closed streamlines. This thesis has opened up several avenues for further work a few of which we list below

1. Experiments and numerical simulations which test the validity of the above theory would

be invaluable in providing a firm foundation for estimating heat transfer from drops in more complex real world applications.

2. While this thesis has considered the case where the resistance to heat transfer is in the region exterior to the drop, the resistance may also lie mainly in the interior region, or may be distributed across both the interior and exterior regions. The insights into the interior streamline topology from this thesis may serve as starting point for analysing heat transfer when the majority of the resistance is in the drop interior.

Part II

Simulation of Collective Motion in Micro-scale Swimmers

Chapter 6

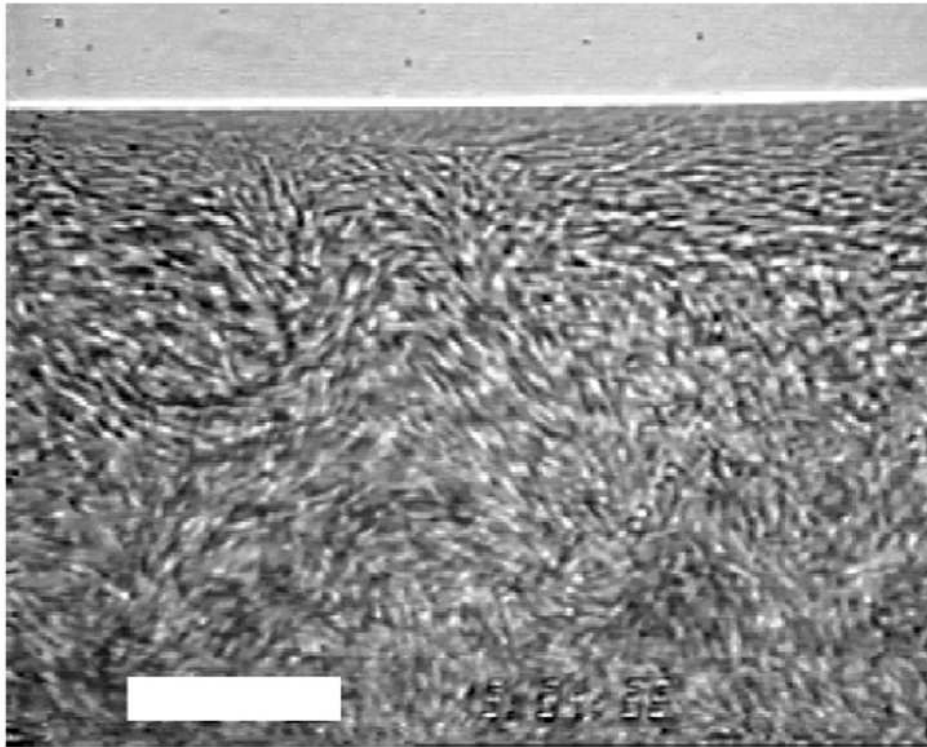
Introduction

The study of swimming microorganisms has, for a long time, been a fascinating field of research in fluid mechanics and transport phenomena. The early research in this field was largely focussed on the detailed mechanism of swimming of such organisms, given the constraints imposed by a low Reynolds number ambient (Gray & Hancock (1955), Gray (1958) Brennen & Winet (1977)). Single swimmer kinematics continues to be an area of interest (Lauga & Powers (2009)). More recently, a great deal of interest has been generated in this field due to observations in experiments of ‘collective behaviour’, especially in dense suspensions of swimming bacteria¹. Experiments with suspensions of *E. Coli* and *Bacillus Subtilis*, for example, have revealed large scale fluid motions in the form of vortices and jets (see Fig. 6.1); the relevant scales being much larger than the size of individual organisms (Mendelson *et al.* (1999), Sokolov *et al.* (2007), Dombrowski *et al.* (2004), Cisneros *et al.* (2011), Dunkel *et al.* (2013)). Other phenomena include swimming speeds much greater than that of an isolated swimmer (Sokolov *et al.* (2007)), enhanced swimmer and tracer diffusivities (Wu *et al.* (2006), Wu & Libchaber (2000)) and efficient fluid mixing. These observations have generated a great deal of interest in these so-called ‘active suspensions’, and have led to a number of theoretical and computational investigations. The interested reader is referred to review articles by Koch & Subramanian (2011), Subramanian & Nott (2012) which provide a summary of these works in the specific context of microorganism suspensions. Note that there are articles which offer a more general viewpoint wherein bacterial suspensions are only one realization of active matter (Ramaswamy (2010)). In this chapter, we briefly survey earlier experimental, theoretical and computational efforts relevant to suspensions of micro-scale swimmers (such as bacteria and algae) in the specific context of the above mentioned collective behaviour. We then move on to motivations for the current work and the questions we seek to address in this thesis.

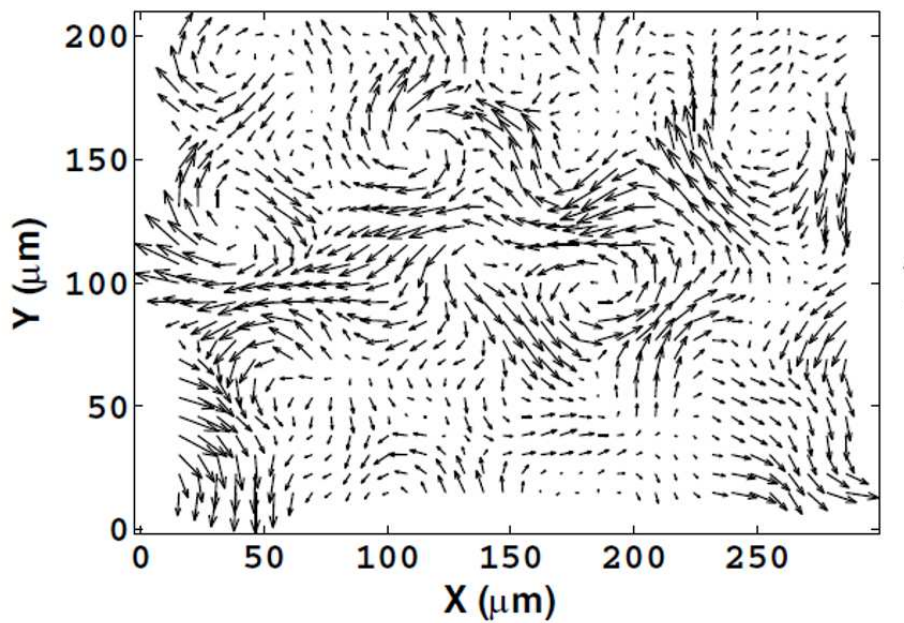
6.1 Experimental Work

The earliest experiments relevant to collective behaviour were by Mendelson *et al.* (1999) who studied a thin liquid film of the bacterium *Bacillus Subtilis* on an agar surface. They observed correlated cell motions as well as vortices and jets in the fluid indicating collective motion of the swimmers on larger length scales. The correlation was seen to extend over length scales of 10 – 100 μ m which is much larger than the length scale of an individual bacterium (length $\approx 4\mu$ m). While the experiments by Mendelson *et al.* (1999) involved swimming near a boundary, Wu & Libchaber (2000) were first to report collective motion in the absence of a nearby solid boundary. These experiments were performed with bacterial suspensions of *E. Coli* in a thin

¹Coherent motion in swimmer suspensions also arises on length scales much larger than those relevant to this work, for instance, due to the effects of gravity; this is referred to as ‘bio-convection’ (Hill & Pedley (2005)).



(a)



(b)

Figure 6.1: Experimental observations of collective behaviour. (a) Collective motion on a sessile drop containing a suspension of *Bacillus subtilis*. (b) Instantaneous flow pattern in a plane of the drop. Reproduced from [Dombrowski *et al.* \(2004\)](#).

soap film with colloidal beads used to study the transport properties. It was found that the long-time diffusivities of these beads immersed in the bacterial bath, was much larger than their Brownian diffusivities ($0.1\mu\text{m}^2\text{s}^{-1}$). The bead diffusivity was also found to increase linearly with the bacterial concentration reaching a peak value of $100\mu\text{m}^2\text{s}^{-1}$ at an $nL^3 \approx 90$, where n and L are the number density and length of the bacterium respectively. Another set of experiments performed with *B. Subtilis* in a soap film was that of [Sokolov *et al.* \(2007\)](#), in which they studied velocities and orientations of the bacteria. They find that the root-mean-square velocity of the bacteria increased smoothly with the number of bacteria per unit area. Also, the fluid velocity correlation length was found to sharply increase from $5\mu\text{m}$ to around $20\mu\text{m}$ at a density of $\rho \approx 0.3$. The authors emphasized the role of hydrodynamic interactions in the origin of collective behaviour.

A second set of experiments have observed collective motion in three-dimensional fluid domains. These studies have looked at bacteria swimming in both sessile and pendant drops ([Dombrowski *et al.* \(2004\)](#), [Tuval *et al.* \(2005\)](#)), and in cylindrical microfluidic wells ([Leptos *et al.* \(2009\)](#), [Wu *et al.* \(2006\)](#), [Dunkel *et al.* \(2013\)](#)). It is important to note that the size of these domains which range from $150 - 1500\mu\text{m}$ are small enough to exclude buoyancy effects (important in the phenomenon of bio-convection discussed above) but still large enough to leave individual bacterial motions unconfined. [Wu *et al.* \(2006\)](#), in particular, measure the diffusivity of *E. Coli* as a function of the bacterial concentration. They find that the diffusivity increases in the dilute limit from $50\mu\text{m}^2\text{s}^{-1}$ to $100\mu\text{m}^2\text{s}^{-1}$ at $nL^3 = 0.18$, this increase was attributed to the emergence of collective motion in the swimmer suspension. Interestingly, they also find that this increase is far greater in a mutant strain of bacteria which does not tumble but only undergoes a gradual change in orientation (a smooth swimmer). As we shall see below, this is in agreement with predictions by [Subramanian & Koch \(2009\)](#) that orientation relaxation mechanisms limit the build up of active stress due to bacteria, and thereby, weaken the collective behaviour.

A common feature of the above experiments is that they all involve rear-actuated swimmers or *pushers*. [Leptos *et al.* \(2009\)](#) have studied the diffusivities of colloidal tracer particles in a suspension of the algae *Chlamydomonas reinhardtii* which is a front-actuated swimmer or *puller*. [Leptos *et al.* \(2009\)](#) observe only a small increase in the diffusivity of the tracer particles when compared to studies of pushers such as [Wu & Libchaber \(2000\)](#). This is consistent with predictions ([Subramanian & Koch \(2009\)](#), [Underhill *et al.* \(2008\)](#), [Saintillan & Shelley \(2007\)](#)) that isotropic suspensions of pushers are linearly unstable to velocity and orientation perturbations whereas suspensions of pullers are stable.

A class of experiments have also dealt with the non-trivial rheology of active suspensions. [Sokolov & Aranson \(2009\)](#) study the viscosity of a thin film of *B. Subtilis*, by measuring the rate of decay of an electromagnetically imposed vortical motion. The suspension viscosity was found to decrease steeply with an increase in bacterial concentration, reaching a minimum which is less than 20 % of the pure solvent viscosity at $nL^3 \approx 18$. Further increase in the bacterial concentration causes an increase in the viscosity. This initial decrease in viscosity is consistent with the shear-induced orientation anisotropy for pushers (such as *B. Subtilis*). The anisotropic active stresses due to the bacterium swimming manifest as a negative viscosity due to preferential alignment of the swimmers along the extensional axis of the local velocity field ([Subramanian &](#)

Koch (2009)). Others have studied the dependence of the viscosity on both the shear-rate and bacteria concentration. Gachelin *et al.* (2013) have performed viscosity measurements in *E. Coli* suspensions using a Y-shaped microfluidic channel which allows measurements at very low shear rates. In this case, the viscosity is inferred by recording the location of the interface between two fluid flowing side-by-side in the microchannel: one fluid is the pure solvent, and the other fluid contains solvent plus bacteria. They find that at low shear rates ($1s^{-1}$) the viscosity is lower than that of the pure solvent; however, on increasing the shear-rate, the viscosity eventually becomes greater than the solvent viscosity at higher shear rates (shear-thickening). At even higher shear rates, the behaviour is again shear-thinning. This is consistent with the mechanism for the instability for pushers proposed by Subramanian & Koch (2009) and mentioned above. At higher shear rates the bacteria are forced to align with the flow instead of the local extensional axis and the negative viscosity mechanism becomes less effective leading to an increase in viscosity. At the highest shear rates, the behaviour might be akin to a shear thinning suspension of passive rods in the high Pe regime. With increasing volume fraction, the viscosity was in general seen to have an increasing trend at high shear rates. At low shear rates, as the concentration is increased the viscosity showed an initial decrease followed by a much sharper increase.

A related set of experiments have been carried out by Karmakar *et al.* (2014). While all the above experiments above adopt indirect methods of probing the swimmer suspension rheology, the experiments of Karmakar *et al.* (2014) use a conventional rheometer and are hence limited to shear rates higher than those accessed by Gachelin *et al.* (2013). Rather interestingly, it was observed in experiments by Karmakar *et al.* (2014) that the viscosity as a function of volume fraction showed a peak which is in striking contrast to the behaviour of passive particles in which case, the viscosity increases monotonically with increasing volume fraction. Suspensions of pullers such as the algae *Chlamydomonas*, on the other hand, have been shown to have much higher viscosities than the pure solvent in experiments by Rafai *et al.* (2010). This is consistent with the fact that pullers have an intrinsic dipole which is contractile in nature, therefore amplifying the Newtonian response of the solvent. While the above experiments pertain to suspensions under shear, our focus in this thesis will be the study of quiescent suspensions. However, the above discussion of finite shear experiments motivates current work in our group where we seek to capture the non-trivial rheology using particle-based simulations.

6.2 Theory and Continuum Models

There have been several efforts to try and explain the non-intuitive phenomena observed in experiments and described in the previous section. Theoretical and computational models of such suspensions must respect various features of the hydrodynamics which may have a bearing on the collective behaviour. Swimmers at low Reynolds numbers are force-free and cause a velocity disturbance field that decays as $1/r^2$, for sufficiently large r , where r is the distance from the swimmer, a behaviour characteristic of a force-dipole. This results in a long-ranged field which is expected to be important in determining the characteristics of the collective behaviour that occurs on length scales larger than the single swimmer dimension. Another important aspect is that swimmers in nature rarely swim in straight lines even in isolation (Berg (1993), Berg (2004)). For example, an isolated bacterium such as an *E. Coli* executes a run-and-tumble

motion where it swims in a directed sense for an amount of time (a run) followed by a sharp change in orientation which is termed a tumble. Furthermore, during a run, the bacterium deviates from a straight path due to imperfections in the flagellar bundle, which resemble a rotary diffusion process (Berg (1993)). This remains true for other micro-scale swimmers such as *Bacillus Subtilis* and *Chlamydomonas Reinhardtii*. Apart from these intrinsic orientation decorrelation mechanisms, the swimmers also change their orientations due to hydrodynamic interactions with other swimmers. Swimmers which lack any intrinsic orientation relaxation mechanisms, and only change their orientation due to hydrodynamic interactions with other swimmers, are termed smooth swimmers.

The importance of long-ranged hydrodynamic interactions and their impact on collective behaviour in swimmer suspensions was first recognized by Simha & Ramaswamy (2002), who proposed a continuum model for orientationally ordered swimmer suspensions. Through a linear stability analysis, they showed that an initial state with either polar or nematic order is unstable to sufficiently long wavelength orientation perturbations. The stability of an isotropic base state, which is more relevant to bacterial suspensions at lower volume fractions was analyzed by Saintillan & Shelley (2008a) and Saintillan & Shelley (2008b), who found that this base state was unstable only for a suspension of pushers. Thus, the underlying cause for collective behaviour was found to be a hydrodynamic instability present only for pushers. This has been confirmed in simulations by Underhill *et al.* (2008). None of the above theoretical efforts, however, consider the effects of tumbling and rotary diffusion, leading to the prediction that an unbounded suspension of pushers is unstable at any non-zero concentration. Experiments with bacterial suspensions, however, report the onset of collective motion only at a finite concentration threshold (Wu *et al.* (2006), Sokolov *et al.* (2007)).

Subramanian & Koch (2009) were the first to analyze a suspension of tumblers and rotary diffusers via a long-wavelength linear stability analysis. They derive a critical value for the concentration for instability which depends on only the intrinsic suspension parameters (the swimmer length L and the swimming speed in isolation U) and does not depend on the box size (as would be the case for simulations of smooth swimmers). The critical volume fraction for a suspension of tumblers is given by:

$$nL^3|_{crit} = \frac{5L}{CU\tau}, \quad (6.1)$$

and for rotary diffusers:

$$nL^3|_{crit} = \frac{30D_rL}{CU}, \quad (6.2)$$

where the constant C depends on the details of the swimming mechanism. This also tells us that, in the dilute limit, the non-dimensional parameter characterizing the instability is given by $nUL^2\tau$ for tumblers and nUL^2/D_r for rotary diffusers. These results are a valuable guide for experiments and simulations which can sweep through a sequence of volume fractions or mean-run-times (τ) to detect the onset of collective behaviour. Experimentally realizing different values of the mean-run-time has been shown to be possible by tailoring different mutant strains of *E. Coli* to have different run times (Karmakar *et al.* (2014)).

This long-wavelength analysis by Subramanian & Koch (2009) has been extended to an

analysis of the complete spectrum by [Saintillan & Shelley \(2008b\)](#) and also by [Subramanian *et al.* \(2011a\)](#) who consider swimmers which tumble. The main results of these studies is that there exists a maximum wavenumber below which there are two stationary unstable modes, only one of which continues to have a finite growth rate as $k \rightarrow 0$. This wavenumber is given by:

$$k_m = 0.027CnL^2. \quad (6.3)$$

Beyond this wavenumber there are a pair of oscillatory unstable modes until a second critical wavenumber given by:

$$k'_m = 0.09CnL^2. \quad (6.4)$$

This wavenumber marks the stability boundary and beyond this wavenumber, there are no unstable discrete modes. For a slightly more detailed description of this stability picture, see section 8.2 in chapter 8 and 9.2.1 in chapter 9.

6.3 Simulations

A common feature of the above theoretical efforts is the assumption of diluteness so that pair-correlations (and higher order correlations) between swimmers may be neglected. Each swimmer, therefore, only sees the effects of others as an imposed ambient field (a mean-field approximation). This limits the validity of these studies to the dilute regime defined by $nL^3 \ll 1$. Particle-level simulations are therefore necessary to study these suspensions at higher concentrations, and also to test the validity of the continuum theories. Additionally, simulations also allow us easier control of certain parameters than experiments especially since the experimental preparation of swimmer suspensions, with swimming parameters in a narrow range, remains a delicate task. Our discussion will centre around simulation efforts that faithfully model the hydrodynamic interactions between the suspended microscopic swimmers. Simulation efforts till date have dealt with a range of swimmer geometries and models for the actuation, but a common feature among them is that they consider neutrally buoyant and force-free swimmers.

[Hernandez-Ortiz *et al.* \(2005\)](#) and [Hernández-Ortiz *et al.* \(2007\)](#) proposed a simple model for force-free swimmers in the form of a dumbbell. Their model consists of two point forces connected by a rod which enforces inextensibility, with actuation applied to one of the beads of the dumbbell. Thus, at large length scales, swimmers interact via a dipolar velocity fields with excluded volume interactions at small separations. [Underhill *et al.* \(2008\)](#) performed simulations using the above model (a regularized point dipole) in a cubic domain which is spatially periodic. Here, they observed that for pushers the diffusivity of non-Brownian tracer particles increased with the simulation domain size. Also, the tracer diffusivities were seen to be much smaller for pullers. The large magnitudes and the box size dependence of tracer diffusivities in pusher suspensions is in agreement with the predictions of linear stability theory ([Subramanian & Koch \(2009\)](#), [Saintillan & Shelley \(2008b\)](#)). Related to the above are the simulations by [Hernandez-Ortiz *et al.* \(2009\)](#), which consider swimmers in a confined geometry between two walls. One drawback of the above model is that the formulation involves point force-dipoles which need to be regularized in order to eliminate the near-field singularities. As a result, many of the

predictions end up depending on the (unphysical) length scale of regularization, an unattractive feature eliminated by considering large-aspect-ratio swimmers with interactions governed by viscous slender body theory.

Slender swimmer models were considered by [Saintillan & Shelley \(2007\)](#), who simulated a suspension of self-propelled rods with a specified tangential stress which causes the rod to swim in either a pusher or puller configuration. Motivated by the predictions of [Simha & Ramaswamy \(2002\)](#), they considered an initial orientational field with either polar or nematic order and found it to be unstable to orientation and velocity fluctuations. Further, they found that the saturated state for pushers and pullers shows very different local order, with close pairs of pushers preferring parallel alignment while pullers prefer anti-parallel alignment. They also found that the orientation decorrelation of the swimmers could be interpreted as a hydrodynamically induced rotary diffusivity which scales as nUL^2 . This is the expected scaling in the case of orientation decorrelation via pair interactions, however, the coefficient observed is far greater than estimates of this pair interaction effect by [Subramanian & Koch \(2009\)](#). Interestingly, even for pushers the translational diffusivity was seen to be well approximated by $U^2/(6D_r)$, implying that even in the presence of bulk fluid motion, the transport of swimmers is mainly governed by the swimming motion along with orientation decorrelations.

The swimmer models discussed till now have been in the form of dumbbells and rods which seek to model large aspect ratio swimmers such as *E. Coli*, *B. Subtilis* and *Chlamydomonas*. Pedley and co-workers, in a series of efforts ([Ishikawa *et al.* \(2008\)](#), [Ishikawa & Pedley \(2008\)](#)) have studied the dynamics and rheology of suspensions of spherical squirmers. These squirmers swim due to a specified tangential velocity at the surface of the particle and may be accurate models for swimmers such as *Paramecium Caudatum* and *Volvox* which swim by waving hair-like projections known as cilia (outward facing flagella in case of *Volvox*) on their surface. These simulations use a modified version of the original Stokesian dynamics methodology ([Brady & Bossis \(1988\)](#), [Durlinsky *et al.* \(1987\)](#)) to model hydrodynamic interactions between swimmers. We note that their spherical shape makes the behaviour of squirmers very different from the slender swimmers discussed above since, in the case of squirmers, there is no obvious means of inducing an orientational anisotropy. Expectedly, in contrast to the previous studies, squirmers show interesting behaviour for the case of pullers where there is a local ordering with close pairs swimming parallel to one another ([Ishikawa *et al.* \(2008\)](#)). This is opposite to what was seen for rod-like pullers in the simulations by [Saintillan & Shelley \(2007\)](#), who observed an anti-parallel orientation of nearby pairs. This indicates that the local properties of these swimmer suspensions are strongly dependent on the swimmer geometry and swimming mechanism. Another work dealing with spherical particles is by [Mehandia & Nott \(2008\)](#), which again uses Stokesian dynamics to model a monolayer of hydrodynamically interacting spherical squirmers. A more recent work related to spherical swimmers is that by [Evans *et al.* \(2011\)](#) who found a polar ordered phase of spherical squirmers driven solely by hydrodynamic interactions.

All the simulation efforts described above lack intrinsic orientation decorrelation mechanisms for the swimmers. The swimmer orientations only decorrelate due to hydrodynamic interactions with other swimmers. Swimmers in nature, however, never swim in straight lines even in isolation. Further, in connection with the study of collective behaviour, the inclusion of intrinsic

decorrelation mechanisms becomes especially important since it allows an estimation of a threshold which is a function of the suspension and swimmer parameters and is independent of the simulation box size. Such an estimate of the threshold from simulations could be used to test the validity of the continuum theories (Subramanian & Koch (2009), Saintillan & Shelley (2008a)). An estimate of the threshold will also serve as a valuable guide for experiments on bacterial suspensions in which intrinsic orientation decorrelation of the swimmers is always present.

6.4 Our Work

In this part of the thesis, we develop the first particle-based simulation model for a suspension of rod-like swimmers with intrinsic decorrelation mechanisms in the form of tumbling and rotary diffusion. Our aim is to study the effects of these decorrelation mechanisms on the swimmer suspension dynamics and estimate (numerically) a threshold for the onset of instability which is a function of the intrinsic suspension parameters and independent of the simulation box size. Further, we seek to compare our results with an existing prediction of the threshold by Subramanian & Koch (2009). The rest of this thesis is organized as follows:

In chapter 7, we present a detailed account of the simulation model used. Starting from our model for the swimmers, which are slender rods, we move on to describing our approach for calculating the hydrodynamic interactions between them. In order to simulate a bulk suspension, we consider a spatially periodic domain in all three dimensions. To compute the interactions between swimmers efficiently in such a periodic setting, we implement an Ewald summation methodology (Ewald (1921)); the swimmer motions are calculated in accordance with viscous slender body theory (Batchelor (1970)). Importantly, in our model we only consider the force distribution on the swimmer which arises due to swimming, and can therefore be specified *a priori*. This intrinsic stress leads to the swimmers being classified into two types based on their swimming mechanism. Rear-actuated swimmers or *pushers*, for which the intrinsic stress behaves as an extensile dipole at large scales. Front-actuated swimmers or *pullers*, for which the intrinsic stress behaves as a contractile dipole at large scales. The extensile nature of the swimmer force-dipole is responsible for the collective behaviour in pusher suspensions (Subramanian & Koch (2009)). The induced stress due to inextensibility of the swimmer only acts to stabilize the suspension (enhancing the aforementioned threshold above its ‘intrinsic’ value). This simplifying assumption leads to a kinematic version of a particle-level simulation with substantial savings in computational effort, and allows us to explore large simulation box sizes. Our largest simulations involve 25600 swimmers in a simulation box which is 40 times the swimmer length, corresponding to a volume fraction of $N(L/2)^3/L_{box}^3 = 0.05$, where N is the number of swimmers, L the swimmer length and L_{box} is the simulation box size. We also describe the modelling approaches used for tumbling and rotary diffusion and validate these models by comparison with theory.

In chapter 8, we validate our kinematic simulation methodology by performing simulations of smooth slender swimmers, devoid of intrinsic relaxation mechanisms, which have been carried out previously by Saintillan & Shelley (2007) and Saintillan & Shelley (2012). We make a comprehensive study of statistical measures related to the swimmers, the suspending fluid and passive tracer particle transport to gain an understanding of the dynamics of the swimmer suspension, and to also characterize the onset of the instability. For characterizing the onset of

the instability, we use our puller simulations (which are predicted to be stable) as a baseline for contrasting our pusher results. We compare our results with those of earlier simulations, and also experiments, and find good qualitative agreement. Our estimate for the stability threshold obeys the scaling laws with box size as implied by the theory of [Subramanian & Koch \(2009\)](#). Further, we find that the tracer diffusivity is the most sensitive indicator of the onset of the collective behaviour, as predicted earlier by [Saintillan & Shelley \(2012\)](#). The tracer diffusivity curves for pushers and pullers exhibit a bifurcation beyond a critical concentration, and this bifurcation point is interpreted as the point for the onset of instability and collective motion.

Having validated our simulation methodology, we use it to study suspensions of swimmers which tumble and rotary diffuse in addition to interacting hydrodynamically with other swimmers, in chapter 9. As expected, the immediate effect of the inclusion of intrinsic decorrelation mechanisms is to stabilize suspensions of pushers. Interestingly, however, even in swimmer suspensions where the swimmers tumble or rotary diffuse, we find that there are systematic differences between pushers and pullers beyond a critical volume fraction. This indicates that a suspension of pushers which tumble continues to remain unstable beyond a critical volume fraction. Motivated by this observation for our volume fraction varying simulations, and the fact that the theoretical threshold involves the product of a volume fraction and a scaled mean-free-path, we examine a complementary approach to observing the instability. We perform simulations where the volume fraction is fixed to a value in the dilute regime and the mean-run-time is varied. As a basis for comparison with these simulations, we extend the theory by [Kasyap *et al.* \(2014\)](#) and derive the tracer diffusivity in a swimmer suspension in a periodic domain which is directly relevant to simulations. This theory reveals a non-trivial effect of the periodic box on the tracer diffusivity. While the theory for an unbounded suspension predicts the tracer diffusivity to be a monotonically increasing function of the mean-run-time, we find that periodicity leads to a non-monotonic variation, with the diffusivity, rather surprisingly, going to zero for very large mean-run-times. With this theory in hand, we perform simulations with interactions between swimmers switched off (precluding instability) and find a very good match between simulation results for the tracer diffusivity with the theory for the periodic box. An important result from these simulations is that the tracer diffusivities are almost identical for pushers and pullers for the fore-aft symmetric swimmers considered in our simulations. On switching on interactions between swimmers, we again observe a bifurcation between pushers and pullers beyond a critical value of the mean-run-time similar to the aforementioned bifurcation in the volume-fraction-varying simulations, with the pushers showing larger values of tracer diffusivities than pullers. Pusher and puller tracer diffusivities remain practically coincident in the stable regime, even with interactions on, since the volume fraction chosen ($\nu = 0.05$) is small enough to minimize the effects of pair-correlations which are different for pushers and pullers. Using the estimates of the critical volume fraction and mean-run-time from the two kinds of simulations (τ fixed variable n , and n fixed variable τ), we find that both of them lead to the same critical value for the dimensionless quantity $nUL^2\tau$, which characterizes the threshold ([Subramanian & Koch \(2009\)](#)). This is one of the central results of this thesis and implies that suspensions of pushers indeed become unstable when the quantity $nUL^2\tau$ exceeds a certain fixed threshold which only depends on the microscopic details of the swimming motion.

Interestingly, we find that our simulations predict an instability threshold which is much smaller in magnitude compared to that predicted by the theory. We have independently confirmed that the same is true even for swimmers which rotary diffuse instead of tumble. In either case, the ratio of the theoretical threshold to that observed in our simulations, remains about the same. This points to a seemingly sub-critical nature of the instability in a swimmer suspension, a novel result worthy of further attention.

In chapter [10](#), we conclude and give directions for future work.

Chapter 7

Simulation Model and Theory

7.1 Introduction

In this chapter, we outline the particle-based model which we use to simulate collective motion in a bulk suspension of micro-scale swimmers. We begin by describing our model for the swimmers before going on to the methods used to model the hydrodynamic interactions between them. We consider rod-like swimmers which operate at low Reynolds numbers, and hence, are force-free at all times. The passive portions of such a swimmer drag the fluid along as it swims while the propulsive parts push fluid in the direction opposite to that of the swimming. Therefore, the disturbance velocity due to a swimmer is dipole-like at long distances, and decays as $1/r^2$, where r is the distance from the swimmer. Since the collective behaviour we are interested in studying is mainly attributed to the intrinsic stresses felt in the fluid due to swimming, we neglect the induced stresses due to the no-slip condition at the swimmer body and the inextensibility of the swimmer. The intrinsic stress can be specified, based on only the swimming parameters and as a result the swimmer disturbance fields are known *a priori*. One only has to now convect and rotate each slender swimmer in a known ambient, and in a manner consistent with viscous slender body theory (Batchelor (1970)). This makes our simulations kinematic in nature since the translational and angular velocities of the swimmers can be calculated explicitly without the need for an iterative procedure. The results from such an approach which solely considers the effects of the intrinsic stresses can be readily compared with theory since the intrinsic and induced stresses can be conveniently separated even in the theory; in other words, there is a known prediction for the stability threshold of a swimmer suspension solely due to the effects of the intrinsic stresses (Subramanian & Koch (2009)). This simplification serves to greatly reduce the computational cost of our simulations compared to earlier efforts (Hernandez-Ortiz *et al.* (2005), Underhill *et al.* (2008), Saintillan & Shelley (2007), Saintillan & Shelley (2012)). Even with this simplification, modelling long-ranged interactions in an infinite periodic suspension requires a specialized method so as to make the simulation computationally efficient. We shall use the well known Ewald summation method (Ewald (1921), Hasimoto (1959), Beenakker (1986), Saintillan *et al.* (2005)) to write the disturbance velocity field due to an infinite periodic array of swimmers as the sum of contributions calculated in real space and Fourier space. Once this ambient disturbance velocity at each swimmer is calculated, we use viscous slender body theory (Cox (1970), Batchelor (1970)) to update their positions and orientations in the next time step. Our interest in studying the collective motion in swimmer suspensions motivates us to study two types of swimmers based on their swimming mechanism, namely, pushers and pullers. The details of the two swimming mechanisms are given in the next section. Experiments have observed (Mendelson *et al.* (1999), Sokolov *et al.* (2007), Dombrowski *et al.* (2004), Cisneros *et al.* (2011)), and theories (Underhill *et al.* (2008), Saintillan & Shelley (2007), Subramanian

& Koch (2009)) have predicted collective motion in the case of pushers. Pullers, on the other hand, are not predicted by theory to show collective motion. The pullers in our simulation, therefore, serve as a base case which we use as a contrast to study the interesting behaviour seen for pushers.

A novel aspect of this work is the inclusion of intrinsic decorrelation mechanisms found in biological swimmers (bacteria such as *E. Coli*) such as tumbling, and also small and continuous random changes in the swimming direction, which are well modelled as a rotary diffusion process. In the sections that follow, we also describe the methodology used to model these stochastic processes and validate our results against theoretical predictions. We conclude the chapter by giving an overview of the simulation algorithm which includes all the above components.

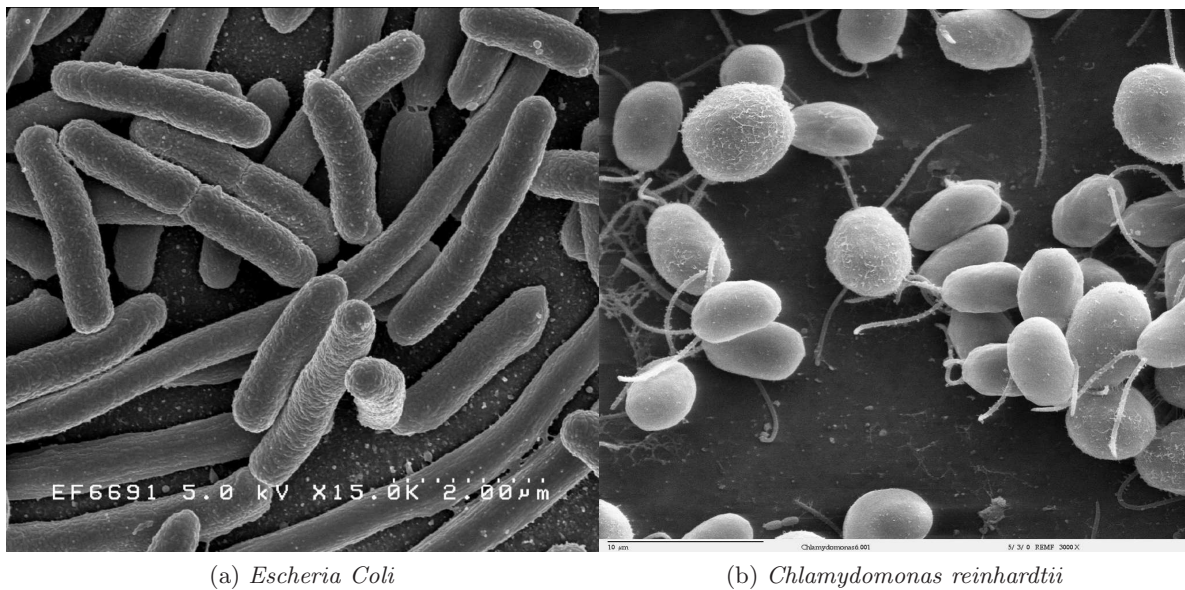


Figure 7.1: Electron micrographs of (a) *E. Coli* and (b) *Chlamydomonas reinhardtii*, two micro-scale swimmers which display pusher and puller-type swimming mechanisms, respectively. As model organisms, they motivate our study of suspensions of general pushers and pullers.

7.2 Single Swimmer Model

We seek to study micro-scale swimmers such as *E. Coli* and *Chlamydomonas* shown in Fig. 7.1. Both these are examples of swimmers which use flagellae, whip-like attachments to the cell body, in order to swim in a viscous ambient fluid. These two organisms differ in their swimming mechanism and we classify them as *pushers* and *pullers*, respectively. Pushers have a propulsive part (the posterior flagellum in a bacterium like *E. Coli*) which pushes the head of the organism through the fluid, leading to an extensile character for the intrinsic dipole (see Fig. 7.2 (a) and (c)). Pullers, on the other hand, are the opposite with the propulsive portion (a pair of anterior flagella) pulling the head through the fluid with the aid of a breast-stroke-like motion, leading to a contractile character¹ for the dipole (see Fig. 7.3 (a) and (c)). The typical disturbance

¹It is important to clarify the nomenclature of an extensile and contractile dipole used in literature (and this thesis) to describe the intrinsic dipole for a pusher and puller, respectively. While this is visually a clear description of

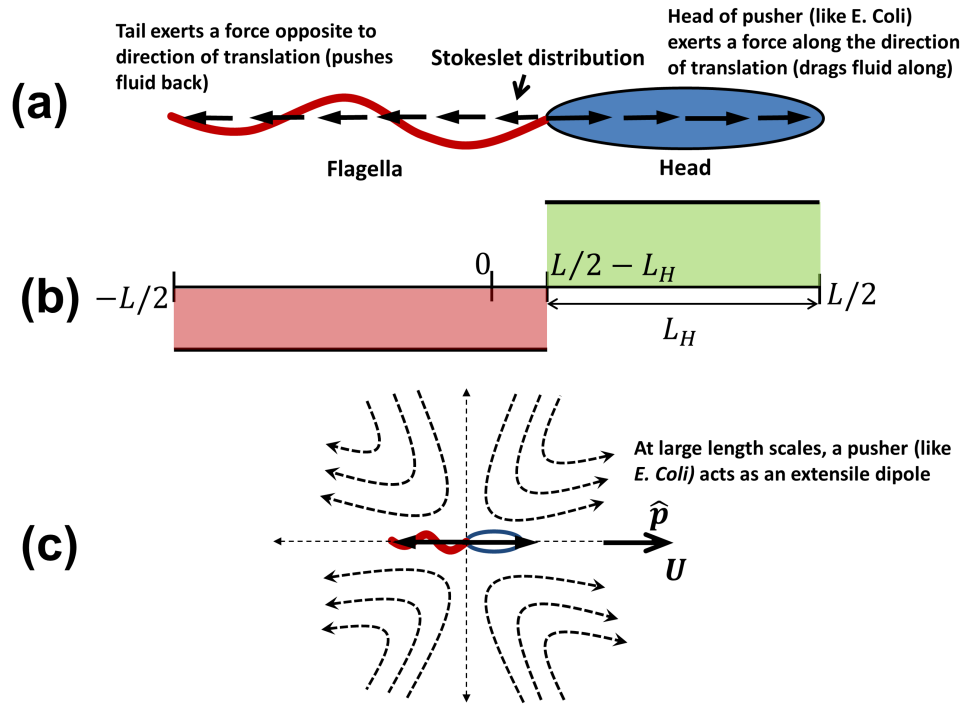


Figure 7.2: Schematic of a pusher-type swimmer. (a) The Stokeslet distribution used to model a pusher is shown along with the variation of the force density with the coordinate along the swimmer axis in (b). (c) Shows the disturbance velocity due to a pusher at large length scales which is that due to an extensile dipole

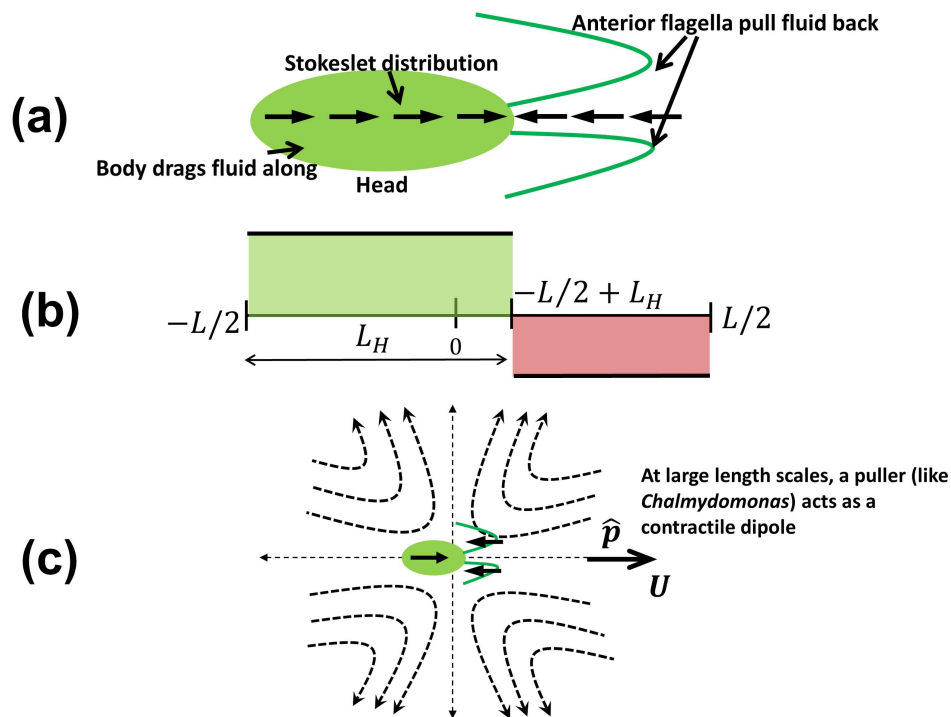


Figure 7.3: Schematic of a puller-type swimmer. (a) The Stokeslet distribution used to model a puller is shown along with the variation of the force density with the coordinate along the swimmer axis in (b). (c) Shows the disturbance velocity due to a puller at large length scales which is that due to a contractile dipole

velocity fields for pushers and pullers are shown in Figs. 7.2(c) and 7.3(c). We model these swimmers as (infinitely) slender rods, which, given the large aspect ratios of these swimmers (~ 6 for *E. Coli* and *Chlamydomonas*), is a fairly good approximation. The intrinsic stress due to swimming is then modelled as a line distribution of Stokeslets (the Stokeslet denotes a point-force, and may be regarded as a Green's function for the Stokes equations; Leal (2007)) aligned with the orientation vector of the swimmer. The magnitude and functional form of this intrinsic force distribution depends on the details of the swimmer such as its swimming speed, geometry of the head and swimming mechanism. The Stokeslets are parallel and anti-parallel to the swimming direction on the passive and propulsive parts of the swimmer, respectively. We define the parameter $\alpha_1 = L_H/L$, where L_H is the length of the (passive) head portion of the swimmer and L is the total length. We assume a Heaviside function for the intrinsic force distribution on the swimmer, where the (linear) force density is piece-wise constant over the propulsive and passive sections. We have also considered a sinusoidal variation of the force density but find no qualitative differences in our results as compared to the Heaviside distribution. Therefore, in this thesis, we only discuss results for the Heaviside distribution. The force density can be written as $\mathbf{f} = f(s)\hat{\mathbf{p}}$, where $f(s)$ is the magnitude of the force density, $\hat{\mathbf{p}}$ is the orientation vector of the swimmer, and s is the coordinate along the swimmer axis. This orientation vector is aligned along the isolated swimming direction of the swimmer. We have verified that the velocity field near the bacterium calculated using such a distribution shows good agreement with the experimentally measured velocity field near a swimming *E. Coli* (Drescher *et al.* (2011)). The functional form of the force distribution for pushers is given by:

$$f(s) = \begin{cases} \frac{-F_D}{(1-\alpha_1)L} & \text{for } -L/2 < s < L(1/2 - \alpha_1), \\ \frac{F_D}{\alpha_1 L} & \text{for } L(1/2 - \alpha_1) < s < L/2, \end{cases} \quad (7.1)$$

where F_D is the drag force on the head which is equal in magnitude and opposite in sign to the thrust force generated by the flagella. Note that distances along the swimmer axis are measured in a coordinate system located at the geometric centre (mid-point) of the swimmer (see Fig. 7.2 (b)) so that the ends of the swimmer correspond to $s = \pm L/2$. For *E. Coli*, whose head is spheroidal in shape with the longer axis along the swimmer axis, the drag force is given by $F_D = C_s \mu U L_H$, where C_s is the drag coefficient for a spheroid translating along its longer axis, U is the swimming speed and μ is the fluid viscosity. We assume for the sake of simplicity that the pullers too have heads which may be described as spheroids². We note here that our intention in modelling pullers is not to describe specific organisms such as *Chlamydomonas*, whose near-field velocity may be complicated by unsteady stroke kinematics and presence of closed streamlines (Guasto *et al.* (2010)), but to study the effect of the contractile nature of the dipole on collective motion. Thus our puller model is the same as that of pushers, but with signs of the force distribution reversed. *The main role for the puller simulations are to serve as*

the nature of the dipole, it is slightly misleading from a fluid mechanical perspective. This is because a suspension of aligned pushers actually result in a compression (rather than tension) along the direction of alignment of the dipoles. Aligned pullers on the other hand lead to tension in the direction of alignment.

²We note that we use the approximation that the head and tail of the swimmer do not interact with each other.

a base-line or contrast for the pusher simulations. The force distribution for pullers is given by:

$$f(s) = \begin{cases} \frac{F_D}{\alpha_1 L} & \text{for } -L/2 < s < L(\alpha_1 - 1/2), \\ \frac{-F_D}{(1 - \alpha_1)L} & \text{for } L(\alpha_1 - 1/2) < s < L/2. \end{cases} \quad (7.2)$$

Figs. 7.2 (b) and 7.3 (b) show the coordinate system used on the swimmer along with the force densities used in the simulations for pushers and pullers. Note that the force density profiles for the puller is such that the head is the posterior part of the swimmer while the propulsive portion is the anterior part (see Fig. 7.3 (a)). The results we present here are mainly for fore-aft symmetric swimmers ($\alpha_1 = 1/2$), with a Heaviside force density distribution. However, we find that changes in the parameter α_1 do not qualitatively alter our results, and this is therefore not an important factor with regard to the questions related to collective motion which we are interested in.

7.3 Hydrodynamic Interactions in a Swimmer Suspension

The swimmers, as they swim along, ‘stir’ the suspending fluid, and thereby, affect the motion of other swimmers. In the low Reynolds regime, relevant to most micro-scale swimmers (For *E. Coli*, the typical values of the swimmer parameters are $L = 12\mu m$, $L_H = 2 - 3\mu m$ and the transverse dimension of the head is around $1\mu m$. Thus the head is a spheroid of aspect ratio around 2. The swimming speed is typically around $10\mu m/s$, so that the Reynolds number defined as $Re = \rho UL/\eta$ is very small and for the case of swimming in water is $\sim 10^{-4}$)³, the governing equations are the Stokes equations with an additional forcing term due to the swimmers, and the continuity equation for an incompressible fluid. This set of equations can be written as:

$$-\nabla p + \nabla^2 \mathbf{u} = \mathbf{B}, \quad (7.3)$$

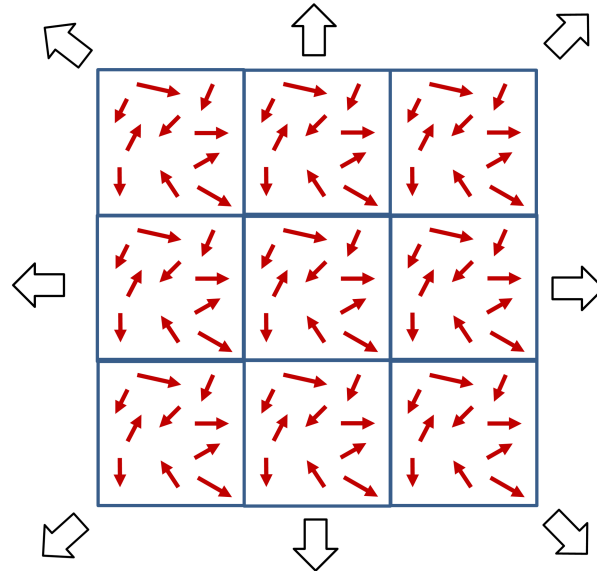
$$\nabla \cdot \mathbf{u} = 0, \quad (7.4)$$

where p and \mathbf{u} are the pressure and velocity fields in the fluid, and

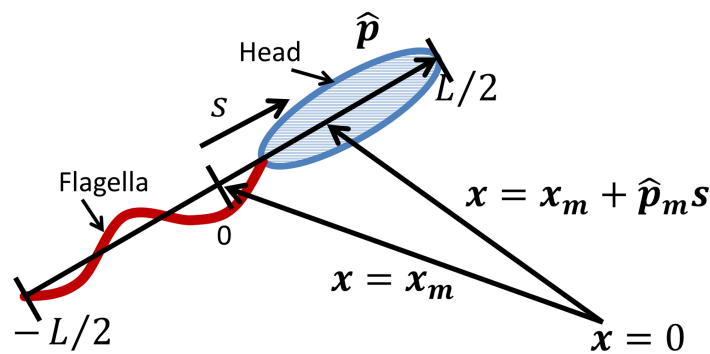
$$\mathbf{B} = - \sum_{m=1}^{\infty} \int_{-L/2}^{L/2} \delta(\mathbf{x} - \mathbf{x}_m - \hat{\mathbf{p}}_m s) f(s) \hat{\mathbf{p}}_m ds \quad (7.5)$$

is the forcing term due to the suspended swimmers. Here, \mathbf{x}_m and $\hat{\mathbf{p}}_m$ are the position and orientation of the m^{th} swimmer. We use the following scales to non-dimensionalize our problem; the length scale is half the swimmer length $l_c = L/2$; the time scale is $t_c = L/(2U)$, which is the time for the swimmer to swim half its own length; forces are scaled by $F_c = \mu UL/2$. Henceforth, we will be using the dimensionless version of all the variables with the same notation as the dimensional variables. In the dimensionless variables the swimmer length is 2 and its isolated swimming speed is unity.

³We note that even the vortices that constitutes collective motion (see [Tuval et al. \(2005\)](#)) only have a Reynolds number of $O(10^{-2})$ based on their length scale, thereby validating the use of the Stokes equations to describe even large-scale motion associated with ‘collective dynamics’.



(a) Periodic swimmer suspension with arrows depicting the periodic images in all three-dimensions



(b) Coordinate system

Figure 7.4: (a) The simulation box with its nearest neighbours in the same plane. The swimmers are represented as arrows along their orientation vectors. Each swimmer has an infinite number of images repeated at the sites of a simple cubic lattice. The periodicity applies into and out of the page as well since we have implemented a periodic boundary condition in three dimensions. (b) The coordinate system used in the simulations where the geometric centre of each swimmer is used to track its position relative to a lab-fixed reference frame. The coordinate system on the swimmer measures the location of points along the swimmer axis with respect to this geometric centre.

Using our particle model we are interested in studying the stability and thence the collective motion in a bulk (infinite) swimmer suspension. However, in a numerical simulation, one can only deal with a finite number of degrees of freedom, and thus to simulate an infinite suspension we need to implement periodic boundary conditions. Therefore, we have the simulation domain which is a cubic unit-cell of side length L_{box} in all three dimensions. Let $\mathbf{a}_1, \mathbf{a}_2, \mathbf{a}_3$ denote the lattice vectors constituting the unit cell. For a cubic unit cell of side L_{box} , the lattice vectors are given by

$$\mathbf{a}_i = L_{box} \hat{\mathbf{x}}_i, i = 1, 2, 3 \quad , \quad (7.6)$$

where the $\hat{\mathbf{x}}_i$ for $i = 1, 2, 3$ constitute the right-handed triplet of Cartesian unit vectors.

In this unit cell we have N swimmers with geometric centres (mid-point along the swimmer's length) at $\mathbf{x}_1 \mathbf{x}_2 \cdots \mathbf{x}_N$ and orientations $\hat{\mathbf{p}}_1, \hat{\mathbf{p}}_2 \cdots \hat{\mathbf{p}}_N$ (henceforth, the position of the swimmer will mean the position of the geometric centre of the swimmer). The positions of the swimmers are specified with respect to an origin located at the vertex of the simulation box such that the edges of the box form the aforementioned right-handed triplet (see Fig. 7.4b). The periodic boundary conditions imply that there are an infinite number of periodic images of these swimmers whose positions are given by an integral number of translations along the lattice vectors. Therefore, the position of the images of the i^{th} swimmer are $\mathbf{x}_i + \mathbf{l}$, where \mathbf{l} is the vector $\mathbf{l} = l_1 \mathbf{a}_1 + l_2 \mathbf{a}_2 + l_3 \mathbf{a}_3$ and l_1, l_2, l_3 are integers. We note that $l_1 = l_2 = l_3 = 0$ corresponds to the simulation unit cell. Fig. 7.4a shows a schematic representation with the simulation box at the centre surrounded by the neighbouring unit cells. With this arrangement, the summation term, involving the original infinite number of swimmers, can be written as:

$$\mathbf{B} = - \sum_{\mathbf{l}} \sum_{i=1}^N \int_{-1}^1 \delta(\mathbf{x} - \mathbf{x}_i - \hat{\mathbf{p}}_i s - \mathbf{l}) f(s) \hat{\mathbf{p}}_i ds, \quad (7.7)$$

where the inner summation denotes summation over the simulation box (index i and $\mathbf{l} = 0$) and the outer summation denotes sum over the infinite periodic images of the simulation box (sum over \mathbf{l}). Further, in simulations, the force distribution along the swimmer axis is specified using point forces at discrete points along the swimmer axis and the integrals involving the force distribution are computed numerically using Gaussian quadrature. Assuming that each swimmer is discretized using M quadrature points, the swimmer forcing term in Eq. 7.7 can be written as:

$$\mathbf{B} = - \sum_{\mathbf{l}} \sum_{i=1}^N \sum_{j=1}^M \delta(\mathbf{x} - \mathbf{x}_i - \hat{\mathbf{p}}_i s_j - \mathbf{l}) f(s_j) w_j \hat{\mathbf{p}}_i, \quad (7.8)$$

where $f(s_j) \hat{\mathbf{p}}_i$ is the j^{th} Stokeslet (point force) on the i^{th} swimmer in the simulation box, and the w_j 's are the quadrature weights. For simplicity of notation, absorbing the quadrature weights into the force density and simplifying the above expression, we have:

$$\mathbf{B} = - \sum_{\mathbf{l}} \sum_{i=1}^N \hat{\mathbf{p}}_i \sum_{j=1}^M \delta(\mathbf{x} - \mathbf{x}_i - \hat{\mathbf{p}}_i s_j - \mathbf{l}) f(s_j). \quad (7.9)$$

The momentum balance equation, upon substituting for \mathbf{B} from Eq. 7.9, is given by:

$$-\nabla p + \nabla^2 \mathbf{u} = - \sum_l \sum_{i=1}^N \hat{\mathbf{p}}_i \sum_{j=1}^M \delta(\mathbf{x} - \mathbf{x}_i - \hat{\mathbf{p}}_i s_j - \mathbf{l}) f(s_j). \quad (7.10)$$

We are therefore interested in a periodic solution to the above Stokes equations. Although we have a periodic array of swimmers (constituted of point forces) in the above equation, one has to, in effect, solve the Stokes equations for NM interlacing simple cubic arrays of point forces (M point forces on N swimmers). Such a solution was first derived for a single periodic array of point forces by Hasimoto (1959) for cases where the array corresponds to the vertices of a simple, Body-Centred-Cubic (BCC) and Face-Centred-Cubic (FCC) lattices, we will only need the solution for the first case. Hasimoto's approach may be readily extended to the case of interlacing arrays (Mackaplow & Shaqfeh (1998), Butler & Shaqfeh (2002)). Using a different approach, interlacing cubic arrays of spheres (not point forces) corresponding to a random array of spheres in the original unit cell were analysed by Beenakker (1986). This alternate approach has been adopted by Brady and co-workers in their Stokesian dynamics approach (Brady & Bossis (1988), Brady *et al.* (1988)). These two approaches are exactly equivalent, a fact we show in appendix D. Our derivation below closely follows that of Hasimoto (1959), but for an array resulting from a discretized version of a line distribution of point forces. Since the swimmer positions are arbitrary (and not regularly spaced), the positions of the line distributions are random within a unit cell, while the unit cell itself is repeated to achieve periodicity thus leading to the individual point forces constituting each swimmer to be part of interleaving cubic arrays. Since the velocity and pressure fields are periodic we can expand them in a Fourier series as:

$$\mathbf{u} = \sum_{\mathbf{k}} \hat{\mathbf{U}}(\mathbf{k}) \exp(-2\pi i \mathbf{k} \cdot \mathbf{x}), \quad (7.11)$$

$$\nabla p = \sum_{\mathbf{k}} \hat{\mathbf{P}}(\mathbf{k}) \exp(-2\pi i \mathbf{k} \cdot \mathbf{x}), \quad (7.12)$$

where

$$\mathbf{k} = n_1 \mathbf{b}_1 + n_2 \mathbf{b}_2 + n_3 \mathbf{b}_3 \quad n_1, n_2, n_3 = 0, \pm 1, \pm 2, \dots, \quad (7.13)$$

defines vectors in the reciprocal lattice such that:

$$\mathbf{k} \cdot \mathbf{a}_j = n_j \quad (j = 1, 2, 3). \quad (7.14)$$

The unit vectors in the reciprocal lattice are given by:

$$\mathbf{b}_1 = \frac{\mathbf{a}_2 \times \mathbf{a}_3}{V}, \quad \mathbf{b}_2 = \frac{\mathbf{a}_3 \times \mathbf{a}_1}{V}, \quad \mathbf{b}_3 = \frac{\mathbf{a}_1 \times \mathbf{a}_2}{V}, \quad (7.15)$$

where the volume of the unit cell in real space is:

$$V = \mathbf{a}_1 \cdot [\mathbf{a}_2 \times \mathbf{a}_3]. \quad (7.16)$$

For the case under consideration, a simple cubic lattice, both $[\mathbf{a}_1, \mathbf{a}_2, \mathbf{a}_3]$ and $[\mathbf{b}_1, \mathbf{b}_2, \mathbf{b}_3]$ are

right-handed Cartesian triplets.

Transforming the Eqs. 7.4 and 7.10, into Fourier space by multiplying with $\exp(2\pi i \mathbf{k} \cdot \mathbf{x})/V$ and integrating over a unit cell in physical space, we get:

$$\mathbf{k} \cdot \hat{\mathbf{U}}(\mathbf{k}) = 0, \quad (7.17)$$

$$-4\pi^2 k^2 \hat{\mathbf{U}}(\mathbf{k}) = -\hat{\mathbf{P}}(\mathbf{k}) - \frac{1}{V} \hat{\mathbf{F}}(\mathbf{k}), \quad (7.18)$$

where

$$\hat{\mathbf{F}}(\mathbf{k}) = \sum_{i=1}^N \mathbf{p}_i \sum_{j=1}^M f(s_j) \exp(2\pi \mathbf{k} \cdot (\mathbf{x}_i + \mathbf{p}_i s_j)). \quad (7.19)$$

The Fourier transform of the pressure gradient satisfies:

$$\hat{\mathbf{P}}(\mathbf{k}) \times \mathbf{k} = 0, \quad (7.20)$$

which can be seen by taking the curl of Eq. 7.12. Considering the $\mathbf{k} = 0$ terms in Eq. 7.18, we have:

$$\hat{\mathbf{P}}(0) = -\frac{\hat{\mathbf{F}}(0)}{V} = -\frac{1}{V} \sum_{i=1}^N \mathbf{p}_i \sum_{j=1}^M f(s_j), \quad (7.21)$$

which implies that the total force per unit volume due to the swimmers in a box, is balanced by a mean pressure gradient in the fluid. Thus, even though the velocity field is spatially periodic, the pressure field is not. This remedies the seeming divergence resulting from summing an infinite array of $1/r$ decaying Stokeslets over three dimensions. Physically, this means that when the average force on the fluid in the unit cell is not zero, there is a resulting backflow and it is the velocity relative to the backflow which is of interest (Hasimoto (1959), Brady & Bossis (1988), Brady *et al.* (1988)). We note here that our swimmers being force-free, and the above mean force and pressure gradient are identically zero. Although $\hat{\mathbf{P}}(0)$ is identically zero in principle, from the numerical point of view, one still needs to exclude the terms corresponding to $\mathbf{k} = 0$ even for a suspension of force-free swimmers. For $\mathbf{k} \neq 0$ taking the scalar product of Eq. 7.18 with \mathbf{k} , we get:

$$\mathbf{k} \cdot \hat{\mathbf{P}}(\mathbf{k}) = -\frac{\mathbf{k} \cdot \hat{\mathbf{F}}(\mathbf{k})}{V}. \quad (7.22)$$

Making use of Eq. 7.20, we can write:

$$\mathbf{k} \times \hat{\mathbf{P}}(\mathbf{k}) \times \mathbf{k} = k^2 \hat{\mathbf{P}}(\mathbf{k}) - (\mathbf{k} \cdot \hat{\mathbf{P}}(\mathbf{k})) \mathbf{k} = 0. \quad (7.23)$$

Using Eq. 7.22 in the above equation, we get:

$$\hat{\mathbf{P}}(\mathbf{k}) = -\frac{(\mathbf{k} \cdot \hat{\mathbf{F}}(\mathbf{k})) \mathbf{k}}{V k^2}. \quad (7.24)$$

Using this in Eq. 7.18, we get the final expression for the Fourier-transformed velocity field as:

$$\hat{\mathbf{U}}(\mathbf{k}) = -\frac{1}{4\pi^2 k^2 V} \left[\frac{(\mathbf{k} \cdot \hat{\mathbf{F}}(\mathbf{k})) \mathbf{k}}{k^2} - \hat{\mathbf{F}}(\mathbf{k}) \right]. \quad (7.25)$$

Converting to real space, we get the final expression for the disturbance velocity, at a general point \mathbf{x} , in an infinite periodic swimmer suspension as:

$$\mathbf{u}(\mathbf{x}) = \frac{1}{4\pi} \left[\mathbf{S}^{(1)} - \nabla(\nabla \cdot \mathbf{S}^{(2)}) \right], \quad (7.26)$$

where

$$\mathbf{S}^{(1)} = \frac{1}{\pi V} \sum_{\mathbf{k} \neq 0} \frac{\exp(-2\pi \mathbf{k} \cdot \mathbf{x})}{k^2} \hat{\mathbf{F}}(\mathbf{k}), \quad (7.27)$$

$$\mathbf{S}^{(2)} = \frac{-1}{4\pi^3 V} \sum_{\mathbf{k} \neq 0} \frac{\exp(-2\pi \mathbf{k} \cdot \mathbf{x})}{k^4} \hat{\mathbf{F}}(\mathbf{k}). \quad (7.28)$$

7.3.1 Ewald Summation Method

Eq. 7.26 constitutes an exact periodic solution to the Stokes equations. This along with Eqs. 7.27 and 7.28, give convergent expressions for the disturbance velocity field. In the previous section, we eliminated the convergence problems at large \mathbf{x} , which appears as a singularity at $\mathbf{k} = 0$. There is still, however, a problem with the expressions in Eqs. 7.27 and 7.28 since they are only conditionally convergent. This conditional convergence at large \mathbf{k} is related to the singular behaviour of the velocity field at small \mathbf{x} due to the singularities (point forces) in physical space. Thus, we need a way of specifying the sequence of the summation so as to obtain a converged result. Further, for practical implementation in simulations, the slow convergence in $1/k^2$ and $1/k^4$ makes a naive summation inefficient, requiring many terms for convergence. Both of the above problems, namely specifying the sequence of the summation as well as accelerating the convergence rate are alleviated by using the Ewald summation technique, first used by Ewald (1921) for electrostatic interactions. This method was extended to the case of hydrodynamic interactions by Hasimoto (1959), and independently, by Beenakker (1986), and will be the one used here to accelerate the convergence. The method involves finding an integral representation for $1/k^{2n}$ for $n = 1, 2$ and introducing a cut-off parameter to split the sum into two parts, one in real space and the other in Fourier space. This splitting parameter or Ewald coefficient is then tuned such that the total cost of the computation is minimized. The derivation of the disturbance velocity field in terms of the real and Fourier sums can be found in a number of places (Hasimoto (1959), Beenakker (1986)), and is re-derived for our case in Appendix C. The final result for the disturbance velocity in terms of the real and Fourier sums is given by:

$$\mathbf{u}(\mathbf{x}) = \frac{1}{4\pi} \left[\sum_l \sum_{i=1}^N \sum_{j=1}^M \mathbf{A}(\alpha, \mathbf{x} - \mathbf{x}_i - \mathbf{p}_i s_j - \mathbf{l}) \cdot f(s_j) \mathbf{p}_i + \sum_{\mathbf{k} \neq 0} \mathbf{B}(\alpha, \mathbf{k}) \cdot \hat{\mathbf{F}}(\mathbf{k}) \exp(-2\pi \mathbf{k} \cdot \mathbf{x}) \right], \quad (7.29)$$

where the two tensors \mathbf{A} and \mathbf{B} are given by:

$$\mathbf{A}(\alpha, \mathbf{x}) = \pi \alpha^{-3/2} \phi_{1/2}(\pi r^2 / \alpha) (\mathbf{I} r^2 + \mathbf{x} \mathbf{x}) - 2 \alpha^{-1/2} \exp(-\pi r^2 / \alpha) \mathbf{I}, \quad (7.30)$$

$$\mathbf{B}(\alpha, \mathbf{k}) = \frac{\pi \alpha^2 \phi_1(\pi \alpha k^2)}{V} [\mathbf{I} k^2 - \mathbf{k} \mathbf{k}], \quad (7.31)$$

where \mathbf{I} is the second order identity tensor. The function ϕ_ν in Eqs. 7.30 and 7.31 is the incomplete Gamma function (Abramowitz & Stegun (1972)) and:

$$\phi_{1/2}(x) = \frac{\exp(-x)}{x} + \frac{\sqrt{\pi}}{2x^{3/2}} \operatorname{erfc}(\sqrt{x}), \quad (7.32)$$

$$\phi_1(x) = \frac{\exp(-x)}{x^2} (1+x). \quad (7.33)$$

While Eq. 7.29 gives the velocity at a general point in the fluid due to a periodic suspension of swimmers, care must be taken while evaluating the same at a swimmer location. In implementing swimmer interactions according to viscous slender body theory, we will require the ‘ambient’ velocity field at points along the swimmer in order to update the positions and orientations of the swimmers. In order to calculate the ambient velocity at points on a given swimmer, we note that the swimmer does not see its own velocity disturbance field, but sees that due to the other swimmers in the simulation unit cell as well as that due to all periodic images including its own. Thus, a self-term must be subtracted from Eq. 7.29 to give the disturbance velocity at a swimmer. This self-term is divided among the real and reciprocal space sums. The removal of the self-term from the real sum is straightforward and is achieved by neglecting the contribution from the index $i = m$ when $\mathbf{l} = 0$, where m is the swimmer at which we are calculating the velocity field. The self-term for the Fourier sum is more involved and is most easily calculated by transforming back into real space. The details of this calculation are not presented here, and we just write down the final result for the self-term for swimmer m as:

$$\mathbf{u}_{self}(\mathbf{x}_m + \mathbf{p}_m s) = \int_{-1}^1 \frac{\operatorname{erf}[\sqrt{\frac{\pi}{\alpha}}(s' - s)]}{4\pi(s' - s)} f(s') \hat{\mathbf{p}}_m ds'. \quad (7.34)$$

We can write the above continuous integral in terms of a discrete one which will be used in the simulations. Thus the self term for swimmer m at a location $\mathbf{x}_m + \mathbf{p}_m s_n$ along its axis is given by:

$$\mathbf{u}_{self}(\mathbf{x}_m + \mathbf{p}_m s_n) = \sum_{j=1}^M \frac{\operatorname{erf}[\sqrt{\frac{\pi}{\alpha}}(s_j - s_n)]}{4\pi(s_j - s_n)} f(s_j) \hat{\mathbf{p}}_m, \quad (7.35)$$

where we note that the quadrature weights are again a part of the force density function $f(s)$. Thus, the disturbance velocity at a swimmer denoted by index m , at a point $\mathbf{x}_m + \mathbf{p}_m s_n$ along its length, is given by the expression:

$$\begin{aligned} \mathbf{u}(\mathbf{x}_m + \mathbf{p}_m s_n) = & \frac{1}{4\pi} \left[\sum_{\mathbf{l}} \sum_{i=1, (l,i) \neq (0,m)}^N \sum_{j=1}^M \mathbf{A}(\alpha, \mathbf{x}_m + \mathbf{p}_m s_n - \mathbf{x}_i - \mathbf{p}_i s_j - \mathbf{l}) \cdot f(s_j) \mathbf{p}_i \right. \\ & \left. + \sum_{\mathbf{k} \neq 0} \mathbf{B}(\alpha, \mathbf{k}) \cdot \hat{\mathbf{F}}(\mathbf{k}) \exp(-2\pi \mathbf{k} \cdot \mathbf{x}) - \sum_{j=1}^M \frac{\operatorname{erf}[\sqrt{\frac{\pi}{\alpha}}(s_j - s_n)]}{(s_j - s_n)} f(s_j) \hat{\mathbf{p}}_m \right]. \quad (7.36) \end{aligned}$$

7.3.2 Ewald Summation Implementation

We note that Eq. 7.36 has an infinite number of terms in both the real and Fourier sums. In practice, these sums are truncated after a certain number of terms such that the error in both the real and Fourier sums is below a certain tolerance level ϵ . In the real sum, the components of

the tensor $\mathbf{A}(\alpha, \mathbf{x})$ decay as we increase $r = |\mathbf{x}|$, and are also a function of the Ewald coefficient α . Therefore, specifying a value for ϵ and α implies that we can omit terms in the sum which are outside a cut-off radius r_c . Similarly, in the Fourier sum, specifying ϵ and α is the same as specifying the number of reciprocal lattice vectors included in the summation, which we denote by K . In our simulations, the value of ϵ is first specified. We found that $\epsilon \sim 10^{-6}$ was a suitably low tolerance level. Once ϵ is specified, the values of α , r_c and K are chosen so as to minimize the cost of both real and Fourier sums. From Eqs. 7.30 to 7.33, we see that the Ewald coefficient α controls the relative contributions of the real and Fourier sums to the total velocity disturbance. A small value of α implies that the Fourier sum has a greater contribution, so that we need a larger number of wave vectors (K) to achieve a given error tolerance ϵ . This also means that the cut-off radius can be kept small for the real sum. A larger value of α means the real sum has a greater contribution so that r_c needs to be increased to achieve the same error tolerance. The number of wave vectors needed in the Fourier sum is now reduced. In summary, for a given value of the error tolerance ϵ , the cut-off radius r_c scales directly with the Ewald coefficient α , while the total number of wave vectors K scales inversely.

7.4 Swimmer Kinematics

Once we have calculated the disturbance velocity along each swimmer's length, we can now calculate the translational and angular velocities of the swimmers so as to update their positions and orientations. Since the swimmers are considered as slender rods, the coupling between the disturbance velocity and the swimmer kinematics is achieved through viscous slender body theory (Batchelor (1970), Leal (2007)). The force balance on the swimmer involves the zeroth moment of the disturbance velocity field, and can be written as:

$$\int_{-1}^1 [C_L \hat{\mathbf{p}}\hat{\mathbf{p}} + C_N(\mathbf{I} - \hat{\mathbf{p}}\hat{\mathbf{p}})] \cdot (\mathbf{u} - \dot{\mathbf{x}}_{GC}) ds + F_T \hat{\mathbf{p}} = 0. \quad (7.37)$$

Here, C_L and C_N are the drag coefficients for motion parallel and perpendicular to the swimmer's axis and $\dot{\mathbf{x}}_{GC}$ is the velocity of the geometric centre of the swimmer. For the sake of simplicity, we assume that the longitudinal drag coefficient C_L is the same for both the head and tail portions of the swimmer. F_T is the magnitude of the total non-dimensional thrust force generated by the tail portion of the swimmer. However, since the tail portion of the swimmer also experiences a drag force, the net thrust driving the swimmer (and balancing the drag F_D on the head portion), is the difference between the total thrust F_T and the drag on the tail. We note that the drag on the tail is given from the portion of the first integral in Eq. 7.37 over the tail portion of the swimmer. In the above expression, \mathbf{u} is the 'ambient' velocity field at a given swimmer due to all other swimmers which was derived in an earlier section. The net force on the swimmer is zero, in keeping with the force-free requirement in the Stokes regime.

In our simulations, the drag due to the head (or body) of the swimmer which is assumed to be a spheroid of aspect ratio $r_e = 2$, and length equal to half the swimmer length with the longer axis aligned with the swimmer axis. This shape is found in swimmers such as *E. Coli*, but will be used here for both pushers and pullers. The drag on such a spheroid is given by $F_D = C_s \mu U L_H$, where C_s is the drag coefficient for the spheroid translating along its longer

axis and is given in [Subramanian & Koch \(2009\)](#). In non-dimensional terms the net thrust/drag force is give as $F_D = F_D/F_c = 2C_s$, since in our case $L_H = L/2$. Taking the scalar product of Eq, [7.37](#) with $\hat{\mathbf{p}}$, we get a relation for the force balance along the swimmer axis which is given by:

$$C_L \int_{-1}^1 \hat{\mathbf{p}} \cdot (\mathbf{u} - \dot{\mathbf{x}}_{GC}) ds + F_T = 0. \quad (7.38)$$

Solving for the magnitude of the component of $\dot{\mathbf{x}}_{GC}$ along the swimmer axis, we get:

$$\dot{\mathbf{x}}_{GC} \cdot \hat{\mathbf{p}} = 1 + \frac{1}{2} \left(\int_{-1}^1 \mathbf{u} \cdot \hat{\mathbf{p}} ds \right), \quad (7.39)$$

where the constant velocity of unity is just the non-dimensional swimming velocity of the swimmer. Similarly equating the components of the force normal to the swimming axis in Eq. [7.37](#), we get:

$$2C_N [\dot{\mathbf{x}}_{GC} - (\dot{\mathbf{x}}_{GC} \cdot \hat{\mathbf{p}})\hat{\mathbf{p}}] = C_N (\mathbf{I} - \hat{\mathbf{p}}\hat{\mathbf{p}}) \cdot \int_{-1}^1 \mathbf{u}(s) ds, \quad (7.40)$$

which can be simplified to:

$$\dot{\mathbf{x}}_{GC} - (\dot{\mathbf{x}}_{GC} \cdot \hat{\mathbf{p}})\hat{\mathbf{p}} = \frac{1}{2} (\mathbf{I} - \hat{\mathbf{p}}\hat{\mathbf{p}}) \cdot \int_{-1}^1 \mathbf{u}(s) ds. \quad (7.41)$$

Adding Eq. [7.39](#) (times the orientation vector $\hat{\mathbf{p}}$) with [7.41](#) we get the total translational velocity of the swimmer as:

$$\dot{\mathbf{x}}_{GC} = 1\hat{\mathbf{p}} + \frac{1}{2} \left(\int_{-1}^1 \mathbf{u} ds \right). \quad (7.42)$$

Writing in terms of a discrete integral to be used in simulations, we get:

$$\dot{\mathbf{x}}_{GC} = 1\hat{\mathbf{p}} + \frac{1}{2} \left(\sum_{j=1}^M \mathbf{u}(s_j) \right), \quad (7.43)$$

where the quadrature weights are already included in $\mathbf{u}(s_j)$. The torque balance on the swimmer involves the first moment of the disturbance velocity and can be written as:

$$\int_{-1}^1 \{s\hat{\mathbf{p}} \times C_N [(\boldsymbol{\Omega} \times \hat{\mathbf{p}})s - \mathbf{u}(s)]\} ds = 0, \quad (7.44)$$

where $\boldsymbol{\Omega}$ is the angular velocity of the swimmer. We note that the swimmers being slender, the angular velocity component along their axis is assumed to be zero i.e $\boldsymbol{\Omega} \cdot \hat{\mathbf{p}} = 0$. Solving, we get $\boldsymbol{\Omega}$ as:

$$\boldsymbol{\Omega} = \frac{3}{2} \hat{\mathbf{p}} \times \int_{-1}^1 s \mathbf{u}(s) ds. \quad (7.45)$$

Which in terms of a discrete integral is given by:

$$\boldsymbol{\Omega} = \frac{3}{2} \hat{\mathbf{p}} \times \sum_{j=1}^M w_j s_j \mathbf{u}(s_j). \quad (7.46)$$

Eqs. [7.43](#) and [7.46](#) give the instantaneous translational and angular velocities of the swimmer

and are used to update the position and orientation of the swimmer at the next time step.

The periodic boundary conditions implies that the swimmers leaving the simulation box need to be placed back using some rule. The rule followed in our simulations is as follows

$$\text{If } x_i \geq L_{box} \text{ then, } x_i = x_i - L_{box} \quad i = 1, 2, 3, \quad (7.47)$$

$$\text{If } x_i \leq 0 \text{ then, } x_i = x_i + L_{box} \quad i = 1, 2, 3, \quad (7.48)$$

where x_i for $i = 1, 2, 3$, are the Cartesian components of the swimmer's position measured relative to a coordinate system whose origin is at vertex of the simulation unit cell.

7.5 Tumbling and Rotary Diffusion Models

7.5.1 Tumbling

Micro-scale swimmers in nature rarely swim in a straight line, even in isolated conditions. Intrinsic orientation decorrelations are a common feature of their motion, where here intrinsic refers to the fact that these occur independently from the orientation de-correlations due to interactions with other swimmers. A novel aspect of this work is that we study the effects of two such intrinsic orientation decorrelation mechanisms, namely, *tumbling* and *rotary diffusion*, a combination of which is observed in the motion ('run-and-tumble' dynamics) of bacteria. The term 'tumbling' refers to the case where the bacterium runs in a directed sense for a certain amount of time before changing its orientation abruptly, and by a large amount. This change in orientation is termed a tumble event and usually lasts for a small duration when compared to the run. For *E. Coli*, the mean-run-time (mean time elapsed between two tumbles) $\tau \sim O(1s)$. The tumbles themselves are of much shorter duration lasting about 0.1s and can therefore be regarded as practically instantaneous (see Fig. 7.5). Having changed its orientation during the tumble, the bacterium once again runs in the new direction which may be correlated to the old one. Such a run-and-tumble motion, on large length scales leads to a random walk in three dimensions that may be characterized by a diffusivity given, for perfectly random tumbles, by $U^2\tau/3$, where U is the swimming speed and τ is the mean-run-time. *E. Coli* use such a run-and-tumble motion, with biased runs, to perform *chemotaxis*, which is a net motion up a favourable chemical gradient in the fluid. Fig. 7.5 shows the dynamics of this run-and-tumble motion for *E. Coli*. In our simulations, we characterize this random walk using a single parameter which is the mean time between two tumble events, or the mean-run-time, denoted by τ . In a homogeneous medium free from chemical gradients, the run-and-tumble statistics are well approximated by a Poisson process (Berg (1993)). The probability of occurrence of exactly n tumbles in a time interval t is:

$$P(n) = \frac{\exp(-t/\tau)(t/\tau)^n}{n!}. \quad (7.49)$$

The time between two tumbles is therefore exponentially distributed with a mean τ . Another parameter characterizing the run-and-tumble events is the correlation, if any, between the pre and post tumble orientations, denoted respectively by $\hat{\mathbf{p}}$ and $\hat{\mathbf{p}}'$. Perfectly random tumbles, where there is no correlation, lead to a mean angle between pre and post-tumble orientations

of 90 degrees (i.e. $\langle \hat{\mathbf{p}} \cdot \hat{\mathbf{p}}' \rangle = 0$). In the case of *E. Coli*, the tumbles are known to have a weak forward correlation with the mean re-orientation being around 68 degrees (Berg (1993)). In our simulations we assume that the tumbles are perfectly random with no correlations between pre and post-tumble orientations as the presence or absence of such a correlation is expected to have no qualitative effect on the phenomenon of interest-collective dynamics. Indeed, it was shown by Subramanian & Koch (2009) that the threshold concentration for the onset of collective behaviour changed by a negligible amount for the case of a forward correlation of 68 degrees when compared to uncorrelated tumbles.

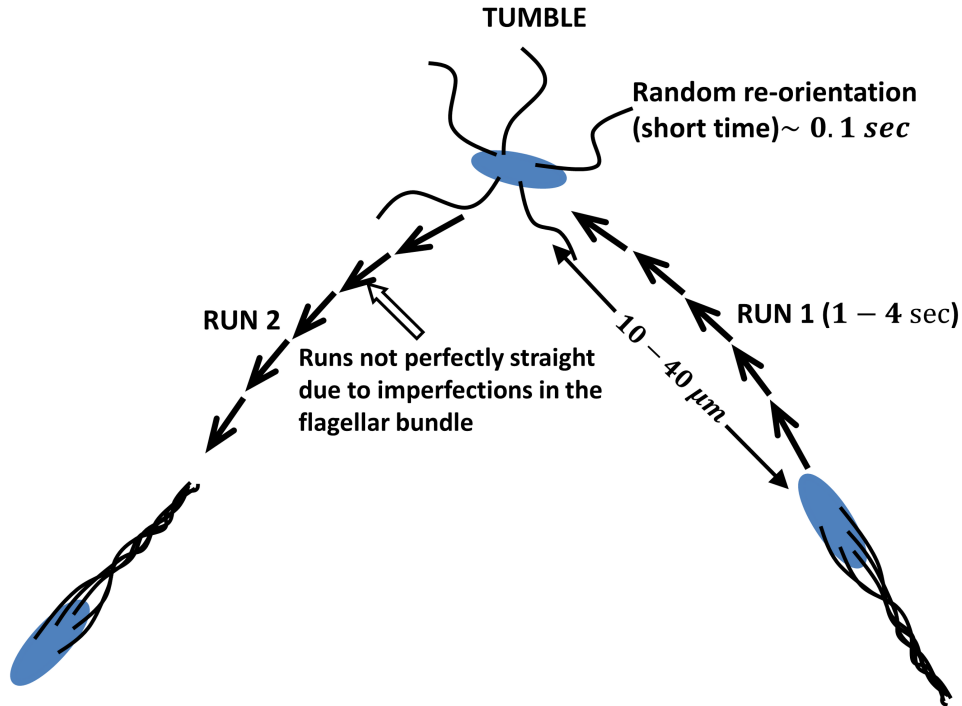


Figure 7.5: A schematic of the run-and-tumble motion executed by peritrichously flagellated swimmers such as *E. Coli*. Reproduced in part from Subramanian & Nott (2012)

Implementation of the Tumbling Model

The implementation of the Poissonian run-and-tumble statistics on a computer makes use of the fact that the probability per unit time that a given run ends is constant. This is because the duration of a given run does not depend on the durations of runs that precede it. We define the mean tumble frequency as $\lambda = 1/\tau$. The Poissonian statistics imply that the probability of a tumble occurring in a given interval Δt is given by $\lambda\Delta t$. We note that this expression is strictly valid only when Δt is a differential quantity; and that the time step used in our simulations is small enough for this relation to hold. Thus, to decide whether a swimmer tumbles during a given time step, a random number is generated which is uniformly distributed between 0 and 1. If this number is less than or equal to $\lambda\Delta t$, then the swimmer is said to tumble and we choose a new orientation for it. If the random number is greater than $\lambda\Delta t$, then the swimmer does not tumble and continues its run. The new orientation, for a swimmer which tumbles, is chosen by generating new random numbers which ensure a uniform distribution of the orientation vector on the unit sphere; this implements a single random tumble event. The details are as

follows. For swimmers that tumble, two additional random numbers are generated, the first uniformly distributed in the interval $[0, 1]$ and the second uniformly distributed in the interval $[-1, 1]$. Let us denote the two random numbers by R_1 and R_2 , respectively. Consider a spherical coordinate system, with θ and ϕ as the polar and azimuthal angles, respectively, with its polar axis aligned with the pre-tumble orientation vector of the swimmer. The ϕ coordinate of the post-tumble orientation is then uniformly distributed in the interval $[0, 2\pi]$, and is therefore given by $\phi = 2\pi R_1$. For a uniform distribution over the unit sphere, the probability distribution in θ must be such that the probability of the angular deviation lying in the interval $(\theta, \theta + d\theta)$ must be proportional to the area of the sector between θ and $\theta + d\theta$ divided by the area of the unit sphere 4π . Mathematically, this is:

$$P(\theta)d\theta = \frac{2\pi \sin \theta d\theta}{4\pi}, \quad (7.50)$$

which automatically gives:

$$P(\theta) = \sin \theta / 2. \quad (7.51)$$

This distribution can be generated using the uniformly distributed random variable R_2 by using the transformations:

$$\cos \theta = R_2, \quad (7.52)$$

$$\sin \theta = (1 - R_2^2)^{1/2}. \quad (7.53)$$

Thus, we have found the (θ, ϕ) for the post-tumble orientation such that it is uniformly distributed on the unit sphere.

7.5.2 Rotary Diffusion

While tumbling causes large changes in orientation of the swimmer, there are small fluctuations in the swimmer orientation even during a run (see Fig. 7.5). This can be seen in tracks of *E. Coli*, whose trajectories are not straight even during a run and show a mean deviation of around 27 degrees (Berg (1993)). The cause for these small orientation changes have been attributed to imperfections in the flagellar bundle in the case of *E. Coli* (Subramanian & Nott (2012)), but more generally these may arise due to imperfections in the swimming mechanism employed particularly when the swimmer is too large to be subject to thermal (Brownian) torques. These small changes in the orientation during a run can be modelled as a rotary diffusion process. Thus, a cell moving in a given direction executes a two-dimensional random walk in the tangent plane orthogonal to its orientation vector corresponding to (θ, ϕ) , where θ and ϕ are from a spherical polar coordinate system with polar axis aligned with the given swimming direction (see Fig. 7.6). The mean angular deviation is therefore given by:

$$\langle \Delta\theta^2 \rangle = 4D_r \Delta t, \quad (7.54)$$

where D_r is the rotational diffusivity of the swimmer. We note that the above identity is only valid for motion in the tangent plane and therefore only accurate for small $\Delta\theta$ and Δt .

Implementation of Rotary Diffusion Model

In simulations the rotary diffusion is modelled as a two-dimensional random walk on the unit sphere (see Fig. 7.6). To do this we simulate a two-dimensional random walk on a plane and enforce that the displacements are small. With this assumption, the effects of curvature are negligible, and the plane may be mapped to the unit sphere surface which appears locally planar for small displacements. This places an upper limit on the time-step which can be used in the simulations. The angular displacement due to rotary diffusion in a given time step Δt is added as a random displacement of amplitude A , such that:

$$\Delta\theta = AR_n, \quad (7.55)$$

where R_n is a random variable uniformly distributed in the interval $[-1/2, 1/2]$. For the swimmer to undergo a two-dimensional random walk, we must have:

$$\langle\theta^2\rangle = 4D_r t, \quad (7.56)$$

which for a given time step becomes $\langle\Delta\theta^2\rangle = 4D_r\Delta t$. Substituting for $\Delta\theta$ from Eq. 7.55, we have:

$$\langle\Delta\theta^2\rangle = A\langle R_n^2\rangle = \frac{A}{12} = 4D_r\Delta t, \quad (7.57)$$

which gives us an expression for the amplitude as $A = (48D_r\Delta t)^{1/2}$. Thus we have:

$$\Delta\theta = (48D_r\Delta t)^{1/2}R_n. \quad (7.58)$$

This gives us the angular displacement of the swimmer's orientation vector. However, this only specifies a cone of half-angle $\Delta\theta$ about the swimmer's initial orientation (see Fig. 7.6). The ϕ angle is again uniformly distributed in the interval $[0, 2\pi]$ and is generated in exactly the same way as in the tumbling case by generating a random variable R uniformly distributed in $[0, 1]$ and specifying $\phi = 2\pi R$.

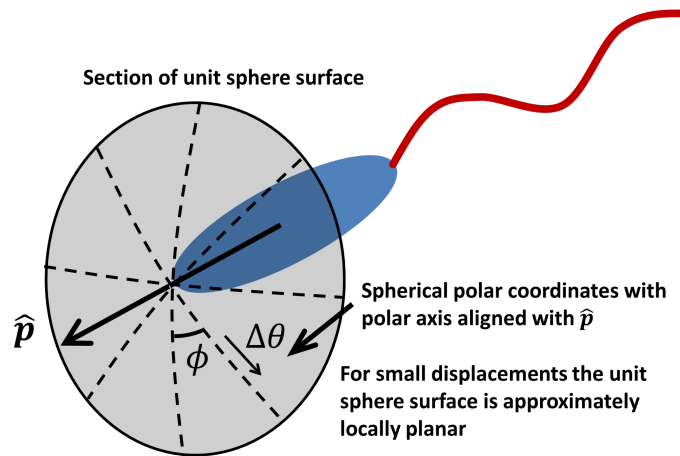


Figure 7.6: A schematic of the rotary diffusion model used. We see a section of a unit sphere on which the tip of the swimmer's orientation vector executes a two-dimensional random walk. The step size is denoted by $\Delta\theta$ and can occur with equal probability in any ϕ direction.

7.5.3 Validation of Tumbling and Rotary Diffusion Models

In order to validate our tumbling model, we do test simulations of 10000 swimmers which do not hydrodynamically interact but tumble with a mean-run-time of τ . Thus, the orientation de-correlation of the swimmers is due to tumbling alone. We compare the simulated variation of orientation decorrelation measures $\langle \hat{\mathbf{p}}(t) \cdot \hat{\mathbf{p}}(0) \rangle$, $\langle (\hat{\mathbf{p}}(t) \cdot \hat{\mathbf{p}}(0))^2 \rangle$ and swimmer mean-square-displacement, with time, and compare them to theoretical predictions of the same. It can be shown (Navaneeth K. Marath (2013)) that the mean-square-displacement of a swimmer which tumbles is given by:

$$\langle r^2(t) \rangle = 2U^2\tau^2 \left[\frac{t}{\tau} - 1 + \exp(-t/\tau) \right] \quad (7.59)$$

or

$$\frac{\langle r^2(t) \rangle}{6t} = \frac{U^2\tau}{3} \left[1 - \frac{t}{\tau} (-1 + \exp(-t/\tau)) \right]. \quad (7.60)$$

The swimmer diffusivity can be derived from Eq. 7.60 by taking the limit $t \rightarrow \infty$, and is seen to be given by $D_{swimmer} = U^2\tau/3$ as mentioned earlier. The aforementioned orientation moments are given by:

$$\langle \hat{\mathbf{p}}(t) \cdot \hat{\mathbf{p}}(0) \rangle = \exp(-t/\tau), \quad (7.61)$$

$$\langle (\hat{\mathbf{p}}(t) \cdot \hat{\mathbf{p}}(0))^2 \rangle = \frac{1}{3} (2 \exp(-t/\tau) + 1). \quad (7.62)$$

Figs. 7.7a and 7.7b show comparisons between theory and simulations for the three measures in Eqs. 7.60, 7.61 and 7.62 for two values of the mean run time of $\tau = 1$ and $\tau = 10$ respectively. The time steps used are $\Delta t = 0.05$ and $\Delta t = 0.2$, respectively. The computer simulation of Poissonian statistics requires that the number of tumble events occurring during a time step must be small, thereby placing a restriction on the time step used relative to the mean-run-time ($\Delta t/\tau \ll 1$). In practice we see that a $\Delta t/\tau \approx 0.2$ is sufficient to ensure faithful reproduction of the theoretical curves by the simulations. It can be seen in Figs. 7.7a and 7.7b that there is very good agreement between the simulations and theoretical predictions both with respect to the swimmer mean-square-displacement as well as the orientation decorrelation measures.

We now present a similar validation of the rotary diffusion model. As for the tumbling case, we consider 10000 non-interacting swimmers whose orientations decorrelate solely due to rotary diffusion. The theoretical predictions for the swimmer mean-square-displacement and orientation decorrelation are given by (Dhont (1996)):

$$\langle r^2(t) \rangle = \frac{U^2}{2D_r^2} [2D_r t - 1 + \exp(-2D_r t)], \quad (7.63)$$

or

$$\frac{\langle r^2(t) \rangle}{6t} = \frac{U^2}{6D_r} \left[1 - \frac{1}{2D_r t} (-1 + \exp(-2D_r t)) \right]. \quad (7.64)$$

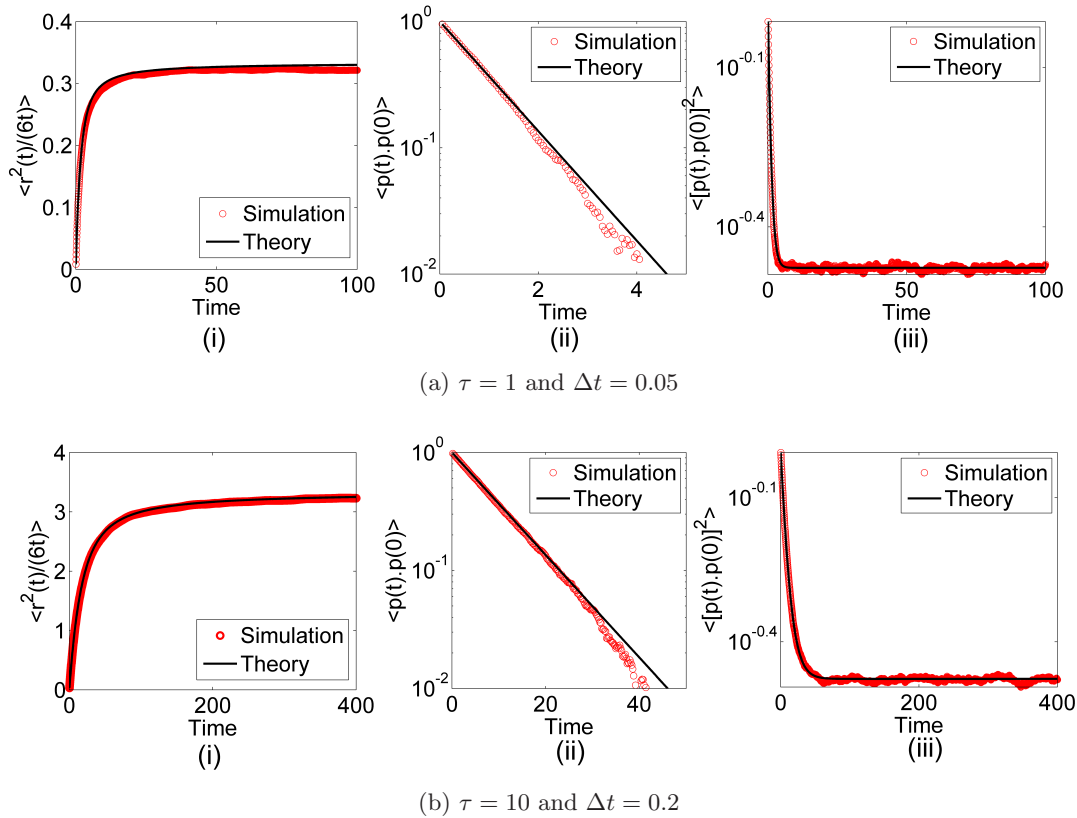


Figure 7.7: Comparison of simulations with theory of three time-dependent statistical quantities for swimmers which tumble. (i) The ratio of mean-square-displacement to time, $\langle r^2(t)/6t \rangle$, plotted with respect to time; (ii) orientation de-correlation measure $\langle \hat{\mathbf{p}}(t) \cdot \hat{\mathbf{p}}(0) \rangle$ and (iii) $\langle (\hat{\mathbf{p}}(t) \cdot \hat{\mathbf{p}}(0))^2 \rangle$ for (a) $\tau = 1$ and $\Delta t = 0.05$ and (b) $\tau = 10$ and $\Delta t = 0.2$.

and

$$\langle \hat{\mathbf{p}}(t) \cdot \hat{\mathbf{p}}(0) \rangle = \exp(-2D_r t). \quad (7.65)$$

Note that the expressions are the same as those for tumbling with τ replaced by $1/(2D_r)$. The swimmer diffusivity can again be derived by taking the limit $t \rightarrow \infty$ in Eq. 7.64, and is given by $D_{swimmer} = U^2/6D_r$.

Figs. 7.8a and 7.8b show comparisons between theory and simulations for the measures in Eqs. 7.64 and 7.65 for two values of the rotary diffusivity of $D_r = 0.5$ and $D_r = 0.02$, respectively. The time steps used are $\Delta t = 0.01$ and $\Delta t = 0.02$, respectively. In this case the restriction on the time step occurs because our rotational diffusion model approximates the unit sphere's surface as locally planar, therefore limiting the orientation displacement in a given time step. We find that $D_r \Delta t \approx 0.02$ is sufficient to reproduce the theoretical curves. We can see from Figs. 7.8a and 7.8b that, with a suitably chosen time step, there is indeed very good agreement between the simulation and theoretical predictions.

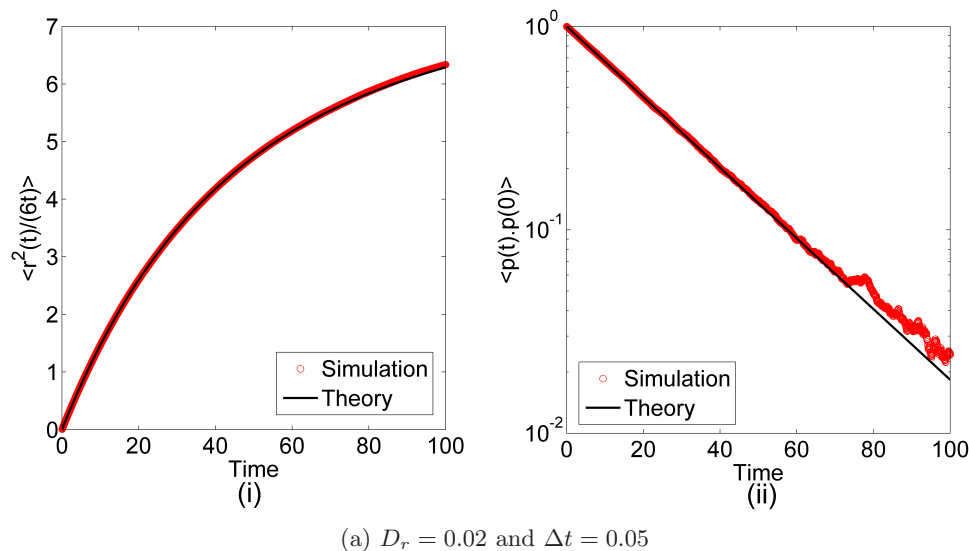
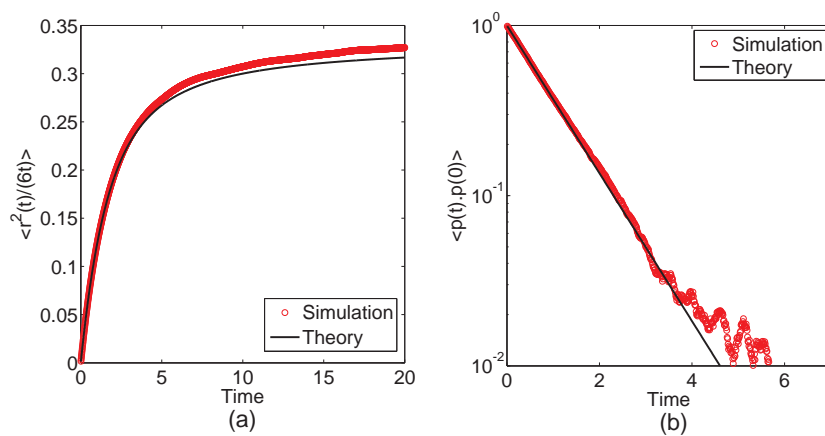
(a) $D_r = 0.02$ and $\Delta t = 0.05$ (b) $D_r = 0.5$ and $\Delta t = 0.01$

Figure 7.8: Comparison of simulations with theory of two time-dependent statistical quantities for rotary diffusing swimmers. (i) The ratio of mean-square-displacement to time, $\langle r^2(t)/6t \rangle$, plotted with respect to time and (ii) orientation de-correlation measure $\langle \hat{p}(t) \cdot \hat{p}(0) \rangle$ for (a) $D_r = 0.02$ and $\Delta t = 0.05$ and (b) $D_r = 0.5$ and $\Delta t = 0.01$.

7.6 Simulation Algorithm

In the preceding sections we have described the various components of the simulation. In this section we describe how they all come together. The initial condition for the simulation is specified by initializing the positions and orientations of the N swimmers in the simulation box. Defining $\mathbf{X} = \{\mathbf{x}_1, \mathbf{x}_2 \cdots \mathbf{x}_N\}$ and $\mathbf{P} = \{\hat{\mathbf{p}}_1, \hat{\mathbf{p}}_2 \cdots \hat{\mathbf{p}}_N\}$, we now initialize the simulation by setting $\mathbf{X} = \mathbf{X}_0$ and $\mathbf{P} = \mathbf{P}_0$. In our simulations the swimmers positions were uniformly distributed in the simulation box and their orientations were chosen to be uniformly distributed on the unit sphere. Note that the swimmers are assumed to be infinitely slender, and excluded volume considerations do not come into play (in swimmer-swimmer interactions). Thus, there is no restriction in the swimmers' (phase-space) coordinates. With the positions and orientations of all the swimmers known, we can compute the velocity disturbance at the quadrature points along the length of each swimmer using the Ewald summation formulation (Eq. 7.36). Since we neglect the induced forces on the swimmers, this step is an explicit operation and does not require any iterations for convergence, thereby leading to substantial savings in computational cost. Consideration of the induced forces would necessitate the solution of a system of linear equations at each step with the forces on the swimmers being the unknowns (as in Mackaplow & Shaqfeh (1998), Saintillan *et al.* (2005)). Once the velocity disturbance is known along the length of all the swimmers, we can use Eqs. 7.43 and 7.46 to calculate the translational and angular velocities of all the swimmers. Since the disturbance velocity at each swimmer is a function of the positions and orientations of all swimmers in the simulation box, we can write the instantaneous translational and angular velocities of the swimmers in a simple way (this is, of course due to the underlying instantaneity of the Stokes equations):

$$\dot{\mathbf{X}} = \mathcal{F}(\mathbf{X}, \mathbf{P}), \quad (7.66)$$

$$\dot{\mathbf{P}} = \mathcal{G}(\mathbf{X}, \mathbf{P}), \quad (7.67)$$

where \mathcal{F} and \mathcal{G} are functions which compute the velocity disturbance along the swimmer's lengths and therefore their translational and angular velocities. The explicit nature of the computation is apparent from the above expressions.

With this information we can now update the positions and orientations of all the swimmers using a suitable time-stepping scheme. In our simulations we find that a second-order Runge-Kutta scheme (Wheatley (1994)), with a suitable time step was sufficient to ensure converged results. In case of tumblers, the swimmers which tumble during the current time step are updated with a new orientation according to the tumbling model described in section 7.5.1. In case of rotary diffusers, a small noise is added to the orientation vector of all the swimmers according to the model in section 7.5.2. These new updated positions and orientations are used in the next time step and so on. Fig. 7.9 gives a flow chart describing the algorithm used in the simulations. Fig. 7.10 gives the details of the Runge-Kutta time stepping method.

The above simulation method was implemented using *MATLAB*, making use of its vectorized operations in order efficiently perform calculations on vectors whose size is $O(N)$. A local parallelization on up to 12 cores was used to speed up the simulations.

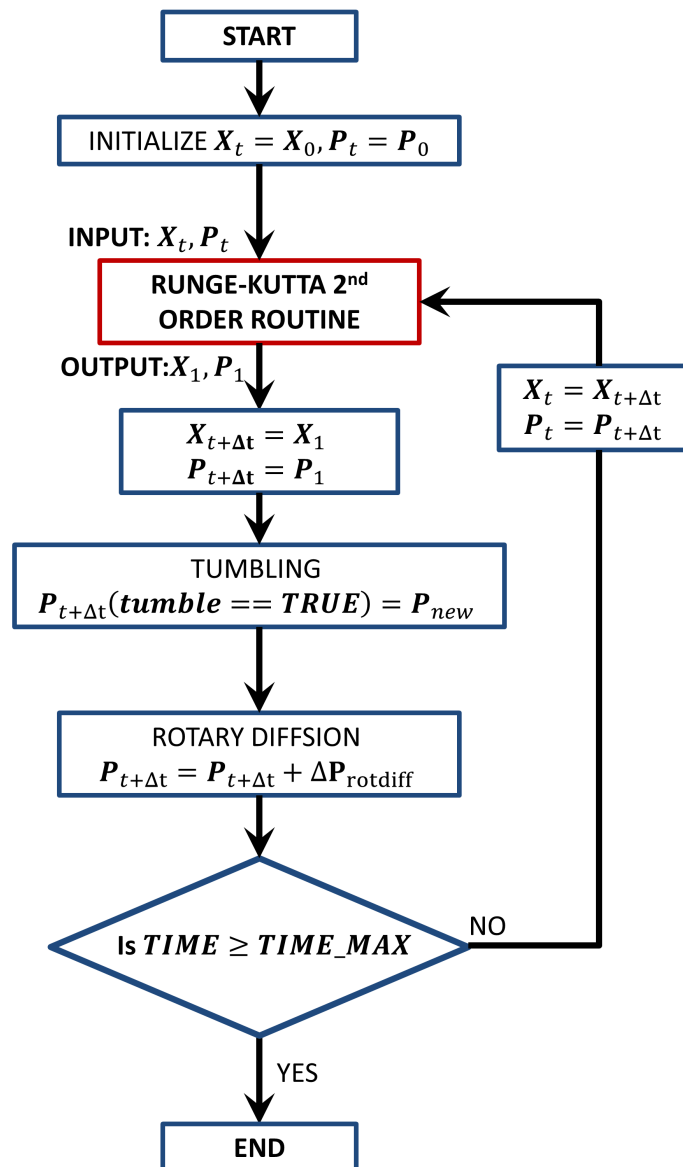


Figure 7.9: Simulation flow chart

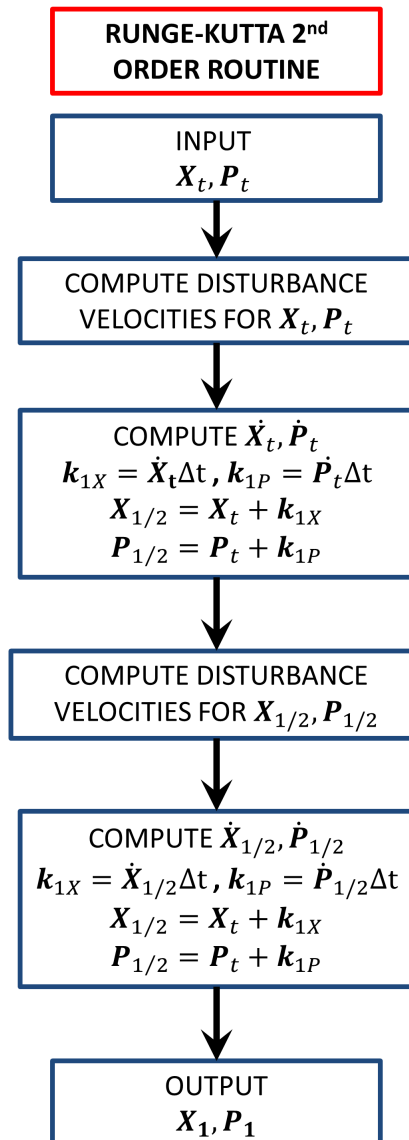


Figure 7.10: Runge-Kutta second order time stepping scheme

Chapter 8

Results and Discussion: Smooth Swimmers

8.1 Introduction

In this chapter we discuss the results of our simulations for the case of smooth swimmers. These swimmers do not possess any intrinsic orientation relaxation mechanisms, and therefore, their orientations decorrelate solely due to hydrodynamic interactions with other swimmers. Earlier simulation efforts have focussed on such smooth swimmers modelled either as slender rods (Saintillan & Shelley (2007), Saintillan & Shelley (2012)) or as regularized point dipoles (Underhill *et al.* (2008), Hernandez-Ortiz *et al.* (2009)). One of our motivations for studying them is to validate our simulation model, specifically, our assumption that the intrinsic stress due to swimming is sufficient for capturing the salient aspects of the collective behaviour. We will present results for both pusher and puller-type swimmers, with the pullers serving as a baseline for contrast, since they are predicted not to give rise to collective behaviour (Saintillan & Shelley (2008a)). We consider various statistical measures involving the swimmers, the intervening fluid and passive tracer particles to develop an understanding of the behaviour of swimmer suspensions. We are particularly interested in characterizing the predicted theoretical threshold, for the hydrodynamic instability (Saintillan & Shelley (2008a), Saintillan & Shelley (2008b), Subramanian & Koch (2009)) which leads to an onset of collective behaviour for the case of pushers, via our simulations. For the smooth swimmers examined in this chapter, we particularly study the effect of the simulation box size on the results. This is important since linear stability theory predicts a long wavelength instability, and therefore, that an unbounded suspension of pushers, that are smooth swimmers, is unstable for any non-zero volume fraction. However, this also means that a finite size simulation box stabilizes the suspension (by excluding the unstable range of wavelengths), and it is therefore of interest to study the effects of varying box size. We then compare the predicted box-size-dependent threshold for pushers, obtained from our simulations, with linear stability theory for an unbounded swimmer suspension (Subramanian & Koch (2009), Subramanian *et al.* (2011a)).

Unless otherwise mentioned all results are presented in dimensionless form with the following scaling parameters used for non-dimensionalization: the length scale is half the swimmer length $l_c = L/2$; the time scale is $t_c = L/2U$ which is the time for the swimmer to swim half its own length; the forces are scaled by $F_c = \mu UL/2$. Using these scales the parameters used in the simulations are as follows. The non-dimensional swimmer length L is 2 and velocity U is 1. We consider cubic simulation boxes ranging from $L_{box} = 5L$ to $L_{box} = 15L$ in order to study the effects of the box size. The volume fraction of the suspension is defined as $\nu = N(L/2)^3/L_{box}^3$ ¹,

¹We note that, the volume fraction as defined above is not the true volume fraction, but is the hydrodynamic

and is varied between the dilute and semi-dilute regimes ($\nu = 0.05 - 1.0$), N being the number of swimmers in the box. In this chapter we consider only smooth swimmers, and this corresponds to a mean-run-time of $\tau \rightarrow \infty$.

8.2 Theory for Smooth Swimmers

In this section we briefly go over earlier theoretical works which have considered the stability of a suspension of smooth swimmers. The linear stability of a suspension of rod-like swimmers like those considered here was carried out by [Subramanian & Koch \(2009\)](#), [Subramanian *et al.* \(2011a\)](#), and independently, by [Saintillan & Shelley \(2008b\)](#). A simple scaling analysis allows us to appreciate the salient aspects of the instability. Consider an initially quiescent swimmer suspension with an isotropic distribution of swimmer orientations. A velocity perturbation with amplitude u' and wavenumber k , which has a velocity gradient $O(ku')$, acts to reorient a swimming bacterium during the time it traverses a single wavelength. This time scale is $O(1/kU)$, where U is the swimming speed. The accumulated orientation anisotropy during this time is $O(u'/U)$. The bacterial stress is given as a density of force dipoles and is $O(nFL)$, where n is the swimmer number density, F the magnitude of the force characterizing the force dipole and L is the swimmer length scale. In an isotropic suspension, this stress is isotropic, and therefore does not modify the viscosity. But it can do so when there is an orientational anisotropy. Thus, the bacterial stress contributing to the viscosity is $O(u'/U)O(nFL)$. We can take $F \sim \mu UL_H$, where L_H is the length of the swimmer head. Thus the bacterial stress is $O(\mu u' n L L_H)$. The stabilizing Newtonian response to the velocity perturbation is $O(\mu k u')$. For a suspension of pushers, due to the extensile nature of the dipole, the bacterium stress opposes the Newtonian response and we have an instability when $\mu u' n L L_H > \mu k u'$, which gives $k < n L_H L$. Since $L_H = \alpha_1 L$, where α_1 is the fraction of head length to total swimmer length, we have the final condition for the instability as $k < O(n L^2)$, or in terms of the perturbation wavelength, $\lambda > O(n L^2)^{-1}$. Thus, a suspension of pushers is always unstable to sufficiently long-wavelength perturbations. This result also implies that, for an unbounded suspension where the largest allowed wavelengths are infinite, the critical volume fraction for the instability is zero.

Therefore, the main results of the linear stability analysis are that pushers are unstable in the limit of long-wavelength velocity perturbations. [Fig. 8.1](#) shows the modal diagram for a suspension of smooth swimming pushers that emerges from a detailed linear stability analysis ([Subramanian *et al.* \(2011a\)](#), [Subramanian & Nott \(2012\)](#)). We see that, in the limit $k \rightarrow 0$, there are a pair of unstable modes. Of these, it is ‘mode 1’ that controls the stability of the suspension to long wavelength perturbations. The growth rate of this mode remains finite and positive, even at $k \rightarrow 0$, indicating a long wavelength instability. This means that an unbounded suspension of smooth swimming pushers is unstable for any non-zero volume fraction, and there is a spectrum of modes with wavelengths of $O(n L^2)^{-1}$ or greater, that all grow at about the same rate of $O(n U L^2)$, the fastest of these being the $k = 0$ modes (see [Fig. 8.1](#)). Unlike pushers, pullers are characterized by a negative value of C and therefore have only decaying modes leading to a stable suspension.

volume fraction; however, this is the relevant parameter in our study, since Stokesian hydrodynamics is dictated by the *longest* length scales of the suspended swimmers.

While the results of [Subramanian *et al.* \(2011a\)](#) give a minimum critical wavenumber (or maximum critical wavelength) below which the suspension is unstable (the stability boundary in Fig. 8.1), there is also a second critical wavenumber k'_m separating the stationary unstable modes from oscillatory solutions (see Fig. 8.1). We consider the boundary between oscillatory and stable modes as the actual stability boundary. This stability boundary is given by the critical wavenumber:

$$k'_m = 0.09CnL^2, \quad (8.1)$$

where n is the number density and L is the swimmer length as before. The constant C is defined as:

$$C = \int_{-1}^1 f(s)sd s, \quad (8.2)$$

where $f(s)$ is the intrinsic force density along the swimmer axis defined in chapter 7 in section 7.2. We note that as long as we interpret the stability threshold using the same C that characterizes the intrinsic force density, any choice of C remains consistent. In our case, the swimmers are *E. Coli*-like swimmers with a spheroidal head of aspect ratio 2 and the length of the head is such that $\alpha_1 = 1/2$. For such fore-aft symmetric swimmers, we get $C = M^{-1}/4$, where $C_L = M^{-1}$ and C_L is the drag coefficient for a spheroid translating along its axis ([Happel & Brenner \(1983\)](#)) and M^{-1} is the inverse of the mobility.

While the theory above predicts that any non-zero volume fraction leads to an instability for an unbounded suspension, the same is not true for the bounded periodic suspension examined in our simulations. The size of the simulation box imposes a restriction on the maximum wavelength (or minimum wavenumber) perturbation which can exist within the box. Thus, for small enough box sizes, the minimum unstable wavenumber can be greater than the critical wavenumber k'_m , implying that the suspension will be stabilized by the imposed periodicity. The simulation box therefore imposes an artificial stabilization for a suspension of pushers. An estimate of the critical concentration above which a periodic suspension is unstable may be calculated by equating the critical wavenumber k'_m with the inverse of the simulation box length:

$$k'_m = 0.09(Cn_{crit}L^2) = \frac{1}{L_{box}}, \quad (8.3)$$

which, on rearranging gives:

$$n_{crit} \left(\frac{L}{2}\right)^3 = \nu_{crit} = \frac{L}{0.72(CL_{box})}. \quad (8.4)$$

Note that we recover the unbounded suspension results of $\nu_{crit} = 0$ when $L/L_{box} \rightarrow 0$. The critical volume fraction for smooth swimmers given by Eq. 8.4 is plotted as a function of L/L_{box} in Fig. 8.2 and the L/L_{box} ratios for which we present simulation results are highlighted.

Physical Mechanism for the Hydrodynamic Instability: We briefly mention the mechanism proposed by [Subramanian & Koch \(2009\)](#) for the instability in a suspension of pushers. The random velocity disturbances experienced by a swimmer in a suspension due to other swimmers can be studied in the form of a imposed velocity wave (Fourier mode). Consider such a long wavelength velocity perturbation, as shown in Fig. 8.3, imposed on a suspension of three

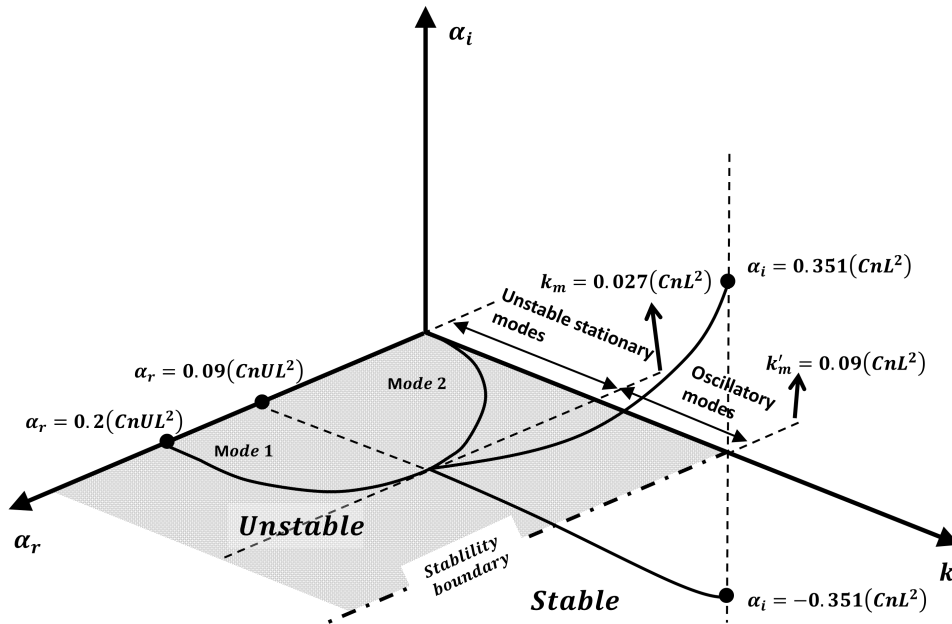


Figure 8.1: Modal digram for a suspension for smooth swimming pushers. Reproduced from [Subramanian *et al.* \(2011a\)](#)

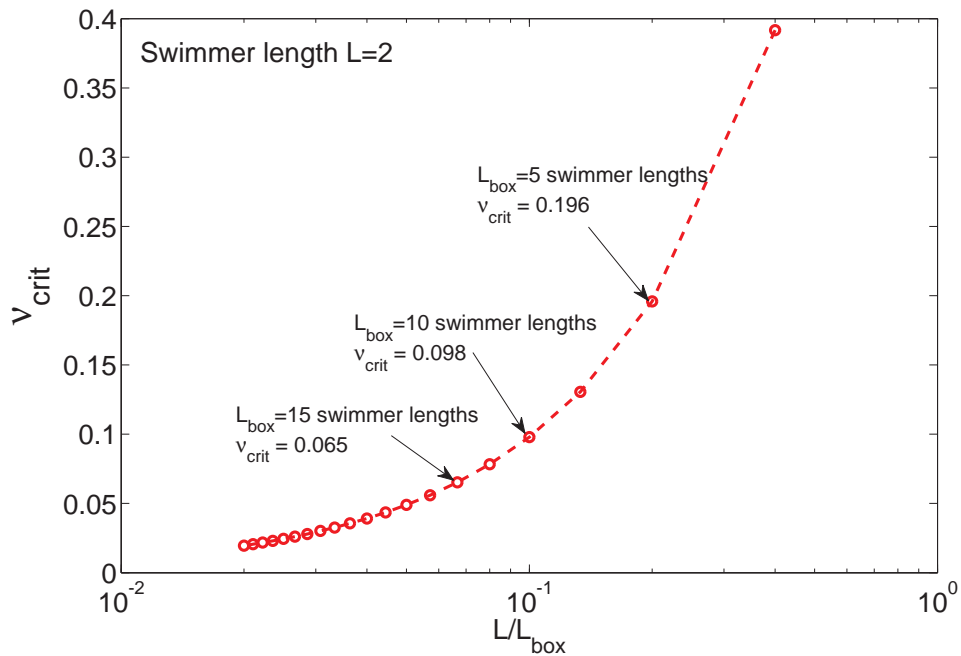


Figure 8.2: Variation of critical volume fraction for onset of instability ν_{crit} with the simulation box size

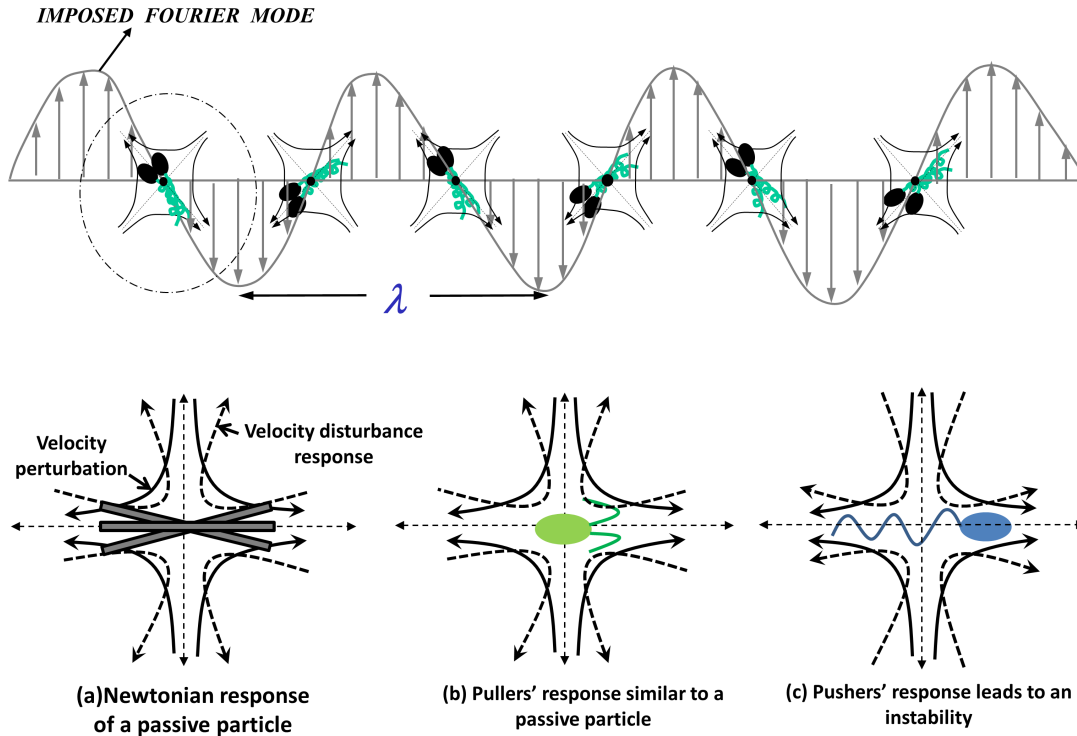


Figure 8.3: Schematic depiction of the response of three types of slender particles to a velocity wave perturbation (Fourier mode) (a) passive rods, (b) puller-type swimmers and (c) pusher-type swimmers.

different types of microscopic slender particles (a) passive rods (b) puller-type swimmers and (c) pusher-type swimmers. When the particle length is small compared to the wavelength of the perturbation, the velocity gradient over the length scale of a particle is constant at leading order. This is typically the case when the length scale of confinement of the suspension is much larger than the length scale of the suspension constituents which is the case with our simulations too, since it is the longest wavelength perturbation, with wavelength of order the box size, that becomes unstable at the threshold. The velocity perturbation can therefore be imagined as a simple shear flow (a constant velocity gradient) at the particle/swimmer location. The vortical component of the simple shear flow causes the slender particles to rotate at a constant angular velocity without affecting the orientation distribution of the suspension. The extensional flow, however, makes the particles align along the local extensional axis, thereby leading to an anisotropy in the orientation distribution. In the case of a passive rod the inextensibility constraint of the rod leads to a passive (induced) stress distribution on the rod which opposes the aligning extensional flow (see Fig. 8.3 (a)). The response of a puller is similar, except that the opposing flow is due to the anisotropic distribution of intrinsic (rather than induced) contractile swimming dipole (see Fig. 8.3 (b)). Both these are Newtonian-type responses which act to damp out the velocity disturbance acting on the particles. In a suspension of pushers, however, the intrinsic extensile dipole enhances the imposed disturbance which in turn exacerbates the original orientational anisotropy, thus leading to an instability (see Fig. 8.3 (c)).

8.3 Simulation Results and Discussion

8.3.1 Fluid Velocity Statistics

We first contrast the disturbance velocity field in the suspending fluid between pusher and puller suspensions. Fig. 8.4 shows the typical disturbance velocity fields for a suspension of pushers and pullers at volume fractions of 0.05 and 0.5 at a single time instant in the statistical steady state. At the lower volume fractions, the fluctuations are only those due to individual uncorrelated swimmers which die off rapidly as we move away from the swimmer, leaving most of the fluid quiescent (Fig. 8.4a). In the suspension of pushers, as one moves to larger volume fractions, one begins to see coherent jets and vortices in the fluid on length scales larger than the particle size (see Fig. 8.4b(i)). These flows are qualitatively similar to the flows observed in experiments (Mendelson *et al.* (1999), Sokolov *et al.* (2007), Dombrowski *et al.* (2004)) of swimming bacteria such as *E. Coli* and *B. subtilis*, which are pusher-type swimmers. It is also in qualitative agreement with previous simulation results (Saintillan & Shelley (2007), Saintillan & Shelley (2012)). Pullers, on the other hand, continue to show an uncorrelated velocity field even at larger volume fractions where the fluctuations are small-scale and random, corresponding to disturbances due to individual swimmers (Fig. 8.4b(ii)). Indeed, for the case of pullers, as we will see later, the fluid velocity correlation lengths actually decreases with an increase in volume fraction. To gain a quantitative picture of the flow field, we next look at the probability distribution function of the fluid velocity (individual components) and velocity magnitude (speed) which are plotted in Figs. 8.5a and 8.5b, respectively. The fluid velocity distribution functions in Fig. 8.5a are seen to be very similar for both pushers and pullers at low volume fractions. The fluctuations are small and the distribution function is quite narrow and sharply peaked around zero. As the volume fraction is increased, both the pusher and puller curves begin to broaden, this increase in variance reflecting larger fluctuations. However, these are much greater in magnitude for pushers, and this leads to a pronounced flattening of the probability distribution compared to that of pullers. The pusher curve for larger volume fractions ($\nu > 0.5$) begins to show a clear Gaussian behaviour as seen in Fig. 8.5a. Further insight may be gained by plotting the distribution function of the fluid velocity magnitude. Again, a clear distinction can be observed between pushers and pullers. At lower volume fractions, both pusher and puller curves have a sharp peak near zero, implying that the fluid velocity disturbance is due to individual swimmers and the rest state remains the most probable state. At higher volume fractions (for $\nu > 0.5$ in Fig. 8.5b) the pusher curves begin to show a clear peak at a non-zero value of the fluid velocity magnitude, implying that coordinated bulk motion is present. The peak is very pronounced at a fluid velocity magnitude of around unity, for the case $\nu = 1.0$, for pushers. In the case of pullers, it is striking that the peak of the probability density remains near zero for all the volume fractions simulated which points to an absence of coordinated fluid flows even at higher volume fractions; the rest state remains the most probable. Finally, we plot the mean fluid kinetic energy versus volume fraction for pushers and pullers in Fig. 8.5c for three different sizes of the simulation boxes (5, 10 and 15 swimmer lengths). The mean fluid kinetic energy for pullers shows an increase with volume fraction which is, however, much weaker than that for pushers. While the two are comparable in magnitude for low volume fractions ($\nu = 0.05$),

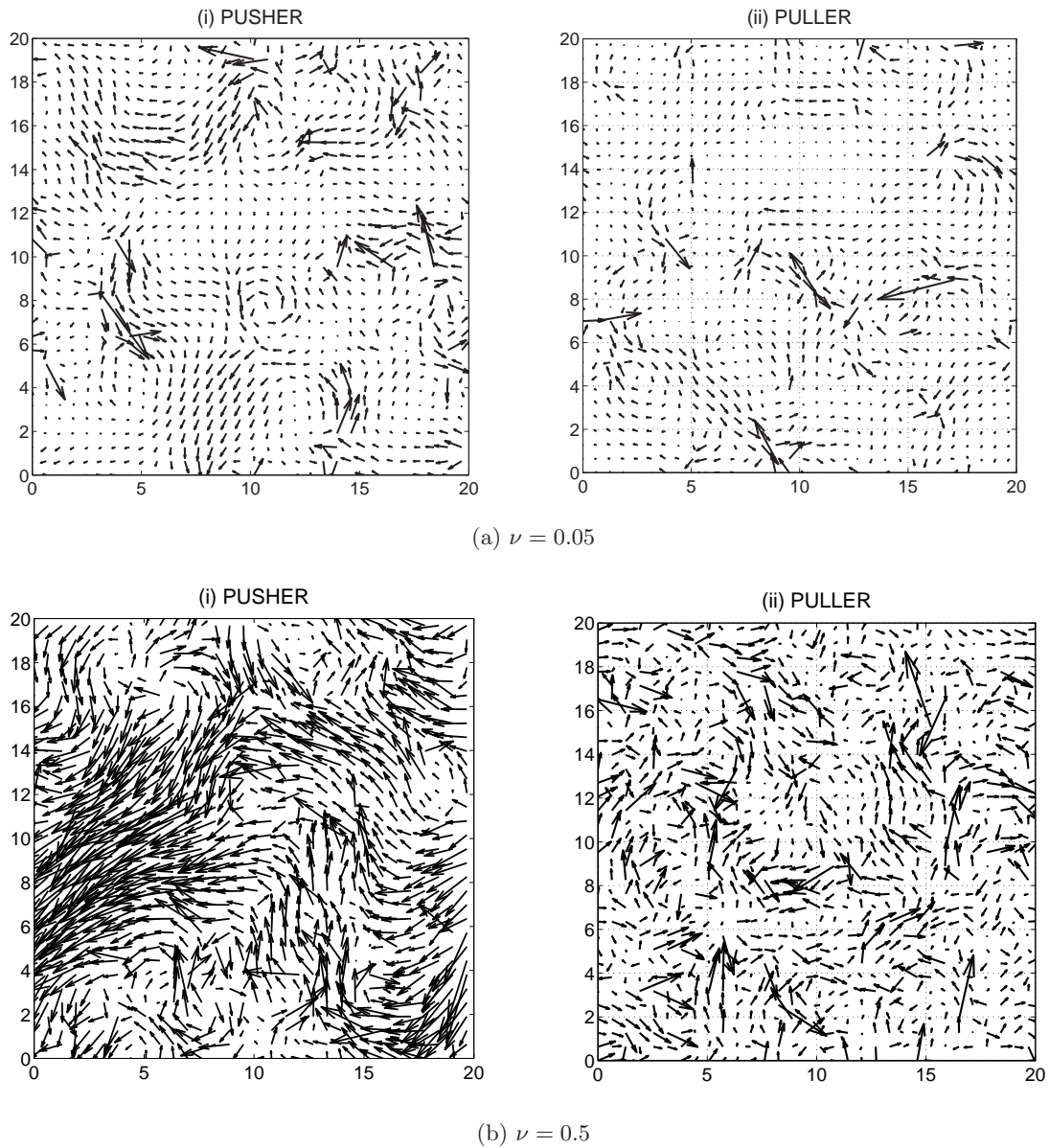


Figure 8.4: Projections on the x_1x_2 plane of fluid velocity vectors lying on a plane at half the height (in x_3 direction) of the simulation box for (a) $\nu = 0.05$ and (b) $\nu = 0.5$ for pushers and pullers. The simulation box size is 10 swimmer lengths ($L_{box} = 10L$).

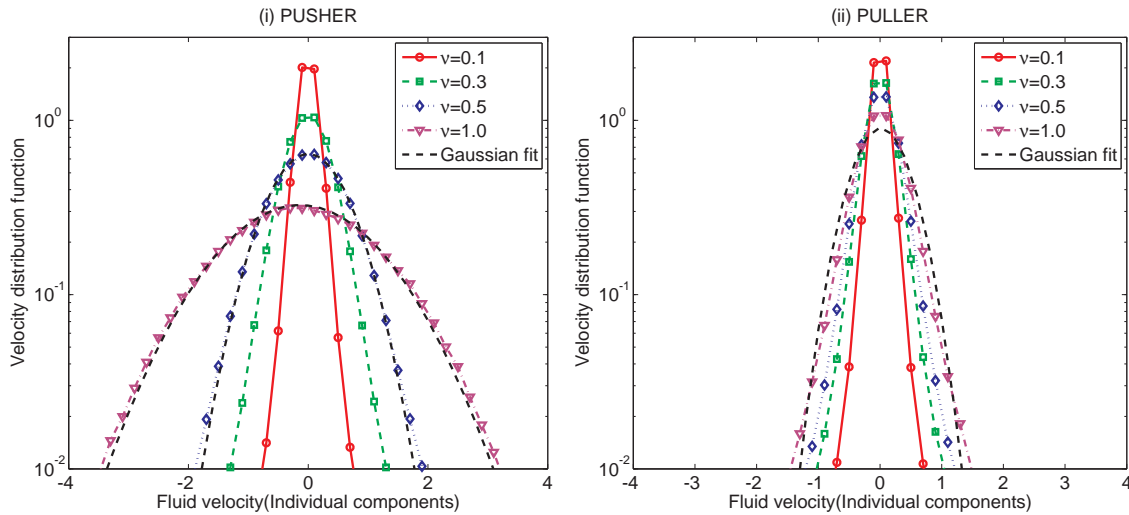
at higher volume fractions the pushers show much larger values (around an order of magnitude larger) arising from collective motion. The effect of box size is also clearly seen for the case of pushers with larger boxes leading to larger values of the fluid kinetic energy and also a steeper rate of increase with ν . This is consistent with linear stability theory in that the larger box sizes allow a greater range of unstable wavelengths, and thence, a more intense fluid motion.

The probability distribution function for the fluid velocities above showed us that the velocity fluctuations are much more pronounced for pushers as compared to pullers at high volume fractions. To gain an understanding of the time dependent dynamics of the flow field, we next look at the fluid velocity autocorrelation function. We consider the Eulerian autocorrelation function which measures the time scale for which the fluid velocity vector at a fixed point in space remains aligned in a given direction. This is formally defined as:

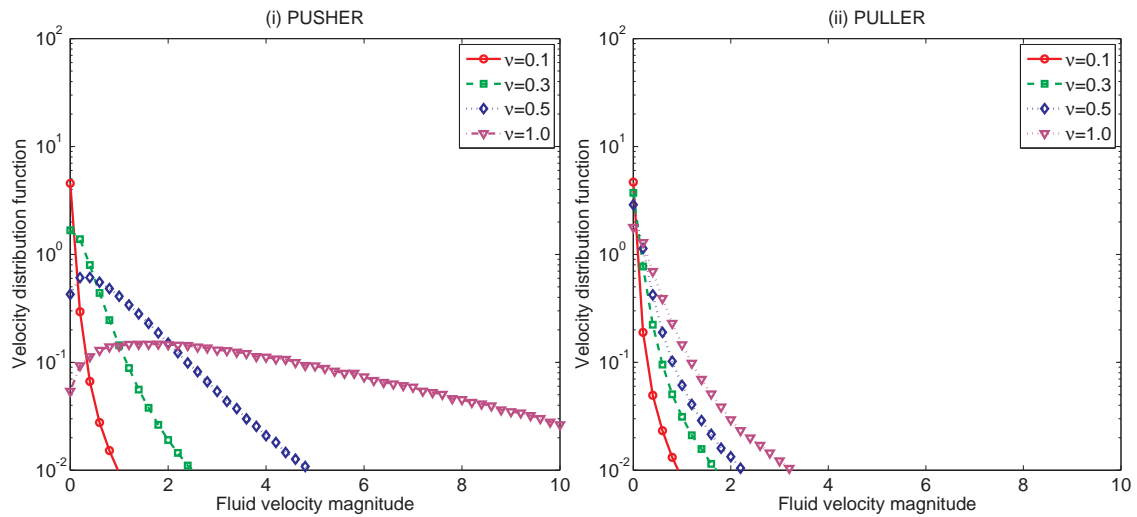
$$F(t) = \langle \mathbf{u}(\mathbf{x}, t) \cdot \mathbf{u}(\mathbf{x}, t_0) \rangle, \quad (8.5)$$

where the angular brackets $\langle \rangle$ denote an average over the number of grid points where the fluid velocity is calculated and also over the initial conditions t_0 , all of which lie in the statistical steady state. The plot of $F(t)$ is shown in Fig. 8.6a for pushers and pullers at different volume fractions. A trend is clearly visible for the pushers where the correlation time shows an initial increase with volume fraction reaching a maximum around $\nu = 0.5$. At these volume fractions, the correlated fluid motions for pushers are persistent over time scales much larger than the single swimmer time scale of $L/2U$ (7 times larger at $\nu = 0.5$). A bit surprisingly, further increasing the volume fraction leads to a decrease in the correlation times. The reasons for this decrease are not entirely apparent, but it may be attributed to a given point in space sampling an increased number of swimmers thereby leading to a randomization of the velocity field when compared to the correlated motions in space and time observed for smaller volume fractions ($\nu \approx 0.5$). The trend for pullers is clearly different from pushers in that they show a monotonic decrease in the correlation times with volume fraction as seen in Figs. 8.6a and 8.6b. This lends support to the fact that the absence of any hydrodynamic instability for the pullers means that the fluid velocities are controlled by individual uncorrelated swimmers. Thus, an increased puller volume fraction leads to an increased frequency of interactions of a fixed point in space with different swimmers, leading to a decrease in the Eulerian correlation times. Fig. 8.6b shows the correlation times, extracted from Fig. 8.6a, plotted as a function of the volume fraction. The correlation times were extracted by assuming a decay of the form $e^{-t/\tau_{corr}}$ and $-1/\tau_{corr}$ is calculated by fitting a straight line to $\ln(F(t))$ and extracting the slope of the line. The effect of box size can be clearly seen in Fig. 8.6b with larger simulation boxes leading to larger correlation times. It is noteworthy that for the larger simulation boxes (10 and 15 swimmer lengths), the fluid correlation times are as high as 7 times the single swimmer time scale $L/2U$. While the pushers show a non-monotonic trend, we see that the pullers show a weak decrease with ν , and further, do not have any noticeable dependence on the simulation box size.

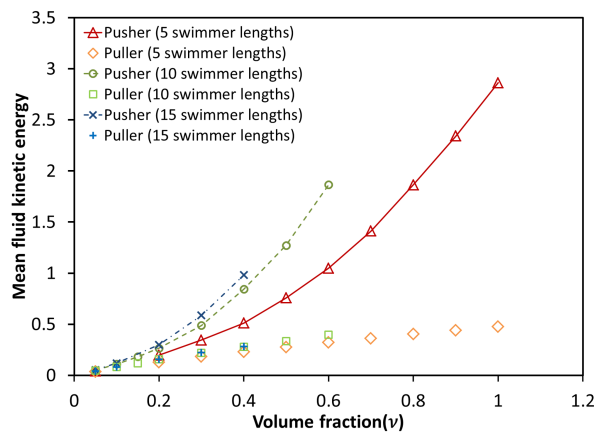
To get a better idea of the length scales of the flow structures in the fluid that might point to collective motion in the unstable regime (for pusher suspensions), we consider the power



(a) Probability distribution function of the fluid disturbance velocity (simulation box size: 10 swimmer lengths)

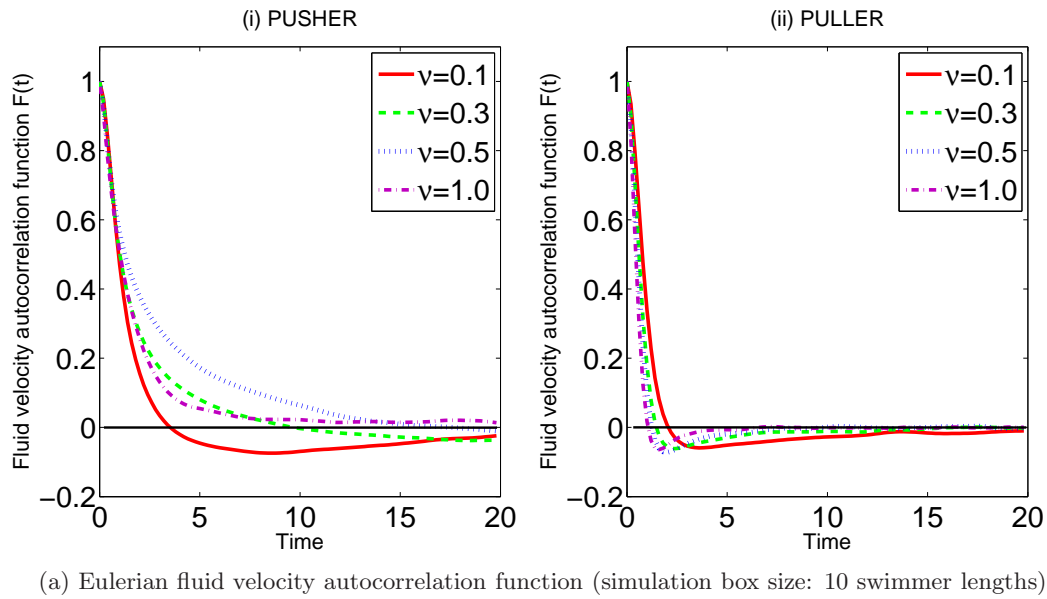


(b) Probability distribution function of fluid disturbance velocity magnitude (simulation box size: 10 swimmer lengths)

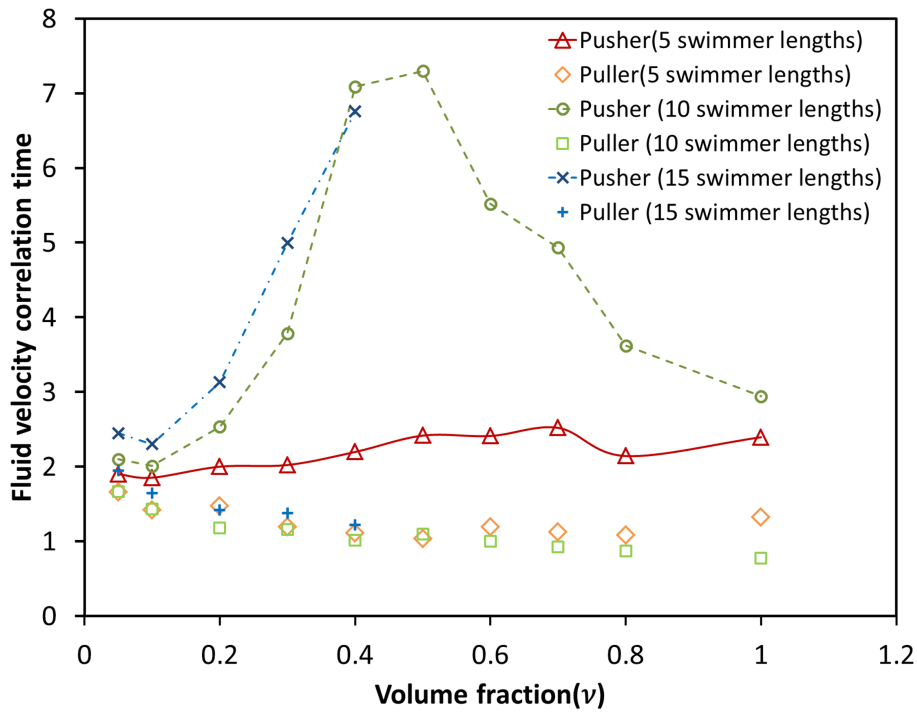


(c) Mean fluid kinetic energy for the case of pusher and puller-type suspensions plotted versus ν

Figure 8.5: Fluid velocity statistics. (a) The probability distribution function of the fluid disturbance velocity plotted for (i)pushers and (ii)pullers for four volume fractions. (b) The probability distribution function of the fluid disturbance velocity magnitude for (i) pushers and (ii) pullers. (c) Mean fluid kinetic energy plotted with respect to ν for pushers and pullers for three box sizes (5, 10 and 15 swimmer lengths)



(a) Eulerian fluid velocity autocorrelation function (simulation box size: 10 swimmer lengths)



(b) Eulerian fluid correlation times vs ν

Figure 8.6: Fluid velocity correlations (a) Fluid velocity autocorrelation function $F(t)$ defined in Eq. 8.5 plotted for pushers and pullers at different volume fractions. (b) The correlation times for pushers and pullers plotted with respect to ν for three different simulation box sizes (5, 10 and 15 swimmer lengths)

spectrum of the fluid velocity defined as:

$$E(\hat{k}) = \frac{1}{2} \int_S \hat{\mathbf{U}}(\hat{\mathbf{k}}) \cdot \hat{\mathbf{U}}^*(\hat{\mathbf{k}}) dS, \quad (8.6)$$

where S is a spherical surface of radius \hat{k} . Expressed in spherical polar coordinates this is:

$$= \frac{1}{2} \int_0^\pi \int_0^{2\pi} \hat{\mathbf{U}}(\hat{\mathbf{k}}) \cdot \hat{\mathbf{U}}^*(\hat{\mathbf{k}}) \hat{k}^2 \sin\theta d\theta d\phi, \quad (8.7)$$

where $\hat{\mathbf{U}}(\hat{\mathbf{k}})$ is the Fourier transform of the fluid velocity field, defined as:

$$\hat{\mathbf{U}}(\hat{\mathbf{k}}) = \int_V d\mathbf{x} \mathbf{u}(\mathbf{x}) \exp(2\pi i \hat{\mathbf{k}} \cdot \mathbf{x}). \quad (8.8)$$

Here, the integral over V denotes an integral over the simulation box and the $*$ denotes the complex conjugate. \hat{k} is the non-dimensional wavenumber defined as $\hat{k} = L_{box}k$. In simulations, the same is calculated by summing contributions lying in a bin of size $\Delta\hat{k}$. In order to have a baseline for comparison, we derive the theoretical power spectrum for both an unbounded and periodic suspension of swimmers. These are derived for the case where the swimmer positions and orientations are uncorrelated. For the sake of brevity, we only write down the final expressions for the theoretical power spectrum. The power spectrum for an unbounded swimmer suspension is given by:

$$E(\tilde{k}) = -\frac{U^2 N L^4}{2\pi^5 M^2 \tilde{k}^4} \int_0^1 \frac{\sin^4\left(\frac{\pi \tilde{k} t}{2}\right) (1-t^2)}{t^2} dt, \quad (8.9)$$

where $\tilde{k} = Lk$. However, for comparison with the periodic theory and simulations we will use L_{box} to rescale the wavenumbers even for the unbounded theory. The theoretical power spectrum for a periodic swimmer suspension is just the discrete wavenumber analogue of the above expression. Therefore, the integral over the spherical annulus in wavenumber space is replaced by a summation, and is given by:

$$E(\hat{k}) = -\frac{U^2 N L_{box}^3}{8\pi^6 M^2} \sum_{k \in (k, k+\Delta k)} \frac{1}{\hat{k}^6} \int_0^1 \frac{\sin^4\left(\frac{\pi \hat{k} L t}{2 L_{box}}\right) (1-t^2)}{t^2} dt. \quad (8.10)$$

Note that here, the wavenumber is scaled by L_{box} and Δk is the thickness of the annulus over which the discrete sum is carried out. Therefore, using the same number of wavevectors in calculating the above expression as those used in the simulations will allow a direct comparison between the two. Also, we note that the above theoretical predictions are the same for pusher and puller suspensions, implying that at least for the fore-aft symmetric case (as in our simulations), the spectrum does not depend on the swimming mechanism. We note some important points about the aforementioned power spectra for unbounded and periodic suspensions. In principle, we can derive a power spectrum for a periodic box using the continuous albeit periodic velocity field of the swimmer suspension. In this case, we expect an agreement between the unbounded

and periodic cases at large \hat{k} , but a deviation as soon as \hat{k} becomes $O(1)$ due to the effects of periodicity. A second effect is introduced due to the discrete sampling of the velocity field (as must be the case in simulations), due to which one does not have information at length scales smaller than the grid spacing used. This absence of information leads to disagreement between the unbounded and periodic (discrete) power spectra at large \hat{k} .

The power spectrum for pusher and puller suspensions for two different volume fractions are shown in Fig. 8.7. We note that, we use a finite number of wavenumbers (the same number used in calculating the simulated spectrum), to calculate the periodic theory, which explains the drooping of the theoretical curve for large \hat{k} . By choosing to use a finite number of wavevectors to calculate the theoretical power spectrum for a periodic box, we are deliberately choosing to neglect information available at higher \hat{k} , in order to compare with simulations. At the lower volume fraction ($\nu = 0.05$), the pusher and puller spectra are very close over the entire range of wavenumbers. Also, for this case, both pusher and puller spectra are in good agreement with the periodic theory. This is because, at low volume fractions, both pushers and pullers are not correlated with respect to their positions and orientations; thus their power spectrum agrees well with the theory (which corresponds to uncorrelated swimmers). However at the higher volume fraction ($\nu = 0.5$), the pusher curve shows a marked increase in the low wavenumber regime. This implies that, as the collective motion sets in for pushers, a larger fraction of the fluid kinetic energy resides in flow structures whose length scale is $O(L_{box})$ (which, as per our scaling, corresponds to $\hat{k} \sim O(1)$). This is in agreement with the fact the hydrodynamic instability for pushers is a long wavelength (small wavenumber) one. As seen in Fig. 8.7, the point of departure of the pusher spectrum from that of the puller for $\nu = 0.5$ is also in good agreement for the theoretically predicted maximum unstable wavenumber (box-size-dependent) for smooth swimmers (see Eq. 8.1). It is to be noted that the maximum of the spectrum occurs at the lowest simulated wavenumber implying that the box size controls the size of the flow structures formed in the fluid. The pullers, in contrast show an opposite trend with the spectrum at lower wavenumbers showing a decrease with an increase in volume fraction.

The above results for the disturbance velocity in the fluid show clear evidence of collective motion for the case of pusher suspensions. We see that, for the case of pushers, beyond a critical, box-size-dependent volume fraction, the fluid velocity fields are characterized by large fluctuations and correlated bulk motions with length scales of $O(L_{box})$. The pullers show a fluid velocity field which remains uncorrelated and random even at higher volume fractions, and consists of contributions from individual uncorrelated swimmers. These results are in qualitative agreement with experiments involving pusher-type swimmers (Mendelson *et al.* (1999), Sokolov *et al.* (2007), Dombrowski *et al.* (2004)) and also earlier simulation efforts of hydrodynamically interacting slender swimmers (Saintillan & Shelley (2007), Saintillan & Shelley (2012)).

8.3.2 Swimmer Statistics

In this section we discuss various statistical measures involving the swimmers themselves. These swimmers, in isolation, swim with a unit speed along their orientation vector. However, the swimmer velocity in a suspension is expected to be different owing to hydrodynamic interactions with other swimmers. Fig. 8.8a shows the probability distribution function for the swimmer

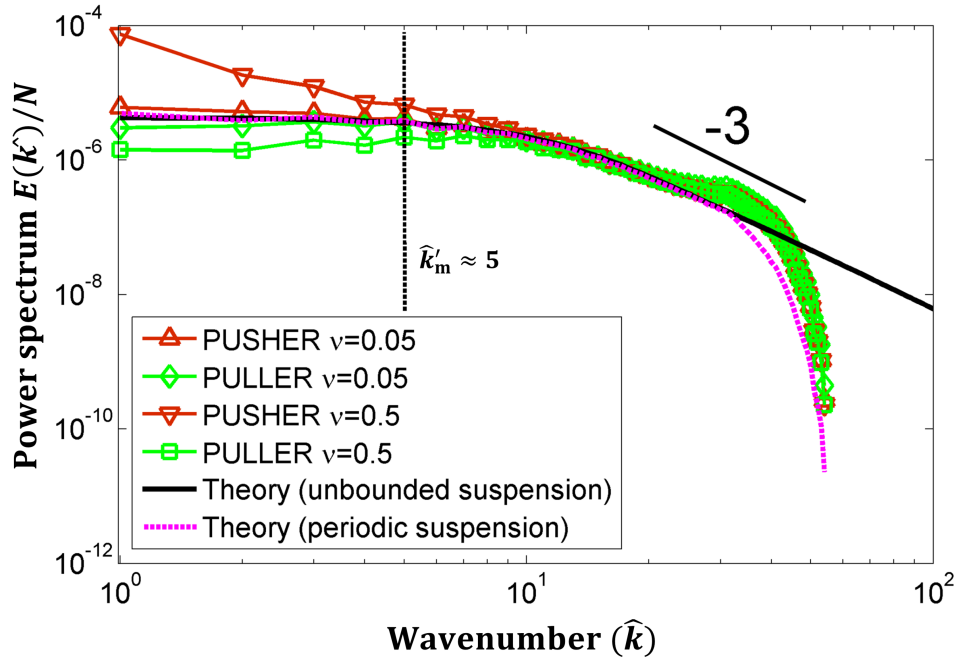


Figure 8.7: Power spectrum of the fluid velocity field, as defined in Eq. 8.6, plotted with respect to the non-dimensional wavenumber $\hat{k} = L_{box}k$ (simulation box size: 10 swimmer lengths)

velocity for four different volume fractions for pushers and pullers. At low volume fractions, the pushers and pullers exhibit similar behaviour with the distribution function resembling a top hat profile. This is the expected profile for a dilute suspension where hydrodynamic interactions are weak and each swimmer basically swims in a straight line at its isolated swimming speed, and along its initial (randomly chosen) orientation. Indeed, it can be shown that a dilute suspension of swimmers, with each swimming at the isolated swimming speed ($U = 1$), with uniformly distributed orientations on the unit sphere, leads to a distribution function given by:

$$P(u_{x_i}) = \begin{cases} 1/2 & \text{for } |u_{x_i}| < 1, \\ 0 & \text{otherwise.} \end{cases} \quad (8.11)$$

We note that the above result is crucially dependent on the dimensionality of the underlying space. For instance, [Mehandia & Nott \(2008\)](#), have a two-dimensional scenario, and their distribution function, at lower volume fractions, has a different form. As expected, the simulation results, in the dilute limit match this profile. With an increase in the volume fraction, one sees a bifurcation in the behaviour of pushers and pullers. The pusher curve flattens with the tails growing fatter indicating the greater likelihood of swimmers swimming at speeds greater than their isolated swimming speed. For pullers on the other hand, the distribution function remains similar to the dilute limit case even for $\nu = 1.0$, indicating no qualitative change in the swimmer's velocity. This can be seen clearly in [8.8b](#), where the peak of the probability density for pushers shifts to larger values with increasing ν . The swimming speed distribution for pullers decays sharply beyond $|U| = 1$ for $\nu = 1.0$, indicating that pullers do not swim significantly faster than in isolation. It is also noteworthy that the pusher velocity distribution function for higher volume fractions is well approximated by a Gaussian curve with the same mean and standard

deviation as the simulation data (in sharp contrast to the puller top-hat profiles).

The variation of the mean swimming speed with volume fraction for pushers and pullers is shown in Fig. 8.8c for three different box sizes. A bifurcation is clearly seen where, beyond $\nu \approx 0.2$, the pusher curve breaks away from the puller curve. The pullers, on the other hand, show only a weak increase with volume fraction when compared to pushers. The effect of box size is also noticeable in Fig. 8.8c where, for larger box sizes, the swimming speed for pushers is greater and also increases more steeply with volume fraction (as was the case for the Eulerian correlation times earlier).

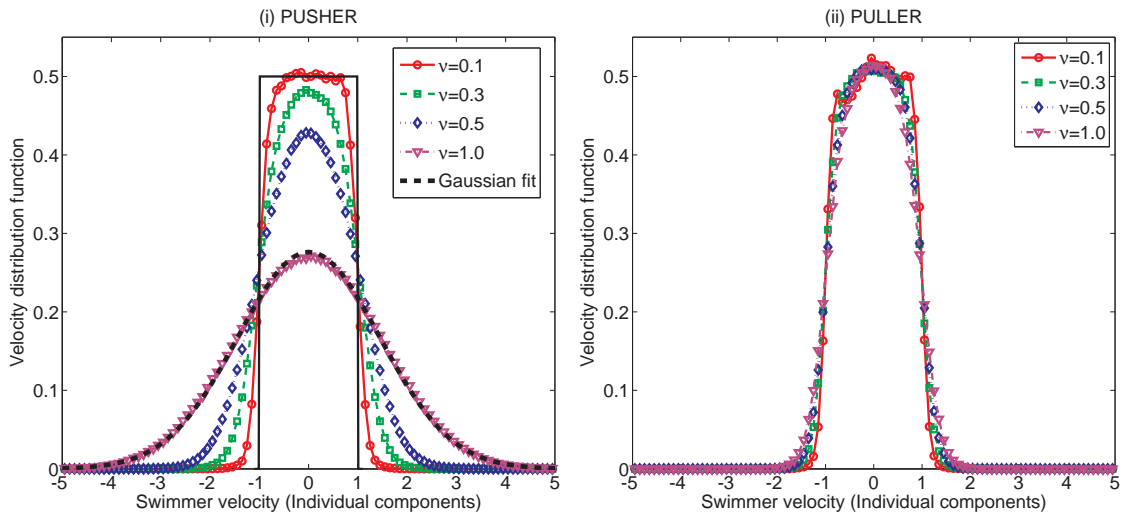
Next, we investigate the pair orientation correlations between swimmers for the case of both pushers and pullers. The polar pair correlation function is defined as (Saintillan & Shelley (2007)):

$$C(r) = \frac{\langle \sum_{i \neq j} \hat{\mathbf{p}}_i \cdot \hat{\mathbf{p}}_j \delta(|\mathbf{x}_i - \mathbf{x}_j| - r) \rangle}{\langle \sum_{i \neq j} \delta(|\mathbf{x}_i - \mathbf{x}_j| - r) \rangle} \quad (8.12)$$

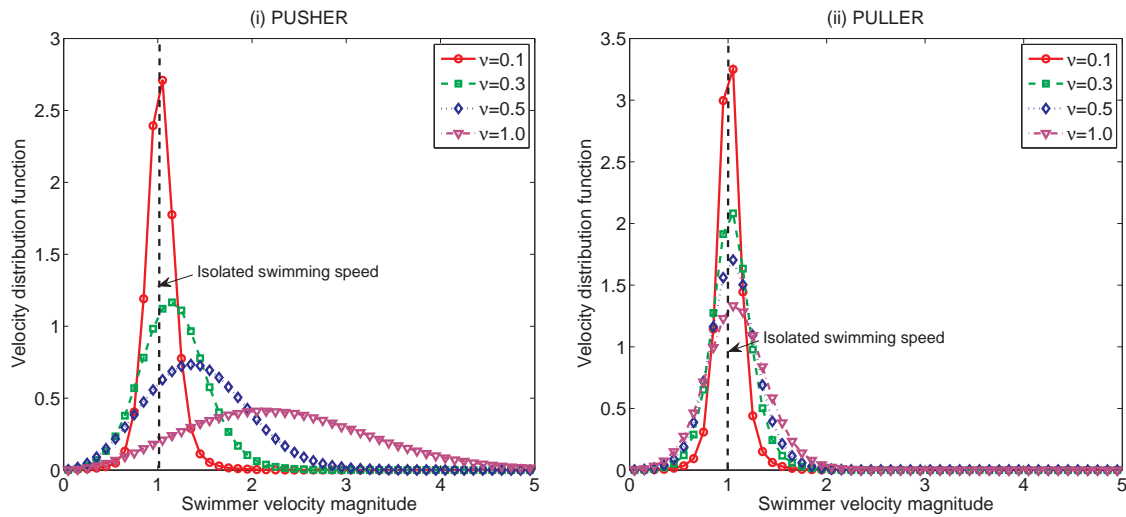
where $\delta(\mathbf{x})$ is the three-dimensional Dirac-delta function and \mathbf{x}_i denotes the i^{th} swimmer's position. We note that, in calculating the polar correlation function, we distinguish between the head and tail of the swimmer (this in contrast with a 'nematic' order where this distinction is not made). The polar pair correlation function is defined such that it will have a value of 1 when neighboring swimmers are aligned exactly parallel to one another (swimming in the same direction), and -1 when neighboring swimmers swim in exactly opposite directions. In a swimmer suspension, a positive or negative value of the function indicates a tendency for swimmers to align in a parallel or anti-parallel sense, respectively.

We see from Fig. 8.9 that pushers and pullers, at low volume fractions (Fig. 8.9a), show a strong positive and negative correlation, respectively. At higher volume fractions (Figs. 8.9b and 8.9c), both pushers and pullers show a weaker positive and negative correlation, respectively. This implies that nearby pushers have a tendency to align with one another and swim in the same direction. Neighboring pullers, on the other hand, tend to align in an anti-parallel manner to one another. Note also that this tendency likely arises from pair-interactions, and higher volume fractions appear to disrupt the effects of pair-hydrodynamic interactions in both cases. Another trend observed from Figs. 8.9a, 8.9b and 8.9c is that pushers show larger correlations lengths compared to pullers for the entire range of volume fractions considered here. The correlation length is defined here as the distance at which the correlation function first becomes zero. With increasing volume fraction, we see that the degree of correlation decreases for both pushers and pullers as seen by the magnitude of the correlation function at small r decreasing (see Fig. 8.9d). Also, the trend with increasing volume fraction is a weak increase in the correlation length for pushers and a decrease of the same for the case of pullers (see Fig. 8.9d).

To further understand the role played by these orientation correlations in the collective behaviour of swimmers, we probe the relation between local orientational order and swimming speed. To do this we consider the pair correlation function averaged over all swimmers within a swimmer length (L) of a given swimmer, and plot this as a function of the swimmer's speed. Such a plot is shown in Fig. 8.10a for two volume fractions ($\nu = 0.5$ and 1.0). For the case of pushers it is clear that there is a positive correlation between local alignment and swimming speeds. Relating this to our orientation correlation results, we see that pushers which are near



(a) Probability distribution function of the swimmer velocity (simulation box size:10 swimmer lengths)



(b) Probability distribution function of the swimmer speed (simulation box size:10 swimmer lengths)

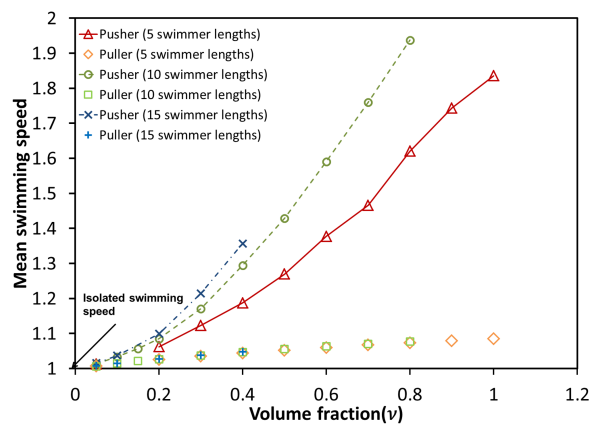
(c) Mean swimming speed of pushers and pullers plotted versus ν

Figure 8.8: Swimmer statistics. (a) The probability distribution function for the swimmer velocity plotted for (i)pushers and (ii) pullers for four volume fractions. The top-hat profile corresponding to uncorrelated swimmers swimming at a speed of unity is also shown. (b) The probability distribution function for the swimmer speed for (i) pushers and (ii) pullers. (c) Mean swimming speed plotted with respect to ν for pushers pullers for three box sizes (5, 10 and 15 swimmer lengths)

one another tend to be aligned and also swim faster. In the case of pullers we see that slowest swimming pullers show the most anti-parallel alignment. In the same vein, we also calculate the correlation between the local volume fraction of the swimmers and their swimming speed. In order to do this the number of swimmers within a sphere of radius L centred at a given swimmer is used to compute the local volume fraction, and the same is plotted against the swimmer's speed (see Fig. 8.10b). In the case of pushers, we see that faster swimming is correlated with a slightly higher local density of swimmers. Such a clear correlation does not appear for pullers. These results are in qualitative agreement with those of [Saintillan & Shelley \(2012\)](#), who also consider the above measures for swimmers. However, we note that local density correlations are much smaller in magnitude than the orientation correlations seen above, which is in keeping with leading logarithmic order slender body theory ([Subramanian & Koch \(2009\)](#)).

Another statistical measure of interest is the degree of alignment of a given swimmer along the local extensional axis of the 'ambient' rate-of-strain tensor, that is, the rate-of-strain resulting from the cumulative effect of the velocity disturbances due to all other swimmers. Slender rods in the limit of small velocity gradients, as is the case in our simulations, tend to align along the extensional axis of the disturbance flow. In the case of pushers, this alignment leads to an orientational anisotropy which reinforces the velocity disturbance causing the anisotropy, thence leading to the hydrodynamic instability (see section 8.2). We plot the mean of $\mathbf{E} : \hat{\mathbf{p}}\hat{\mathbf{p}}$ over all the swimmers with respect to time in Fig. 8.11 (it is worth noting that, in calculating the rate-of-strain at a given swimmer, its own contribution must be subtracted from the total disturbance velocity field at that point). We see that both pushers and pullers show a weak parallel alignment at lower volume fraction. At the higher volume fraction, the degree of alignment increases for both pushers and pullers, but the alignment is consistently greater for pushers which appears consistent with the underlying mechanism for the instability ([Subramanian & Koch \(2009\)](#), [Subramanian & Nott \(2012\)](#)) which involving mutual reinforcement of velocity and orientation fluctuations.

Our analysis of the swimmer velocity distributions, mean swimming speeds, orientation correlations, local order and density, and the degree of alignment allows us to build a picture for the collective motion observed in pusher suspensions. Above a certain critical volume fraction, pushers show orientation correlations over a few swimmer lengths, where nearby swimmers tend to align and swim faster than in isolation. The orientation correlation lengths for pushers are found to be greater than that for pullers, consistent with bulk fluid motion on longer scales. Both pushers and pullers show a local alignment with the extensional axis of the disturbance velocity field. In pushers, unlike pullers, this alignment leads to an amplification of this disturbance velocity causing more swimmers in the vicinity to align. This instability also manifests in the form of correlated fluid motions in the form of whorls and jets with significant correlation times studied in section 8.3.1.

To study the global transport of the swimmers, we now look at the mean-square displacements of the swimmers as a function of time and extract the long-time translational diffusivities. As seen in Fig. 8.12a, the mean-square-displacement curves show a short-time ballistic regime with a quadratic growth in time followed by long-time diffusive behaviour with a linear growth in time. In contrast to the other measures considered here, the swimmer transport surprisingly

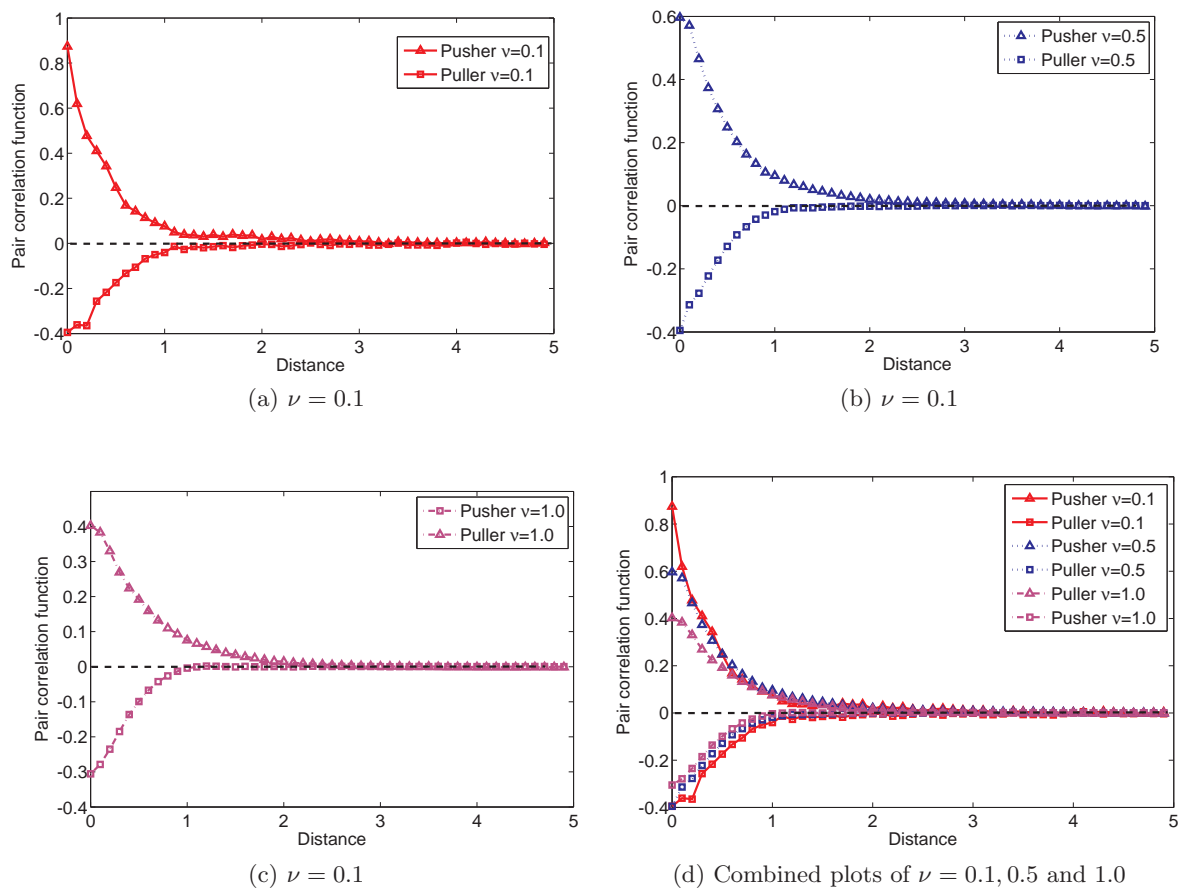
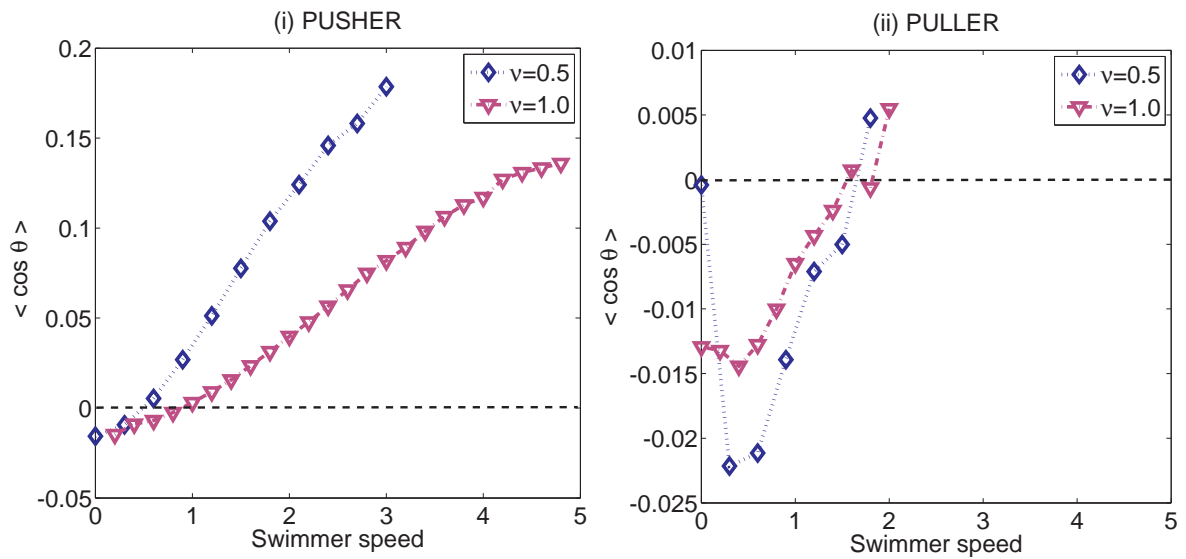
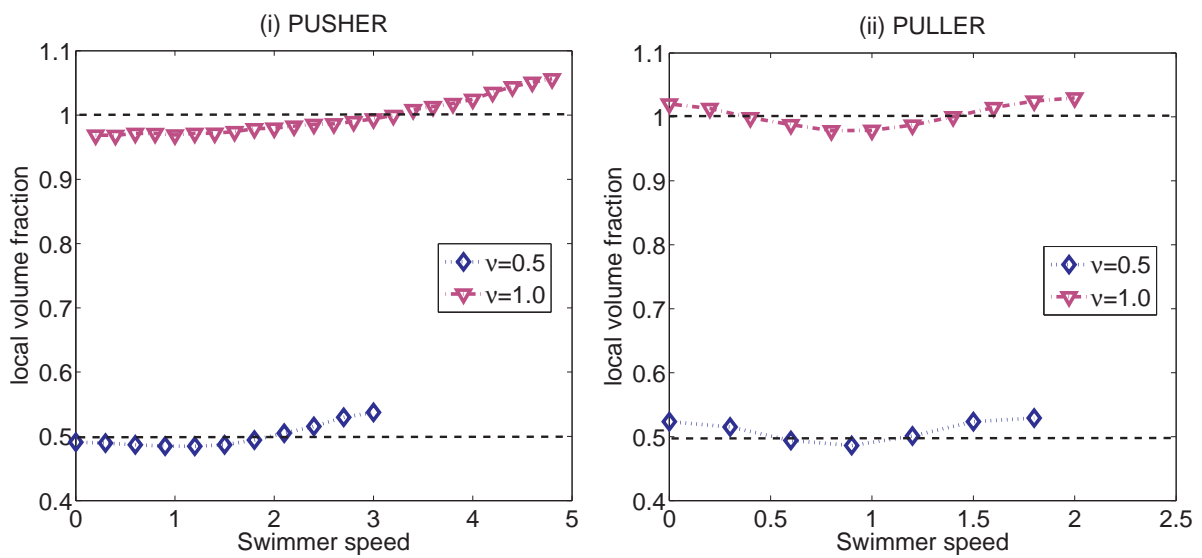


Figure 8.9: Plot of pair correlation function as a function of distance from the swimmer for three volume fractions (a) $\nu = 0.1$ (b) $\nu = 0.5$ (c) $\nu = 1.0$ and (d) a combined plot with all three volume fraction. The distance from the swimmer is expressed in non-dimensional form in units of half the swimmer length $L/2$. The results are for simulation box of size 10 swimmer lengths.



(a) Swimmer speed distribution function



(b) Local volume fraction

Figure 8.10: Two local measures, (a) the local volume fraction and (b) local order parameter plotted as a function of the swimmer speed (simulation box size:10 swimmer lengths).

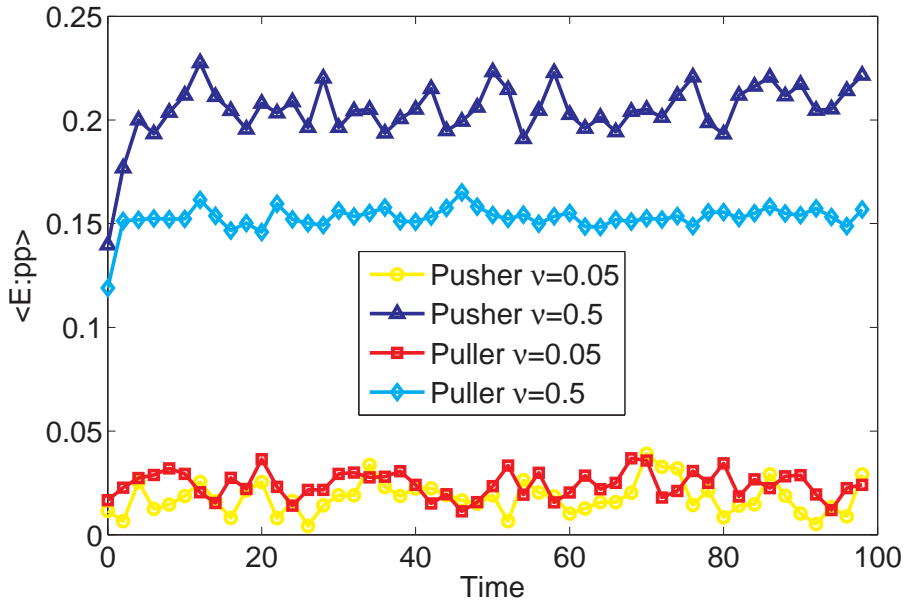


Figure 8.11: A measure of the swimmer alignment with the local extensional axis of the rate-of-strain tensor \mathbf{E} , given by the scalar $\mathbf{E} : \hat{\mathbf{p}}\hat{\mathbf{p}}$. A positive value indicates a tendency for the swimmers to orient parallel to the local extensional axis (simulation box size:10 swimmer lengths).

shows little or no evidence of collective motion as seen by comparing pusher and puller suspensions in Fig. 8.12a. We can extract the diffusivities of the swimmers from the long-time values of mean-square displacement as:

$$D_{swimmer} = \lim_{t \rightarrow \infty} \frac{\langle (\mathbf{x}(t) - \mathbf{x}(0))^2 \rangle}{6t}, \quad (8.13)$$

where $\mathbf{x}(t)$ is the position of the swimmer at time t . The swimmer diffusivities are plotted in Fig. 8.12b as a function of the volume fraction. In the dilute limit, the swimmer diffusivity is seen to obey an inverse scaling with the volume fraction as evidenced by the slope of -1 in the log-log plot. This is attributed to the swimmer orientations decorrelating via pair interactions (see scaling arguments below). The orientation decorrelation function, $\langle \hat{\mathbf{p}}(t) \cdot \hat{\mathbf{p}}(0) \rangle$ is plotted as a function of time in Fig. 8.13. By assuming an exponential decay of the form $e^{-t/\tau_{corr}}$, we can calculate the correlation time τ_{corr} for the swimmer orientations. Note that this correlation time can be equivalently interpreted in terms of a hydrodynamic rotary diffusivity $D_{rh} = 1/2\tau_{corr}$ (Dhont (1996)) when the mechanism of decorrelation is a rotary diffusion process. From Fig. 8.13 we see that as one increases the volume fraction, both pusher and puller orientations decorrelate more rapidly. This suggests that the orientation decorrelations are governed by pair swimmer interactions which occur at an increased frequency at higher volume fractions. Note that the pusher orientations decorrelate faster than pullers as we increase the volume fraction. The swimmer diffusivity scales as $D_{swimmer} \sim U'^2\tau_{corr}$, where U' is the swimmer speed in the suspension and equals U (the isolated swimming speed) in the dilute limit. When the orientations decorrelate via pair interactions, the correlation time is just the inverse of the collision frequency between swimmers $\tau_{corr} \sim 1/(nUL^2)$, where n is the number density. Written in terms of the volume fraction, this is just $\tau_{corr} \sim 8L/(U\nu)$, thus giving a swimmer diffusivity

which scales as $D_{swimmer} \sim UL/\nu$. Our results for the swimmer diffusivity are in agreement with this inverse scaling with ν as seen in Fig. 8.12b. The faster decorrelation of orientations for pushers (see Fig. 8.13 (i)) may be responsible for the pusher diffusivities being smaller than the pullers at higher volume fractions. Unlike other measures we have considered previously, the long-time swimmer diffusivity shows surprisingly little dependence on the simulation box size. This may be attributed to the opposing effects of increased swimming speeds and increased rate of orientation decorrelation with the box size. As seen from the above scaling for the swimmer diffusivity, this would indeed lead to weaker dependence on the box size.

The translational swimmer diffusivity may also be calculated from the orientation decorrelation using a generalized Taylor's dispersion theory (Brenner (1979)), which gives the swimmer diffusivity as:

$$D_{swimmer} = \frac{U^2}{6D_{rh}}, \quad (8.14)$$

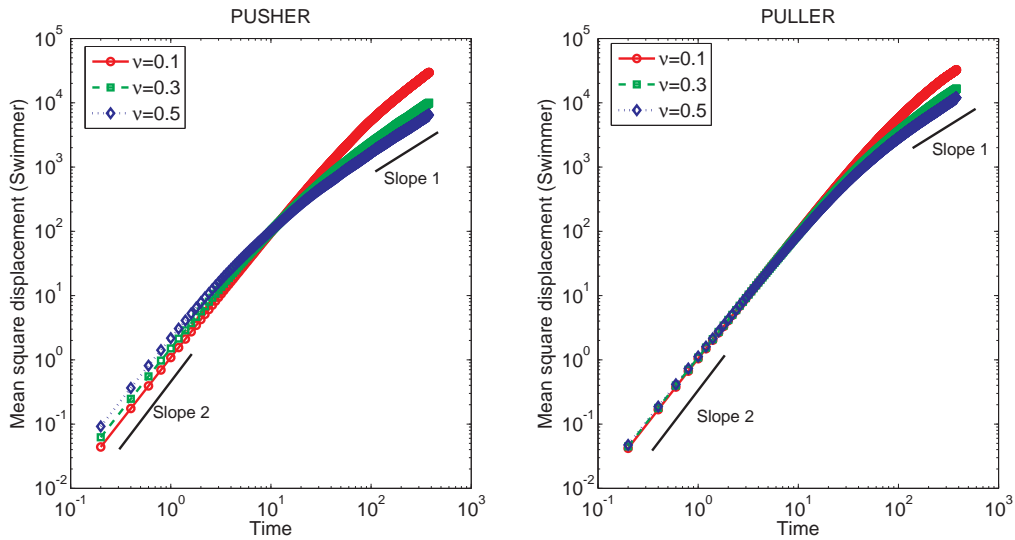
where D_{rh} is the hydrodynamic rotary diffusivity defined above. A third method to calculate the swimmer diffusivity is from the auto-correlation function of the particle velocities, and is given by:

$$D_{swimmer} = \frac{1}{3} \int_0^\infty \langle \dot{\mathbf{x}}_{GC}(t) \cdot \dot{\mathbf{x}}_{GC}(0) \rangle dt, \quad (8.15)$$

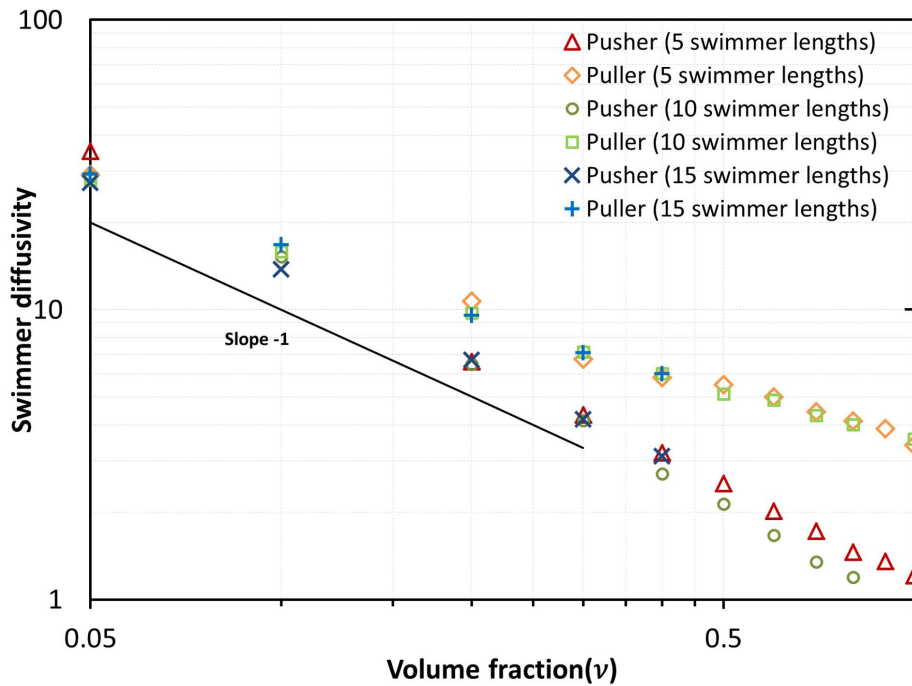
where $\dot{\mathbf{x}}_{GC}$, is the velocity of the geometric centre of the swimmers. Fig. 8.14, shows a comparison of the diffusivities calculated through the three methods given by Eqs. 8.13, 8.14 and 8.15. Of these three, Eqs. 8.13 and 8.15 give the exact translational diffusivity of the swimmers while Eq. 8.14 is an approximation. This approximation arises since there are two mechanisms by which the swimmer can translationally diffuse, and the Taylor dispersion formula neglects the contribution arising from the convection of the centre-of-mass by the disturbance velocity field. We note that the pusher diffusivity predicted by from the mean-square-displacement and the velocity autocorrelation function are higher than those predicted from Eq. 8.14 since we have used the isolated swimming velocity in calculating the swimmer diffusivity and also because, as mentioned above, Eq. 8.14 only approximates the diffusivity. Our results for the swimmer diffusivity are in agreement with earlier simulation efforts by Saintillan & Shelley (2007).

8.3.3 Tracer Transport

In this section we study the transport of passive tracer particles which are convected by the swimmers' disturbance fields. We are motivated by the fact that one of the earliest experiments on bacterial suspensions by Wu & Libchaber (2000) involved the measurement of tracer diffusivities, although the measurements were likely restricted to the unstable regime. Fig. 8.16a shows the time evolution of the tracer mean-square displacements. An initial ballistic regime is clearly seen followed by long-time diffusive behaviour. The mean-square displacements of tracers in pusher and puller suspensions are comparable at low volume fractions ($\nu = 0.1$); however, there is a remarkable increase for the case of pushers at higher volume fractions (two orders of magnitude higher at $\nu = 0.6$). This can be appreciated visually from Fig. 8.15. We see from the tracer particle trajectories in the right side column that for the case of pullers, the tracer particles seem to execute a random trajectory which does not lead to a significant displacement



(a) Swimmer mean-square-displacement (simulation box size: 10 swimmer lengths)



(b) Long-time diffusivities of the swimmers plotted as a function of volume fraction

Figure 8.12: Swimmer transport. (a) Mean-square-displacement with respect to time for (i) pushers and (ii) pullers. (b) Translational diffusivities of the swimmers plotted with respect to ν for pushers pullers for three box sizes (5, 10 and 15 swimmer lengths).

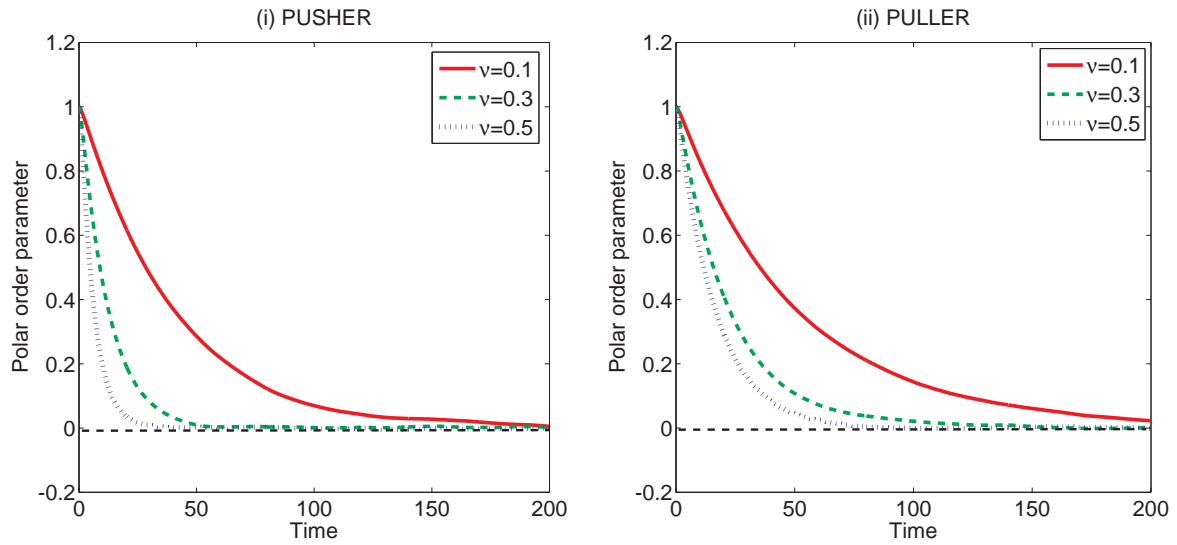


Figure 8.13: Evolution of the orientation decorrelation function $\langle \hat{\mathbf{p}}(t) \cdot \hat{\mathbf{p}}(0) \rangle$ with time. The results are for a simulation box of size 10 swimmer lengths.

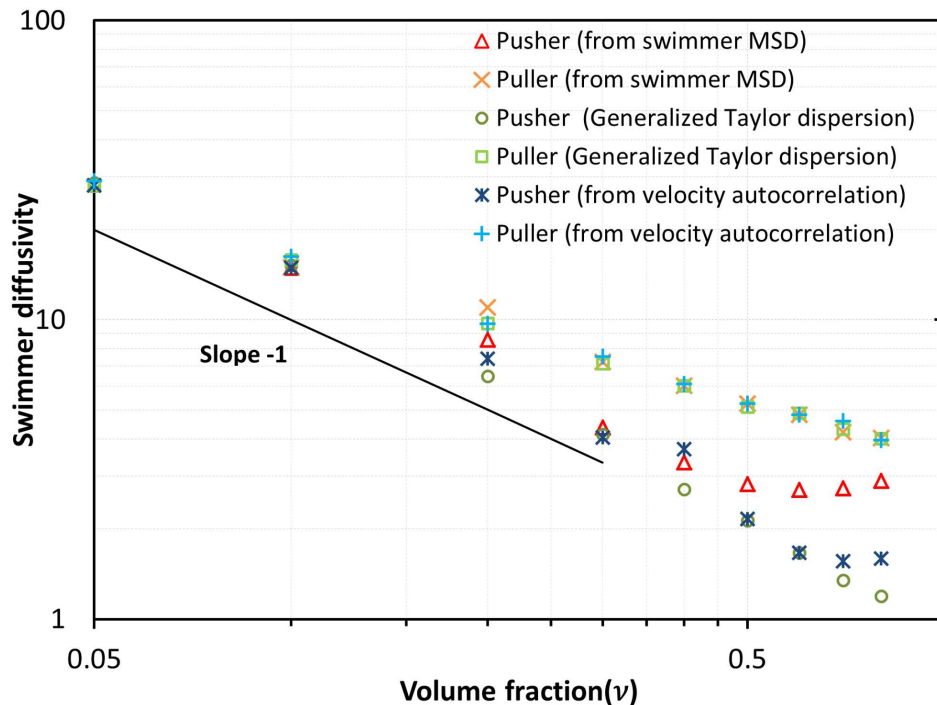


Figure 8.14: The swimmer diffusivity calculated using three methods (i) long-time mean-square-displacement (ii) swimmer orientation decorrelation using a generalized Taylor dispersion theory (iii) swimmer velocity auto-correlation (simulation box size: 10 swimmer lengths).

even at long times (see Figs. 8.15a and 8.15b). In striking contrast, the tracer particle trajectories in pusher suspensions show significant correlated motions leading to trajectories which undergo significant displacement. This leads to the trajectories filling up the entire field of view as seen in Fig. 8.15d. The tracer diffusivity can be extracted from the long-time value of the mean-square displacement as:

$$D_{tracer} = \lim_{t \rightarrow \infty} \frac{\langle (\mathbf{x}_{tracer}(t) - \mathbf{x}_{tracer}(0))^2 \rangle}{6t} \quad (8.16)$$

where $\mathbf{x}_{tracer}(t)$ is the position of the tracer particle at time t . The average in the above equations is over the number of tracer particles N_{tracer} in the suspension (a value of $N_{tracer} = 5000$ was found to be sufficient to obtain good statistics). Fig. 8.16b shows a plot of the tracer diffusivities, as a function of the swimmer volume fraction, for pushers and pullers. The pusher curves show a clear bifurcation beyond a critical volume fraction with diffusivities that are much larger than those for pullers. The tracer diffusivities in puller suspensions show only a weak increase with the volume fraction. Importantly, the simulation box size has a marked effect and we see that the bifurcation point shifts to lower volume fractions as the box size is increased. This is because, for pushers, the tracer diffusivities at a given volume fraction (beyond the bifurcation point) increase with the box size. It is important to note that the puller curves seem fairly independent of the box size, pointing to the absence of any instability and collective motion. The bifurcation point for the simulations is in excellent agreement with those predicted by the linear theory (see Eq. 8.4 and Fig. 8.2). Physically, as argued earlier, the trend with box size is due to the long-wavelength nature of the instability for pushers which means that as the box size increased there is a greater range of unstable wavelengths which can be captured by the simulation box. Among all the statistical measures considered here, we see that the tracer diffusivity is the most sensitive measure of the onset of collective motion. This can be seen by comparing Fig. 8.16b with earlier plots of the mean fluid kinetic energy (Fig. 8.5c) and fluid velocity correlation times (Fig. 8.6b). This was earlier reported in simulations by [Saintillan & Shelley \(2012\)](#). The reason for this can be seen through a simple scaling argument. The tracer diffusivity scales as $D_{tracer} \sim \langle u^2 \rangle \tau_{corr}$, where $\langle u^2 \rangle$ is the mean fluid kinetic energy and τ_{corr} is the fluid velocity correlation time. For pushers we saw that both the fluid velocity magnitude and correlation time showed an increasing trend with volume fraction after the onset of collective motion (the correlation time shows a decrease for higher volume fractions but still remains much higher than the puller values). The combined effect therefore is to cause an even larger increase in the trace diffusivity for the case of pushers. The tracer diffusivity is therefore a very sensitive indicator of the onset of collective motion and will be used henceforth to identify the bifurcation point between pushers and pullers which is the threshold for the onset of collective motion. In particular, we will use it to identify the box-size-independent threshold for instability in a suspension of pushers that undergo a run-and-tumble motion. As will be seen in the next chapter, the pusher-puller bifurcation in this case is much more subtle, and the choice of a sensitive statistical measure is crucial.

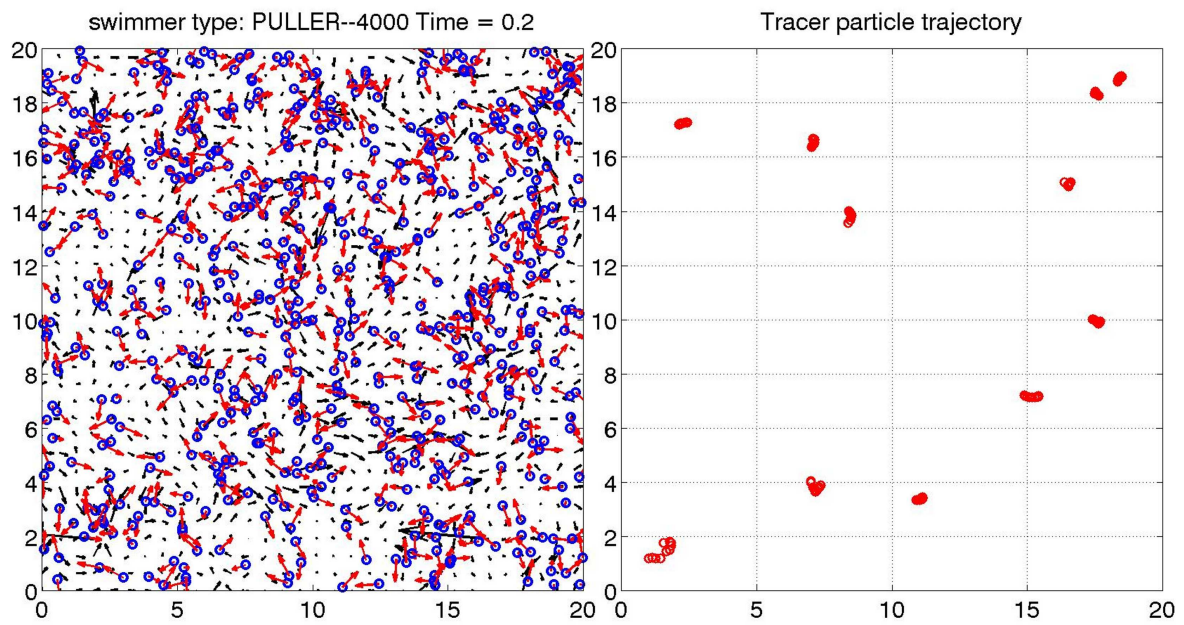
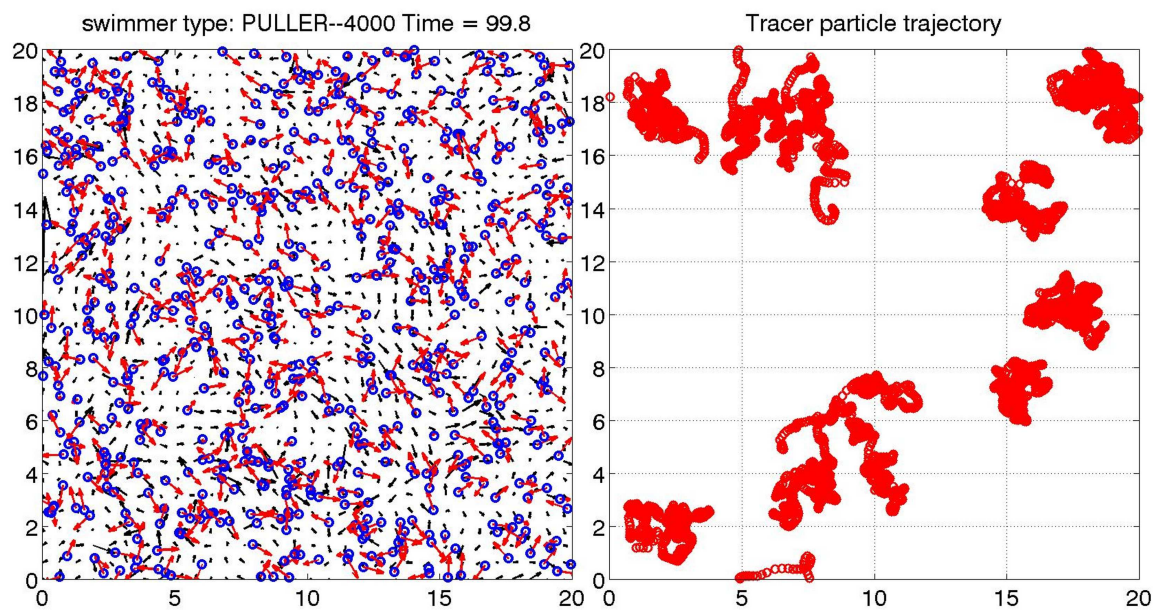
(a) Puller suspension: simulation snapshot at $t = 0.2$ (b) Puller suspension: simulation snapshot at long times $t \approx 100$

Figure 8.15

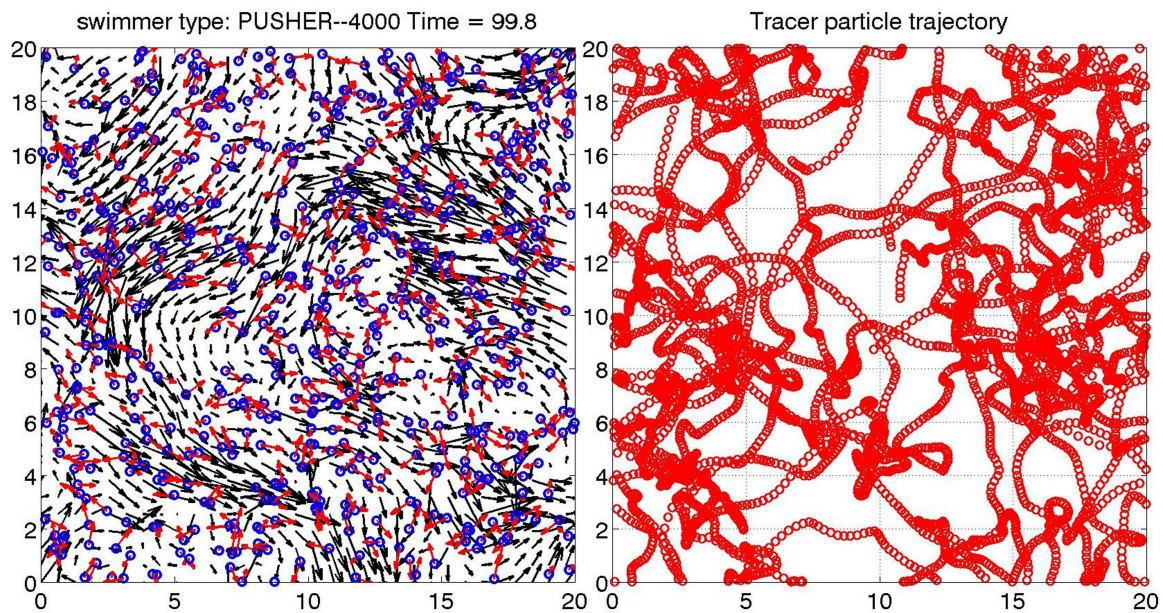
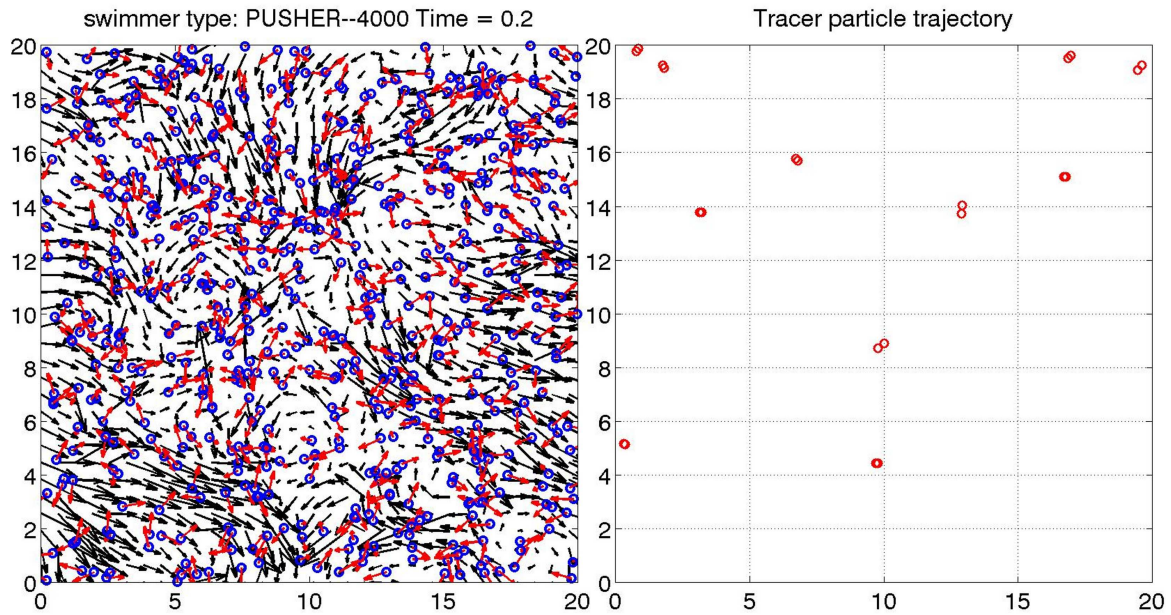
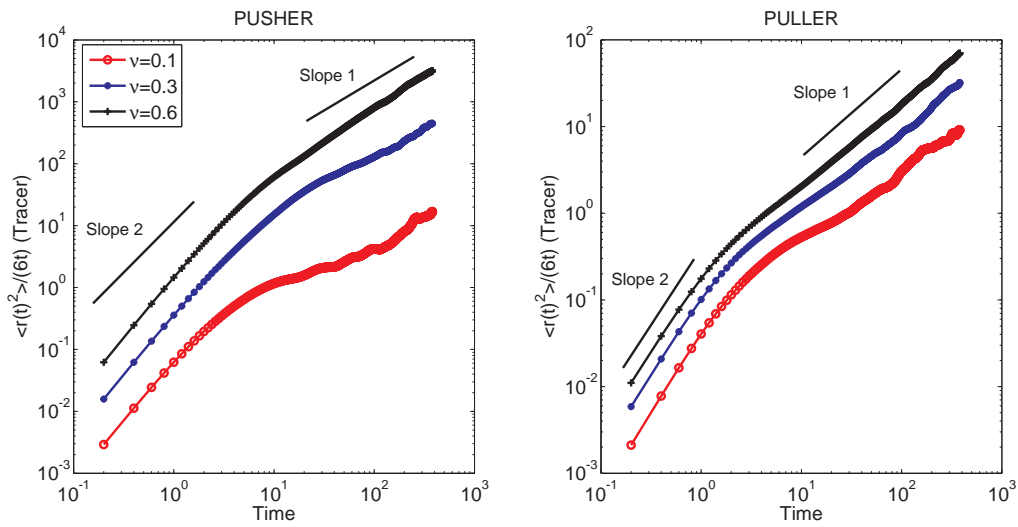
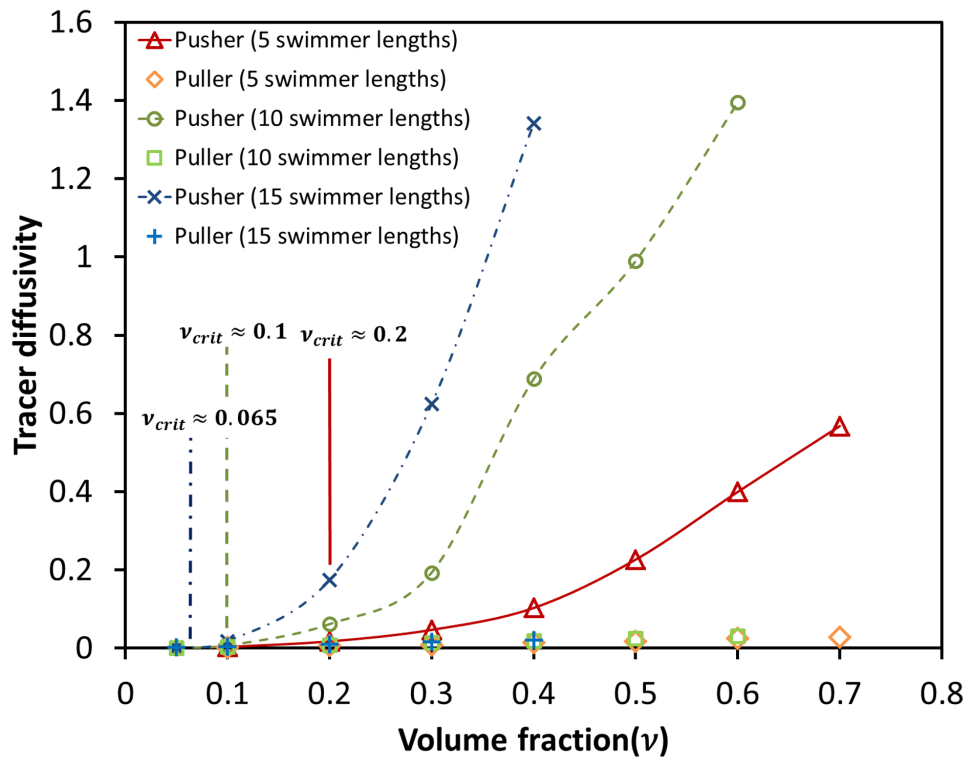


Figure 8.15: Simulation snapshots showing the swimmers' positions and the fluid disturbance velocity vectors on the left side column and trajectories of tracer particles on the right column. The simulation box size is 10 swimmer lengths and the volume fraction is $\nu = 0.5$, which for pushers lies in the unstable regime. The blue circles represent the geometric centres of the swimmers and the red arrows correspond to the swimmers' orientation vectors. The black arrows depict the fluid velocity vectors. In the right column, the red circles represent the positions of the tracer particles. (a) Puller suspension near the start of the simulation and (b) puller suspension at long times. (c) Pusher suspension near the start of the simulation, (b) pusher suspension at long times. We only display swimmers and tracers which lie in a slab of size $20 \times 20 \times 3$ in the x_1 , x_2 and x_3 directions, respectively, centred at the midpoint of the simulation box in the x_3 direction. The fluid velocity vectors lie on the plane at the midpoint of the simulation box in the x_3 direction.



(a) Tracer mean-square-displacement (simulation box size: 10 swimmer lengths)



(b) Long-time diffusivities of the swimmers plotted as a function of volume fraction

Figure 8.16: Tracer transport. (a) Mean-square displacements for the tracer particles plotted with respect to time for (i) pushers and (ii) pullers. (b) Diffusivities of the tracer particles plotted with respect to ν for pushers pullers for three box sizes (5, 10 and 15 swimmer lengths). The vertical lines indicate the box-size-dependent theoretical prediction for the instability threshold given by Eq. 8.4.

Chapter 9

Results and Discussion: Tumblers and Rotary Diffusers

9.1 Introduction

From last chapter's discussion on smooth swimmer suspensions, we now move on to swimmers with intrinsic orientation relaxation mechanisms such as tumbling and rotary diffusion. Such intrinsic orientation relaxation mechanisms are a widely observed and important feature of the motion of bacteria (Berg (1993), Berg (2004)), Algae (Polin *et al.* (2009)) and artificial microswimmers (Walther & Müller (2008), Ebbens & Howse (2010)). Therefore, modelling such swimmers brings us that much closer to studying collective motion in real swimmer suspensions, and also in achieving a sensible comparison between theory, simulations and experiments. In this chapter our main focus will be to study the impact of intrinsic orientation relaxation mechanisms on the onset of collective motion in pusher suspensions. Pullers, with the same intrinsic decorrelation mechanisms included will once again serve as a basis for contrast. We seek to identify the instability threshold for suspensions of both tumblers and rotary diffusers based on our simulations, and compare the same with the box-size-independent threshold predicted by Subramanian & Koch (2009). Note that this box-size-independence is in sharp contrast to the case of smooth swimmers where, as seen in the previous chapter, the threshold is an artefact of the finite box size used in the simulations. Such a threshold would be a valuable result since it would enable comparisons with, and serve as a useful guide for experiments involving bulk suspensions of these swimmers.

9.2 Theory

9.2.1 Stability Theory: Swimmers with Intrinsic Orientation Decorrelation Mechanisms

In this section we give an overview of the theory developed by Subramanian & Koch (2009) for swimmer suspensions with intrinsic orientation decorrelation mechanisms. From the last chapter on smooth swimmers, we recall that the instability for pushers was due to a mutual reinforcement of perturbations in the orientation and velocity fields (the suspension at linear order remains spatially homogeneous). We saw that a suspension of pushers is always unstable to sufficiently long-wavelength perturbations. In addition, we saw that for an unbounded suspension, where the largest allowed perturbation wavelengths are infinite, the critical volume fraction for the instability is zero.

The above picture is modified when orientation relaxation mechanisms are added. Now the

accumulation of orientation anisotropy is controlled by the smaller of two time scales. The first is the time scale for the bacterium to swim a distance of order the wavelength of the disturbance which is $O(\lambda/U)$ with $\lambda = L_{box}$ being the largest possible wavelength in simulations. The other is the time scale for intrinsic orientation decorrelation, which for tumbling is the mean-run-time τ and for rotary diffusion is $O(1/D_r)$ (for details about these orientation relaxation mechanisms in the context of bacteria such as *E. Coli* refer to chapter 7). If the time scale for orientation decorrelation is much larger than λ/U , then one expects to recover the smooth swimmer behaviour. On the other hand when $\tau < \lambda/U$, the orientation bias only accumulates for a time τ and is therefore $O(u'\tau/\lambda)$ or $O(u'\tau k)$. The bacterial stress, as in the smooth swimmer case is given by $O(u'\tau k)O(nFL)$. We can take $F \sim \mu UL_H$, where $L_H = \alpha_1 L$ is the length of the swimmer head. This, for pushers, overcomes the stabilizing Newtonian response ($O(\mu k u')$) when $\tau > O(nUL^2)^{-1}$ which yields a threshold in terms of the critical value of $nUL^2\tau$. Thus in a similar fashion to smooth swimmers we have an instability when $(\lambda, U\tau) > O(nL^2)^{-1}$. The range of unstable wavelengths for both smooth swimmers and tumblers is in the interval $O(nL^2)^{-1} < \lambda < \infty$. In terms of a wavenumber the unstable interval is $0 < k < O(nL^2)$. The above scaling arguments can be extended to the case of rotary diffusers by replacing τ by $1/D_r$, so that for rotary diffusers the threshold is given in terms of a critical value of nUL^2/D_r .

The modal diagram for a suspension of tumblers is shown in Fig. 9.1. We can confine our attentions to the ‘mode 1’ branch which results in a finite positive value for the growth rate even at $k = 0$. As shown by Subramanian & Koch (2009), the growth rate of the unstable modes for tumblers follows the relationship $\alpha_{tumblers} = \alpha_{smooth} - 1/\tau$, where α_{smooth} is the growth rate for smooth swimmers presented in chapter 8. Thus, the modal diagram for tumblers can be obtained by shifting the growth rate curves for smooth swimmers (see Fig. 8.1) by an amount $1/\tau$ in the negative growth rate direction. At a certain value of the mean-run-time, the modal diagram shifts completely into the stable side. This corresponds to equating the growth rate of the fastest growing $k = 0$ modes to zero, which from Fig. 9.1 gives us the neutral curve for the instability as:

$$0.2(CnUL^2) = \frac{1}{\tau}, \quad (9.1)$$

which gives:

$$nUL^2\tau|_{critical} = \frac{5}{C}, \quad (9.2)$$

consistent with scaling arguments above. The complete modal picture (for arbitrary wavelengths) for rotary diffusers is not amenable to analysis, and appears more complicated from available numerical evidence (Hohenegger & Shelley (2010), Saintillan (2010)). But, the threshold condition must involve a critical value of nUL^2/D_r , as mentioned above, and the precise value is mentioned below.

Subramanian & Koch (2009) present a solution for the neutral curve for both wild type

tumblers and also rotary diffusers. For a suspension of wild-type tumblers this is given by:

$$nL^3|_{crit} = \frac{\frac{5}{C\mathcal{F}(\gamma)} \left(\frac{L}{U\tau}\right)}{\left(1 - \frac{5\mathcal{G}(\gamma)}{2C\mathcal{F}(\gamma)} \left(\frac{L}{U\tau}\right)\right)}, \quad (9.3)$$

and, for a suspension of rotary diffusers, the threshold is given by:

$$nL^3|_{crit} = \frac{\frac{30}{C\mathcal{F}(\gamma)} \left(\frac{D_r L}{U}\right)}{\left(1 - \frac{15\mathcal{G}(\gamma)}{C\mathcal{F}(\gamma)} \left(\frac{D_r L}{U}\right)\right)}. \quad (9.4)$$

In the above equations C is a constant characterizing the swimming dipole, defined in chapter 8, $\mathcal{F}(\gamma)$ is a dimensionless function of the aspect ratio γ defined as $\mathcal{F}(\gamma) = (\gamma^2 - 1)/(\gamma^2 + 1)$ for a bacterial head of a spheroidal geometry. For our case, $\mathcal{F}(\gamma) = 1$, since we consider the swimmers to be slender rods for which $\gamma \rightarrow \infty$. The function $\mathcal{G}(\gamma)$ is related to the induced dipole and is zero in our simulations since we neglect the effects of the induced dipole. With these simplifications, the thresholds relevant to our simulations for the case of tumblers is given by:

$$nL^3|_{crit} = \frac{5}{C} \left(\frac{L}{U\tau}\right), \quad (9.5)$$

and, for rotary diffusers, we have:

$$nL^3|_{crit} = \frac{30}{C} \left(\frac{LD_r}{U}\right). \quad (9.6)$$

We note that Eq. 9.5 is exactly same as Eq. 9.2. These are very important results with respect to simulations and experiments, since they tell us that there are two possible ways of crossing the threshold for instability. In the first the volume fraction is varied with the mean-run-time or D_r held fixed. In the second, we keep the volume fraction fixed while varying the mean-run-time or D_r . As we see later, the second method is specially useful since it allows us to study relatively dilute suspensions for which pair-correlations and higher order correlations may be neglected, in which case puller suspensions serve as a true contrast. This allows us to compare our results to linear stability theory (Subramanian & Koch (2009)), which is also valid in the dilute limit. Recent experiments by Karmakar *et al.* (2014) with modified strains of *E. coli* which display a range of mean-run-times also motivate our study of τ variation.

In simulations, the relevant growth rate is not that corresponding to the $k = 0$ mode but that due to the smallest wavenumber in the simulations which is $O(1/L_{box})$. This introduces a correction to the $k = 0$ threshold in Eq. 9.2 of $O(L/L_{box})^2$. For the sake of brevity we only write down the final result for this correction:

$$nUL^2\tau|_{critical} = \frac{5}{C} \left[1 + \frac{0.289}{\nu^2} \left(\frac{L}{L_{box}}\right)^2\right] \quad (9.7)$$

Fig. 9.2, shows a plot of the critical value of $nUL^2\tau$ as a function of L/L_{box} for the case of $\nu = 0.05$, which will be relevant to the results presented later in this chapter. The simulation boxes for which we present results are marked in the abscissa of Fig. 9.2.

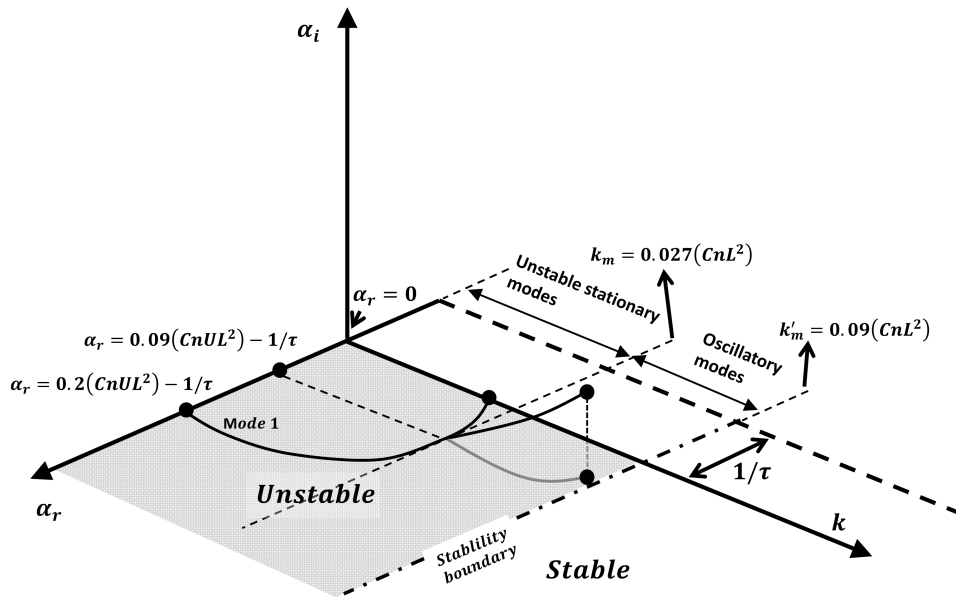


Figure 9.1: Modal digram for a suspension of pushers with tumbling as the intrinsic orientation relaxation mechanism. Reproduced from [Subramanian *et al.* \(2011a\)](#).

The rest of this chapter is organized as follows. We first present the existing theory for tracer transport in an unbounded suspension of tumblers in the stable regime in section 9.2.2. We then go on to modify this theory to account for the tracer diffusion in an infinite periodic suspension in section 9.2.2. The latter theory comes in useful while discussing our simulation results for tracer diffusion in tumbler suspensions. Moving on to the results, in section 9.3.1 we first consider a suspension of tumblers with a fixed value of τ but for varying volume fractions and contrast them to the smooth swimmers considered earlier. We then look at the effects of varying the mean-run-time keeping the volume fraction fixed in section 9.3.2. In both cases we contrast the tracer diffusion curves in pusher and puller suspensions in order to estimate the threshold for onset of collective behaviour. We conclude the chapter by presenting similar results for swimmers where rotary diffusion is the means of orientation decorrelation in section 9.4.

9.2.2 Theory: Tracer Transport in Swimmer Suspensions

In this section we summarize some results for tracer transport in an unbounded suspension of pushers and pullers, in the stable regime, by [Kasyap *et al.* \(2014\)](#), and then, extend the theory for a periodic box. The periodic box results are relevant to the simulation results presented later in this chapter, and serve as a valuable base for validation of the simulations.

Tracer Transport in an Unbounded Domain

We begin by giving an overview of results for an unbounded suspension by [Kasyap *et al.* \(2014\)](#). They consider a dilute suspension of swimmers ($nL^3 \ll 1$), such that swimmer-swimmer and many swimmer-tracer pair-correlations can be neglected. Each tracer particle is therefore connected by the velocity field due to a single bacterium. The main result is an expression for the hydrodynamic tracer diffusivity i.e the tracer diffusivity due to the bacterial disturbance velocity

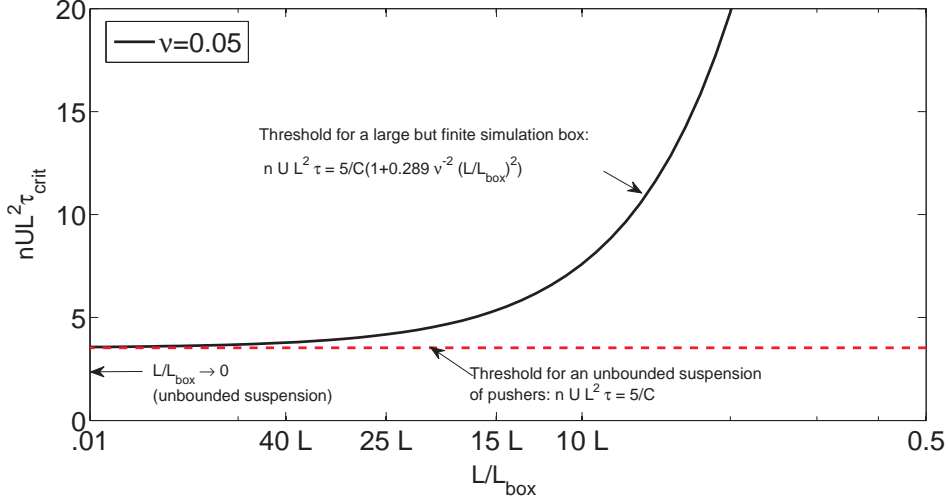


Figure 9.2: Plot of the critical value of $nUL^2\tau$ for a periodic swimmer array as a function of L/L_{box} for $\nu = 0.05$. The red dashed line represents the result for an unbounded suspension ($L/L_{box} \rightarrow \infty$). The simulation box sizes for which we present results: 10, 15, 25 and 40 swimmer lengths, are marked on the abscissa.

field. This diffusivity is given by:

$$D_h = nL^3UL\tilde{D}_h, \quad (9.8)$$

where \tilde{D}_h is the dimensionless tracer diffusivity. This is given in terms of the Fourier transformed disturbance velocity field as (see Eq. (21) in [Kasyap et al. \(2014\)](#)):

$$D_h = \frac{n}{12\pi} \int d\mathbf{p} \int d\mathbf{k} \frac{\hat{\mathbf{U}}(\mathbf{k}) \cdot \hat{\mathbf{U}}(-\mathbf{k})}{(2\pi k)^2 D + 2\pi i \mathbf{k} \cdot \mathbf{p} U + \frac{1}{\tau}}, \quad (9.9)$$

where $\hat{\mathbf{U}}(\mathbf{k})$, is the Fourier transform of the velocity field given by:

$$\hat{\mathbf{U}}(\mathbf{k}) = \int_{\mathbf{x}} d\mathbf{x} \mathbf{u}'(\mathbf{x}) e^{-2\pi i \mathbf{k} \cdot \mathbf{x}}. \quad (9.10)$$

In the above equation, $\mathbf{u}'(\mathbf{x})$ is the disturbance velocity at \mathbf{x} due to an unbounded suspension of swimmers, where the position is measured relative to a coordinate system on the swimmer. Using the expressions for $\hat{\mathbf{U}}(\mathbf{k})$ as given in [Kasyap et al. \(2014\)](#), scaling the wavenumber by the factor $(2\pi L)^{-1}$, and rescaling the terms in the denominator, we get:

$$\tilde{D}_h = \frac{1}{96\pi^4 M^2} \int d\mathbf{p} \int d\mathbf{k} \frac{[k^2 - (\mathbf{k} \cdot \mathbf{p})^2] F(\mathbf{k} \cdot \mathbf{p}) F(-\mathbf{k} \cdot \mathbf{p})}{k^6 \left(\frac{1}{\tau^*} + i \mathbf{k} \cdot \mathbf{p} + \frac{k^2}{Pe} \right)}. \quad (9.11)$$

Here, $Pe = UL/D$ and measures the relative strength of convection due to the swimmers and the thermal diffusion of the tracer and $\tau^* = U\tau/L$, which is the average distance the bacterium swims before tumbling relative to its own length. Note that since we use $L/(2U)$ as the time scale, the non-dimensional mean-run-time for our case is $2U\tau/L = 2\tau^*$. We will use our scaling for τ from hereon (this merely involves replacing $1/\tau^*$ with $2/\tau$ in Eq. 9.11 since we will continue using τ to represent the dimensionless mean-run-time). The term $F(\mathbf{k} \cdot \mathbf{p})$ in Eq. 9.11 involves

the Fourier transform of the bacterial force density, and is defined as:

$$F(\mathbf{k} \cdot \mathbf{p}) = -\frac{1}{i\mathbf{k} \cdot \mathbf{p}} \left\{ e^{-i\alpha_1 \mathbf{k} \cdot \mathbf{p}/2} - \frac{1}{1-\alpha_1} e^{i\alpha_1 \mathbf{k} \cdot \mathbf{p}/2} + \frac{\alpha_1}{1-\alpha_1} e^{i[1-\alpha_1/2]\mathbf{k} \cdot \mathbf{p}} \right\}. \quad (9.12)$$

For the case of fore-aft symmetric swimmers ($\alpha_1 = 1/2$), as is the case in our simulations, we can simplify the above expression and we have:

$$F(\mathbf{k} \cdot \mathbf{p})F(-\mathbf{k} \cdot \mathbf{p}) = \frac{16 \sin^4(\mathbf{k} \cdot \mathbf{p}/4)}{(\mathbf{k} \cdot \mathbf{p})^2}. \quad (9.13)$$

Since $F(\mathbf{k} \cdot \mathbf{p})$ is proportional to the intrinsic force-dipole, the quadratic combination of $F(\mathbf{k} \cdot \mathbf{p})F(-\mathbf{k} \cdot \mathbf{p})$ implies the expression Eq. 9.13 remains the same for pullers (when $\alpha_1 = 1/2$, as is the case in our simulations). Therefore, the analysis from hereon is equally applicable to both pushers and pullers, the tracer diffusivity in the dilute regime considered being independent of the swimming mechanism. Substituting in Eq. 9.11, we get:

$$\tilde{D}_h = \frac{1}{6\pi^4 M^2} \int d\mathbf{p} \int d\mathbf{k} \frac{[k^2 - (\mathbf{k} \cdot \mathbf{p})^2] \sin^4(\mathbf{k} \cdot \mathbf{p}/4)}{(\mathbf{k} \cdot \mathbf{p})^2 k^6 \left(\frac{2}{\tau} + i\mathbf{k} \cdot \mathbf{p} + \frac{k^2}{Pe} \right)}. \quad (9.14)$$

Proceeding as in Kasyap *et al.* (2014), one defines a cylindrical coordinate system with its axis along \mathbf{p} , such that $d\mathbf{k} = 2\pi k_\perp dk_\perp dk_\parallel$ where $k_\parallel = \mathbf{k} \cdot \mathbf{p}$ and $k_\perp = |\mathbf{k} - (\mathbf{k} \cdot \mathbf{p})\mathbf{p}|$. Transforming Eq. 9.14 to the cylindrical coordinate system, and considering the limit where tracers are only convected by the swimmer velocity field ($Pe \rightarrow \infty$), we have:

$$\tilde{D}_h = \frac{1}{6\pi^4 M^2} \int d\mathbf{p} \int_{-\infty}^{\infty} dk_\parallel \int_0^{\infty} 2\pi k_\perp dk_\perp \frac{k_\perp^2 \sin^4(k_\parallel/4)}{k_\parallel^2 (k_\parallel^2 + k_\perp^2)^3 \left(\frac{2}{\tau} + ik_\parallel \right)}, \quad (9.15)$$

$$\tilde{D}_h = \frac{1}{3\pi^3 M^2} \int d\mathbf{p} \int_{-\infty}^{\infty} dk_\parallel \frac{\sin^4(k_\parallel/4)}{k_\parallel^2 \left(\frac{2}{\tau} + ik_\parallel \right)} \int_0^{\infty} dk_\perp \frac{k_\perp^3}{(k_\parallel^2 + k_\perp^2)^3}. \quad (9.16)$$

We can perform the integral with respect to k_\perp and \mathbf{p} analytically which gives:

$$\tilde{D}_h = \frac{1}{3\pi^2 M^2} \int_{-\infty}^{\infty} \frac{\sin^4(k_\parallel/4)}{k_\parallel^4 \left(\frac{2}{\tau} + ik_\parallel \right)} dk_\parallel. \quad (9.17)$$

We can evaluate the remaining integral over k_\parallel numerically via adaptive Gaussian quadrature in MATLAB. It is straightforward to derive the small- τ asymptote of the tracer diffusivity by expanding the denominator of the integrand in Eq. 9.17. The leading order term is then given by:

$$\tilde{D}_h = \frac{\tau}{576\pi M^2} \quad (9.18)$$

The evaluation of the large τ asymptote requires a little more care and has been done by Kasyap *et al.* (2014). Considering Eq. 9.17 in the limit of $\tau \rightarrow \infty$, we see from the denominator of the integrand that the domination contribution comes from a region in k_\parallel which $O(1/\tau^*)$ or smaller.

Expanding the integrand for small k_{\parallel} , we get:

$$\tilde{D}_h = \lim_{\tau \rightarrow \infty} \frac{1}{768\pi^2 M^2} \int_{-\infty}^{\infty} \frac{1}{\left(\frac{2}{\tau} + ik_{\parallel}\right)} dk_{\parallel} \quad (9.19)$$

The neglect of the term $1/(2\tau)$ from the denominator of Eq. 9.19 leads to a divergent integral which must be interpreted in the sense of a Cauchy principal value. On evaluating the integral, with such an interpretation, one gets:

$$\tilde{D}_h = \frac{1}{768\pi M^2} \quad (9.20)$$

The results for the non-dimensional tracer diffusivity, as a function of the mean-run-time τ , is plotted in Fig. 9.3. It is interesting to note that the tracer diffusivity for smooth swimmers does not go to zero as predicted in earlier works (Morozov & Marenduzzo (2014)). The above analysis tells us, rather surprisingly, that, for smooth swimmers, the contribution to the tracer diffusivity comes from length scales much larger than the swimmer length, or equivalently, from the small wavenumber contribution in the tracer diffusion integral where tumbling continues to be important. This peculiarity implies that the result above could not have been arrived at from the purely deterministic limit where the symmetric nature of the deterministic swimmer trajectories would lead to a zero diffusivity. This raises an interesting question regarding the tracer diffusivity in a periodic box which is relevant to simulations where such a cancellation will not occur once the length of the trajectory exceeds the box dimensions. Since the simulation box is finite in size, the wavenumber space is discrete and the smallest wavenumber is inversely proportional to the size of the simulation box. We therefore expect a non-trivial effect of using a finite simulation box, since for large enough τ ($\tau > L_{box}/(2U)$), the dominant contribution will be from wavenumbers less than $O(1/L_{box})$ in the simulations; unlike the unbounded theory, where the dominant contribution continues to come from a wavenumber interval of $O(1/L)$. The understanding of this singular effect of periodicity motivates our derivation of the tracer diffusivity in a periodic box.

Tracer Transport in Periodic Domains

To evaluate the tracer diffusivity in a periodic box, our approach follows that of Kasyap *et al.* (2014). We consider a cubic simulation box of size L_{box} with periodic boundary conditions in all three dimensions. We again start from Eq. (21) in Kasyap *et al.* (2014) which gives the tracer diffusivity as a function of the Fourier transformed disturbance velocity field. For the periodic box case, the integral over wavenumber space is replaced by a summation over discrete wave vectors normalized by the volume of the simulation box, and is given by:

$$D_h = \frac{n}{12\pi L_{box}^3} \int d\mathbf{p} \sum_{\mathbf{k} \neq 0} \frac{\hat{U}(\mathbf{k}) \cdot \hat{U}(-\mathbf{k})}{(2\pi k)^2 D + 2\pi i \mathbf{k} \cdot \mathbf{p} U + \frac{1}{\tau}}, \quad (9.21)$$

where $\hat{U}(\mathbf{k})$, is the Fourier transform of the velocity field given by:

$$\hat{U}(\mathbf{k}) = \int_{\mathbf{x}} d\mathbf{x} \mathbf{u}'(\mathbf{x}) e^{-2\pi i \mathbf{k} \cdot \mathbf{x}}. \quad (9.22)$$

In the above equation, $\mathbf{u}'(\mathbf{x})$ is the periodic disturbance velocity at \mathbf{x} due to an infinite cubic array of swimmers, where the position is measured relative to a coordinate system on the swimmer. We note that for $\mathbf{k} = 0$, the above is just the average of the disturbance velocity over the periodic box, which is zero for a suspension of force-free swimmers. We can therefore neglect $\mathbf{k} = 0$ terms. As discussed in Brady *et al.* (1988), even for the case where each particle exerts a force, this term is related to average back-flow in the suspension, and must therefore be excluded from the summation. Recall that the above expression in slightly different form has been derived earlier in the context of the Ewald summation method in chapter 7 in section 7.3. The expression for $\hat{U}(\mathbf{k})$ can be shown to be given by:

$$\hat{U}(\mathbf{k}) = \frac{UL_{box}^3}{Mk^2} \left[\mathbf{p} - \frac{(\mathbf{k} \cdot \mathbf{p})\mathbf{k}}{k^2} \right] F(\mathbf{k} \cdot \mathbf{p}), \quad (9.23)$$

where $F(\mathbf{k} \cdot \mathbf{p})$ is given by:

$$F(\mathbf{k} \cdot \mathbf{p}) = -\frac{1}{i\mathbf{k} \cdot \mathbf{p}} \left\{ e^{-\frac{i\alpha_1 \mathbf{k} \cdot \mathbf{p}}{2} \frac{L}{L_{box}}} - \frac{1}{1 - \alpha_1} e^{\frac{i\alpha_1 \mathbf{k} \cdot \mathbf{p}}{2} \frac{L}{L_{box}}} + \frac{\alpha_1}{1 - \alpha_1} e^{i[1 - \frac{\alpha_1}{2}] \mathbf{k} \cdot \mathbf{p} \frac{L}{L_{box}}} \right\}. \quad (9.24)$$

In the Eqs. 9.23 and 9.24, the wavenumber is scaled by the factor $(2\pi L_{box})^{-1}$. Substituting Eqs. 9.23 and 9.24 in Eq. 9.21, and rescaling the terms in the denominator, we get:

$$D_h = \frac{n}{12\pi L_{box}^3} \int d\mathbf{p} \sum_{\mathbf{k} \neq 0} \frac{\left(\frac{UL_{box}^3}{Mk^2} \right)^2 \left(\mathbf{p} - \frac{(\mathbf{k} \cdot \mathbf{p})\mathbf{k}}{k^2} \right) \cdot \left(\mathbf{p} - \frac{(\mathbf{k} \cdot \mathbf{p})\mathbf{k}}{k^2} \right) F(\mathbf{k} \cdot \mathbf{p}) F(-\mathbf{k} \cdot \mathbf{p})}{\frac{k^2 D}{L_{box}^2} + \frac{i\mathbf{k} \cdot \mathbf{p} U}{L_{box}} + \frac{2U}{L\tau}}, \quad (9.25)$$

where we have rescaled τ by $L/(2U)$, such that $\tau = \tau/(L/(2U))$, and we retain the same notation for simplicity. Using this rescaling, we get:

$$D_h = \frac{nU^2 L_{box}^3}{12\pi M^2} \int d\mathbf{p} \sum_{\mathbf{k} \neq 0} \frac{[k^2 - (\mathbf{k} \cdot \mathbf{p})^2] F(\mathbf{k} \cdot \mathbf{p}) F(-\mathbf{k} \cdot \mathbf{p})}{k^6 \left[\frac{k^2 D}{L_{box}^2} + \frac{i\mathbf{k} \cdot \mathbf{p} U}{L_{box}} + \frac{2}{\tau} \right]}. \quad (9.26)$$

Simplifying, we get:

$$D_h = \frac{nUL_{box}^3 L}{12\pi M^2} \int d\mathbf{p} \sum_{\mathbf{k} \neq 0} \frac{[k^2 - (\mathbf{k} \cdot \mathbf{p})^2] F(\mathbf{k} \cdot \mathbf{p}) F(-\mathbf{k} \cdot \mathbf{p})}{k^6 \left[k^2 \frac{D}{LU} \frac{L^2}{L_{box}^2} + i\mathbf{k} \cdot \mathbf{p} \frac{L}{L_{box}} + \frac{2}{\tau} \right]}, \quad (9.27)$$

$$D_h = nL^3 UL \left(\frac{L_{box}}{L} \right)^3 \frac{1}{12\pi M^2} \int d\mathbf{p} \sum_{\mathbf{k} \neq 0} \frac{[k^2 - (\mathbf{k} \cdot \mathbf{p})^2] F(\mathbf{k} \cdot \mathbf{p}) F(-\mathbf{k} \cdot \mathbf{p})}{k^6 \left[k^2 Pe \frac{L^2}{L_{box}^2} + i\mathbf{k} \cdot \mathbf{p} \frac{L}{L_{box}} + \frac{2}{\tau} \right]}, \quad (9.28)$$

where we have used, as before, $Pe = UL/D$. For the specific case relevant to our simulations, we use $\alpha_1 = 1/2$, which gives:

$$F(\mathbf{k} \cdot \mathbf{p}) F(-\mathbf{k} \cdot \mathbf{p}) = \frac{16 \sin^4 \left(\frac{\mathbf{k} \cdot \mathbf{p}}{4} \frac{L}{L_{box}} \right)}{(\mathbf{k} \cdot \mathbf{p})^2}. \quad (9.29)$$

Substituting the above expression in Eq. 9.28, and considering the $Pe \rightarrow \infty$ limit (a non-Brownian tracer, as is the case in the simulations), we get:

$$\tilde{D}_h = \frac{4}{3\pi M^2} \left(\frac{1}{L^*}\right)^3 \int d\mathbf{p} \sum_{\mathbf{k} \neq 0} \frac{[k^2 - (\mathbf{k} \cdot \mathbf{p})^2] \sin^4\left(\frac{L^* \mathbf{k} \cdot \mathbf{p}}{4}\right)}{(\mathbf{k} \cdot \mathbf{p})^2 k^6 [i\mathbf{k} \cdot \mathbf{p} L^* + \frac{2}{\tau}]}, \quad (9.30)$$

where we have denoted the ratio $L/L_{box} = L^*$. Interchanging the integral and summation, and using a polar coordinate system aligned in the \mathbf{k} direction, we have $\mathbf{k} \cdot \mathbf{p} = k \cos \theta$ and $d\mathbf{p} = \sin \theta d\theta d\phi$. Using these, the integral over the unit sphere can be written as:

$$\tilde{D}_h = \frac{4}{3\pi M^2} \left(\frac{1}{L^*}\right)^3 \sum_{\mathbf{k} \neq 0} \frac{1}{k^8} \int_0^{2\pi} d\phi \int_0^\pi d\theta \sin \theta \frac{[k^2 - k^2 \cos^2 \theta] \sin^4\left(\frac{kL^* \cos \theta}{4}\right)}{\cos^2 \theta [ik \cos \theta L^* + \frac{2}{\tau}]}. \quad (9.31)$$

Simplifying, we get:

$$\tilde{D}_h = \frac{8}{3M^2} \left(\frac{1}{L^*}\right)^3 \sum_{\mathbf{k} \neq 0} \frac{1}{k^6} \int_0^\pi d\theta \sin \theta \left(\frac{1 - \cos^2 \theta}{\cos^2 \theta}\right) \frac{\sin^4\left(\frac{kL^* \cos \theta}{4}\right)}{[ik \cos \theta L^* + \frac{2}{\tau}]}. \quad (9.32)$$

Making the transformation, $m = \cos \theta$, we get:

$$\tilde{D}_h = \frac{8}{3M^2} \left(\frac{1}{L^*}\right)^3 \sum_{\mathbf{k} \neq 0} \frac{1}{k^6} \int_{-1}^1 dm \left(\frac{1 - m^2}{m^2}\right) \frac{\sin^4\left(\frac{kL^* m}{4}\right)}{[ikmL^* + \frac{2}{\tau}]}. \quad (9.33)$$

Eq. 9.33 is the final expression for the non-dimensional tracer diffusivity in a periodic box. The integral over m can be performed numerically using the adaptive Gaussian quadrature implemented in MATLAB. The sum over \mathbf{k} excluding $\mathbf{k} = 0$ is performed numerically by specifying a tolerance of 10^{-8} for convergence.

The two asymptotic limits of $\tau \rightarrow 0$ and $\tau \rightarrow \infty$ follow immediately from Eq. 9.33. Considering first the $\tau \rightarrow 0$ limit, we can rewrite Eq. 9.33 as:

$$\tilde{D}_h = \frac{4}{3M^2} \left(\frac{1}{L^*}\right)^3 \tau \sum_{\mathbf{k} \neq 0} \frac{1}{k^6} \int_{-1}^1 dm \left(\frac{1 - m^2}{m^2}\right) \frac{\sin^4\left(\frac{kL^* m}{4}\right)}{[ikmL^* \frac{\tau}{2} + 1]}. \quad (9.34)$$

Expanding the denominator ($ikmL^* \tau/2 + 1$) in a geometric series and considering the leading order term, we have:

$$\tilde{D}_h = \frac{8}{3M^2} \left(\frac{1}{L^*}\right)^3 \tau \sum_{\mathbf{k} \neq 0} \frac{1}{k^6} \int_0^1 dm \left(\frac{1 - m^2}{m^2}\right) \sin^4\left(\frac{kL^* m}{4}\right), \quad (9.35)$$

where we have used the fact that the integrand is an even function of m . From Eq. 9.35 we see that, for small values of τ , the non-dimensional tracer diffusivity is linear in τ reaching a value of zero at $\tau = 0$, which physically corresponds to swimmers which tumble constantly. As a result, the tracer sees a velocity field that decorrelates almost instantaneously, leading to a vanishingly small diffusivity. This expression is analogous to the small τ asymptote obtained for the case of an unbounded domain (see Eq. 9.18), implying that periodicity is a regular effect for $\tau \rightarrow 0$.

To derive the $\tau \rightarrow \infty$ limit, we rewrite Eq. 9.33 as:

$$\tilde{D}_h = \frac{8}{3M^2} \left(\frac{1}{L^*}\right)^3 \sum_{\mathbf{k} \neq 0} \frac{1}{k^6} \int_{-1}^1 dm \left(\frac{1-m^2}{m^2}\right) \frac{\sin^4\left(\frac{kL^*m}{4}\right)}{ikmL^* \left[1 + \frac{2}{ikmL^*\tau}\right]}. \quad (9.36)$$

Expanding the denominator $[1 + 2/(ikmL^*\tau)]$ in a geometric series, we get:

$$\tilde{D}_h = \frac{8}{3M^2} \left(\frac{1}{L^*}\right)^3 \sum_{\mathbf{k} \neq 0} \frac{1}{k^6} \int_{-1}^1 dm \left(\frac{1-m^2}{m^2}\right) \frac{\sin^4\left(\frac{kL^*m}{4}\right)}{ikmL^*} \left[1 - \frac{2}{ikmL^*\tau}\right]. \quad (9.37)$$

The first term is odd in m and hence is zero. The second term, therefore, gives the leading-order contribution to the diffusivity, as:

$$\tilde{D}_h = \frac{32}{3M^2} \left(\frac{1}{L^*}\right)^5 \frac{1}{\tau} \sum_{\mathbf{k} \neq 0} \frac{1}{k^8} \int_0^1 dm \left(\frac{1-m^2}{m^4}\right) \sin^4\left(\frac{kL^*m}{4}\right). \quad (9.38)$$

Note the inverse scaling with τ in Eq. 9.38. This leads to the surprising conclusion that the tracer diffusivity in a periodic box in the limit of $\tau \rightarrow \infty$ (smooth swimmer) goes to zero. We recall that this was not the case for an unbounded suspension which involved a finite value emerging from a principal-value integral, and is therefore a non-trivial effect of the finite box size. This is an important result due to its relevance in our simulations. The reason for this singular role of periodicity can be deduced from Eq. 9.17, where we saw that, in the limit of large τ , the dominant contribution to the integral came from wavenumbers of $O(1/\tau)$ or smaller. However, in a periodic box, we see from the denominator of Eq. 9.33 that the smallest wavenumber is $O(L^*)$ or in dimensionless form $O(1/L_{box})$. Thus, for $1/\tau \ll L^*$, the dominant contribution in the unbounded case is not captured by the discrete sum over \mathbf{k} , leading to the long-time tracer diffusivity going to zero. The dimensionless (non-Brownian) tracer diffusivity is plotted in Fig. 9.3 for a number of box sizes along with the result for an unbounded suspension. The tracer diffusivity in an unbounded suspension increases monotonically with τ , with the large τ asymptote given by Eq. 9.20 that is $O(nUL^4)$ (see Kasyap *et al.* (2014)), and therefore, independent of τ . However, we see that the periodic-box diffusivity is non-monotonic with a maximum at a finite value of τ , as expected from the above scalings. The small and large τ asymptotes in this case are given by Eqs. 9.35 and 9.38 and are also shown in Fig. 9.3. One can clearly see the periodic box results systematically approaching the unbounded one as one increases the size of the simulation box. This non-monotonic trend in simulations of tracer transport in a periodic box was erroneously attributed to the closed-loop nature of the tracer particles by Morozov & Marenduzzo (2014). Later in this chapter, we compare our simulation results with the theoretical results derived above, which serve as a valuable standard of reference.

The tracer diffusivity is not strongly affected by box size only when $U\tau \ll L_{box}$, where the parameters are now in dimensional form. Physically this implies the run length of the swimmer is small when compared to the simulation box size. Therefore, as long as we stay in the regime $U\tau \ll L_{box}$, the finite box size does not affect the tracer diffusion results and we can predict a box-size-independent threshold by monitoring the tracer diffusivities in pusher and puller suspensions. In contrast, for smooth swimmers, the rate of orientation decorrelation due

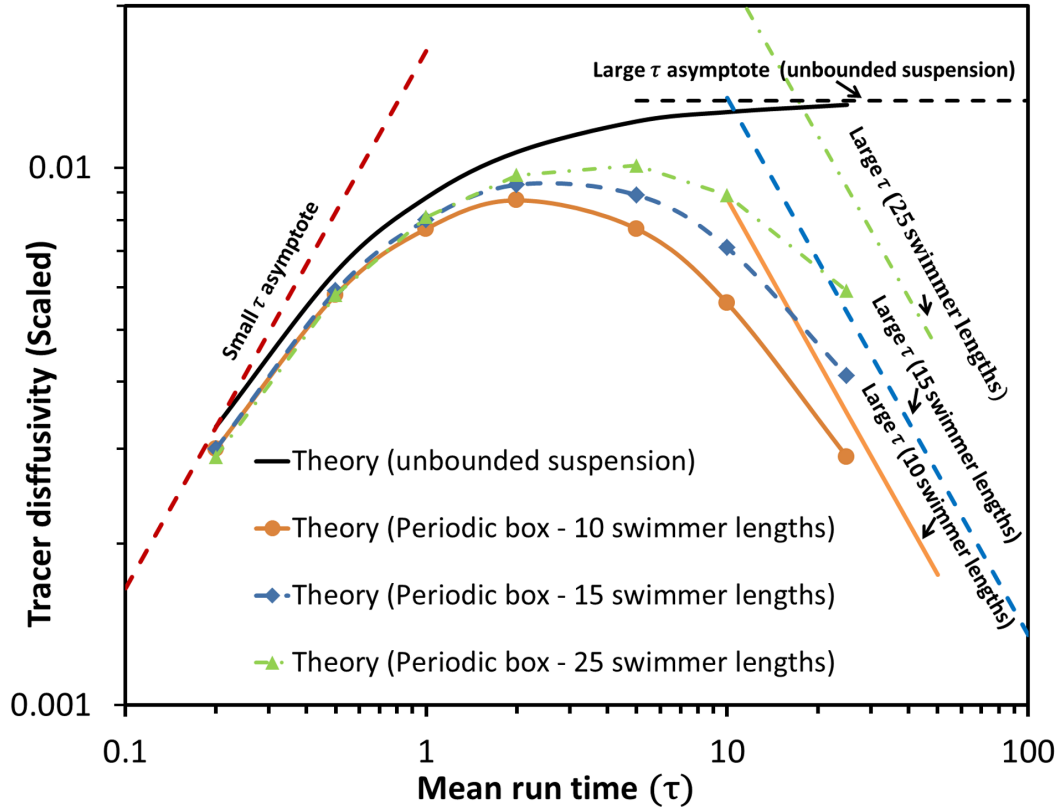


Figure 9.3: Theoretical predictions for the tracer diffusivity in an unbounded suspension, and in an infinite periodic swimmer array. Note that in an unbounded suspension (solid black curve) the diffusivity monotonically increases with a well defined large τ asymptote. The periodic box results show a non-monotonic trend, with large τ asymptote which is $\sim O(1/\tau)$. The small τ asymptotes of the periodic swimmer array are also shown.

to hydrodynamic interactions is, by definition, comparable to the periodicity time scale at the stability threshold.

9.3 Results and Discussions: Tumblers

9.3.1 Comparison between Tumblers and Smooth Swimmers: Volume Fraction Variation

In this section, we present results for suspensions of pushers and pullers which tumble at a certain fixed rate ($\tau = 1$) for two different box sizes (10 and 15 swimmer lengths). Using statistical measures for the swimmers, the intervening fluid and tracer transport, we now study the dynamics of a suspension of tumblers and contrast it with our earlier results for smooth swimmers.

Fluid Velocity Statistics

We first consider the probability distribution for the fluid velocity plotted in Fig. 9.4a. In contrast to the smooth swimmer case (see Fig. 8.5a in chapter 8), here we see that, even at higher volume fractions, pushers and pullers display similar behaviour. The fluctuations do

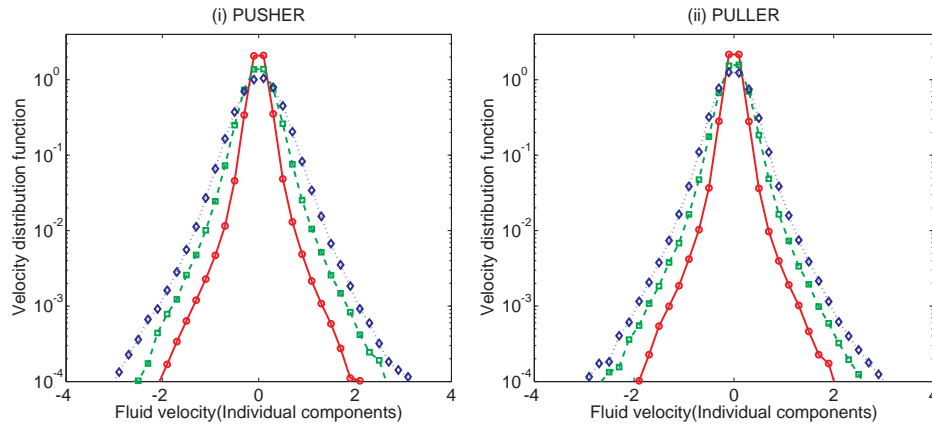
increase in magnitude with increasing volume fraction for pushers, however this increase is much smaller compared to that seen earlier for smooth swimming pushers. The qualitative behaviour for pullers which tumble is not very different from the smooth swimming case. For tumblers, as seen in Fig. 9.4b, there is no clear evidence of bulk motion in the plots of the probability distribution for the fluid velocity magnitude. This is in contrast to smooth swimming pushers which show clear evidence of bulk motion in the fluid (see Fig. 8.5b). To detect the signature of weak bulk motion (if any) for pushers, we will use other measures such as the fluid velocity power spectrum and the tracer diffusivity, specially the latter given it is sensitive to the onset of collective motion, as shown in the previous chapter. However, on plotting the mean fluid kinetic energy as a function of volume fraction (Fig. 9.4c), we see that a small yet systematic difference still exists between pushers and pullers. These grow with volume fraction, with pushers showing marginally (6%) greater fluid kinetic energy than pullers at $\nu = 0.05$ and around 45% greater at $\nu = 0.5$. Thus, we see that pushers which tumble are characterized by larger velocity fluctuations than pullers. We also note that these differences do not show a strong trend with box size, with results for a 15 swimmer lengths box staying very close to those for a 10 swimmer lengths box (see Fig. 9.4c).

Fig. 9.5 shows the fluid velocity spectrum for a suspension of tumblers at two different volume fractions ($\nu = 0.05$ and $\nu = 0.5$). In this case, it is seen that at higher volume fractions, the pusher spectrum shows an increase for small wavenumbers which correspond to length scales of $O(L_{box})$, although, the increase is smaller in magnitude compared to that in smooth swimmers (see Fig. 8.7 in chapter 8), indicating the stabilization of the suspension due to tumbling. This implies the presence of spatially correlated motions in the fluid (bulk motion), though these hold a smaller fraction of the fluid kinetic energy when compared to the case of smooth swimmers. The maximum of the spectrum still occurs at the lowest wavenumber which seems to suggest that the size of the structures formed in the fluid are still controlled by the size of the simulation box.

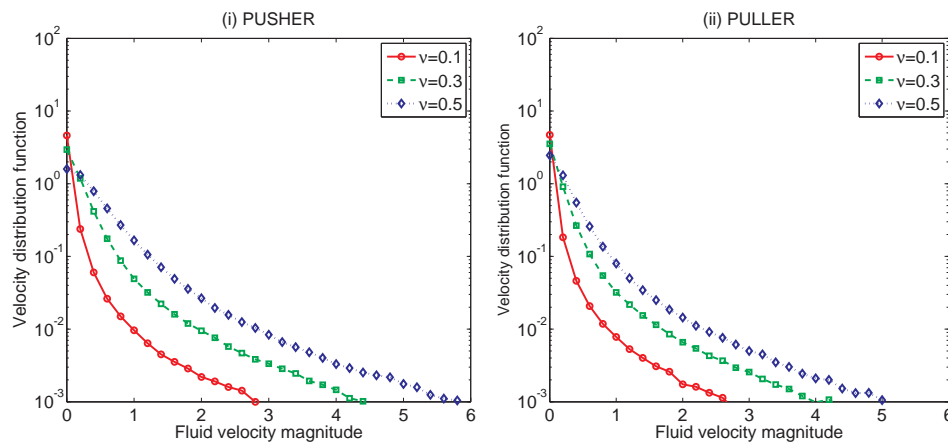
Another measure of the fluid velocity field is the Eulerian correlation time for the velocity vector at a fixed point in space. This function is plotted for a suspension of pushers and pullers which tumble with $\tau = 1$, at two different volume fractions of 0.05 and 0.5, in Fig. 9.6. We see that correlation times for pullers show a decrease with an increase in volume fraction. This is due to the interactions between swimmers becoming more frequent leading to faster orientation decorrelation of the swimmers and hence of the fluid velocity. This trend is similar to that seen for smooth swimming pullers (see Fig. 8.6). For pushers, in contrast, we see a small increase in the correlation time which seems to be related to the onset of the instability. This same increase was seen for smooth swimming pushers (see Fig. 8.6), but for tumblers it is smaller in extent pointing to the stabilization due to tumbling.

Swimmer Statistics

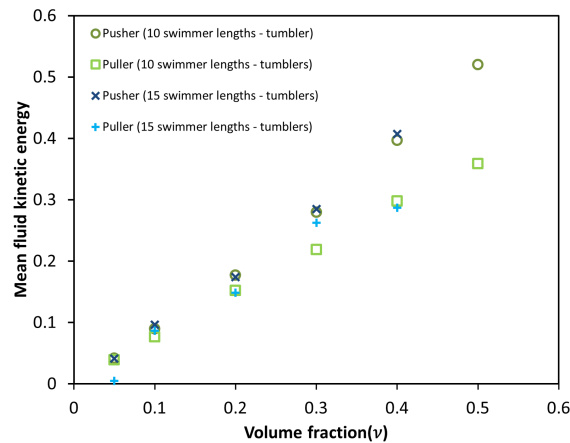
Fig. 9.7a shows a plot of the probability distribution function for the swimmer velocity. Again, tumbling stabilizes the suspension with the pushers and puller distribution function not showing much qualitative differences even at higher volume fractions. The tails of the distribution function for pushers at higher volume fractions are slightly larger when compared to pullers implying larger fluctuations. The swimmer-speed distribution function for pushers shows a flattening, and



(a) Probability distribution function for the fluid disturbance velocity ($\tau = 1$). Simulation box size: 10 swimmer lengths.



(b) Probability distribution function for the fluid disturbance velocity magnitude ($\tau = 1$). Simulation box size: 10 swimmer lengths.



(c) Mean fluid kinetic energy for the case of pushers and pullers plotted versus ν ($\tau = 1$).

Figure 9.4: Fluid velocity statistics for a suspension of tumblers with $\tau = 1$. (a) The probability distribution function for the fluid disturbance velocity plotted for (i) pushers and (ii) pullers for three volume fractions. (b) The probability distribution for the fluid disturbance velocity magnitude plotted for (i) pushers and (ii) pullers for three volume fractions. (c) Mean fluid kinetic energy plotted with respect to ν for pushers and pullers. The simulation box sizes are 10 and 15 swimmer lengths.

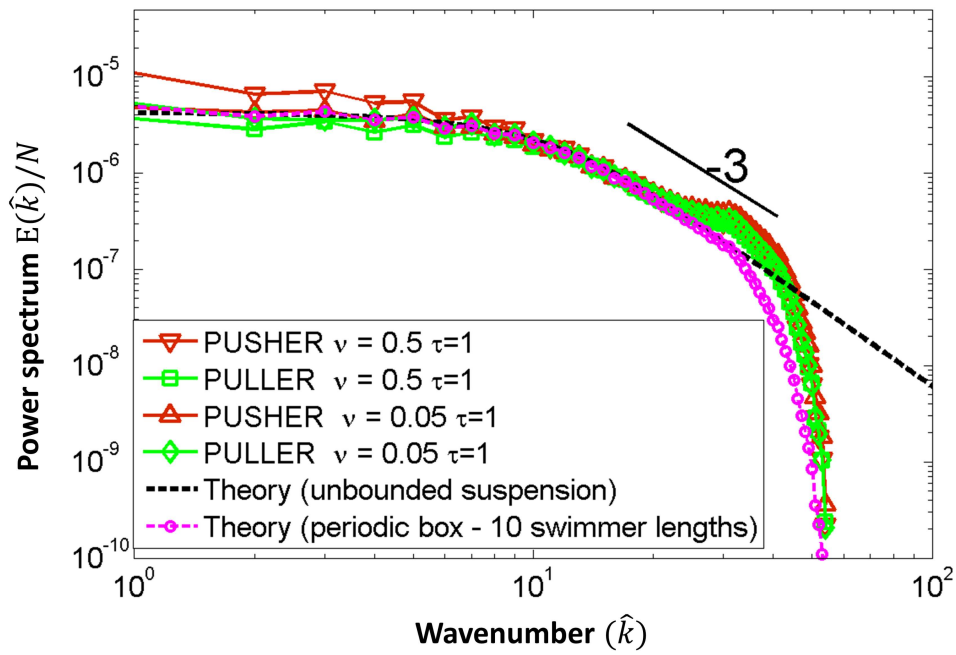


Figure 9.5: Fluid velocity power spectrum, normalized by the number of swimmers, for a suspension of tumblers where the mean-run-time is fixed at $\tau = 1$; and for two different volume fractions: $\nu = 0.05$ and 0.5 . Simulation box size: 10 swimmer lengths.

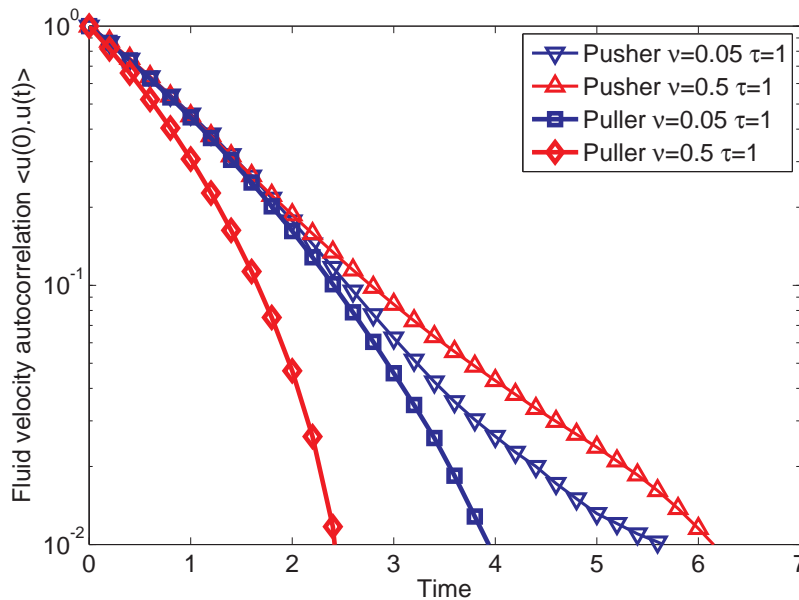


Figure 9.6: Fluid velocity correlation function (Eulerian) for a suspension of tumblers where the mean-run-time is fixed at $\tau = 1$ and for two different volume fractions of 0.05 and 0.5 . Simulation box size: 10 swimmer lengths.

also a small increase in the mean swimming speed as compared to pullers at a volume fraction of $\nu = 0.5$ (see Fig. 9.7b). The mean swimming speed, plotted with volume fraction in Fig. 9.7c confirms this trend with the pushers showing marginally larger values of the swimming speed compared to pullers, the difference growing with volume fraction. We see that the increase in swimming speed is much smaller than what was seen for the mean fluid kinetic energy in the previous section (around 5% relative increase for pushers at $\nu = 0.5$), but nevertheless significant and certainly beyond the typical fluctuations at the relevant volume fractions.

Tracer Transport

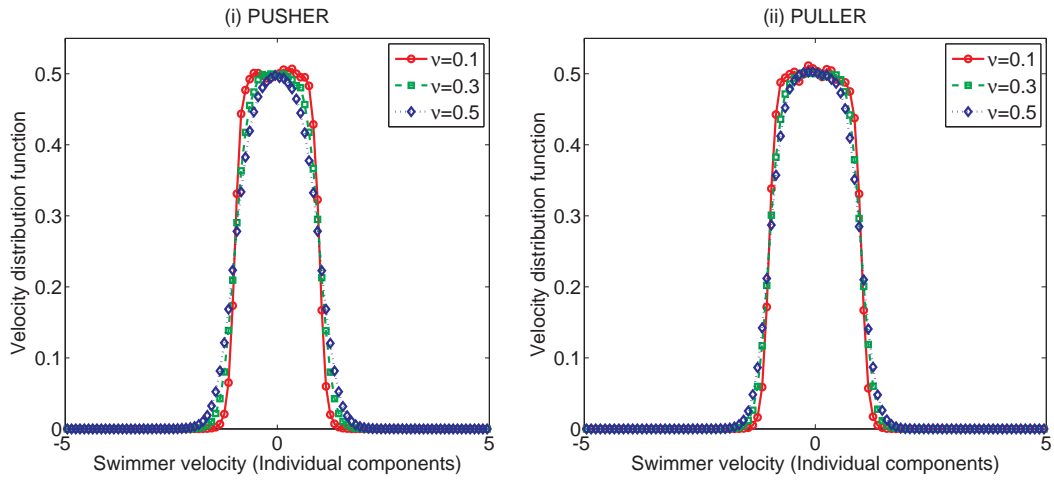
As for the smooth swimmer case, it is instructive to study the tracer transport in a suspension of tumblers. As expected, we see in Fig. 9.8 that the tracer diffusivities for pushers which tumble are much smaller when compared to their smooth swimming counterparts. The tracer diffusivities for tumblers are more than an order of magnitude smaller than those for smooth swimmers at $\nu = 0.6$. On the other hand, no such difference can be seen for pullers whose behaviour is not qualitatively different from the smooth swimmer case. Fig. 9.9a shows a comparison between the pusher and puller tracer diffusivities for the case where both tumble with a mean-run-time of $\tau = 1$. We note from this figure the important result that a suspension of pushers which tumble is unstable beyond a critical volume fraction ($\nu \approx 0.2$ in Fig. 9.9a) although the pusher-puller bifurcation is much more subtle than in the case of smooth swimmers.

The above increase in tracer diffusivity for pusher suspensions relative to pullers, both of which tumble, is consistent with the velocity measures we presented in section 9.3.1. We expect the tracer diffusivity to scale as $u^2\tau_{corr}$, where u is the magnitude of disturbance velocity in the fluid and τ_{corr} is a correlation time for the fluid velocity. We saw in section 9.3.1 that both the mean fluid velocity and correlation time was greater for pushers as compared to pullers. The combined effect translates to much larger tracer diffusivities for pushers as we saw above. As mentioned in the chapter on smooth swimmers (chapter 8), this is the underlying reason for the sensitivity of the tracer diffusivity to the instability and our choice of this measure to detect the onset of collective behaviour.

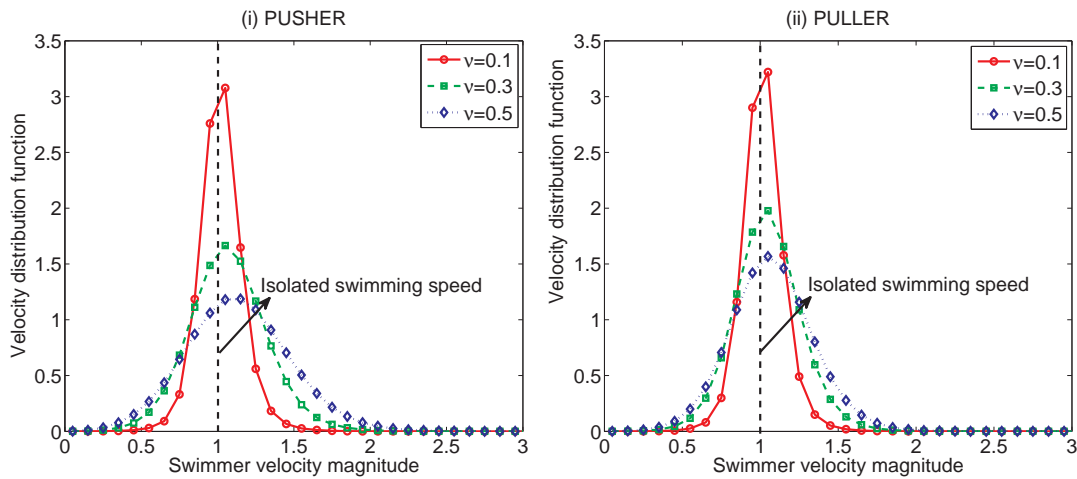
The above result, that pushers that tumble are unstable beyond a critical volume fraction, indicates that tumbling alone is not sufficient to stabilize a suspension and we expect both the volume fraction and tumble rate to play a role in deciding the stability threshold. We recall that the linear stability theory predicts the threshold for tumblers to be in the form of a critical value of the parameter $nUL^2\tau$. To study this, we look at simulations at a fixed volume fraction ($\nu = 0.05$) and varying τ . Fig. 9.9b shows the tracer diffusivity for the case of pusher and puller suspensions as a function of τ , and once again we see a clear pusher-puller bifurcation, this time at a critical value of τ . This critical value of τ is seen to be given by $\tau_{crit} \approx 2$. The other simulation parameters for this case are $n = N/L_{box}^3 = 0.05$ and $L = 2$. This gives the critical value of $nUL^2\tau$ as:

$$nUL^2\tau|_{crit} \approx 0.4. \quad (9.39)$$

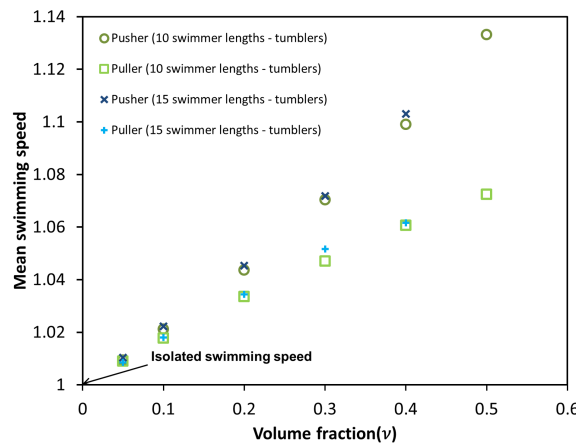
In our scaling $L = 2$ such that $N/L_{box}^3 = N(L/2)^3/L_{box}^3$, which implies $\nu = n$. Our earlier volume fraction variation simulations allows us another independent method of calculating this



(a) Probability distribution function for the swimmer velocity ($\tau = 1$). Simulation box size: 10 swimmer lengths.



(b) Probability distribution function for the swimmer velocity magnitude ($\tau = 1$). Simulation box size: 10 swimmer lengths.



(c) Mean swimming speed for the case of pushers and pullers plotted versus ν ($\tau = 1$)

Figure 9.7: Swimmer statistics for a suspension of tumblers with $\tau = 1$. (a) The probability distribution function for the swimmer velocity plotted for (i) pushers and (ii) pullers for three volume fractions. (b) The probability distribution function for the swimmer velocity magnitude plotted for (i) pushers and (ii) pullers for three volume fractions. (c) Mean swimming speed plotted with respect to ν for pushers pullers. The simulation box sizes are 10 and 15 swimmer lengths

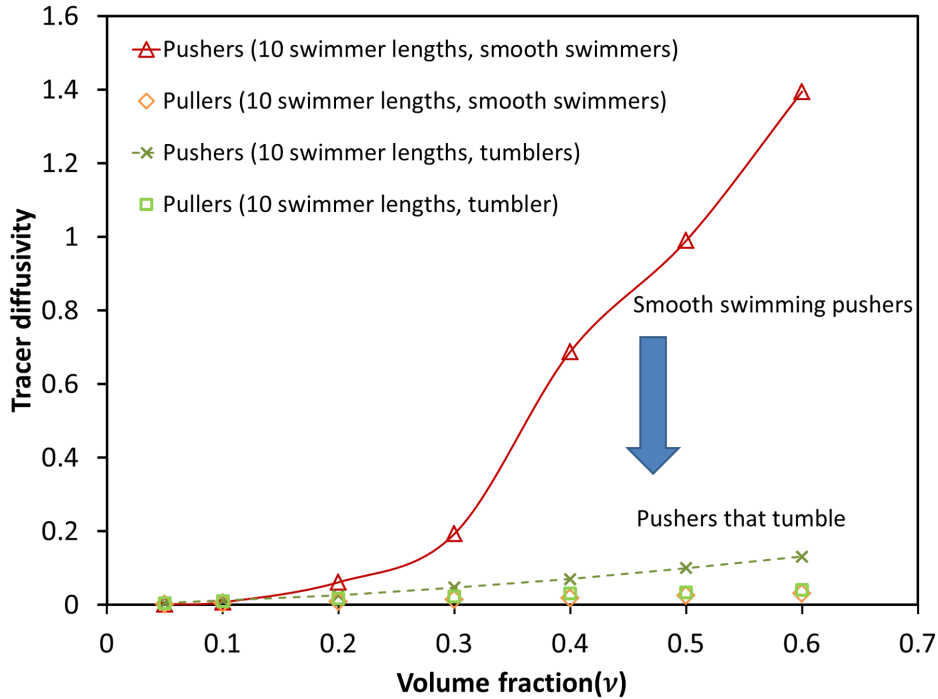


Figure 9.8: Tracer diffusivities plotted as a function of volume fraction. Plots are shown for both smooth swimmers and tumblers with mean-run-time $\tau = 1$. Simulation box size: 10 swimmer lengths.

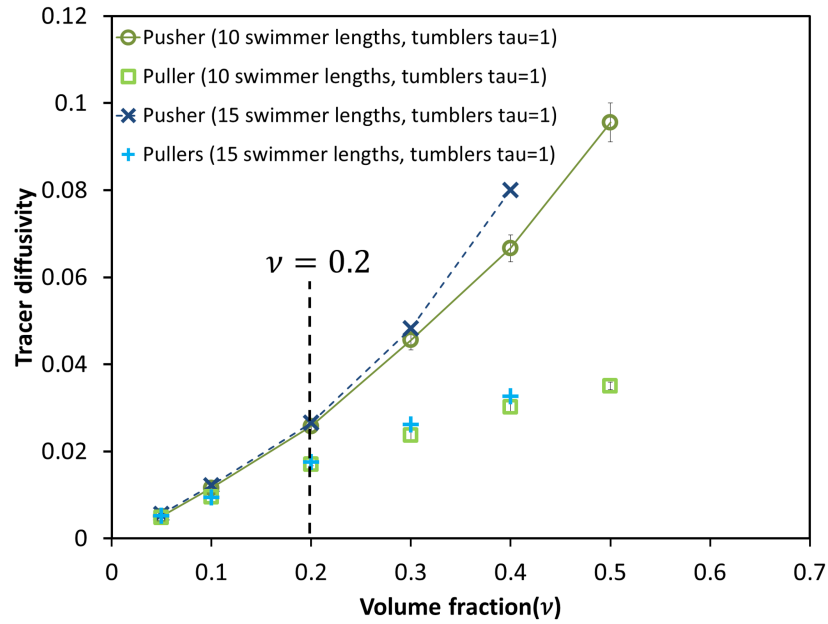
threshold. We saw in that case that $\nu_{crit} = n_{crit} = 0.1$ (see Fig. 9.9a), $L = 2$ and $\tau = 1$ giving:

$$nUL^2\tau|_{crit} \approx 0.4. \quad (9.40)$$

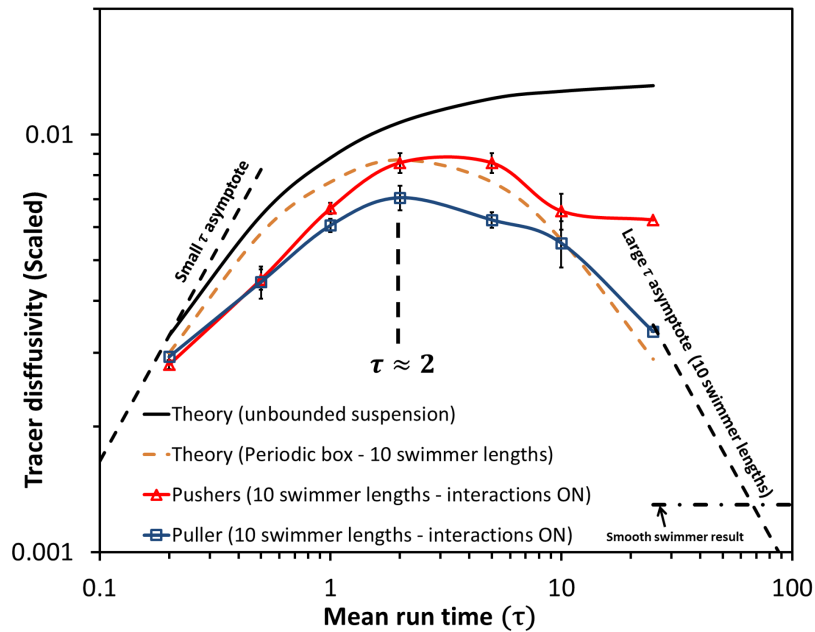
Thus, the two independent methods of calculating the dimensionless instability threshold (shown in Figs. 9.9a and 9.9b) for pushers give the same result which is in agreement with the stability theory prediction that $nUL^2\tau|_{crit}$ is a constant. This validation of the instability criterion is crucial since it allows us to study, in the next section, the tracer diffusivity at a fixed volume fraction ($\nu = 0.05$) at different values of τ . As mentioned earlier, the choice of a small volume fraction helps us compare our simulations to theory which exists for dilute suspensions (section 9.2.2). We will also focus on systematically studying the effects of the box size on the tracer diffusivities by considering simulations in different (larger) box sizes.

9.3.2 Identifying the Stability Threshold Based on Varying Tumble Rate

In this section, we present results for suspensions of pushers and pullers at a fixed volume fraction of $\nu = 0.05$ for varying τ and different box sizes. Since the tracer diffusivity is seen to be the most sensitive measure of the instability, we confine ourselves to this measure from here onward. To compare our simulations with theory developed in section 9.2.2, we first carry out simulations where the hydrodynamic interactions between swimmers are switched off. In such simulations, swimmers swim in straight lines and their orientation relaxation is due to tumbling alone. The



(a) Tracer diffusivity as a function of ν for a fixed mean-run-time $\tau = 1$ (simulation box size: 10 and 15 swimmer lengths)



(b) Tracer diffusivity as a function of τ for a fixed volume fraction $\nu = 0.05$ (simulation box size: 10 swimmer lengths)

Figure 9.9: Two independent methods of predicting the stability threshold for a suspension of tumblers. (a) Tracer diffusivity as a function of volume fraction for a fixed mean-run-time $\tau = 1$ for two different box sizes (10 and 15 swimmer lengths). (b) Tracer diffusivity as a function of τ for a fixed volume fraction and a box size of 10 swimmer lengths. Symbols represent a mean over simulations run with different initial conditions and the error bars represent the standard deviation.

tracers, however, are affected by the disturbance velocity field of the swimmers. Switching off the swimmer interactions implies that the swimmer orientation distribution is unaffected by other swimmers, immediately implying stability. Note that, excluding inter-swimmer interactions will eliminate pair-correlations between swimmers which might exist even in the stable regime. This kind of simulation therefore mimics the conditions of the theory for the tracer diffusivity calculation, where the suspension is dilute and stable, and the interactions between swimmers are neglected. We then compare these results to simulations where the interactions between swimmers are switched on, and there is therefore a possibility of an instability beyond a critical τ . This lets us isolate the effects of the instability on the tracer diffusivity.

The results for the dimensionless tracer diffusivity (scaled by the factor nUL^4 , where n is the number density of swimmers), as a function of τ , are plotted in Fig. 9.10 for *four* different sizes of the simulation box (10, 15, 25 and 40 swimmer lengths). The left column in Fig. 9.10 contains the interactions-off result while the column to the right contains results with swimmer interactions switched on. Successive rows correspond to an increasing box size. Looking first at the interactions-off results, we see that there is good agreement between simulations and the theory for a periodic suspension (left column of Fig. 9.10). Importantly, we see that for the whole range of τ and box sizes considered here, the pusher and puller diffusivities are practically identical. This is in agreement with the theory and provides evidence that, in the absence of interactions or correlations, the tracer diffusivity does not depend on whether the swimming mechanism is a pusher or puller type. A small deviation from theory can be observed at smaller values of τ (eg. $\tau < 5$), where the simulation value is lower than that predicted by theory. This is mainly attributed to the excluded volume between swimmer and tracer which is implemented in the simulations and not in the theory. The excluded volume leads to a decrease in the tracer diffusivity since the tracer particle cannot access the stronger velocity fields near a bacterium. In simulating the swimmer tracer interactions, it was found necessary to include an excluded volume around the swimmer, because, in the absence of an excluded volume, it was found there were a significant proportion of events where the tracer particles were dragged along with the swimmers for distances of order the box size. An excluded volume helps prevent such spurious events from affecting the tracer transport.

One can now contrast these interactions-off results with those on the right column of Fig. 9.10, for which the interactions between swimmers are switched on. A bifurcation between pushers and pullers beyond a critical value of $\tau \approx 2$ can be clearly seen. In general, for all the box sizes, we see that pusher curve rises above the theoretical curve for a periodic suspension, while the puller curve dips below. The behaviour of the puller curve is attributed to the hydrodynamic orientation decorrelation which occurs over and above that due to tumbling. At the smaller values of τ , the orientation decorrelation rate is dominated by the tumbling events and we see that the puller tracer diffusivities, with interactions switched off and on, lie very close to each other. At larger τ 's, the hydrodynamic decorrelation rate starts to become comparable to that due to tumbling and the combined effective decorrelation rate is perceptively larger, leading to a decrease in the diffusivity when compared to interactions-off simulations and theory (see puller curves in Fig. 9.10). It is interesting to see where the smooth swimmer results, presented earlier, figure in these plots. The smooth swimmer results for pullers at a volume fraction of $\nu = 0.05$

are shown in Figs. 9.10b and 9.10d, and they are much lower than the diffusivity of tumbling pullers at $\tau = 25$. This can be explained by calculating an effective time scale for orientation decorrelation due to hydrodynamic interactions (see Fig. 8.13 in chapter 8). We find that, for a volume fraction of 0.05, $\tau_{hydrodynamic} \approx 85$, which is much greater than the largest τ we consider ($\tau = 25$). This larger decorrelation time, as expected from our theoretical analysis, leads to a diffusivity which is small due to the finite size of the simulation box. Comparing the smooth swimmer results from Fig. 9.10b and 9.10d with the large τ asymptote in Fig. 9.3, we see that the simulation results for smooth swimmers are almost an order of magnitude smaller than that predicted by theory for an unbounded suspension. This supports our earlier observation that the smooth swimmer tracer diffusivity is very strongly affected by the finiteness of the simulation box at least in the range of box sizes used. This box size dependence would begin to go away only beyond $L_{box} \approx U\tau_{hydrodynamic}$ (a box size much larger than the largest box sizes used in our simulations).

The pusher curves in the right hand column of Fig. 9.10 rise above the puller curves, and also the periodic box theoretical prediction beyond a critical value of τ . Another important trend is that the tracer diffusivity for pushers show an increasing trend with the simulation box size. This can be seen clearly by looking at the pusher curves for larger values of τ ($\tau > 2$) in Figs. 9.10b, 9.10d, 9.10f and 9.10h. As the box size is increased the diffusivities for large τ move closer to and eventually beyond the theory for an unbounded suspension. This bifurcation between pushers and pullers at a critical value of τ , together with the sensitivity of the pusher curves to box size, leads us to conclude that what we are seeing is indeed the pusher instability. The role of differing pair-interactions in the stable regime in causing a difference between pushers and pullers, may be safely ruled out since this cannot account for the increase in the pusher diffusivity with box size at a fixed volume fraction. The pair-interactions between two swimmers are local in nature and must extend over a distance of order the swimmer length. Therefore, they cannot lead to a dependence on the size of the simulation box.

Once again, we can link the above increase in tracer diffusivity for pushers to other measures for the fluid disturbance velocity. In Fig. 9.11 we plot the power spectrum for suspensions of pushers and pullers at a given volume fraction ($\nu = 0.05$) at two different values of τ , one in the stable regime ($\tau = 0.5$) and the other in the unstable regime ($\tau = 5$). We see that spectrum in all cases is in good agreement with the periodic theory. However, there is only a small increase in the pusher spectrum compared to pullers at small \hat{k} . This seems to indicate that the structures in the flow field are not very different in the stable and unstable regimes when τ is varied. This is unlike the case of the volume fraction variation results, where the power spectrum, normalized by number of swimmers shows a clear increase in the small \hat{k} limit for pushers (see Fig. 9.5). We next look at the fluid velocity correlation functions for pushers and pullers in the stable and unstable regimes which are plotted in Fig. 9.12. Here, we see that pushers and pullers have practically identical correlation times in the stable regime ($\tau = 0.5$). In the unstable regime, however, a clear increase is seen for the pusher case. This indicates that the increase in tracer diffusivity due to τ variation is mainly due to the increase in the fluid velocity correlation time.

As expected, the difference between the pusher and puller tracer diffusivities is smaller than that seen for the results where the volume fractions are varied at a fixed τ . To quantify the

differences between pusher and puller tracer diffusivities, we compare them in the unstable regime. In the volume fraction varying simulations, at $\nu = 0.5$ (10 swimmer lengths box size, see Fig. 9.9a), which is well into the unstable regime, the tracer diffusivity for pushers is around *three* times that of the corresponding puller value, to be precise, a relative increase of around 172%. For the simulations where τ is varied, at $\tau = 5$ (10 swimmer lengths, see Fig. 9.10b) which is in the unstable regime but not significantly affected by periodicity, the tracer diffusivity for pushers is around 1.3 times that for pullers, to be precise, a relative increase of around 36%. It is important to keep in mind that, in contrast, the relative difference between pusher and puller tracer diffusivities in the stable regime is around 6% (volume fraction variation at $\nu = 0.05$ and $\tau = 1$, see Fig. 9.9a). Therefore, the increase in the tracer diffusivity for pushers relative to pullers for the τ variation case, though smaller than that due to volume fraction increases, is still well beyond the typical variance in the stable regime.

9.3.3 Estimating the Instability Threshold for Tumblers

The above results allow us to calculate the instability threshold based on a critical value of τ . From Figs. 9.10b, 9.10d, 9.10f and 9.10h, we see that the critical value of τ at which the bifurcation between pushers and pullers occurs is given by $\tau_{crit} \approx 2$. We see that this critical value is a weak function of the box size for the $L_{box} > 25L$ and moves to smaller values of τ for larger box sizes as shown in Fig. 9.2. The instability theory by Subramanian & Koch (2009) tells us that the critical parameter for a suspension of tumblers is given by $nUL^2\tau$. The value for our case with $\tau_{crit} \approx 2$, $n = N/L_{box}^3 = 0.05$ and $L = 2$ is:

$$nUL^2\tau|_{crit} \approx 0.4. \quad (9.41)$$

The predicted value of this constant by Subramanian & Koch (2009) is $nUL^2\tau|_{crit} = 5/C$, where $C = M^{-1}\alpha_1/2$ which for our case gives $C \approx 1.42$. Thus the theoretical prediction gives:

$$nUL^2\tau|_{crit,theory} \approx 3.5. \quad (9.42)$$

The critical value of the threshold predicted by simulations is therefore much smaller than that of linear stability theory. The reason for this seemingly sub-critical nature of the instability is currently being investigated.

9.4 Results and Discussion: Rotary Diffusers

Our approach to studying the effects of rotary diffusion closely parallels that used for tumbling above. We again use the tracer diffusivity as the primary measure to estimate the instability threshold. First, we consider simulations of pushers and pullers where the rotary diffusivity of the swimmers is kept constant (here, $D_r = 0.5$), while the volume fraction of the suspension is varied. This value of the rotary diffusivity is chosen since it is close to what is typically observed in bacteria. Note that the rotary diffusion of bacteria has an athermal origin, and occurs due to imperfections in their swimming mechanism (the value for *E. Coli* is around $D_r = 0.12$, where D_r is scaled by $L/(2U)$ (Berg (1993))). Plotting the tracer diffusivity for pushers and pullers

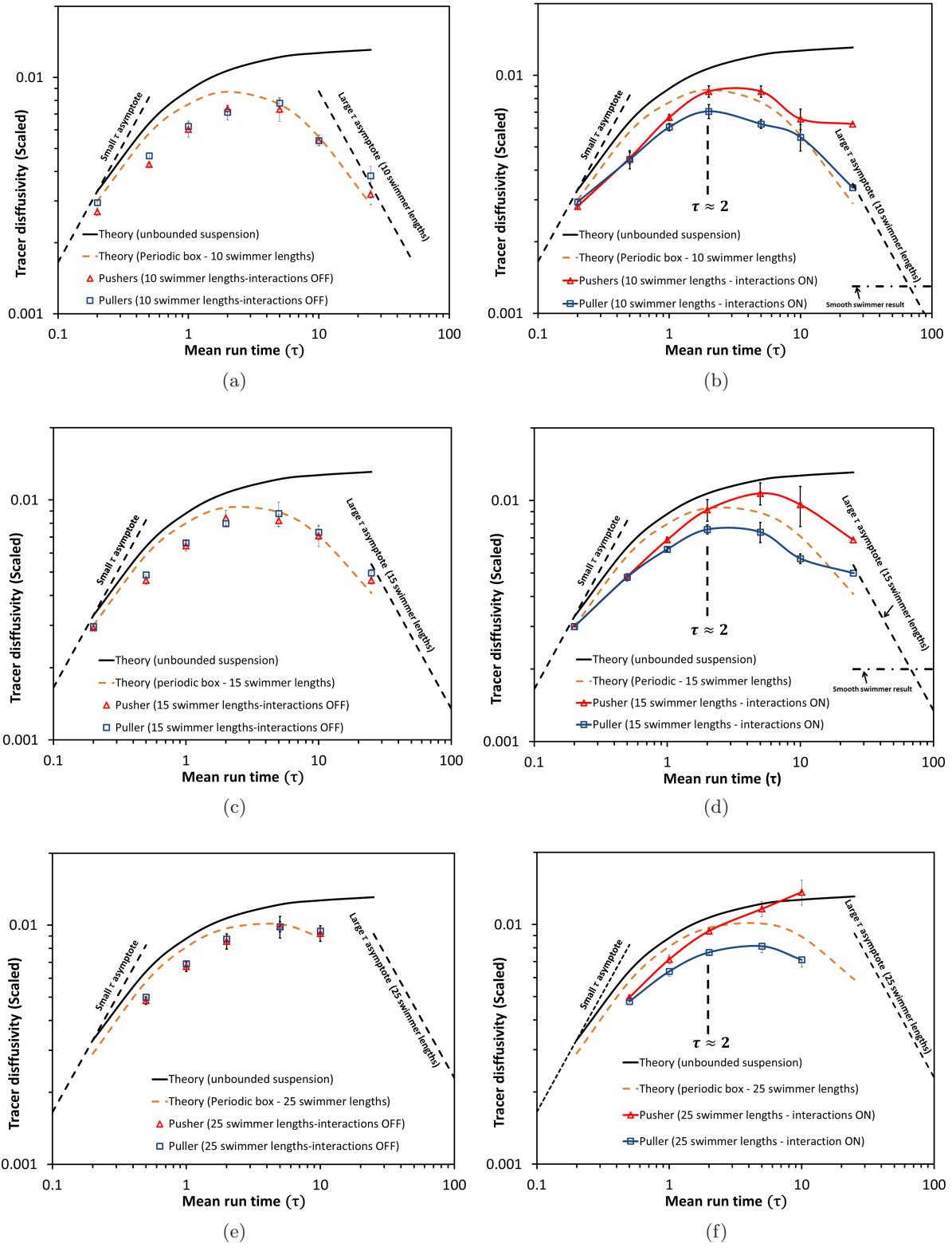


Figure 9.10

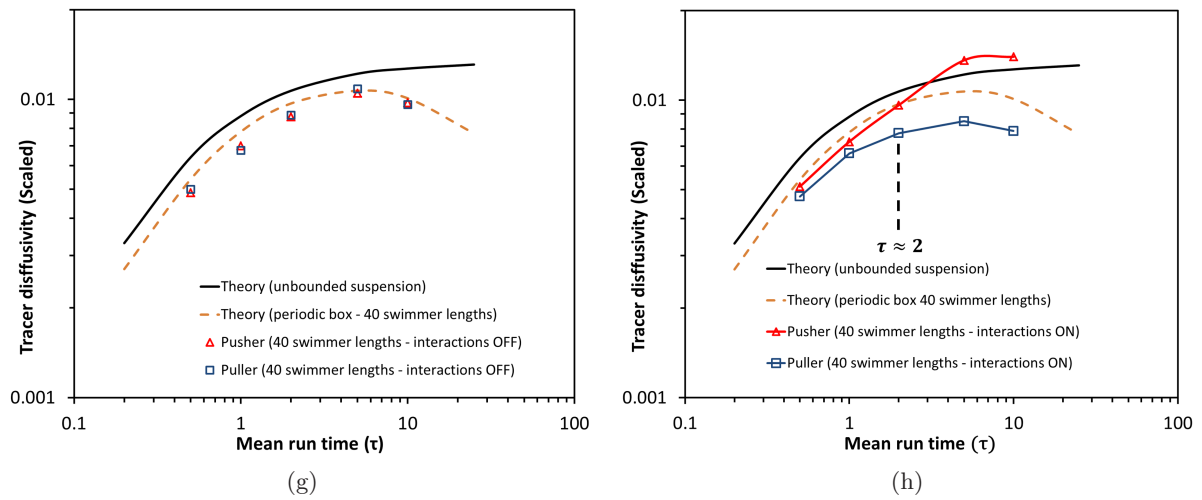


Figure 9.10: Non-dimensional tracer diffusivity for a suspension of tumblers, at a volume fraction of $\nu = 0.05$, for different values of τ . (a), (c), (e) and (g) show the results of interactions-off simulations for box sizes of 10, 15, 25 and 40 swimmer lengths, respectively. (b), (d), (f) and (h) show the results of interactions-on simulations for box sizes of 10, 15, 25 and 40 swimmer lengths, respectively. Symbols represent a mean over simulations run with different initial conditions and the error bars represent the standard deviation.

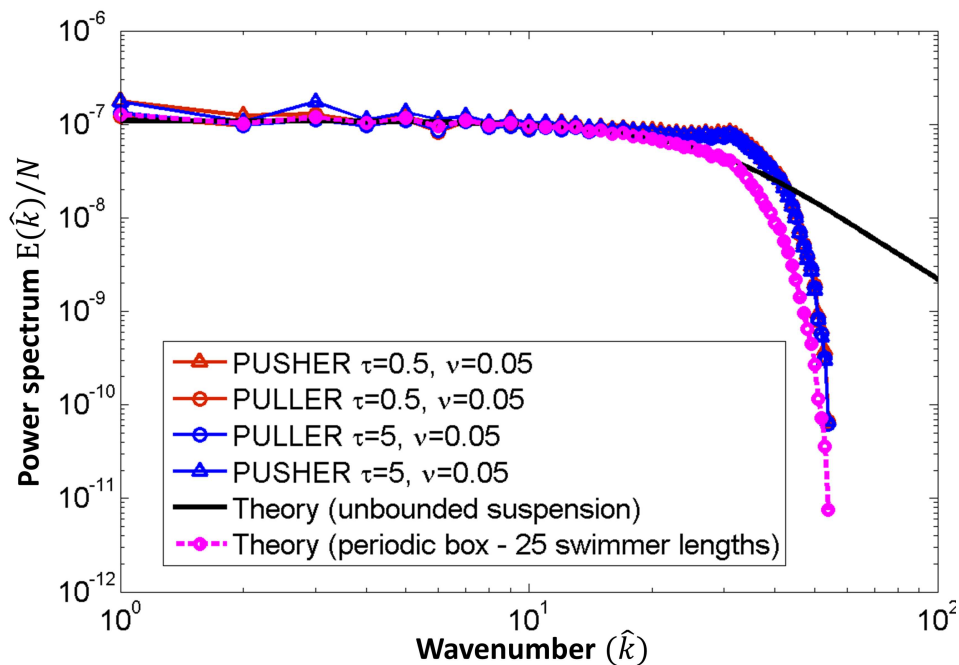


Figure 9.11: Fluid velocity power spectrum, normalized by number of swimmers, for a suspension of tumblers with fixed volume fraction of $\nu = 0.05$ and two different values of τ ($\tau = 0.5$ and $\tau = 5$). Simulation box size: 25 swimmer lengths.

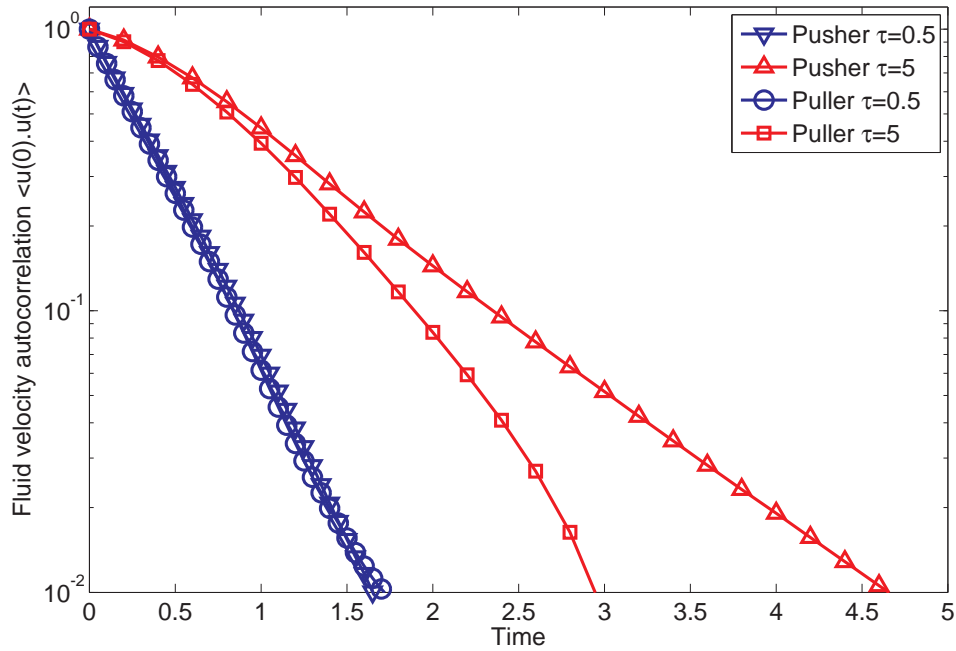


Figure 9.12: Fluid velocity correlation function for a suspension of tumblers with fixed volume fraction of $\nu = 0.05$ and two different values of τ ($\tau = 0.5$ and $\tau = 5$). Simulation box size: 25 swimmer lengths.

as a function of volume fraction in Fig. 9.13, one sees a clear bifurcation at $\nu \approx 0.3$, beyond which pushers show larger values than pullers. Thus, just as in the tumbling case, a suspension of pushers that rotary diffuse becomes unstable beyond a critical volume fraction.

Next, we consider simulations where the volume fraction is constant ($\nu = 0.05$) and the rotary diffusivity of the swimmers is varied. Here, we contrast the tracer diffusivity in suspensions of pushers and pullers in two sets of simulations, the first with interactions between swimmers switched off and the second set with interactions switched on. The results for both these sets are presented in Fig. 9.14 for three different box sizes (10, 15 and 30 swimmer lengths), with each row corresponding to a given box size and the left and right columns corresponding to interactions being switched off and on, respectively. Focussing first on the interactions-off results (left column in Fig. 9.14), we see a trend very similar to that seen in the case of tumblers. As the value of D_r decreases, the swimmer orientation remains correlated for longer times, thereby leading to an increase in the tracer diffusivity. However, as we approach the smooth swimming limit ($1/D_r \rightarrow \infty$), the effects of the periodic box begin to show themselves and the tracer diffusivity shows a decrease. Also, as for the tumbler case, we find that in the absence of interactions, the pusher and puller tracer diffusivities are practically equal, over most of the D_r range considered here, revealing the independence of tracer transport on the swimming mechanism employed. However, at large values of D_r (small values of $1/D_r$), there seems to be differences between the pusher and puller tracer diffusivities. Though the reasons for this are not entirely clear, a possible cause is the excluded volume around a swimmer leading to short-range steric interactions which modify the tracer transport differently for pushers and pullers.

When interactions are switched on, a clear bifurcation can be seen between pushers and pullers (right column in Fig. 9.14). Beyond a critical value of $1/D_r$, pushers show higher values

of tracer diffusivity when compared to pullers. Significantly, the pusher tracer diffusivity, at a fixed volume fraction, shows a clear increase with increasing box size, once again pointing to the hydrodynamic instability as a possible cause (and ruling out differences in correlations in the stable regime). We can extract the critical value of $1/D_r$ from Figs. 9.14b, 9.14d and 9.14f to be $1/D_r|_{crit} \approx 10$. The linear stability theory tells us that the threshold for rotary diffusers is in the form of a critical value of nUL^2/D_r . Calculating this quantity based on our simulation results with $n = 0.05$ gives:

$$\left. \frac{nUL^2}{D_r} \right|_{crit} \approx 2. \quad (9.43)$$

Using our earlier results of the volume fraction varying simulations (Fig. 9.13), where $\nu_{crit} \approx 0.3$ and $D_r = 0.5$, we find that:

$$\left. \frac{nUL^2}{D_r} \right|_{crit} \approx 2.4. \quad (9.44)$$

The values of nUL^2/D_r , for the two methods are therefore reasonably close to one another which is in agreement with the prediction of the linear stability analysis that the threshold corresponds to a fixed value of $nUL^2/D_r|_{crit}$. However, the critical value, according to the theory, is given by (Subramanian & Koch (2009)):

$$\left. \frac{nUL^2}{D_r} \right|_{crit,theory} = \frac{30}{C} \approx 21. \quad (9.45)$$

However, as in the tumbling case, we see that the predicted value of the threshold from simulations is well below that given by the theory (by almost the same factor). Once again this points to a possible sub-critical nature of the swimmer instability and is being currently investigated by us.

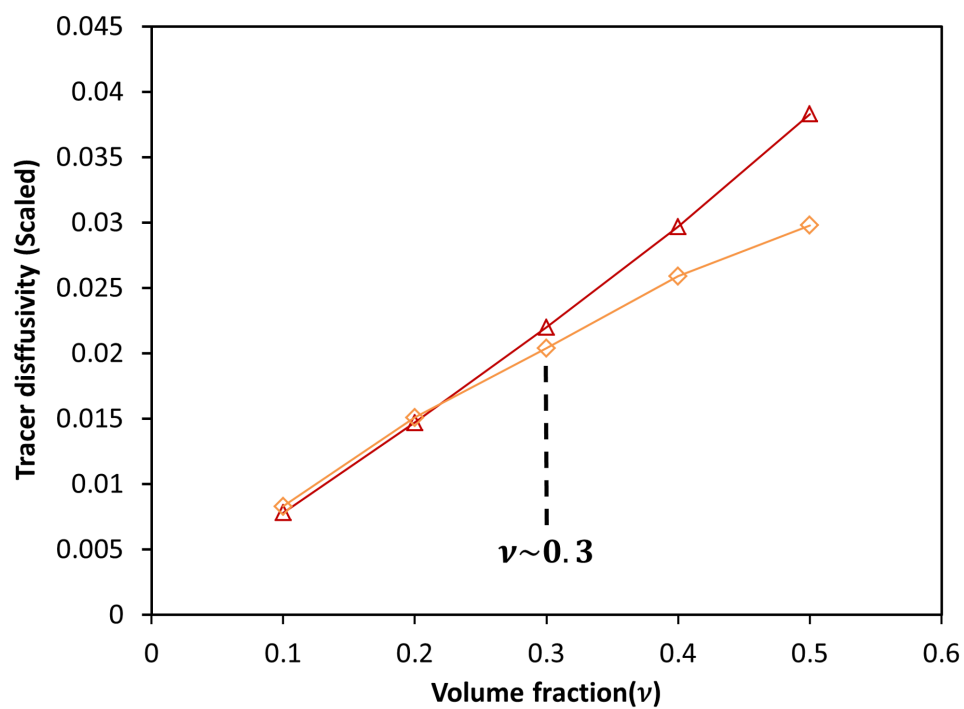


Figure 9.13: Tracer diffusivity as a function of volume fraction for a suspension of rotary diffusers with $D_r = 0.5$ (simulation box size: 10 swimmer lengths)

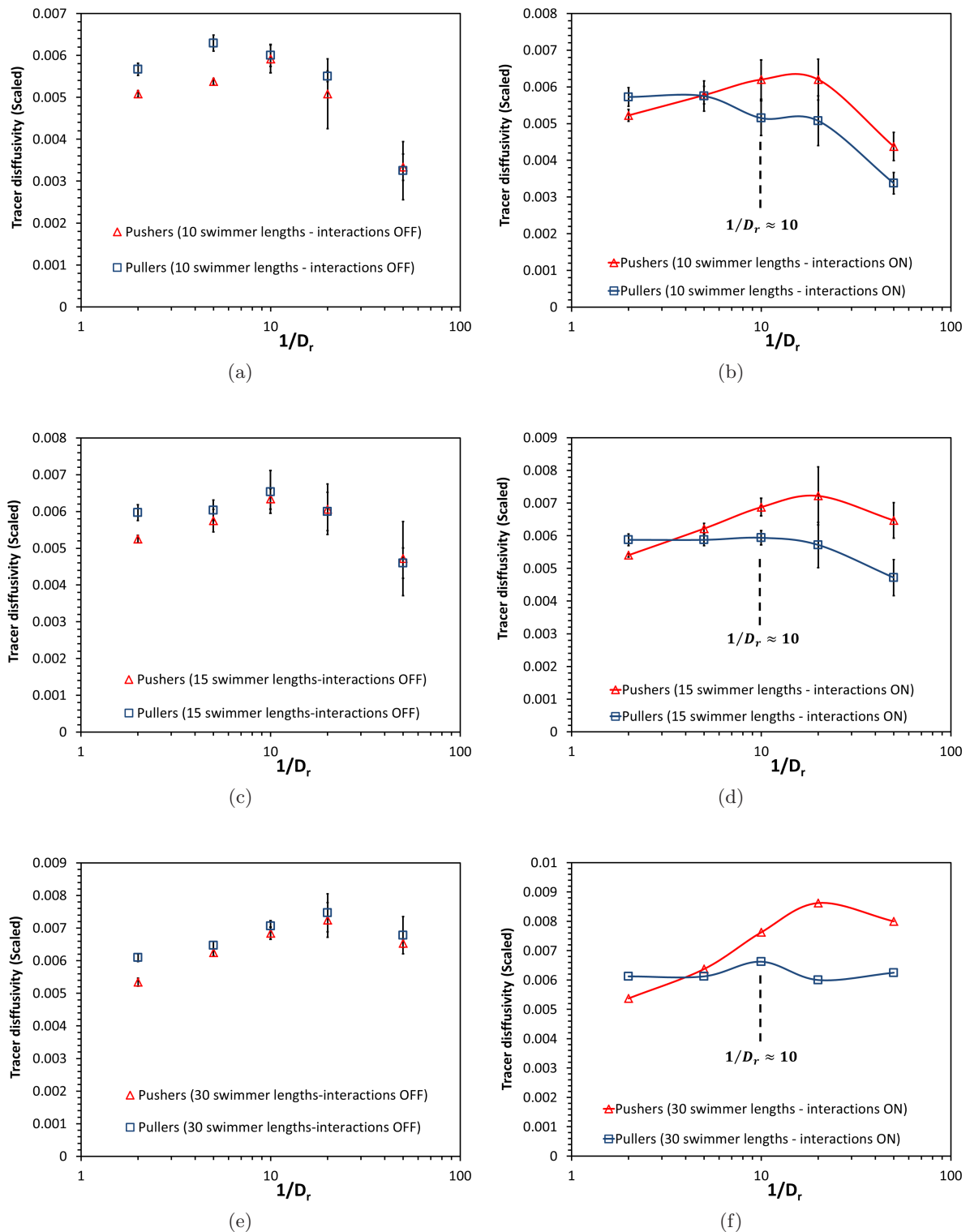


Figure 9.14: Non-dimensional tracer diffusivity for a suspension of rotary diffusers at a volume fraction of $\nu = 0.05$ for different values of $1/D_r$. (a), (c) and (e) show the results for interactions-off simulations for box sizes of 10, 15 and 30 swimmer lengths respectively. (b), (d) and (f) show the results for interactions-on simulations for box sizes of 10, 15 and 30 swimmer lengths respectively. Symbols represent a mean over simulations run with different initial conditions and the error bars represent the standard deviation.

Chapter 10

Conclusions and Future Work

In this part of the thesis, we have studied collective behaviour in a suspension of swimmers, with intrinsic orientation relaxation mechanisms via numerical simulations. We give here an overview of the salient results from this work.

To study collective behaviour, we have developed a particle-based simulation methodology, to study hydrodynamically interacting rod-like swimmers in a three-dimensional spatially periodic domain. We make the important simplifying assumption that the intrinsic stresses on the swimmers, which arise due to swimming, are sufficient to capture the features of the collective behaviour. This makes our simulations kinematic in nature, leading to substantial savings in computational effort. We use an Ewald summation method to calculate hydrodynamic interactions in a periodic domain along with viscous slender body theory to update the swimmer positions and orientations at each time step. In chapter 8, we validated our model by first using it to study smooth swimmers which lack intrinsic decorrelation mechanisms. Our model clearly shows a transition to collective behaviour for pushers beyond a critical volume fraction, while pullers do not show any such behaviour. Specifically, a suspension of pushers displays large velocity fluctuations and clear evidence of bulk, correlated motion in the form of vortices and jets. The length scale of these fluid structures is of the order of the simulation box size. For pullers, we see no such correlated motion, with fluid velocity fluctuations, of a much smaller scale, caused mainly due to individual weakly correlated swimmers. In the unstable regime, pushers are also seen to swim much faster than in isolation, with groups of pushers swimming in locally aligned groups which are slightly denser than the ambient suspension. Pullers swim no faster than in isolation and also tend to prefer local anti-parallel alignment. Passive non-Brownian tracer particles in a suspension of pushers show much larger diffusivities (an order of magnitude higher) than those in a puller suspension. This tracer diffusivity is seen to be the most sensitive measure of the instability threshold and we use it to extract the critical value of the concentration from our simulations. This critical concentration, for smooth swimmers, scales inversely with the simulation box size and our predictions are in good agreement with theory. Surprisingly, the translational diffusivity of the swimmers themselves did not show any sign of the transition to collective behaviour. All our observations for smooth swimmers are consistent with earlier theoretical predictions and simulation results.

With our model thus validated, we explored swimmers with intrinsic orientation relaxation mechanisms in chapter 9. We find that a suspension of pushers which tumble or rotary diffuse continues to remain unstable beyond a critical concentration. This points to the fact that the concentration, as well as the time scale for orientation decorrelation, determine the onset of collective behaviour. To test this rigorously we perform extensive simulations with the volume fraction held constant and varying mean-run-time (τ) or rotary diffusivity (D_r). For the case of varying τ , we derive an analytical expression for the tracer diffusivity in a periodic swimmer

suspension in the dilute limit. Our theory reveals that there is a non-trivial effect of the periodicity with the tracer diffusivity having a non-monotonic variation with τ and going to zero in the limit of very large τ , which corresponds to the smooth swimmer limit. In contrast, the tracer diffusivity in an unbounded suspension is predicted to increase monotonically with τ . To compare with the periodic suspension theory, we perform simulations with the hydrodynamic interactions between swimmers switched off, but with tracer particles still interacting with the swimmers. We see excellent agreement between our simulation results and theory, with the simulations predicting the expected non-monotonic trend with τ . When we switch-on interactions between swimmers, we see a clear bifurcation at a critical value of τ beyond which the tracer diffusivity is larger for pushers in relation to pullers. Further, we see that the difference between pushers and pullers grows systematically with the size of the simulation box, while the critical τ is only a weak function of box size. This clearly points to an instability in the pusher suspension. The above simulations allow two independent ways of estimating the critical value of the quantity $nUL^2\tau$. Indeed, we find that both methods lead to about the same critical value of $nUL^2\tau$ with a very weak dependence on box size for large enough boxes. We independently study suspensions of rotary diffusers, and just as in the tumbling case, find a critical value for nUL^2/D_r . This is in agreement with the theory that the critical value of $nUL^2\tau$ (nUL^2/D_r) for tumblers (rotary diffusers) is a constant which only depends on the intrinsic parameters of the swimmers. In a final twist, we note that simulation predictions for these thresholds are much smaller than the corresponding predictions by theory, with both tumblers and rotary diffusers smaller by almost the same factor of approximately 9. This points to a possible sub-critical nature of the instability for pushers.

We list here some of the avenues for future work that have been opened up by this thesis

1. It would be interesting to study the rheology of active suspensions under finite shear with inclusion of orientation relaxation mechanisms using the particle-based simulation methodology outlined here. There are several unanswered questions related to the viscosity behaviour as a function of the volume fraction in both the low ([Gachelin *et al.* \(2013\)](#)) and high ([Karmakar *et al.* \(2014\)](#)) shear rate regimes. This, along with the effects of the mean-run-time, leads to a rich parameter space which can be systematically investigated via simulations. It would be straightforward to extend our current particle-based simulation model to include finite shear via methods already implemented in the context of homogeneous sheared turbulence ([Rogallo \(1981\)](#)).
2. The sub-critical nature of the pusher instability which was discovered in this work needs to be investigated further. In particular, it would be interesting to see if the system exhibits hysteresis when a certain parameter is slowly varied about its critical value. This would also shed light on the role of the initial conditions, and on what is the statistically stable state that the system chooses at long times.

Appendices

Appendix A

$O(Re)$ Velocity and Pressure Field Constants for a Drop

The $O(Re)$ exterior velocity and pressure fields for a spherical drop in a linear flow was derived by [Raja *et al.* \(2010\)](#) and are reproduced below:

$$\begin{aligned}
 \mathbf{u}^{(1)} = & \frac{1}{(\lambda+1)} \left[\left(-\frac{c_1}{4r^{11}} + \frac{c_2}{2r^{10}} - \frac{7c_3}{4r^9} + \frac{c_4}{3r^8} - \frac{c_5}{12r^5} \right) (\mathbf{\Gamma} : \mathbf{r}\mathbf{r})^2 \mathbf{r} + \left(\frac{c_1}{18r^9} - \frac{3c_2}{32r^8} \right. \right. \\
 & + \frac{c_6}{r^7} - \frac{c_4}{36r^6} - \frac{c_7}{2r^5} + \frac{c_5}{18r^3} \left. \right) (\mathbf{\Gamma} : \mathbf{r}\mathbf{r}) (\mathbf{\Gamma} \cdot \mathbf{r}) + \left(\frac{c_1}{18r^9} - \frac{3c_2}{32r^8} + \frac{c_8}{r^7} - \frac{c_4}{36r^6} + \frac{c_7}{2r^5} \right. \\
 & - \frac{c_5}{9r^3} \left. \right) (\mathbf{\Gamma} : \mathbf{r}\mathbf{r}) (\mathbf{\Gamma}^\dagger \cdot \mathbf{r}) + \left(\frac{c_1}{36r^9} - \frac{3c_2}{32r^8} + \frac{c_9}{r^7} - \frac{5c_4}{36r^6} - \frac{c_{10}}{r^5} + \frac{c_5}{36r^3} \right) (\mathbf{\Gamma} \cdot \mathbf{r}) \cdot (\mathbf{\Gamma} \cdot \mathbf{r}) \mathbf{r} \\
 & + \left(\frac{c_1}{18r^9} - \frac{3c_2}{16r^8} + \frac{c_9 + c_{11}}{r^7} - \frac{5c_4}{18r^6} + \frac{c_5}{18r^3} \right) (\mathbf{\Gamma} \cdot \mathbf{r}) \cdot (\mathbf{\Gamma}^\dagger \cdot \mathbf{r}) \mathbf{r} + \left(\frac{c_1}{36r^9} - \frac{3c_2}{32r^8} \right. \\
 & + \frac{c_{11}}{r^7} - \frac{5c_4}{36r^6} + \frac{c_{10}}{r^5} + \frac{c_5}{36r^3} \left. \right) (\mathbf{\Gamma}^\dagger \cdot \mathbf{r}) \cdot (\mathbf{\Gamma}^\dagger \cdot \mathbf{r}) \mathbf{r} + \left(-\frac{c_1}{126r^7} + \frac{c_2}{32r^6} - \frac{c_{17}}{r^5} + \frac{c_4}{36r^4} \right. \\
 & - \frac{\lambda+1}{30r^3} + \frac{c_5}{9r} \left. \right) \mathbf{\Gamma} \cdot (\mathbf{\Gamma} \cdot \mathbf{r}) + \left(\frac{c_1}{126r^7} + \frac{c_2}{32r^6} - \frac{c_{18}}{r^5} + \frac{c_4}{36r^4} + \frac{\lambda+1}{30r^3} - \frac{c_5}{18r} \right) \mathbf{\Gamma}^\dagger \cdot (\mathbf{\Gamma}^\dagger \cdot \mathbf{r}) \\
 & + \left(\frac{c_1}{126r^7} + \frac{c_2}{32r^6} - \frac{c_{12}}{r^5} + \frac{c_4}{36r^4} - \frac{c_7}{6r^3} + \frac{c_5}{9r} \right) \mathbf{\Gamma}^\dagger \cdot (\mathbf{\Gamma} \cdot \mathbf{r}) + \left(\frac{c_1}{126r^7} + \frac{c_2}{32r^6} - \frac{c_{13}}{r^5} \right. \\
 & + \frac{c_4}{36r^4} + \frac{c_7}{6r^3} - \frac{c_5}{18r} \left. \right) \mathbf{\Gamma} \cdot (\mathbf{\Gamma}^\dagger \cdot \mathbf{r}) + \left(\frac{c_1}{252r^7} + \frac{c_2}{48r^6} - \frac{c_{12} + c_{13}}{2r^5} + \frac{c_4}{18r^4} - \frac{c_5}{36r} \right) \\
 & \left. (\mathbf{\Gamma} : \mathbf{\Gamma}^\dagger + \mathbf{\Gamma} : \mathbf{\Gamma}) \mathbf{r} \right], \tag{A.1}
 \end{aligned}$$

$$\begin{aligned}
 p^{(1)} = & -\frac{1}{2} (\mathbf{\Gamma} \cdot \mathbf{r}) \cdot (\mathbf{\Gamma}^\dagger \cdot \mathbf{r}) + \frac{1}{(\lambda+1)} \left[\left(-\frac{5c_{14}}{2r^{12}} + \frac{c_2}{r^{10}} - \frac{7c_3}{4r^9} + \frac{3c_4}{4r^8} - \frac{5c_7}{r^7} + \frac{c_5}{2r^5} \right) (\mathbf{\Gamma} : \mathbf{r}\mathbf{r})^2 \right. \\
 & + \left(-\frac{c_{14}}{2r^{10}} + \frac{c_3}{2r^7} - \frac{c_4}{4r^6} - \frac{c_{15}}{r^5} - \frac{c_5}{6r^3} \right) (\mathbf{\Gamma} \cdot \mathbf{r}) \cdot (\mathbf{\Gamma} \cdot \mathbf{r}) + \left(-\frac{c_{14}}{r^{10}} + \frac{c_3}{r^7} - \frac{c_4}{2r^6} + \frac{c_7}{r^5} \right) (\mathbf{\Gamma} \cdot \mathbf{r}) \cdot \\
 & (\mathbf{\Gamma}^\dagger \cdot \mathbf{r}) + \left(-\frac{c_{14}}{2r^{10}} + \frac{c_3}{2r^7} - \frac{c_4}{4r^6} + \frac{2c_{10}}{r^5} + \frac{c_5}{6r^3} \right) (\mathbf{\Gamma}^\dagger \cdot \mathbf{r}) \cdot (\mathbf{\Gamma}^\dagger \cdot \mathbf{r}) + \left(-\frac{c_3}{10r^5} + \frac{c_4}{12r^4} \right. \\
 & \left. - \frac{c_5}{6r} \right) (\mathbf{\Gamma} : \mathbf{\Gamma}^\dagger + \mathbf{\Gamma} : \mathbf{\Gamma}) \left. \right]. \tag{A.2}
 \end{aligned}$$

where $\mathbf{\Gamma}^\dagger$ denotes the transpose of $\mathbf{\Gamma}$ and the constants c_1 to c_{18} are given below:

$$\begin{aligned}
c_1 &= \frac{5005\lambda^3 + 7722\lambda^2 + 2288\lambda + 112}{1144(\lambda + 1)^2}, \\
c_2 &= \frac{5\lambda^2 + 2\lambda}{\lambda + 1}, \\
c_3 &= \frac{19305\lambda^3 + 29172\lambda^2 + 11440\lambda + 1032}{10296(\lambda + 1)^2}, \\
c_4 &= \frac{(5\lambda + 2)^2}{4(\lambda + 1)}, \\
c_5 &= \frac{5\lambda + 2}{2}, \\
c_6 &= \frac{42042\lambda^4 + 177177\lambda^3 + 204204\lambda^2 + 76996\lambda + 6304}{41184(2\lambda + 5)(\lambda + 1)^2}, \\
c_7 &= \frac{\lambda}{2}, \\
c_8 &= \frac{35178\lambda^4 + 132561\lambda^3 + 133276\lambda^2 + 41532\lambda + 4016}{41184(2\lambda + 5)(\lambda + 1)^2}, \\
c_9 &= \frac{426426\lambda^4 + 1728441\lambda^3 + 1942512\lambda^2 + 735778\lambda + 90412}{144144(2\lambda + 5)(\lambda + 1)^2}, \\
c_{10} &= \frac{3\lambda^2 + 3\lambda + 1}{9(\lambda + 1)}, \\
c_{11} &= \frac{234234\lambda^4 + 959673\lambda^3 + 1077648\lambda^2 + 383426\lambda + 26348}{144144(2\lambda + 5)(\lambda + 1)^2}, \\
c_{12} &= \frac{282282\lambda^4 + 1134705\lambda^3 + 1268124\lambda^2 + 480828\lambda + 63504}{288288(2\lambda + 5)(\lambda + 1)^2}, \\
c_{13} &= \frac{138138\lambda^4 + 582153\lambda^3 + 675532\lambda^2 + 248596\lambda + 15456}{288288(2\lambda + 5)(\lambda + 1)^2}, \\
c_{14} &= \frac{\lambda^2}{4(\lambda + 1)}, \\
c_{15} &= \frac{3\lambda^2 + 3\lambda + 4}{18(\lambda + 1)}, \\
c_{17} &= \frac{1075074\lambda^4 + 4448301\lambda^3 + 5107388\lambda^2 + 1947684\lambda + 205408}{1441440(2\lambda + 5)(\lambda + 1)^2}, \\
c_{18} &= \frac{1027026\lambda^4 + 4135989\lambda^3 + 4610892\lambda^2 + 1699436\lambda + 189392}{1441440(2\lambda + 5)(\lambda + 1)^2}.
\end{aligned}$$

Appendix B

$O(Re)$ Neutral Curve (wake) Location on Drop Surface

The neutral curve $C_{neutral}$ which satisfies $u_{drift}(C) = 0$ (see Eq. 2.66 in chapter 2) is found to be given by:

$$\begin{aligned} C^* = & \left(2\sqrt{7}\sqrt{(-1852717440\alpha - 1852717440\alpha^2 + 1852717440\alpha^3 + 1852717440\alpha^4} \right. \\ & + 926358720\lambda - 13263273856\alpha\lambda - 15115991296\alpha^2\lambda + 13263273856\alpha^3\lambda + 14189632576\alpha^4\lambda \\ & + 6631636928\lambda^2 - 37342174952\alpha\lambda^2 - 50605448808\alpha^2\lambda^2 + 37342174952\alpha^3\lambda^2 + 43973811880\alpha^4\lambda^2 \\ & + 18671087476\lambda^3 - 53953567920\alpha\lambda^3 - 91295742872\alpha^2\lambda^3 + 53953567920\alpha^3\lambda^3 + 72624655396\alpha^4\lambda^3 \\ & + 26976783960\lambda^4 - 43110819466\alpha\lambda^4 - 97064387386\alpha^2\lambda^4 + 43110819466\alpha^3\lambda^4 + 70087603426\alpha^4\lambda^4 \\ & + 21555409733\lambda^5 - 18855575882\alpha\lambda^5 - 61966395348\alpha^2\lambda^5 + 18855575882\alpha^3\lambda^5 + 40410985615\alpha^4\lambda^5 \\ & + 9427787941\lambda^6 - 4097979600\alpha\lambda^6 - 22953555482\alpha^2\lambda^6 + 4097979600\alpha^3\lambda^6 + 13525767541\alpha^4\lambda^6 \\ & + 2048989800\lambda^7 - 331273800\alpha\lambda^7 - 4429253400\alpha^2\lambda^7 + 331273800\alpha^3\lambda^7 + 2380263600\alpha^4\lambda^7 \\ & \left. + 165636900\lambda^8 - 331273800\alpha^2\lambda^8 + 165636900\alpha^4\lambda^8) \right) / (\sqrt{(7274042944 + 24938726400\alpha} \\ & + 35329366912\alpha^2 + 24938726400\alpha^3 + 7274042944\alpha^4 + 12278826336\lambda + 195191646720\alpha\lambda \\ & + 365825640768\alpha^2\lambda + 195191646720\alpha^3\lambda + 12278826336\alpha^4\lambda - 86362141836\lambda^2 + 573975978304\alpha\lambda^2 \\ & + 1320676240280\alpha^2\lambda^2 + 573975978304\alpha^3\lambda^2 - 86362141836\alpha^4\lambda^2 - 363709811676\lambda^3 \\ & + 800320554176\alpha\lambda^3 + 2328060731704\alpha^2\lambda^3 + 800320554176\alpha^3\lambda^3 - 363709811676\alpha^4\lambda^3 \\ & - 588400542515\lambda^4 + 560598088336\alpha\lambda^4 + 2297997261702\alpha^2\lambda^4 + 560598088336\alpha^3\lambda^4 \\ & - 488697797302\lambda^5 + 187810159680\alpha\lambda^5 + 1353015913964\alpha^2\lambda^5 + 187810159680\alpha^3\lambda^5 \\ & - 488697797302\alpha^4\lambda^5 - 588400542515\alpha^4\lambda^4 - 215692744839\lambda^6 + 23851713600\alpha\lambda^6 \\ & + 479088916878\alpha^2\lambda^6 + 23851713600\alpha^3\lambda^6 - 215692744839\alpha^4\lambda^6 - 46799172420\lambda^7 \\ & \left. + 93598344840\alpha^2\lambda^7 - 46799172420\alpha^4\lambda^7 - 3736032300\lambda^8 + 7472064600\alpha^2\lambda^8 - 3736032300\alpha^4\lambda^8) \right) \end{aligned} \quad (B.1)$$

Appendix C

Ewald summation method

In this appendix we re-derive the Ewald summation technique (Hasimoto (1959)) used to split the slowly converging sums in Eqs. 7.27 and 7.27 in chapter 7 to two quickly converging ones in real space and Fourier space. We note that in our case the unit cell consists of N randomly positioned and oriented rods while in Hasimoto's analysis Hasimoto (1959), the unit cell has a single point force. Our starting point is Eqs. 7.26-7.28 in chapter 7. These involve sums of the form:

$$\sigma_m = \sum_{\mathbf{k} \neq 0} \frac{e^{-2\pi i \mathbf{k} \cdot \mathbf{x}}}{k^{2m}} \hat{\mathbf{F}}(\mathbf{k}). \quad (\text{C.1})$$

Starting from an integral representation for $1/k^{2m}$:

$$\frac{1}{k^{2m}} = \frac{\pi^m}{\Gamma(m)} \int_0^\infty e^{-\pi k^2 \beta} \beta^{m-1} d\beta. \quad (\text{C.2})$$

Multiplying the above equation by $e^{-2\pi i \mathbf{k} \cdot \mathbf{x}}$ and summing with respect to \mathbf{k} for $\mathbf{k} = 0$, we get:

$$\sigma_m = \frac{\pi^m}{\Gamma(m)} \sum_{\mathbf{k} \neq 0} \hat{\mathbf{F}}(\mathbf{k}) \int_0^\infty e^{-\pi k^2 \beta - 2\pi i \mathbf{k} \cdot \mathbf{x}} \beta^{m-1} d\beta, \quad (\text{C.3})$$

$$= \frac{\pi^m}{\Gamma(m)} \int_0^\infty \beta^{m-1} \left[\sum_{\mathbf{k}} e^{-\pi k^2 \beta - 2\pi i \mathbf{k} \cdot \mathbf{x}} \hat{\mathbf{F}}(\mathbf{k}) - \hat{\mathbf{F}}(0) \right] d\beta. \quad (\text{C.4})$$

We note that in our case, the swimmers being force-free, $\hat{\mathbf{F}}(0) = 0$. We now split the integral into two parts, the first from 0 to α and the second from α to ∞ , and apply Ewald's theta transformation formula to the first part. This transformation for our case (Sierou & Brady (2001), Nijboer & De Wette (1957)) has the form:

$$\sum_{\mathbf{k}} \hat{\mathbf{F}}(\mathbf{k}) e^{-\pi k^2 \beta - 2\pi i \mathbf{k} \cdot \mathbf{x}} = \frac{V}{\beta^{3/2}} \sum_{\mathbf{l}} \sum_{i=1}^N \sum_{j=1}^M e^{-\frac{\pi(\mathbf{x} - \mathbf{x}_i - \hat{\mathbf{p}}_i s_j - \mathbf{l})^2}{\beta}} f(s_j) \hat{\mathbf{p}}_i. \quad (\text{C.5})$$

Using the result C.5 in the first integral in C.4, we get:

$$\sigma_m = \frac{\pi^m \alpha^m}{\Gamma(m)} \left[V \alpha^{-3/2} \sum_{\mathbf{l}} \sum_{i=1}^N \sum_{j=1}^M \phi_{-m+1/2} \left(\frac{\pi(\mathbf{x} - \mathbf{x}_i - \hat{\mathbf{p}}_i s_j - \mathbf{l})^2}{\alpha} \right) f(s_j) \hat{\mathbf{p}}_i + \sum_{\mathbf{k} \neq 0} e^{-2\pi i \mathbf{k} \cdot \mathbf{x}} \phi_{m-1}(\pi \alpha k^2) \hat{\mathbf{F}}(\mathbf{k}) \right], \quad (\text{C.6})$$

where we have used $\beta = \alpha/\xi$ in the first integral and $\beta = \alpha\xi$ in the second. The function ϕ_ν is the incomplete Γ - function:

$$\phi_\nu(x) = \int_1^\infty \xi^\nu e^{-x\xi} d\xi. \quad (\text{C.7})$$

Using the above expression for σ_m in the expressions for $\mathbf{S}^{(1)}$ and $\mathbf{S}^{(2)}$ (Eqs. 7.26-7.28 in chapter 7), we get the Ewald summation expression for the disturbance velocity field as:

$$\mathbf{u}(\mathbf{x}) = \frac{1}{4\pi} \left[\sum_{\mathbf{l}} \sum_{i=1}^N \sum_{j=1}^M \mathbf{A}(\alpha, \mathbf{x} - \mathbf{x}_i - \mathbf{p}_i s_j - \mathbf{l}) \cdot f(s_j) \mathbf{p}_i + \sum_{\mathbf{k} \neq 0} \mathbf{B}(\alpha, \mathbf{k}) \cdot \hat{\mathbf{F}}(\mathbf{k}) \exp(-2\pi i \mathbf{k} \cdot \mathbf{x}) \right], \quad (\text{C.8})$$

where the the two tensors \mathbf{A} and \mathbf{B} are given by:

$$\mathbf{A}(\alpha, \mathbf{x}) = \pi \alpha^{-3/2} \phi_{1/2}(\pi r^2/\alpha) (\mathbf{I}r^2 + \mathbf{x}\mathbf{x}) - 2\alpha^{-1/2} \exp(-\pi r^2/\alpha) \mathbf{I}, \quad (\text{C.9})$$

$$\mathbf{B}(\alpha, \mathbf{k}) = \frac{\pi \alpha^2 \phi_1(\pi \alpha k^2)}{V} [\mathbf{I}k^2 - \mathbf{k}\mathbf{k}], \quad (\text{C.10})$$

where we have used $\beta = \alpha/\xi$ in the first integral and $\beta = \alpha\xi$ in the second. The function ϕ_ν is the incomplete Γ - function:

$$\phi_\nu(x) = \int_1^\infty \xi^\nu e^{-x\xi} d\xi. \quad (\text{C.11})$$

Appendix D

Equivalence of the formulations by Hasimoto and Beennakker

In this appendix we explicitly demonstrate the equivalence between two alternate approaches to formulating periodic solutions to the Stokes equations. The first of these is Hasimoto's approach (Hasimoto (1959)) in which periodic solutions are found for flow past a periodic array of spheres. The approach utilises the periodicity of the solution by writing the velocity disturbance due to the periodic array of spheres in terms of a Fourier sum. This sum is however, only slowly converging and the Ewald summation technique is applied to split it into two parts, the first in real space and a second in Fourier space. Each of these is rapidly converging and can be used in simulations. Though Hasimoto's original analysis is for a single sphere, it is straightforward to extend it to the general case where there are N spheres in the unit cell. The extension to our simulations where there are M point forces along each swimmer's length is again straightforward. Hasimoto's expression for the disturbance velocity due to N point forces in a periodic unit cell array can be derived by using Eqs. 7.29 through 7.33 in chapter 7 and is given by:

$$\mathbf{u}(\mathbf{x}) = \sum_{\mathbf{l}} \sum_{i=1}^N \left[\left(\frac{\text{erfc}(\xi r)}{8\pi r} - \frac{\xi e^{-\xi^2 r^2}}{4\pi^{3/2}} \right) \mathbf{I} + \left(\frac{\text{erfc}(\xi r)}{8\pi r} + \frac{\xi e^{-\xi^2 r^2}}{4\pi^{3/2}} \right) \frac{(\mathbf{x} - \mathbf{x}_i - \mathbf{l})(\mathbf{x} - \mathbf{x}_i - \mathbf{l})}{r^2} \right] \cdot \mathbf{F}_i + \frac{1}{4\pi^2 V} \sum_{\mathbf{k} \neq 0} \frac{e^{-\pi k^2 / \xi^2}}{k^2} \left(1 + \frac{\pi^2 k^2}{\xi^2} \right) \left(\mathbf{I} - \frac{\mathbf{k}\mathbf{k}}{k^2} \right) \cdot \hat{\mathbf{F}}(\mathbf{k}) e^{-2\pi i \mathbf{k} \cdot \mathbf{x}}, \quad (\text{D.1})$$

where \mathbf{F}_i is the force due to sphere i on the fluid which is equal and opposite to the force on the sphere and $\xi = \sqrt{\pi/\alpha}$. In the above expression $r = |\mathbf{x} - \mathbf{x}_i|$; $\mathbf{l} = l_1 \mathbf{a}_1 + l_2 \mathbf{a}_2 + l_3 \mathbf{a}_3$ and l_1, l_2, l_3 are integers and $\mathbf{a}_i, i = 1, 2, 3$ are the unit cell vectors. The first part of the above expression constitutes the real sum and the second part the Fourier sum. The term $\hat{\mathbf{F}}(\mathbf{k})$ is defined as:

$$\hat{\mathbf{F}}(\mathbf{k}) = \sum_{i=1}^N \mathbf{F}_i e^{2\pi i \mathbf{k} \cdot \mathbf{x}_i}, \quad (\text{D.2})$$

where \mathbf{x}_i is the position of the i^{th} sphere.

Beenakker's approach (Beenakker (1986)), in a sense, is complimentary to that of Hasimoto's. Beenakker considers a three-dimensional periodic lattice in which each unit cell (labelled by index \mathbf{l}) contains N spherical particles (labelled by index i) of radius a . Also in Beenakker's analysis an assumption is made that that total force on the particles in a unit cell sums to zero:

$$\sum_{i=1}^N \mathbf{F}_i = 0, \quad (\text{D.3})$$

where \mathbf{F}_i is the force acting on particle i . We show that this assumption is not an essential one, however it does remain true for our case since the swimmers are force-free. Beenakker uses the Rotne-Prager mobility tensor to calculate a lattice sum which is nothing but the disturbance velocity at a given sphere's location due to the motion of all other spheres due to a force \mathbf{F}_i which is acting on them. The connection to Hasimoto's analysis can easily be made merely by considering a coordinate system moving with any one of the spheres. In order to simplify the analysis and make the connection with our case, we only consider the point-force contribution to the force which is $O(a)$, while neglecting the finite size contribution which scales as $O(a^3)$. Beenakker's method is to write down the lattice sum for the disturbance velocity in real space and then use a suitable function to split the real sum into two rapidly converging ones in real and Fourier space. With these considerations, Eq. 4 in Beenakker (1986) expressed in terms of a velocity disturbance in non-dimensional form is given by:

$$\mathbf{u}(\mathbf{x}) = \sum_{\mathbf{l}} \sum_{i=1}^N \left[\left(\frac{\text{erfc}(\xi r)}{8\pi r} - \frac{3\xi e^{-\xi^2 r^2}}{4\pi^{3/2}} + \frac{\xi^3 r^2 e^{-\xi^2 r^2}}{2\pi^{3/2}} \right) \mathbf{I} + \left(\frac{\text{erfc}(\xi r)}{8\pi r} + \frac{\xi e^{-\xi^2 r^2}}{4\pi^{3/2}} - \frac{\xi^3 r^2 e^{-\xi^2 r^2}}{2\pi^{3/2}} \right) \frac{(\mathbf{x} - \mathbf{x}_i - \mathbf{l})(\mathbf{x} - \mathbf{x}_i - \mathbf{l})}{r^2} \right] \cdot \mathbf{F}_i + \frac{1}{4\pi^2 V} \sum_{\mathbf{k} \neq 0} \frac{e^{-\pi k^2 / \xi^2}}{k^2} \left(1 + \frac{\pi^2 k^2}{\xi^2} + \frac{2\pi^4 k^4}{\xi^4} \right) \left(\mathbf{I} - \frac{\mathbf{k}\mathbf{k}}{k^2} \right) \cdot \hat{\mathbf{F}}(\mathbf{k}) e^{-2\pi i \mathbf{k} \cdot \mathbf{x}} \quad (\text{D.5})$$

In the rest of this appendix we show that Eqs. D.1 and D.5 are exactly equivalent. One way to do this is to inverse transform the third term in the Fourier sum in Eq. D.5 into real space and add it as a contribution to the real space sum. In this way we see already that the Fourier sums in Eq. D.1 and Eq. D.5 are exactly the same. Writing down the third term in the Fourier sum:

$$\begin{aligned} &= \frac{1}{4\pi^2 V} \sum_{\mathbf{k} \neq 0} \frac{e^{-\pi k^2 / \xi^2}}{k^2} \frac{2\pi^4 k^4}{\xi^4} \left(\mathbf{I} - \frac{\mathbf{k}\mathbf{k}}{k^2} \right) \cdot \hat{\mathbf{F}}(\mathbf{k}) e^{-2\pi i \mathbf{k} \cdot \mathbf{x}} \\ &= \frac{\pi^2}{2\xi^4 V} \sum_{\mathbf{k} \neq 0} e^{-\pi k^2 / \xi^2} k^2 \left(\mathbf{I} - \frac{\mathbf{k}\mathbf{k}}{k^2} \right) \cdot \hat{\mathbf{F}}(\mathbf{k}) e^{-2\pi i \mathbf{k} \cdot \mathbf{x}} \end{aligned} \quad (\text{D.6})$$

Since for force-free swimmers $\hat{\mathbf{F}}(0) = 0$, we can write the above expression with the $\mathbf{k} = 0$ included in the summation

$$= \frac{\pi^2}{2\xi^4 V} \sum_{\mathbf{k}} e^{-\pi k^2 / \xi^2} k^2 \left(\mathbf{I} - \frac{\mathbf{k}\mathbf{k}}{k^2} \right) \cdot \hat{\mathbf{F}}(\mathbf{k}) e^{-2\pi i \mathbf{k} \cdot \mathbf{x}} \quad (\text{D.7})$$

Considering first the term

$$\frac{\pi^2}{2\xi^4 V} \sum_{\mathbf{k}} e^{-\pi k^2 / \xi^2} k^2 \mathbf{I} \cdot \hat{\mathbf{F}}(\mathbf{k}) e^{-2\pi i \mathbf{k} \cdot \mathbf{x}} \quad (\text{D.8})$$

and substituting for $\hat{\mathbf{F}}(\mathbf{k})$ from Eq. D.2, we get

$$\frac{\pi^2}{2\xi^4 V} \sum_{\mathbf{k}} e^{-\pi k^2/\xi^2} k^2 \mathbf{I} \cdot \sum_{i=1}^N \mathbf{F}_i e^{2\pi \mathbf{k} \cdot \mathbf{x}_i} e^{-2\pi i \mathbf{k} \cdot \mathbf{x}} \quad (\text{D.9})$$

We can rearrange the order of summation to give

$$\frac{\pi^2}{2\xi^4 V} \sum_{i=1}^N \mathbf{F}_i \sum_{\mathbf{k}} e^{-\pi k^2/\xi^2} k^2 \mathbf{I} \cdot e^{-2\pi i \mathbf{k} \cdot (\mathbf{x} - \mathbf{x}_i)} \quad (\text{D.10})$$

We introduce the variable \mathbf{k}_c to denote the continuous wave vector variable and write the summation over the discrete wave vectors as an integral over a sum of dirac-delta functions at the discrete wave vectors

$$\frac{\pi^2}{2\xi^4 V} \sum_{i=1}^N \mathbf{I} \cdot \mathbf{F}_i \int_{\mathbf{k}_c} \sum_{\mathbf{k}} \delta(\mathbf{k}_c - \mathbf{k}) e^{-\pi k_c^2/\xi^2} k_c^2 e^{-2\pi i \mathbf{k}_c \cdot (\mathbf{x} - \mathbf{x}_i)} d\mathbf{k}_c \quad (\text{D.11})$$

The above integral is of the form

$$\int \hat{\mathbf{F}}(\mathbf{k}) \hat{\mathbf{G}}(\mathbf{k}) e^{-2\pi i \mathbf{k} \cdot \mathbf{x}'} d\mathbf{k} \quad (\text{D.12})$$

which is nothing but the inverse transform of the convolution integral with $\mathbf{x}' = \mathbf{x} - \mathbf{x}_i$. Therefore we have

$$\int \hat{\mathbf{F}}(\mathbf{k}) \hat{\mathbf{G}}(\mathbf{k}) e^{-2\pi i \mathbf{k} \cdot \mathbf{x}'} d\mathbf{k} = \int_{\bar{\mathbf{x}}} f(\mathbf{x}' - \bar{\mathbf{x}}) g(\bar{\mathbf{x}}) d\bar{\mathbf{x}} \quad (\text{D.13})$$

where f and g are the three-dimensional inverse Fourier transforms of $\hat{\mathbf{F}}$ and $\hat{\mathbf{G}}$ respectively. We can apply this formula to Eq. D.11 with $\hat{\mathbf{F}}(\mathbf{k}_c) = \sum_{\mathbf{k}} \delta(\mathbf{k}_c - \mathbf{k})$ and $\hat{\mathbf{G}}(\mathbf{k}_c) = e^{-\pi k_c^2/\xi^2} k_c^2$. It is straightforward to evaluate the inverse transforms of $\hat{\mathbf{F}}$ (Nijboer & De Wette (1957)) which is given by

$$\int_{\mathbf{k}_c} \sum_{\mathbf{k}} \delta(\mathbf{k}_c - \mathbf{k}) e^{-2\pi i \mathbf{k}_c \cdot \mathbf{x}} d\mathbf{k}_c = V \sum_{\mathbf{l}} \delta(\mathbf{x} - \mathbf{l}) \quad (\text{D.14})$$

The inverse transform of $\hat{\mathbf{G}}$ is found to be

$$\int_{\mathbf{k}_c} e^{-\pi k_c^2/\xi^2} k_c^2 e^{-2\pi i \mathbf{k}_c \cdot \mathbf{x}} d\mathbf{k}_c = -e^{-\xi^2 r^2} \xi^5 \left(\frac{2\xi^2 r^2 - 3}{2\pi^{7/2}} \right) \quad (\text{D.15})$$

Using Eqs. D.13-D.15 in Eq. D.11, we get

$$\frac{\pi^2}{2\xi^4 V} \sum_{i=1}^N \mathbf{F}_i \cdot \mathbf{I} \int_{\bar{\mathbf{x}}} V \sum_{\mathbf{l}} \delta(\mathbf{x}' - \bar{\mathbf{x}} - \mathbf{l}) g(\bar{\mathbf{x}}) d\bar{\mathbf{x}} \quad (\text{D.16})$$

$$= \frac{\pi^2}{2\xi^4} \sum_{\mathbf{l}} \sum_{i=1}^N \mathbf{F}_i \cdot \mathbf{I} g(\mathbf{x}' - \mathbf{l}) \quad (\text{D.17})$$

Substituting for g from Eq. D.15, we get

$$\sum_l \sum_{i=1}^N \mathbf{F}_i \cdot \mathbf{I} \left(-\frac{\xi^3 r^2}{2\pi^{3/2}} e^{-\xi^2 r^2} + \frac{3\xi e^{-\xi^2 r^2}}{4\pi^{3/2}} \right) \quad (\text{D.18})$$

We can proceed in a similar manner to transform the second term in Eq. D.7 into real space. The second term reduces to

$$-\frac{\pi^2}{2\xi^4 V} \sum_{i=1}^N \mathbf{F}_i \int_{\mathbf{k}_c} \sum_{\mathbf{k}} \delta(\mathbf{k}_c - \mathbf{k}) e^{-\pi k_c^2 / \xi^2} \mathbf{k}_c \mathbf{k}_c \cdot \mathbf{I} e^{-2\pi i \mathbf{k}_c \cdot (\mathbf{x} - \mathbf{x}_i)} d\mathbf{k}_c \quad (\text{D.19})$$

Now this is in the same form as Eq. D.12 with $\hat{F}(\mathbf{k}_c) = \sum_{\mathbf{k}} \delta(\mathbf{k}_c - \mathbf{k})$ and $\hat{G}(\mathbf{k}_c) = e^{-\pi k_c^2 / \xi^2} \mathbf{k}_c \mathbf{k}_c$. The inverse transform of \hat{G} can be shown to be given by

$$\int_{\mathbf{k}_c} e^{-\pi k_c^2 / \xi^2} \mathbf{k}_c \mathbf{k}_c e^{-2\pi i \mathbf{k}_c \cdot \mathbf{x}} d\mathbf{k}_c = -\frac{\xi^3}{4\pi^{7/2}} \nabla \nabla (e^{-\xi^2 r^2}) \quad (\text{D.20})$$

$$= \frac{\xi^5}{2\pi^{7/2}} \left(e^{-\xi^2 r^2} \mathbf{I} - 2\xi^2 e^{-\xi^2 r^2} \mathbf{x} \mathbf{x} \right) \quad (\text{D.21})$$

where $r = |\mathbf{x}|$. The inverse transform of \hat{F} is given by Eq. D.14. Substituting for inverse transform of \hat{F} and \hat{G} in Eq. D.19, we get the final expression in real space as

$$\sum_l \sum_{i=1}^N \mathbf{F}_i \cdot \left[-\frac{\xi e^{-\xi^2 r^2}}{4\pi^{3/2}} \mathbf{I} + \frac{\xi^3 e^{-\xi^2 r^2}}{2\pi^{3/2}} (\mathbf{x} - \mathbf{x}_i - \mathbf{l})(\mathbf{x} - \mathbf{x}_i - \mathbf{l}) \right] \quad (\text{D.22})$$

Adding Eqs. D.18 and D.22 to Eq. D.5 and simplifying we get

$$\begin{aligned} \mathbf{u}(\mathbf{x}) = \sum_l \sum_{i=1}^N \left[\left(\frac{\text{erfc}(\xi r)}{8\pi r} - \frac{\xi e^{-\xi^2 r^2}}{4\pi^{3/2}} \right) \mathbf{I} + \left(\frac{\text{erfc}(\xi r)}{8\pi r} + \frac{\xi e^{-\xi^2 r^2}}{4\pi^{3/2}} \right) \frac{(\mathbf{x} - \mathbf{x}_i)(\mathbf{x} - \mathbf{x}_i)}{r^2} \right] \cdot \mathbf{F}_i \\ + \frac{1}{4\pi^2 V} \sum_{\mathbf{k} \neq 0} \frac{e^{-\pi k^2 / \xi^2}}{k^2} \left(1 + \frac{\pi^2 k^2}{\xi^2} \right) \left(\mathbf{I} - \frac{\mathbf{k} \mathbf{k}}{k^2} \right) \cdot \hat{\mathbf{F}}(\mathbf{k}) e^{-2\pi i \mathbf{k} \cdot \mathbf{x}} \end{aligned} \quad (\text{D.23})$$

(D.24)

which is exactly the same as Eq. D.1. Thus we have shown the equivalence between the two approaches by Hasimoto and Beenakker.

References

- ABRAMOWITZ, M. & STEGUN, I. A. 1972 *Handbook of mathematical functions: with formulas, graphs, and mathematical tables*. Courier Dover Publications.
- ACRIVOS, A. 1971 Heat transfer at high pecelet number from a small sphere freely rotating in a simple shear field. *Journal of Fluid Mechanics* **46** (02), 233–240.
- ACRIVOS, A. 1980 A note on the rate of heat or mass transfer from a small particle freely suspended in a linear shear field. *Journal of Fluid Mechanics* **98** (02), 299–304.
- ACRIVOS, A. & GODDARD, J. 1965 Asymptotic expansions for laminar forced-convection heat and mass transfer. *Journal of Fluid Mechanics* **23** (02), 273–291.
- ACRIVOS, A. & TAYLOR, T. D. 1962 Heat and mass transfer from single spheres in stokes flow. *Physics of Fluids (1958-1988)* **5** (4), 387–394.
- ARIS, R. 2012 *Vectors, tensors and the basic equations of fluid mechanics*. Courier Dover Publications.
- BATCHELOR, G. 1970 Slender-body theory for particles of arbitrary cross-section in stokes flow. *Journal of Fluid Mechanics* **44** (03), 419–440.
- BATCHELOR, G. 1979 Mass transfer from a particle suspended in fluid with a steady linear ambient velocity distribution. *Journal of Fluid Mechanics* **95** (02), 369–400.
- BATCHELOR, G. K. 2000 *An introduction to fluid dynamics*. Cambridge university press.
- BEARD, K. & PRUPPACHER, H. R. 1971 A wind tunnel investigation of the rate of evaporation of small water drops falling at terminal velocity in air. *Journal of the atmospheric Sciences* **28** (8), 1455–1464.
- BEENAKKER, C. 1986 Ewald sum of the rotne–prager tensor. *The Journal of chemical physics* **85** (3), 1581–1582.
- BERG, H. C. 1993 *Random walks in biology*. Princeton University Press.
- BERG, H. C. 2004 *E. coli in Motion*. Springer.
- BRADY, J. F. & BOSSIS, G. 1988 Stokesian dynamics. *Annual review of fluid mechanics* **20**, 111–157.

- BRADY, J. F., PHILLIPS, R. J., LESTER, J. C. & BOSSIS, G. 1988 Dynamic simulation of hydrodynamically interacting suspensions. *Journal of Fluid Mechanics* **195**, 257–280.
- BRENNEN, C. & WINET, H. 1977 Fluid mechanics of propulsion by cilia and flagella. *Annual Review of Fluid Mechanics* **9** (1), 339–398.
- BRENNER, H. 1963 Forced convection heat and mass transfer at small pecllet numbers from a particle of arbitrary shape. *Chemical Engineering Science* **18** (2), 109–122.
- BRENNER, H. 1979 Taylor dispersion in systems of sedimenting nonspherical brownian particles. i. homogeneous, centrosymmetric, axisymmetric particles. *Journal of Colloid and Interface Science* **71** (2), 189–208.
- BROOKS, B. 2010 Suspension polymerization processes. *Chemical Engineering & Technology* **33** (11), 1737–1744.
- BUTLER, J. E. & SHAQFEH, E. S. 2002 Dynamic simulations of the inhomogeneous sedimentation of rigid fibres. *Journal of Fluid Mechanics* **468**, 205–237.
- CISNEROS, L. H., KESSLER, J. O., GANGULY, S. & GOLDSTEIN, R. E. 2011 Dynamics of swimming bacteria: Transition to directional order at high concentration. *Physical Review E* **83** (6), 061907.
- COX, R. 1969 The deformation of a drop in a general time-dependent fluid flow. *Journal of Fluid Mechanics* **37** (03), 601–623.
- COX, R. 1970 The motion of long slender bodies in a viscous fluid part 1. general theory. *Journal of Fluid mechanics* **44** (04), 791–810.
- COX, R., ZIA, I. & MASON, S. 1968 Particle motions in sheared suspensions xxv. streamlines around cylinders and spheres. *Journal of Colloid and Interface Science* **27** (1), 7–18.
- DHONT, J. K. 1996 *An introduction to dynamics of colloids*. Elsevier.
- DOMBROWSKI, C., CISNEROS, L., CHATKAEW, S., GOLDSTEIN, R. E. & KESSLER, J. O. 2004 Self-concentration and large-scale coherence in bacterial dynamics. *Physical Review Letters* **93** (9), 098103.
- DRESCHER, K., DUNKEL, J., CISNEROS, L. H., GANGULY, S. & GOLDSTEIN, R. E. 2011 Fluid dynamics and noise in bacterial cell–cell and cell–surface scattering. *Proceedings of the National Academy of Sciences* **108** (27), 10940–10945.
- DUGUID, H. & STAMPFER JR, J. 1971 The evaporation rates of small, freely falling water drops. *Journal of the atmospheric sciences* **28** (7), 1233–1243.
- DUNKEL, J., HEIDENREICH, S., DRESCHER, K., WENSINK, H. H., BÄR, M. & GOLDSTEIN, R. E. 2013 Fluid dynamics of bacterial turbulence. *Physical review letters* **110** (22), 228102.
- DURLOFSKY, L., BRADY, J. F. & BOSSIS, G. 1987 Dynamic simulation of hydrodynamically interacting particles. *Journal of fluid mechanics* **180**, 21–49.

- EBBENS, S. J. & HOWSE, J. R. 2010 In pursuit of propulsion at the nanoscale. *Soft Matter* **6** (4), 726–738.
- EVANS, A. A., ISHIKAWA, T., YAMAGUCHI, T. & LAUGA, E. 2011 Orientational order in concentrated suspensions of spherical microswimmers. *Physics of Fluids (1994-present)* **23** (11), 111702.
- EWALD, P. P. 1921 Die berechnung optischer und elektrostatischer gitterpotentiale. *Annalen der Physik* **369** (3), 253–287.
- FRANKEL, N. A. & ACRIVOS, A. 1968 Heat and mass transfer from small spheres and cylinders freely suspended in shear flow. *Physics of Fluids* **11**, 1913.
- GACHELIN, J., MIÑO, G., BERTHET, H., LINDNER, A., ROUSSELET, A. & CLÉMENT, É. 2013 Non-newtonian viscosity of escherichia coli suspensions. *Physical review letters* **110** (26), 268103.
- GODDARD, J. & ACRIVOS, A. 1966 Asymptotic expansions for laminar forced-convection heat and mass transfer part 2. boundary-layer flows. *Journal of Fluid Mechanics* **24** (02), 339–366.
- GRAY, J. 1958 The movement of the spermatozoa of the bull. *Journal of Experimental Biology* **35** (1), 96–108.
- GRAY, J. & HANCOCK, G. 1955 The propulsion of sea-urchin spermatozoa. *Journal of Experimental Biology* **32** (4), 802–814.
- GUASTO, J. S., JOHNSON, K. A. & GOLLUB, J. P. 2010 Oscillatory flows induced by microorganisms swimming in two dimensions. *Physical review letters* **105** (16), 168102.
- GUPALO, I. P. & RIAZANTSEV, I. S. 1972 Diffusion on a particle in the shear flow of a viscous fluid. approximation of the diffusion boundary layer: Pmm vol. 36, nâ 3, 1972, pp. 475–479. *Journal of Applied Mathematics and Mechanics* **36** (3), 447–451.
- GUPALO, I. P., RIAZANTSEV, I. S. & ULIN, V. 1975 Diffusion on a particle in a homogeneous translational-shear flow. *Prikladnaia Matematika i Mekhanika* **39**, 497–504.
- HAPPEL, J. & BRENNER, H. 1983 *Low Reynolds number hydrodynamics: with special applications to particulate media*, , vol. 1. Springer.
- HASIMOTO, H. 1959 On the periodic fundamental solutions of the stokes equations and their application to viscous flow past a cubic array of spheres. *Journal of Fluid Mechanics* **5** (02), 317–328.
- HERNÁNDEZ-ORTIZ, J. P., DE PABLO, J. J. & GRAHAM, M. D. 2007 Fast computation of many-particle hydrodynamic and electrostatic interactions in a confined geometry. *Physical review letters* **98** (14), 140602.
- HERNANDEZ-ORTIZ, J. P., STOLTZ, C. G. & GRAHAM, M. D. 2005 Transport and collective dynamics in suspensions of confined swimming particles. *Physical Review Letters* **95** (20), 204501.

- HERNANDEZ-ORTIZ, J. P., UNDERHILL, P. T. & GRAHAM, M. D. 2009 Dynamics of confined suspensions of swimming particles. *Journal of Physics: Condensed Matter* **21** (20), 204107.
- HILL, N. & PEDLEY, T. 2005 Bioconvection. *Fluid Dynamics Research* **37** (1), 1–20.
- HINCH, E. & LEAL, L. 1972 The effect of brownian motion on the rheological properties of a suspension of non-spherical particles. *Journal of Fluid Mechanics* **52** (04), 683–712.
- HOHENEGGER, C. & SHELLEY, M. J. 2010 Stability of active suspensions. *Phys. Rev. E* **81**, 046311.
- ISHIKAWA, T., LOCSEI, J. & PEDLEY, T. 2008 Development of coherent structures in concentrated suspensions of swimming model micro-organisms. *Journal of Fluid Mechanics* **615**, 401–431.
- ISHIKAWA, T. & PEDLEY, T. 2008 Coherent structures in monolayers of swimming particles. *Physical review letters* **100** (8), 088103.
- JEFFERY, G. B. 1922 The motion of ellipsoidal particles immersed in a viscous fluid. *Proceedings of the Royal Society of London. Series A* **102** (715), 161–179.
- KAO, S., COX, R. & MASON, S. 1977 Streamlines around single spheres and trajectories of pairs of spheres in two-dimensional creeping flows. *Chemical Engineering Science* **32** (12), 1505–1515.
- KARMAKAR, R., GULVADY, R., S, T. M. & VENKATESH, K. V. 2014 Effect of run and tumble on the rheological behaviour of a suspension of pushers. *Physics of Fluids (1994-present)* .
- KASYAP, T. V., KOCH, D. L. & WU, M. 2014 Tracer transport in bacterial suspensions .
- KINZER, G. D. & GUNN, R. 1951 The evaporation, temperature and thermal relaxation-time of freely falling waterdrops. *Journal of Meteorology* **8** (2), 71–83.
- KOCH, D. L. & SUBRAMANIAN, G. 2011 Collective hydrodynamics of swimming microorganisms: Living fluids. *Annual Review of Fluid Mechanics* **43**, 637–659.
- KOSSACK, C. A. & ACRIVOS, A. 1974 Steady simple shear flow past a circular cylinder at moderate reynolds numbers: a numerical solution. *Journal of Fluid Mechanics* **66** (02), 353–376.
- LAUGA, E. & POWERS, T. R. 2009 The hydrodynamics of swimming microorganisms. *Reports on Progress in Physics* **72** (9), 096601.
- LEAL, L. & HINCH, E. 1971 The effect of weak brownian rotations on particles in shear flow. *Journal of Fluid Mechanics* **46** (04), 685–703.
- LEAL, L. G. 2007 *Advanced transport phenomena: fluid mechanics and convective transport processes*, , vol. 7. Cambridge University Press.

- LEPTOS, K. C., GUAUTO, J. S., GOLLUB, J. P., PESCI, A. I. & GOLDSTEIN, R. E. 2009 Dynamics of enhanced tracer diffusion in suspensions of swimming eukaryotic microorganisms. *Physical review letters* **103** (19), 198103.
- MACKAPLOW, M. B. & SHAQFEH, E. S. 1998 A numerical study of the sedimentation of fibre suspensions. *Journal of Fluid Mechanics* **376**, 149–182.
- MEHANDIA, V. & NOTT, P. R. 2008 The collective dynamics of self-propelled particles. *Journal of Fluid Mechanics* **595**, 239–264.
- MENDELSON, N. H., BOURQUE, A., WILKENING, K., ANDERSON, K. R. & WATKINS, J. C. 1999 Organized cell swimming motions in bacillus subtilis colonies: patterns of short-lived whirls and jets. *Journal of bacteriology* **181** (2), 600–609.
- MOROZOV, A. & MARENDUZZO, D. 2014 Enhanced diffusion of tracer particles in dilute bacterial suspensions. *Soft Matter* .
- NAVANEETH K. MARATH, G. S. 2013 Private communication .
- NIJBOER, B. & DE WETTE, F. 1957 On the calculation of lattice sums. *Physica* **23** (1), 309–321.
- POE, G. & ACRIVOS, A. 1975 Closed-streamline flows past rotating single cylinders and spheres: inertia effects. *Journal of Fluid Mechanics* **72** (04), 605–623.
- POE, G. & ACRIVOS, A. 1976 Closed streamline flows past small rotating particles: heat transfer at high péclet numbers. *International Journal of Multiphase Flow* **2** (4), 365–377.
- POLIN, M., TUVAL, I., DRESCHER, K., GOLLUB, J. & GOLDSTEIN, R. E. 2009 Chlamydomonas swims with two âgearsâ in a eukaryotic version of run-and-tumble locomotion. *Science* **325** (5939), 487–490.
- POLYANIN, A. 1984 Three-dimensional diffusive boundary-layer problems. *Journal of Applied Mechanics and Technical Physics* **25** (4), 562–571.
- POWELL, R. 1983 External and internal streamlines and deformation of drops in linear two-dimensional flows. *Journal of colloid and interface science* **95** (1), 148–162.
- RAFAÏ, S., JIBUTI, L. & PEYLA, P. 2010 Effective viscosity of microswimmer suspensions. *Phys. Rev. Lett.* **104**, 098102.
- RAJA, R. V., SUBRAMANIAN, G. & KOCH, D. L. 2010 Inertial effects on the rheology of a dilute emulsion. *Journal of Fluid Mechanics* **646**, 255–296.
- RAMASWAMY, S. 2010 The mechanics and statistics of active matter. *The Mechanics and Statistics of Active Matter* **1**, 323–345.
- RHINES, P. & YOUNG, W. 1983 How rapidly is a passive scalar mixed within closed streamlines? *Journal of Fluid Mechanics* **133**, 133–145.

- ROBERTSON, C. & ACRIVOS, A. 1970a Low reynolds number shear flow past a rotating circular cylinder. part 1. momentum transfer. *Journal of Fluid Mechanics* **40** (04), 685–703.
- ROBERTSON, C. & ACRIVOS, A. 1970b Low reynolds number shear flow past circular cylinder. part 2. heat transfer. *J. Fluid Mech* **40** (part 4), 705–718.
- ROGALLO, R. S. 1981 *Numerical experiments in homogeneous turbulence*, , vol. 81315. National Aeronautics and Space Administration.
- SAINTILLAN, D. 2010 Extensional rheology of active suspensions. *Physical Review E* **81** (5), 056307.
- SAINTILLAN, D., DARVE, E. & SHAQFEH, E. S. 2005 A smooth particle-mesh ewald algorithm for stokes suspension simulations: The sedimentation of fibers. *Physics of Fluids (1994-present)* **17** (3), 033301.
- SAINTILLAN, D. & SHELLEY, M. J. 2007 Orientational order and instabilities in suspensions of self-locomoting rods. *Physical review letters* **99** (5), 058102.
- SAINTILLAN, D. & SHELLEY, M. J. 2008a Instabilities and pattern formation in active particle suspensions: kinetic theory and continuum simulations. *Physical Review Letters* **100** (17), 178103.
- SAINTILLAN, D. & SHELLEY, M. J. 2008b Instabilities, pattern formation, and mixing in active suspensions. *Physics of Fluids (1994-present)* **20** (12), 123304.
- SAINTILLAN, D. & SHELLEY, M. J. 2012 Emergence of coherent structures and large-scale flows in motile suspensions. *Journal of the Royal Society Interface* **9** (68), 571–585.
- SIEROU, A. & BRADY, J. F. 2001 Accelerated stokesian dynamics simulations. *Journal of Fluid Mechanics* **448**, 115–146.
- SIMHA, A. R. & RAMASWAMY, S. 2002 Hydrodynamic fluctuations and instabilities in ordered suspensions of self-propelled particles. *Physical review letters* **89** (5), 058101_1–058101_4.
- SOKOLOV, A. & ARANSON, I. S. 2009 Reduction of viscosity in suspension of swimming bacteria. *Physical Review Letters* **103** (14), 148101.
- SOKOLOV, A., ARANSON, I. S., KESSLER, J. O. & GOLDSTEIN, R. E. 2007 Concentration dependence of the collective dynamics of swimming bacteria. *Physical Review Letters* **98** (15), 158102.
- SUBRAMANIAN, G. & KOCH, D. 2006a Centrifugal forces alter streamline topology and greatly enhance the rate of heat and mass transfer from neutrally buoyant particles to a shear flow. *Physical review letters* **96** (13), 134503.
- SUBRAMANIAN, G. & KOCH, D. L. 2006b Inertial effects on the transfer of heat or mass from neutrally buoyant spheres in a steady linear velocity field. *Physics of Fluids (1994-present)* **18** (7), 073302.

- SUBRAMANIAN, G. & KOCH, D. L. 2009 Critical bacterial concentration for the onset of collective swimming. *Journal of Fluid Mechanics* **632**, 359–400.
- SUBRAMANIAN, G., KOCH, D. L. & FITZGIBBON, S. R. 2011a The stability of a homogeneous suspension of chemotactic bacteria. *Physics of Fluids (1994-present)* **23** (4), 041901.
- SUBRAMANIAN, G., KOCH, D. L., ZHANG, J. & YANG, C. 2011b The influence of the inertially dominated outer region on the rheology of a dilute dispersion of low-reynolds-number drops or rigid particles. *Journal of Fluid Mechanics* **674**, 307–358.
- SUBRAMANIAN, G. & NOTT, P. R. 2012 The fluid dynamics of swimming microorganisms and cells. *Journal of the Indian Institute of Science* **91** (3), 283–314.
- TORZA, S., HENRY, C., COX, R. & MASON, S. 1971 Particle motions in sheared suspensions. xxvi. streamlines in and around liquid drops. *Journal of Colloid and Interface Science* **35** (4), 529–543.
- TUVAL, I., CISNEROS, L., DOMBROWSKI, C., WOLGEMUTH, C. W., KESSLER, J. O. & GOLDSTEIN, R. E. 2005 Bacterial swimming and oxygen transport near contact lines. *Proceedings of the National Academy of Sciences of the United States of America* **102** (7), 2277–2282.
- UNDERHILL, P. T., HERNANDEZ-ORTIZ, J. P. & GRAHAM, M. D. 2008 Diffusion and spatial correlations in suspensions of swimming particles. *Physical review letters* **100** (24), 248101.
- VIVALDO-LIMA, E., WOOD, P. E., HAMIELEC, A. E. & PENLIDIS, A. 1997 An updated review on suspension polymerization. *Industrial & engineering chemistry research* **36** (4), 939–965.
- WALTHER, A. & MÜLLER, A. H. 2008 Janus particles. *Soft Matter* **4** (4), 663–668.
- WHEATLEY, G. 1994 Applied numerical analysis.
- WU, M., ROBERTS, J. W., KIM, S., KOCH, D. L. & DELISA, M. P. 2006 Collective bacterial dynamics revealed using a three-dimensional population-scale defocused particle tracking technique. *Applied and environmental microbiology* **72** (7), 4987–4994.
- WU, X.-L. & LIBCHABER, A. 2000 Particle diffusion in a quasi-two-dimensional bacterial bath. *Physical Review Letters* **84** (13), 3017.
- YANG, C., ZHANG, J., KOCH, D. L. & YIN, X. 2011 Mass/heat transfer from a neutrally buoyant sphere in simple shear flow at finite reynolds and peclet numbers. *AIChE Journal* **57** (6), 1419–1433.
- YU-FANG, P. & ACRIVOS, A. 1968 Heat transfer at high peclet number in regions of closed streamlines. *International Journal of Heat and Mass Transfer* **11** (3), 439–444.

